# Photocatalytic HER Activity of Semiconductor Heterostructures and the Structures and Properties of Cadmium Phosphohalides

**A Thesis Submitted for the Degree of**

## Doctor of Philosophy

**By**


## Anand Kumar Roy




**New Chemistry Unit**

**Jawaharlal Nehru Centre for Advanced Scientific Research**

**(A Deemed University)**

**Jakkur, Bangalore-560064 (India)**


May 2019

**Dedicated to my Late Grandfather and to all my Teachers**

# DECLARATION

I hereby declare that the matter embodied in this thesis entitled **"Photocatalytic HER Activity of Semiconductor Heterostructures and the Structures and Properties of Cadmium Phosphohalides"** is the result of investigations carried out by me under the supervision of Prof. C. N. R. Rao, FRS at the New Chemistry Unit, JNCASR, Bangalore, India and that it has not been submitted elsewhere for the award of any degree or diploma.

In keeping with the general practice in reporting scientific observations, due acknowledgement has been made whenever the work described is based on the findings of other investigators.

(Anand Kumar Roy)

# CERTIFICATE

I hereby certify that the matter embodied in this thesis entitled **"Photocatalytic HER Activity of Semiconductor Heterostructures and the Structures and Properties of Cadmium Phosphohalides"** has been carried out by Mr. Anand Kumar Roy at the New Chemistry Unit, Jawaharlal Nehru Centre for Advanced Scientific Research, Bangalore, India under my supervision and it has not been submitted elsewhere for the award of any degree or diploma.

Prof. C. N. R. Rao
(Research Supervisor)

# ACKNOWLEDGEMENTS

First and foremost, I take this opportunity to express my sincere gratitude to my research supervisor, **Prof. C. N. R. Rao, FRS,** for giving me the opportunity to work under him and introducing me to the area of material science. He has always been supportive and encouraging. He has not only been instrumental in shaping my research, but my entire personality, my outlook towards life as a whole. I express my deepest gratitude to him.

My sincere thanks to my collaborators, Prof. Umesh V. Waghmare, Dr. Anjali Singh, Dr. S. Lingampalli, Dr. Assa Aravindh, Dr. Kouser, Dr. Chithaiah, Dr. K. Manjunath Dr. Shenoy Dr. Manjeet, Ms. Suchitra Mr. Sujay, Mr. Swaraj for their valuable discussions and contributions.

I shall remain ever thankful to all my seniors for their valuable suggestions. It has been a wonderful experience working with all my past and present labmates, Dr. Moses, Dr. Naidu, Dr. Urmi Maitra, Dr. Nitesh Kumar, Dr. Rana Saha, Dr. Gopal, Dr. Ram Kumar, Dr. Sunita Dey, Dr. Pratap Vishnoi, Dr. K. Manjunath, Dr. Pramoda, Dr. Sreedhara, Dr. Uttam, Dr. Chhetri, Mr. Monis, Ms. Manaswee, Mr. S. Manjunatha, Mr. Rajesh, Mr. Amit Mr. Rohit, Mr. Reetendera, Mr. Swaraj, and I thank them all for their help in various occasions.

I thank the faculties namely**,** Prof. A. Sundaresan, Prof. S. Kulkarni, Prof. S. M. Shivaprasad, Prof. T. K. Maji, Prof. Eswaramoorthy, Prof. S. J. Gerorge, Prof. T. Govindaraju, Dr. Ujjal K. Gautam, Prof. R. Viswanatha, Dr. Sebastian C. Peter and for all the courses and discussions.

I thank the coordinator of POCE, Prof. S. N. Bhat for giving me an opportunity to interact with the enthusiastic young minds.

I am very thankful to the all the faculty members of school of chemistry at university of Hyderabad for wonderful course work and experimental trainings. I am especially thankful to Prof. S. Pal, Prof. S. K. Das, Prof. M. Durga prasad Prof. M. Periasamy Prof. K. C. Kumara swamy, Prof. T. P. Radhakrishnan for always been supportive and source of motivation.

I shall always remain thankfull to the Pandit Madan Mohan Malaviya founder of Banaras Hindu University which has immense contribution in shaping my life.

I thank the help of the technical staff namely Ms. N. R. Selvi (for FESEM), Mrs. T. Usha (for TEM), Mr. Vasu (for UV, PL, IR, TGA), Mr. Anil (for XRD), Mr. Srinath, Mr. Srinivasa Rao, Mr. Srinivas (for technical assistance), Mr. Mahesh, Dr. Joy, Mr. Prajwal, Mr. Jagadesh and Mr. Shivkumar. I thank Mrs. Shashi, Mrs. Sudha, Mr. Gowda and Mr. Victor for their help in various aspects.

I thank the Council of Scientific and Industrial Research (CSIR), India for the fellowship. I also thank SSL-RAK-CAM for the student fellowship. I thank JNCASR and IISc for extending course work and research facilities. The hostel, Admin, Academic, Library and Dhanvantari and other departmental staff for all their help during my stay here.

I take this opportunity to thank Mrs. Indumati Rao for all the affection and love I have received. I consider myself blessed to have received all these cares and more than everything the wisdom of advice. I take this opportunity to thank Mr. Sanjay Rao for his hospitality and friendly behavior.

Thanks to all my batchmates and friends, Pawan, Manjeet, Rajaji, Aditya, KD, Samarth, Somo, with whom I started my life at this center and whose cheerful company made these six years of life so wonderful.

Finally, I thank my parents and family members for their support.

# PREFACE

This thesis deals with the synthesis, properties and applications of various semiconductor-based materials for energy applications. Seminal increase in the world population has created alarming signs of energy crisis and environmental pollution. Dependence on the carbonaceous source of fuel for energy production has undesired effects such as $CO_2$ and CO emission known to adversely affect the atmosphere. In this regard, artificial photosynthesis has gained tremendous importance because of green way of energy production. It has a potential to replace the conventional fuels with sustainable and renewable energy sources. There have been several efforts to develop stable, efficient, low-cost and scalable photocatalysts. Present thesis deals with the various aspects of artificial photosynthesis, material design and strategies to obtain better performance in converting solar energy into chemical fuel. Thesis is divided into two parts, wherein **Part 1** deals with the photocatalytic hydrogen generation by semiconductor-based heterostructures with CdS as a photosensitizer, **Part 2** deals with the synthesis and properties of semiconductor materials obtained by the partial or complete aliovalent anionic substitution of various metal chalcogenides. **Part 1** is divided into three chapters of which **Chapter 1** gives an overview of the photocatalytic splitting of water. **Chapter 2** discusses the role of the surface area and morphology of oxide nanostructures on the visible-light induced hydrogen generation in heterostructure of formula $ZnO(TiO_2)$/Pt/CdS. **Chapter 3** discusses the synthesis, properties and application of $TiO_2$/NiO/$Cd_{0.8}Zn_{0.2}S$ and ZnO/NiO/CdS heterostructures for visible-light induced hydrogen generation wherein emphasis has been given in replacing scarce and costly noble metal cocatalyst Pt, by earth abundant and and economically viable NiO cocatalyst.

**Part 2** is divided into six chapters with **Chapter 1** gives a brief overview of aliovalent anionic substitution in inorganic semiconductor materials, **Chapter 2** deals with the aliovalent anionic substitution, of $P^{3-}$ and $Cl^-$ in the place of $S^{2-}$, in CdS and the effect of co-substitution on the electronic structure and properties. **Chapter 3** describes the synthesis and properties of a compounds of compositions $Cd_4P_2Cl_3$, $Cd_4As_2Br_3$, and $Cd_4Sb_2I_3$ which are analogues of CdS, CdSe, and CdTe respectively. Synthesis and properties of family of cadmium phosphohalides with different Cd/P

and Cd/Cl ratios are discussed in **Chapter 4**, along with their HER activity. **Chapter 5** describes the synthesis, and unique photocatalytic properties of a family of compound of formula $Cd_4P_2X_3$ (X= Cl, Br or I) and their application in HER and $CO_2$ reduction reaction. Effect of different halides in $Cd_4P_2X_3$ (X= Cl, Br, and I) on the photophysical and electronic properties has been investigated. **Chapter 6**, describes the affect of $Mn^{2+}$ substitution in cadmium phosphochloride compounds.

# TABLE OF CONTENTS

# Part 1

## Hydrogen Generation through Water Splitting, using Semiconductor Heterostructures Based on CdS.

# Chapter 1

# An Overview of Photochemical Hydrogen Generation from Water


## Summary*

Photochemical approach to transforming solar energy into chemical fuel ($H_2$) is practically achievable and has the potential for large scale production. Various aspects of this technology such as reaction involved, physiochemical conditions, types of photocatalyst materials such as oxide, oxysulfides, nitrides, oxynitrides, sulfides have been discussed. Various approaches to obtain efficient conversion of solar energy into chemical fuel have

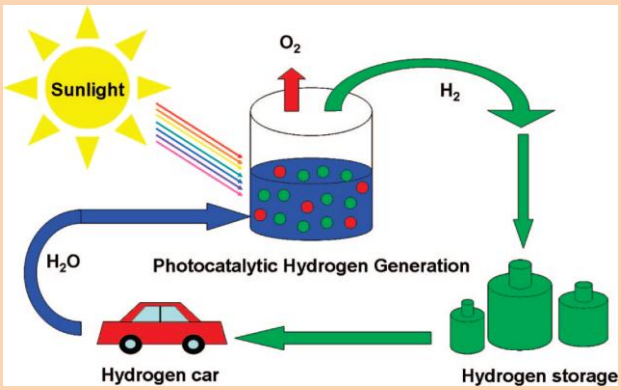


also been discussed. Narrowing the band gap of the semiconductor photocatalyst by different means such as doping of cations or anions, making solid solutions helps in the harvesting of large fraction solar radiation. Charge carrier life-time has a critical role in determining the catalytic activity of a material. Increasing the life-time of charge carriers by the use of co-catalysts, semiconductor heterostructure and other means provides better photocatalytic activity. Role of surface area, morphology, and crystallinity on catalytic activity of photocatalyst have been described. Hydrogen production from the sacrificial-based system is also discussed wherein selection of sacrificial donors is essential. It is adviced that commonly found water pollutant such as $H_2S$ or organic pollutant should be used as sacrificial agents. A brief description of the importance of sea-water splitting using sun-light is also discussed.

# 1. Introduction

Increase in the world population has led to notable increase in the energy consumption rate, resulting in a significant dependence on carbonaceous fuels. Limited availability along with environmental hazards related to carbonaceous fuel highlight the need for the clean and renewable sources of energy.[1] Since it is known that hydrogen is a clean source of energy ($H_2O$ as a byproduct) with energy density value as high as 142 MJ/kg, motivates researchers to find methods to produce hydrogen on a large scale using economically viable routes.[2] Almost 85 to 90 % of $H_2$ is presently being produced by natural gas reforming which requires high temperature (up to 900 ºC) and pressure (1.5-3 MPa) and results in the evolution of like hazardous byproducts CO and $CO_2$.[3] It is therefore, highly desirable to produce hydrogen by employing a renewable source of energy with minimum environmental hazard. In doing so, natural photosynthesis involving sunlight inspires us to use abundant solar energy. The well-known process of photosynthesis in plants involves a redox reaction wherein $CO_2$ is converted into carbohydrate and $H_2O$ is oxidize into $O_2$ by the photoexcited electrons and holes respectively. The process of photosynthesis involves single or two photosystems (Z-scheme). There have been strategies to convert solar energy into chemical energy mimicking natural photosynthesis wherein $CO_2$ and $H_2O$ are used as reactants.[4] These processes involve the use of photocatalysts with action similar to the chloroplast in plants which absorbs sunlight and generates excited electron and hole pairs which then take part in the reduction and oxidation of $H_2O$ respectively. These materials can be directly used as a suspension in the pool of water (Photochemical water splitting) or can be coated on a conductive substrate in the form of a film and used in the assistance of minimum voltage (photoelectrochemical $H_2O$ splitting (**Figure 1**).[5] It should be noted that splitting of $H_2O$ into $H_2$ and $O_2$ is a thermodynamically uphill reaction ($\Delta G$ = 237 kJ/mol) and requires careful experimental strategies.[6] Since the discovery of hydrogen production from n-$TiO_2$ using the photoelectrochemical (PEC) method by Honda and Fujisima's, there have been enormous efforts to develop technologies for semiconductor-based hydrogen evolution by water splitting.[5b] Over the last four decades, several semiconductor photocatalysts such as $La_2Ti_2O_7$, $Sr_2M_2O_7$( M= Nb, Ta), $TiO_2$, $Ga_2O_3$,

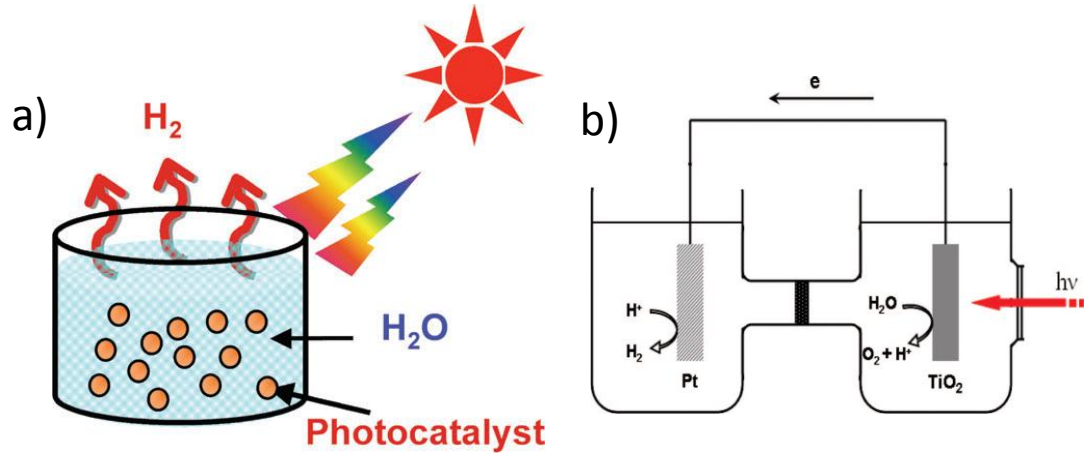


Figure1. a) Schematic representation of Photochemical hydrogen evolution. Reproduced with permission from ref 6. Copyright The Royal Society of Chemistry 2009. and b) Photoelectrochemical (PEC) hydrogen evolution. Reproduced with permission from ref 5b. Copyright 1972 Nature Publishing Group.

$K_2La_2Ti_3O_{10}$, $NaTiO_3$, β-$Ge_3N_4$, etc. have been reported for splitting water into $H_2$ and $O_2$ under UV-light.[7] Considering that only 4-5 % of solar radiation contains UV-light whereas visible-light contribution is 46-50%, it is necessary to develop stable and efficient visible-light-harvesting semiconductor photocatalyst to transform a large proportion of solar energy into chemical energy ($H_2$). Over the last decade, several noble visible-light absorbing semiconductor photocatalysts have been discovered and they harvest a large fraction of the solar radiation and perform efficient water splitting reaction.

## 2. Basic Principles of Photocatalytic Water Splitting

Photocatalytic water splitting is a process in which $H_2O$ can be splitted into $H_2$ and $O_2$ in the presence of artificial or natural light (sunlight) using photocatalyst materials.[5a] Photocatalysts are semiconductor materials with a finite band gap which absorbs solar radiation of energy equal to or greater than the band gap. Semiconductors possess non-overlapping valence and conduction band which upon photoexcitation generates electrons ($e^-$) and holes ($h^+$) in the conduction and valence band respectively. These electrons and holes are called photogenerated charge carriers and these take part in the reduction and oxidation of water to produce $H_2$ and $O_2$ respectively.[6] Reduction of water to $H_2$ is a two-electron process whereas oxidation of water to $O_2$ is a four-

electron process. A requirement of four electrons make oxidation of water kinetically more challenging than reduction of water and hence is a rate-limiting step of water splitting.

It should be noted that splitting of water into $H_2$ and $O_2$ can only be facilitated by photogenerated electron-hole pair with required thermodynamic potential wherein conduction band minimum (CBM), and valence band maxima (VBM) of semiconductor material employed for water splitting should be more negative and more positive than the water redox potential respectively at a given pH (**Figure 2**).[4-5]

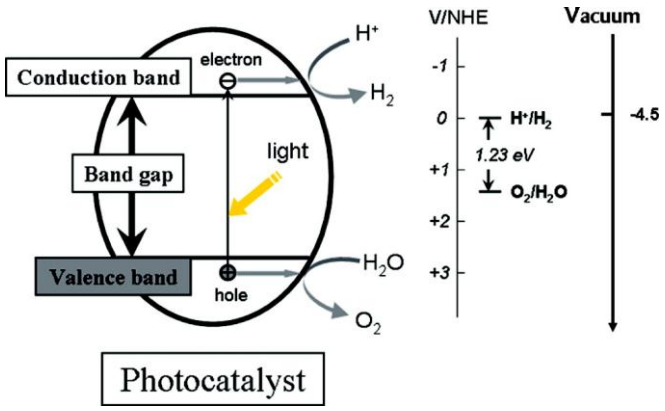


Figure 2. Fundamental principle involved in the semiconductor-based water splitting. Reproduced with the permission from ref 5. Copyright 2010 American Chemical Society.

At pH 0, $H^+/H_2$ and $O_2/H_2O$ redox potential values are 0 and 1.23 V respectively hence theoretical minimum band gap of semiconductor material to perform water splitting should be 1.23 eV corresponding to the solar spectrum of wavelength till 1100 nm.[6] Library of the semiconductor materials with their band gaps and band edge positions with respect to water redox potential are shown in **Figure 3** indicating their thermodynamic suitability for photoreduction, photooxidation and overall water splitting.[4] Semiconductors with suitable CBM and VBM positions ideally can be used for overall water splitting whereas semiconductors with only suitable CBM or VBM position can be used for photoreduction or photooxidation of water respectively. The band edges of semiconductor materials usually vary with a change in the electrolyte pH (**Figure 4**).[5a, 8] Screening of semiconductors for water splitting

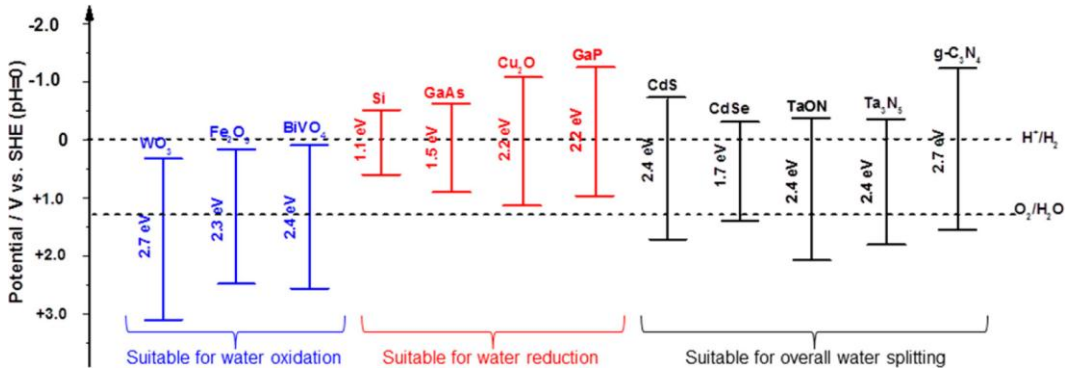


Figure 3. Band positions and band gaps of semiconductors with respect to $H_2O$ redox potential at pH=0. Reproduced with the permission from ref 4. Copyright 2018 American Chemical Society.

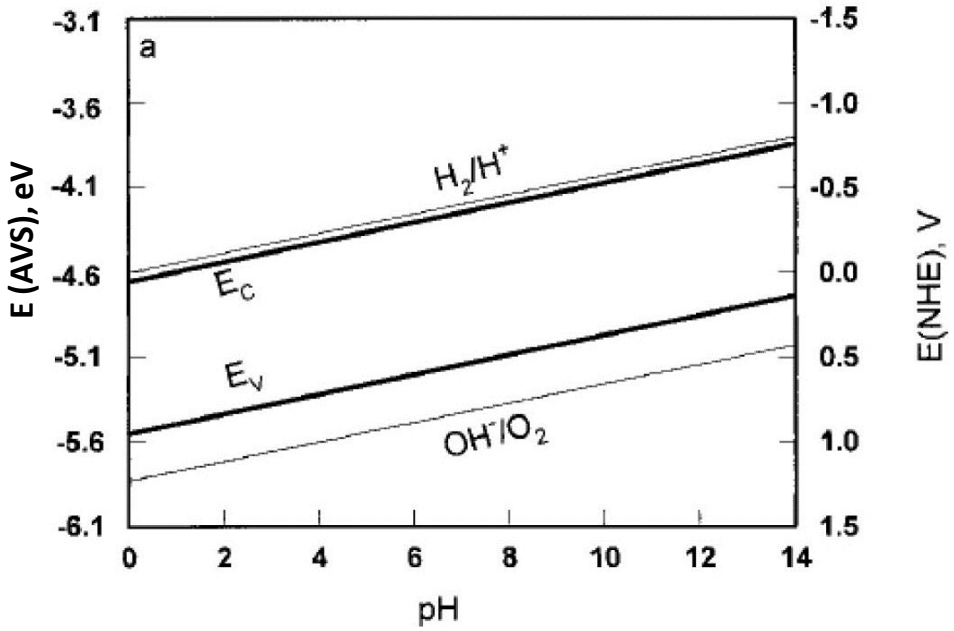


Figure 4. Dependence of VBM and CBM positions on pH of the reaction medium. Reproduced with permission from ref 8. Copyright 2000 The Mineralogical Society of America.

on the basis of band alignment is just the thermodynamic criteria, photocatalytic performance of materials depends on so many other factors such as charge mobility, overpotential, lifetime of charge carriers.

## 2.1 The Process involved in Photocatalytic water splitting

**Figure 5** shows the steps involved in photocatalytic water splitting.[5a, 9] Absorption of light by suitable semiconductor cause excitation of the valence band (HOMO)

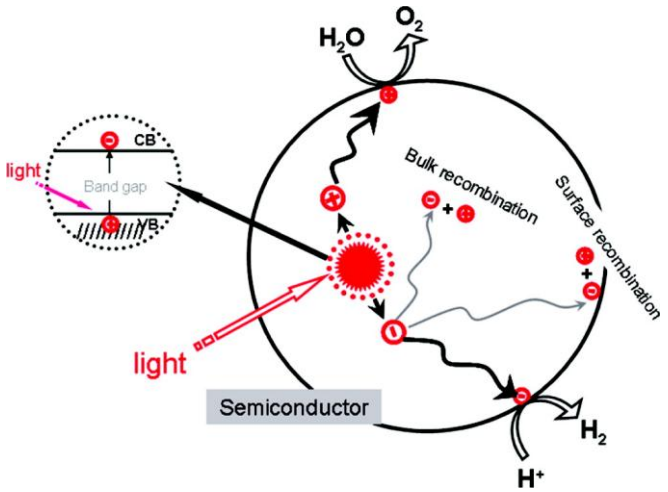


Figure 5. The process involved in semiconductor-based photocatalytic water splitting. Reproduced with the permission from ref. 9. Copyright 1995 American Chemical Society.

electrons ($e^-$) to the conduction band (LUMO), leaving behind holes ($h^+$) in the valence band. Photogenerated electrons and holes can follow these paths a) bulk recombination due to columbic attraction, b) separation and migration towards the surface, and c) recombination at the surface. Recombination of the charge carriers is a very facile process resulting in the loss of the carriers in the form of heat or radiation; however, separation of the charge carriers require external field. Therefore, a critical step deciding catalytic activity is charge carriers separation/recombination rate. Surface available charge carriers involved in the redox reaction result in the formation of $H_2$ and $O_2$. The final yield of hydrogen production is dependent on all the involved steps. The rate of hydrogen evolution reaction (HER) and oxygen evolution reaction (OER) markedly depends on the number of photoexcited electrons and holes available at the interface of semiconductor photocatalyst and water. Clearly, any process which reduces the number of photogenerated charge carriers should be avoided to obtain higher hydrogen and oxygen yield. Since surface back reaction (SBR) wherein produced $H_2$ and $O_2$ forms $H_2O$ is a thermodynamically downhill reaction, it should be avoided to obtain a higher yield of $H_2$ and $O_2$.

## 2.2 Reaction Setup and Evaluation of Photocatalytic Activity

The most common reaction setup includes a reaction cell made of quartz (for UV-active catalyst) or glass (for visible-light active catalyst) cells, light source (high

pressure Hg-lamp for UV-active catalyst or Xe-lamp with cut-off filter for visible light studies), gas chromatography (to measure the evolved $H_2$ and $O_2$ gas), vacuum pump (to remove dissolved oxygen in photocatalytic solution), inert gas purging system. If the photocatalytic activity is too high to measure by gas chromatography , volumetric method comes into use to evaluate the amount of evolved gases.

Performance of a catalyst can be represented using different parameters such as activity (μmol/h), Apparent quantum yield (AQY), solar to hydrogen conversion efficiency (STH).

$$Apparent\ quantum\ yield$$

$$= 2 \times \frac{Number\ of\ evolved\ hydrogen\ molecules}{Number\ of\ incident\ photons} X100$$

$$= 4 \times \frac{Number\ of\ evolved\ oxygen\ molecules}{Number\ of\ incident\ photons} X\ 100$$

$$Solar\ energy\ convesion\ (\%) = \frac{Output\ energy\ of\ hydrogen\ evolved}{Energy\ of\ incident\ solar\ light} \times 100$$

Apparent quantum yield and solar energy conversion are the most authentic way to describe the performance of a photocatalyst. It should be noted that normalization of catalytic activity by mass of photocatalyst is not the correct way to define the performance of catalyst since the activity does not increase linearly with increasing catalyst amount.

# 3. Selection of Photocatalysts

## UV- Active Photocatalysts

Transition metal oxides based photocatalyst with wide band gaps (band gap >3 eV) generates charge carriers under UV-irradiation can be classified into i) $d^0$ system and ii) $d^{10}$ system.

## 3.1 Transition metal oxide based photocatalysts with $d^0$ electron

The first semiconductor explored for water splitting was $TiO_2$, which crystallizes in the rutile, anatase and brookite phase.[10] The valence band in $TiO_2$ is made up of O2p-orbitals and conduction band is made up of vacant 3d-orbitals of Ti. Excitation

of electrons from O2p to Ti3d state requires UV-radiation. $TiO_2$ in the presence of $RuO_2$ and Pt co-catalysts exhibits a quantum yield of ~ 30 % for $H_2$ production along with the stoichiometric amount of $O_2$ from pure water.[11] Doping of Ga in $TiO_2$ is known to split pure water stoichiometrically. Doping of lanthanides in $TiO_2$ has been studied by Zalas and La, with the best activity observed for Gd-oxide doped sample in the presence of aqueous methanol.[12] Titanates such as $Na_2Ti_3O_7$, $K_2Ti_4O_9$, and $K_2Ti_2O_5$ show HER in the bare form in an aqueous methanol solution.[13] Explored by Lee and co-workers series of perovskites, $La_2TiO_5$, $La_2Ti_3O_9$, and $La_2Ti_2O_7$ with different layer thickness exhibit superior catalytic activity than bulk $LaTiO_3$.[14] $ZrO_2$ in the bare form performs photocatalytic decomposition of $H_2O$ under UV-light.[15] Similar to $ZrO_2$; $BaZrO_3$ also (cubic perovskite) performs photocatalytic water splitting without any co-catalyst assistance under UV-light.[16] Substitution of Ba by Sn resulted in the enhancement in the photocatalytic activity of this compound.[17] Pristine $Nb_2O_5$ with a band gap of 3.4 eV does not exhibit HER; however, in the presence of Pt co-catalyst, it catalyzes the HER efficiently in aqueous methanol solution. A mesoporous form of $Nb_2O_5$ exhibit significantly higher activity than bulk $Nb_2O_5$.[18] Niobates such as $K_4Nb_6O_{17}$ explored by Domen and co-workers show a high yield of $H_2$ with robust activity from aqueous methanol solution without any co-catalyst assistance.[19] Alkaline earth niobates such as $SrNb_2O_6$, $Sr_2Nb_2O_7$, and $Sr_5Nb_4O_{15}$ show very good photocatalytic water splitting activity under UV-light.[20] Ta-based oxide such as $Ta_2O_5$ with a band gap of 4.0 eV exhibits excellent activity for overall water decomposition in the presence of NiO and $RuO_2$ co-catalysts.[21] Reported by Kato and Kudo alkali tantalates ATaO3 (A= Li, Na, and K) exhibit good activity for $H_2$ and $O_2$ production under UV-light and their activity follows the trend $LaTaO_3$>$NaTaO_3$>$KTaO_3$.[21-22] Chen and co-workers studied the water splitting from $La_2AlTaO_7$ in this compound CBM has major contribution from Al 3s3p-states.[23] This catalyst performs water splitting in pure water in the bare form. $PbWO_4$ with $WO_4$ tetrahedron exhibit overall decomposition of water when loaded with $RuO_2$ co-catalyst, however, $CaWO_4$ does not show any catalytic activity.[24] The catalytic activity of $PbWO_4$ and $CaWO_4$ is linked with the dispersion of band edges. $PbMoO_4$ catalyzes HER from an aqueous methanolic solution. Photocatalytic activities of tungstates and molybdates such as $Na_2W_4O_{13}$ and $Bi_2W_2O_9$ have been studied by Kudo and co-workers.[25] These materials with layered structure are active for

hydrogen and oxygen evolution in the presence of suitable sacrificial agents. $VO_2$ with the body-centered cubic crystal structure (band gap 2.7 eV) exhibits excellent HER from a solution of water and ethanol in UV-light.[26]

## 3.2 Transition metal oxide based photocatalysts with $d^{10}$ electron

Various $d^{10}$ metal oxides such as $In_2O_3$, $Ga_2O_3$, ZnO, $SnO_2$ exhibit photocatalytic water splitting under UV-light irradiation. Ni-$Ga_2O_3$ is the best catalyst for water splitting among all, wherein catalytic activity can be improved by doping Ca, Cr, Zn, Sr, Ba, and Ta ions.[27] Among all the dopant $Zn^{2+}$ shows the best result.

## 3.3 $f^0$ metal oxide based photocatalyst

$CeO_2$ exhibits OER activity in an aqueous solution of $Fe^{3+}$ and $Ce^{4+}$ as an electron acceptor.[28] Doping of $Sr^{2+}$ in $CeO_2$ makes it a better catalyst which performs overall decomposition of water in the presence of $RuO_2$ co-catalyst.[29]

## 3.4 Nonoxide Photocatalysts

ZnS with highly negative conduction band edge is known to perform excellent HER in the presence of $Na_2SO_3$ sacrificial agent yielding a quantum yield as high as 90 % at 313 nm wavelength without any co-catalyst assistance.[30] Among metal phosphides, InP is known to exhibit excellent HER activity in the presence of sacrificial electron donors.[31] Photocatalytic activity of GaN, discovered by Maeda et al., exhibits a strong dependence on the crystallinity of the sample. Crystallized GaN loaded with $Rh_{2-y}Cr_yO_3$ co-catalyst nanoparticles exhibits stoichiometric decomposition of water into $H_2$ and $O_2$ under UV-light.[32] Doping of $Mg^{2+}$ in GaN is known to enhance its catalytic activity and stability.[33] β-$Ge_3N_4$ is another metal nitride photocatalyst which is active in UV-light and decomposes water.[34]

## 3.5 Strategies to develop visible-light harvesting photocatalyst

Although photocatalysts mentioned above show excellent activity and stability for water splitting, the primary concern is they work under UV-light (4-5 % of solar radiation). In order to transform solar energy into chemical fuel efficiently, it is highly desirable to develop photocatalyst which can harvest visible fraction (45-55 % of solar radiation) of sunlight. There have been several attempts such as doping of cations and anions, solid solution synthesis, and use of dye to alter the band gap and electronic structure of transition metal oxides to obtain visible-light absorption.

**Cation doping as a tool to alter the band gap**

Doping of metal ions into wide band gap materials create states either near to the valence band (donor level) or the conduction band (acceptor level). Formation of such states reduces the band gap and therefore, results in the harvesting of longer wavelength radiations (**Figure 6**).[5a]

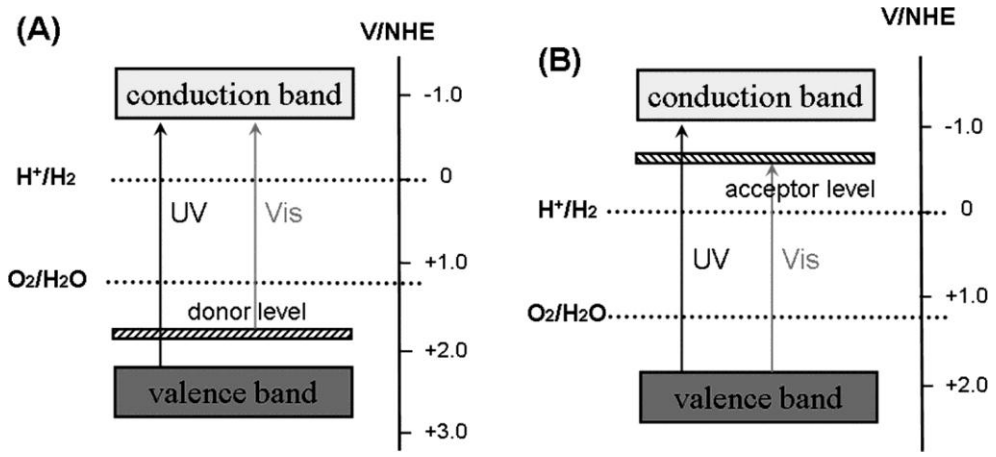


Figure 6. Metal doping in wide bandgap semiconductor creates a) donor level, and b) acceptor level. Reproduced with permission from ref. 5a. Copyright 2010 American Chemical Society.

$TiO_2$ has been doped with several transition metal ions such as V, Ni, Cr, Fe, Sn, Mn, which makes it active in the visible-light.[35] 3d-metal doping creates a state in the band gap or near to valence band corresponding to $t_{2g}$ orbitals. Excitation of an electron between $t_{2g}$ state and conduction or valence band of $TiO_2$ results in the visible-light absorption. Cao et al. used a chemical vapor deposition method to synthesize $Sn^{4+}$-doped $TiO_2$ nanoparticles which exhibit superior catalytic activity than pristine $TiO_2$ in UV as well as visible-light.[36] $Sn^{4+}$ forms acceptor level below

the conduction band and the excitation of valence band electron to the $Sn^{4+}$ state results in the visible-light absorption. $V^{4+}$ doping in $TiO_2$ also results in the absorption of visible-light, originated as a result of the transition between donor level of V-3d and conduction band of $TiO_2$.[37] Ru doping is known to extend the absorption edge of $TiO_2$ from UV to visible-region resulting in the photocatalytic oxidation of water in the presence of $Fe^{3+}$ as an electron acceptor.[38]

Doping of different concentration of Cr-ion in $SrTiO_3$ gives $SrTi_{1-x}Cr_xO_3$ (x= 0.0, 0.02, 0.05, 0.10) which show visible-light induced hydrogen generation. Visible-light absorption originates from the transition between Cr-3d donor state to the hybrid orbital of Cr 3d+Ti 3d.[39] Kudo and co-workers have reported visible-light induced $O_2$ production from Mn and Ru-doped $SrTiO_3$.[40] Ru, Rh, and Ir-doped $SrTiO_3$ perform HER in an aqueous methanol solution under visible-light ($\lambda$>440 nm) irradiation. Visible-light absorption in Rh-doped $SrTiO_3$ was originated due to the transition between donor states of Rh and conduction level of Ti3d. $Rh^{3+}$ and $Cu^{2+}$ doped $CaTiO_3$ exhibits visible-light induced hydrogen evolution.[41] Doping of Cr and Fe in layered perovskite $La_2Ti_2O_7$ forms a partially filled band in the band gap of this compound.[42] Excitation of electrons from dopant band to the conduction band of $La_2Ti_2O_7$ requires visible-photons, and generated excited electrons possess the potential to perform water reduction.

V-doping in $InTiO_5$ produces a significant change in the band gap and photocatalytic properties, allowing it to harvest entire visible-region (400-800 nm). Zou and co-workers have studied the doping effect of metal ions such as Mn, Fe, Co, Ni, Cu in $InTaO_4$, among all $In_{0.9}Ni_{0.1}TaO_4$ exhibited best photocatalytic activity for water splitting into $H_2$ and $O_2$ stoichiometrically.[43] Quantum yield obtained from this system is 0.66 % at 402 nm. A reduction in the band gap of $InTaO_4$ on Ni-doping is due to the formation of donor level above the valence band. $La^{3+}/Cr^{3+}$ co-doped $NaTiO_3$ exhibit excellent HER activity under visible-light in the presence of methanol as hole-scavenger.[44]

ZnS is a very active catalyst for HER because of the highly negative conduction band position; however, it has a wide band gap of 3.4 eV which limits its application to UV-light.[45] In order to make ZnS active in visible-light, doping of $Cu^{2+}$ and $Ni^{2+}$ has been tried. Interestingly, Ni and Cu-doped ZnS shows excellent HER activity even without any co-catalyst loading in visible light in the presence of

$Na_2S$ as a hole-scavenger.[35d, 46] The origin of visible absorption comes from the donor level in the band gap of ZnS by 3d orbitals of $Cu^{2+}$ and $Ni^{2+}$. Reported by Ren et al., CdS based photocatalyst with dopant $MInS_2$ (M= Cu, Ag) exhibit narrow band gap and superior HER activity in comparison to undoped CdS.[47] Doping of Cu and Mn in CdS is also known to improve its HER performance.[48] Cu-doping in $Zn_{1-x}Cd_xS$ photocatalyst shifts the band towards higher wavelength resulting in better HER performance.[49] Shen et al. have reported that Cu-doping in $ZnIn_2S_4$ enhances the visible-light absorption compared to the undoped sample. Such Cu-doped samples exhibit superior HER activity than undoped $ZnIn_2S_4$, sample having 0.5 wt% Cu showing the best activity (**Figure 7**).[50]

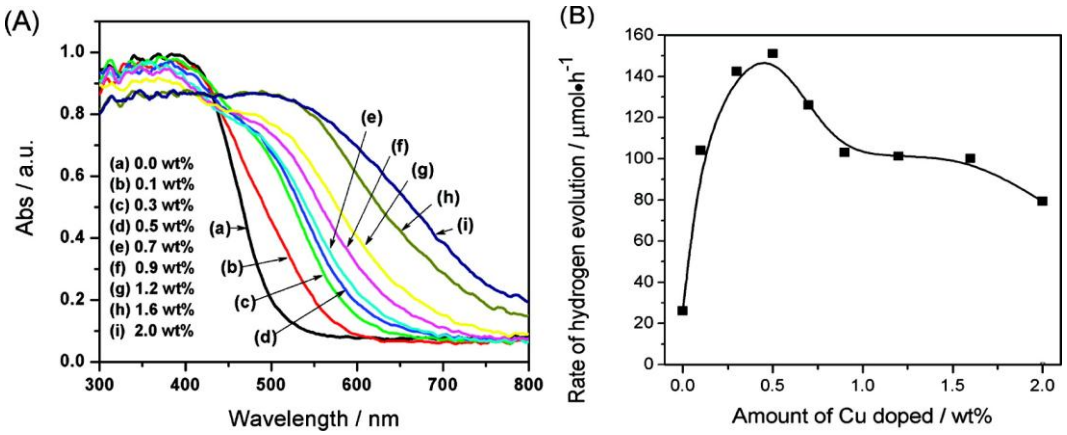


Figure 7. a) Diffuse-reflectance spectra of Cu-doped $ZnIn_2S_4$, and b) Variation in the photocatalytic $H_2$ evolution activity with the Cu-doping amount. Reproduced with the permission from ref 50. Copyright 2008 American Chemical Society.

**Anion doping as a tool to alter the band gap**

Doping of anions in wider band gap materials is another strategy to alter the absorption properties. Anion doping generally shifts the valance band edge of materials and do not form donor or acceptor states like cation substitution (**Figure 8**).[5a] $TiO_2$ has been doped with several anions such as C, N, S, etc. which show red-shift in the absorption spectra and higher catalytic activity than undoped $TiO_2$.[51] Among anions mentioned above effect of N, doping is most prevalent wherein N2p forms a state above O2p resulting in the reduction of the band gap. $TiO_{2-x}N_x$ exhibits superior photocatalytic activity than undoped $TiO_2$. The effect of S-doping in $TiO_2$ has also been studied in detail. A study done by Nishijima and co-workers shows

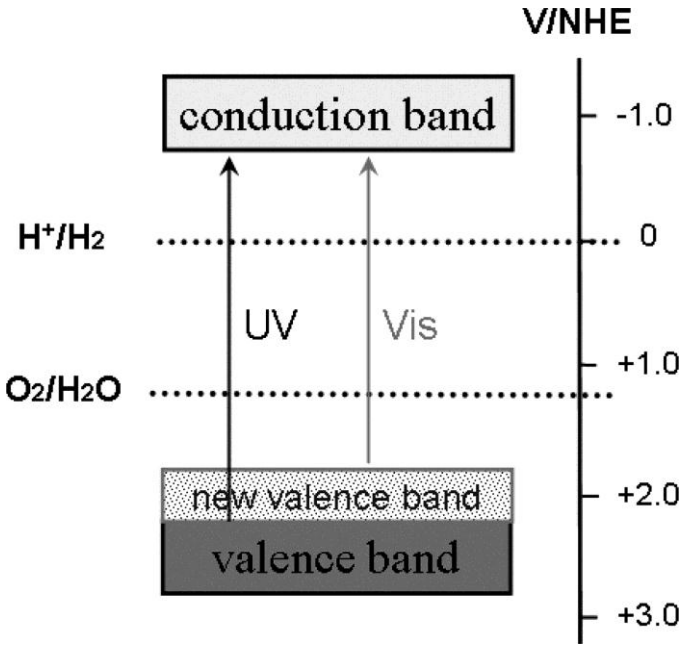


Figure 8. Creation of new valence band by the non-metal doping in an inorganic semiconductor. Reproduced with permission from ref. 5a. Copyright 2010 American Chemical Society.

superior HER activity of S-doped $TiO_2$ compare to N-doped $TiO_2$ under visible-light irradiation.[52] C-doped $TiO_2$ is known to show extended absorption and better water splitting performance than un-doped $TiO_2$.[53]

Co-doping of nonmetals in $TiO_2$ is known to produce more beneficial effects than the isovalent/monovalent anion doping. $TiO_2$ has been co-doped with F/B, F/N, S/F, N/Br, P/F, and C/S which show significant photocatalytic activity under visible-light.[54] Luo et al. have reported much superior water splitting performance of Cl/Br co-doped $TiO_2$ than the either Cl or Br doped $TiO_2$.[55] Rao and co-workers have shown a shift in band edge of $TiO_2$ from UV to visible-region by co-doping of N and F. The co-doped sample exhibited HER activity in the visible-light (**Figure 9**).[56] N/S co-doped samples show remarkable HER performance under visible-light.[57] B/N co-doped $TiO_2$ was reported by Liu et al. wherein N-doping reduces the band gap whereas B doping helps in the prolonging the life-time of charge carriers.[58]

N-doping in $Ta_2O_5$ also results in the reduction in the band gap due to the formation of N2p states on the top of O2p states in valence band.[59] TaON and $Ta_3N_5$ obtained by the $NH_3$ treatment of $Ta_2O_5$ at a specific temperature, possess band gap in the visible-region and performs water splitting. TaON is an excellent catalyst for

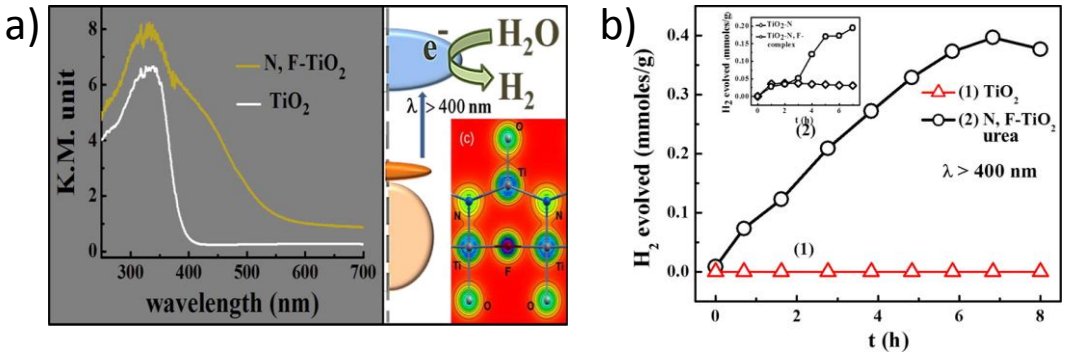


Figure 9. a) UV-vis absorption spectra of pristine and N, F co-doped $TiO_2$, and b) Photocatalytic $H_2$ evolution from pristine and N, F co-doped $TiO_2$. Reproduced with permission from ref 56. Copyright 2013 American Chemical Society.

water oxidation (AQY = 34 %) under visible-light irradiation in the presence of sacrificial electron acceptor like $AgNO_3$.[60] N-doping in $SrTiO_3$ causes a band gap to reduce and resulted in the absorption of the visible-light photons.[61] $LaTiO_2N$ with a band gap of 2.1 eV performs water reduction and oxidation under visible-light in the presence of suitable sacrificial agents.[62] Other than Ti and Ta-based oxides, $Sr_2Nb_2O_7$ also shows reduction in the band gap as a result of N-doping and doped sample exhibit superior photocatalytic activity.[63] C-doping in $In_2O_3$ and $Nb_2O_5$ is known to alter their absorption properties and related photocatalytic activity.[64] Absorption features of $ZrW_2O_8$ was significantly improved by S-doping, shifting band edge to 510 nm.[65]Visible-absorption was attributed due to S 3p-states. Doped sample exhibits $H_2$ and $O_2$ evolution in visible-region. Ishikawa and co-workers developed $Sm_2Ti_2S_2O_5$ photocatalyst which exhibits $H_2$ and $O_2$ evolution in visible-light in the presence of suitable sacrificial agents.[66] Sasikala et al. studied co-doping of In and N in $TiO_2$ at cationic and anionic lattice sites respectively and found a significant reduction in the band gap of $TiO_2$.[67] Such co-doped samples exhibit visible-light absorption and photocatalysis under visible-irradiation.

A metal-free polymeric g-$C_3N_4$ catalyst possesses a band gap of ~ 2.7 eV consisting of N $p_z$-orbitals in valance band and C $p_z$-orbitals in the conduction band.[68] It performed very stable water splitting under visible-light. S-doping in $C_3N_4$ is known to increase absorption edge and photocatalytic activity.[69]

**Solid Solutions to Control the Band Structure**

Solid solutions are formed by mixing the narrow and wide band gap semiconductors. The resultant compound possesses band gap value in between the parent materials used, and their band gap and band positions can be altered by changing the proportion of parent semiconductor materials (**Figure 10**).[5a]

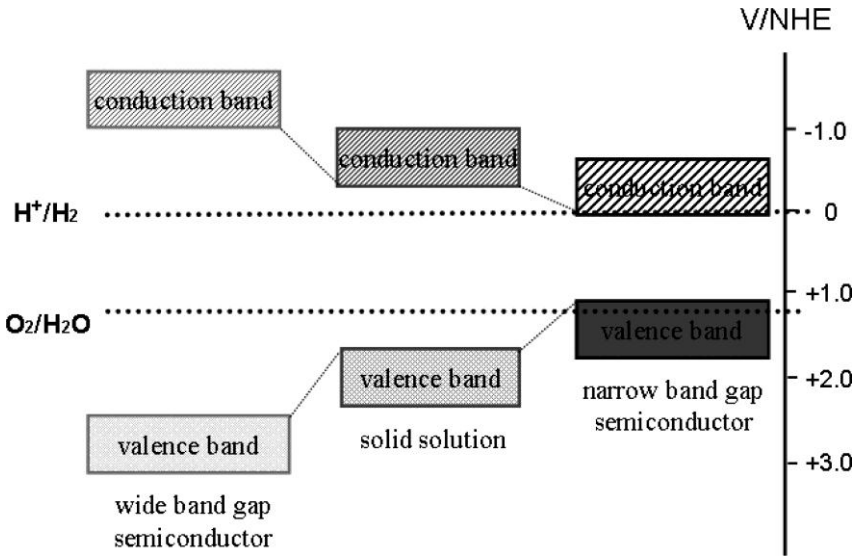


Figure 10. Modification of band structure by making solid solution. Reproduced with permission from ref 5a. Copyright 2010 American Chemical Society.

Oxynitrides are materials synthesized by mixing oxides (wide band gap) and nitrides (narrow band gap). $(SrTiO_3)_{1-x}(LaTiO_2N)_x$ solid solution was prepared mixing wide band gap $SrTiO_3$ with narrow band gap $LaTiO_2N$ under ammonia atmosphere.[70] Change in the x results the change in the band gap and CBM and VBM positions making it suitable for photocatalytic water splitting under visible-light.

GaN-ZnO solid solution developed by Domen's et al. represented by the formula $(Ga_{1-x}Zn_x)(N_{1-x}O_x)$ shows remarkable tuning of band gap from UV to visible-region by changing x (**Figure 11a**).[71] Interestingly both ZnO and GaN are wide band gap semiconductor with absorption in UV-region, however, mixing of ZnO and GaN in ammonia atmosphere forms solid solution wherein valence band maxima is contributed by N2p, Zn3d, and O2p orbitals and conduction band is contributed by Ga 4s and 4p-orbitals. d-p repulsion between N2p and Zn3d states shifts the valence band

upwards whereas conduction band position remains fixed resulting in the narrowing of the band gap (**Figure 11b**).[71c] Noteworthy that $(Ga_{1-x}Zn_x)(N_{1-x}O_x)$ possess suitable band positions for water splitting and performs overall decomposition of water into stoichiometric $H_2$ and $O_2$ under visible-light irradiation. $(Ga_{1-x}Zn_x)(N_{1-x}O_x)$ loaded with $Rh_{2-y}Cr_yO_3$ as a co-catalyst yield a very stable overall decomposition of water with a quantum yield of ~ 6% at 420-440 nm.

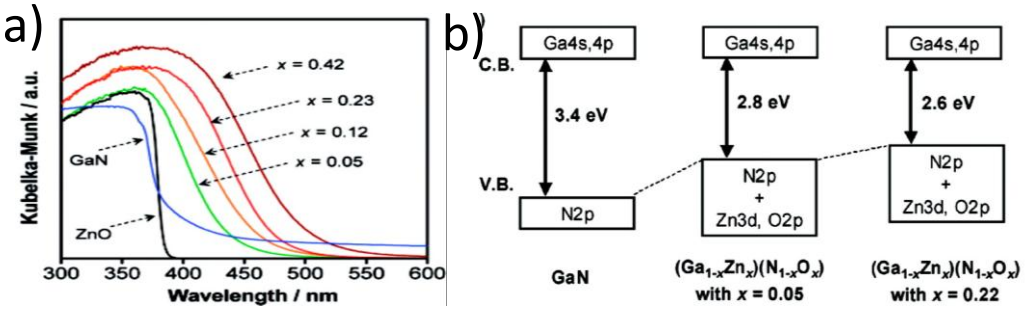


Figure 11. a) UV-Vis absorption spectra of $(Ga_{1-x}Zn_x)(N_{1-x}O_x)$ solid solutions. Reproduced with permission from ref 71a. Copyright 2005 American Chemical Society. and b) Schematic band structure of $(Ga_{1-x}Zn_x)(N_{1-x}O_x)$. Reproduced with permission from ref 71c. Copyright 2005 Ameican Chemical Society.

The same group has developed solid solution of formula $(Zn_{1+x}Ge)(N_2O_x)$ by mixing $ZnGeN_2$ and ZnO which also exhibit stable overall water splitting under visible-light.[72]

Recently Kibria and co-workers have reported overall $H_2O$ splitting using Mg-doped InGaN metal wires with a record high quantum yield of 12.3 % for pure water splitting (pH 7) at 400-475 nm irradiation.[73] It should be noted that among group III metal nitrides only InGaN can show band gap alternation in the whole range of solar spectrum along with suitable conduction and valence band position for water splitting.

A highly negative conduction band position of ZnS makes it excellent HER catalyst, however, the requirement of UV-irradiation to generate charge carriers is the primary limiting factor. Substitution of $Zn^{2+}$ by $Cd^{2+}$ in ZnS provides a solid solution of general formula $Cd_xZn_{1-x}S$, wherein band gap can be tuned from UV to visible-region. $Cd_xZn_{1-x}S$ solid solution exhibits excellent HER under visible-light irradiation in the presence of $Na_2S$ and $Na_2SO_3$ as a sacrificial hole scavenger.[74]

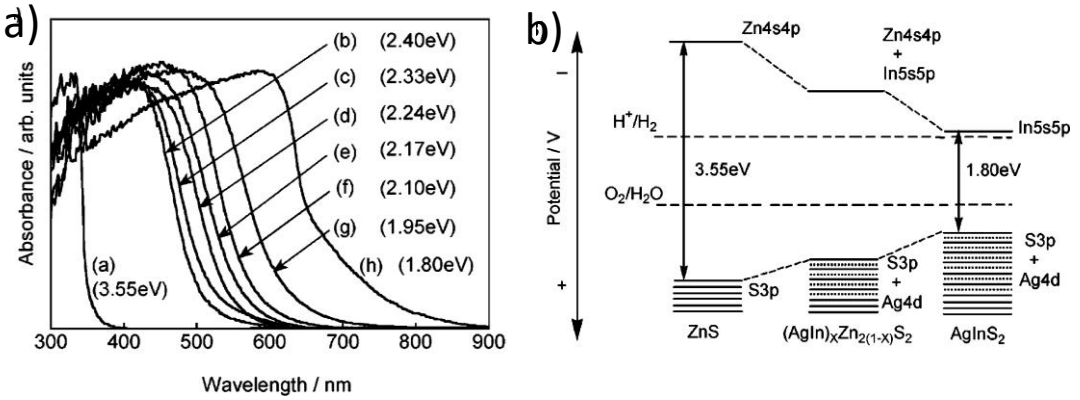


Figure 12. a) Diffuse reflectance spectra of $(AgIn)_xZn_{2(1-x)}S_2$ solid solution, and b) Band structure of $(AgIn)_xZn_{2(1-x)}S2$ solid solution. Reproduced with the permission from ref 75. Copyright 2004 American Chemical Society.

Kudo et al. have investigated the photophysical and photocatalytic properties of compounds formed by mixing ZnS (wide band gap) and $MInS_2$ (M= Ag, Cu) (narrow band gap).[75] The optical absorption spectrum of the solid solution can be tuned in a broad range changing the compositions. A solid solution of ZnS-$AgInS_2$ shows monotonic shift in the CBM and VBM positions along with their band gap with the change in the composition (**Figure 12**). Pt-loaded $(AgIn)_{0.22}Zn_{1.56}S_2$ with the band gap of 2.33 eV, show a quantum yield of 20 % for hydrogen evolution in visible-light at 420 nm.[75] $AgGa_{1-x}In_xS_2$ ($0<x<1$) solid solution shows a band gap in the range of 1.9 to 2.6 eV, and possesses HER activity in the presence of $Na_2S$-$Na_2SO_3$ electron donors.[76] $AgGa_{0.9}In_{0.1}S_2$ exhibits the highest HER activity.

**3.6 Visible-Light Induced Hydrogen Generation using Dye as a Photosensitizer**

A different approach is to use dye, as a photosensitizer in the presence of catalytic materials such as $TiO_2$, $MoS_2$, $MoSe_2$, graphene. Photoexcitation of dye (Eosin Y) generates singlet excited state ($EY^{1*}$), which transforms into triplet state ($EY^{3*}$) followed by the formation of $EY^-$ after accepting electrons from sacrificial electron donors.[77] This electron migrates to the surface of the catalytic material wherein it reduces the adsorbed $H^+$ into $H_2$ (**Figure 13**).[77] $MoS_2$ (p-type) composite with N-doped graphene (n-type) significantly enhances HER due to the efficient charge separation.[77] 1T-$MoS_2$ is known to be catalytically better than 2H form. There have been recent reports wherein 2H, and 1T form of $MoSe_2$ have been used with Eosin-Y. Noteworthy to mention that 1T-$MoSe_2$ showed superior activity than 2H $MoSe_2$ and $MoS_2$ analogs.[78]

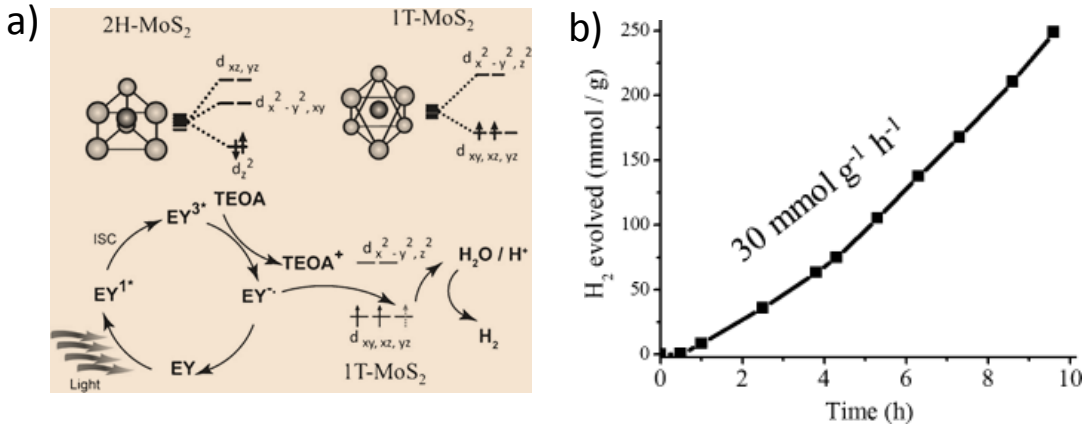


Figure 13. a) crystal-field-splitting induced electronic configuration of 2H-$MoS_2$ and 1T-$MoS_2$ and a proposed mechanism for catalytic activity of 1T-$MoS_2$, and b) Time course of $H_2$ evolved by freshly prepared 1T-$MoS_2$. Reproduced with permission ref 77. Copyright 2013 Wiley-VCH Verlag GmbH & Co. kGaA, Weinheim.

## 4. Strategies to Develop Efficient Separation of Charge Carriers

Apart from developing photocatalysts which can harvest a significant fraction of solar radiation, there has also been enormous efforts to improve the lifetime of photogenerated charge carriers. As mentioned earlier photoexcitation of semiconductor generates electrons and holes which has a great tendency to recombine due to columbic interaction. In order to achieve good catalytic activity, it is essential to reduce the process of recombination. Following strategies are generally used to separate the photogenerated charge carriers.

### 4.1 Use of cocatalyst

One of the very effective strategies to suppress the charge carrier recombination is to use a co-catalyst. Co-catalyst are materials when loaded on the semiconductor photocatalyst surface provides separation to the charge carriers and reduces the activation energy barrier of the reaction hence improves the catalytic activity.[79] **Figure 14a** shows the working of HER and OER co-catalyst on the surface of a semiconductor photocatalyst.[79] The photogenerated electron in the conduction band of semiconductor migrates to the HER co-catalyst and reduces $H^+$ into $H_2$, whereas photogenerated holes in the valance band migrates to the OER co-catalyst and

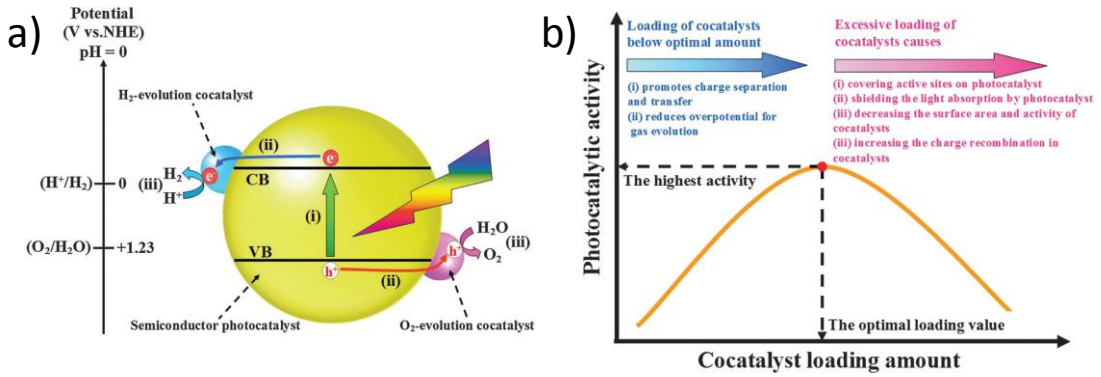


Figure 14. a) Schematic representation of photocatalytic water splitting on semiconductor surface loaded with $H_2O$ oxidation and reduction co-catalyst, and b) Volcano plot showing a relation between loading amount of co-catalyst and photocatalytic activity. Reproduced with permission from ref 79. Copyright The Royal Society of Chemistry 2014.

oxidizes $H_2O$ into $O_2$. The critical factor facilitating electron and hole transfer from semiconductor to co-catalyst surface is lower Fermi level of co-catalyst and junction formed between semiconductor and co-catalyst. Co-catalysts are also known to reduce the photocorrosion and hence enhances the stability of photocatalyst. Factors such as loading amount of co-catalyst, particle size and structure, affect the rate of catalytic activity. As shown in **Figure 14b** a plot of catalytic activity against co-catalyst loading amount possesses volcano shape plot, wherein initially introduction of co-catalyst on semiconductor significantly enhances the photocatalytic activity which reaches to highest value at an optimum loading amount, and catalytic activity start decreasing with the further increase in the co-catalyst amount.[79] A decrease in the catalytic activity above optimum loading amount originates because of the shielding of light by co-catalyst, covering of surface active sites of semiconductor photocatalyst which are in the contact of $H_2O$ and sacrificial agents, and creation of trap states by co-catalyst. Generally at the same loading amount co-catalyst materials with smaller particle size exhibit higher catalytic activity than the larger particles.

**Noble Metal co-catalysts**

Noble metals such as Pt, Pd, Ag, Au, Ru, and Rh show excellent activity when loaded on semiconductors photocatalysts.[79] Among noble metals, Pt has been widely used as a co-catalyst with different semiconductor materials. However, Pt nanoparticles

cannot stop the surface back reaction wherein $H_2$ and $O_2$ react to form $H_2O$. Iwase et al. reported efficient hydrogen evolution using Au nanoparticles wherein surface back reaction was ceased, unlike Pt.[80] Remarkable increase in the visible-light hydrogen evolution activity of TaON was observed after Ru incorporation.[81] Loading of Pt/Ru together on $LaTaON_2$ showed a synergistic effect with much enhanced HER activity.[82] Overall decomposition of water into $H_2$ and $O_2$ is achieved by loading Pt on $C_3N_4$ under visible-light irradiation.[83]

**Transition Metal Oxide Co-catalysts**

Various transition metal oxides such as NiO, CoOx, $RuO_2$, $IrO_2$ possesses co-catalytic activity.[79] β-$Ge_3N_4$ loaded with $RuO_2$ exhibits water splitting activity under UV-light whereas bare semiconductor showed almost negligible activity.[84] Maeda at al. reported that the loading of $RuO_2$ on $C_3N_4$ is critical to obtain good $O_2$ evolution activity along with the stability of photocatalyst.[85] $IrO_2$ has also been reported as a water oxidation catalyst.[86] $(Ga_{1-x}Zn_x)(N_{1-x}O_x)$ loaded with Cr-M (M= Fe, Co, Ni, Cu, Ru, Rh, Ir, or Pt) mixed oxide as co-catalyst by Maeda and co-workers have been reported.[87] Among mixed oxides, Rh-Cr (1 wt% Rh and 1.5 wt% Cr) incorporation showed the best results for overall water splitting. Loading of mixed oxide co-catalyst not only favors charge separation but also increases active sites for proton reduction. A noble Rh/$Cr_2O_3$-core/shell co-catalyst is also reported by the same author, wherein Rh-core separates the photogenerated carriers in $(Ga_{1-x}Zn_x)$ $(N_{1-x}O_x)$ as well as tunnel the electron to $Cr_2O_3$-shell which act as an active site for $H_2$ production.[88]

There have been so many reports wherein NiO is used as a co-catalyst for water splitting.[89] Reduction-reoxidation process form a double-layer NiO/Ni structure, wherein NiO Fermi level lies below the Ni fermi level causing photogenerated electrons to transfer from semiconductor to Ni and from Ni to NiO surface which act as proton reduction site. Such multiple transfers of electrons reduce the chances of recombination and enhance catalytic activity markedly.

**Transition metal phosphides and sulfides co-catalysts**

Transition metal phosphides such as $Ni_2P$, $Ni_xP_y$, $Co_2P$, FeP, and CuP have been recently reported to show excellent HER activity when loaded on visible-light absorbing photocatalyst such as CdS.[90] Noteworthy to mention that many phosphide

co-catalysts has shown significantly higher catalytic activity than noble metals such as Pt. Transition metal sulfides such as NiS, $Co_2S$, $MoS_2$ also show excellent performance when used as a co-catalyst.[79]

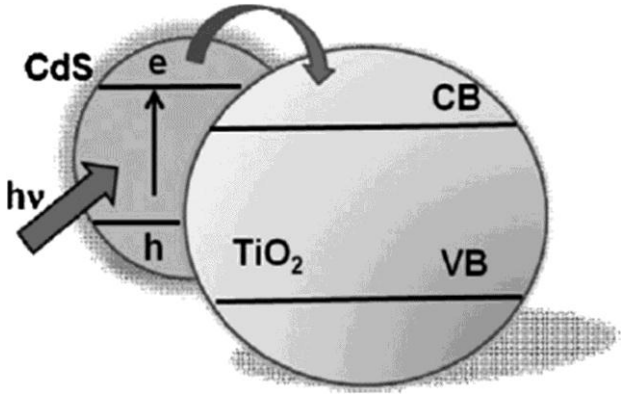


Figure 15. $CdS/TiO_2$ combination showing charge separation under visible-light irradiation. Reproduced with permission from ref 95c. Copyright 2009 Wiley-VCH.

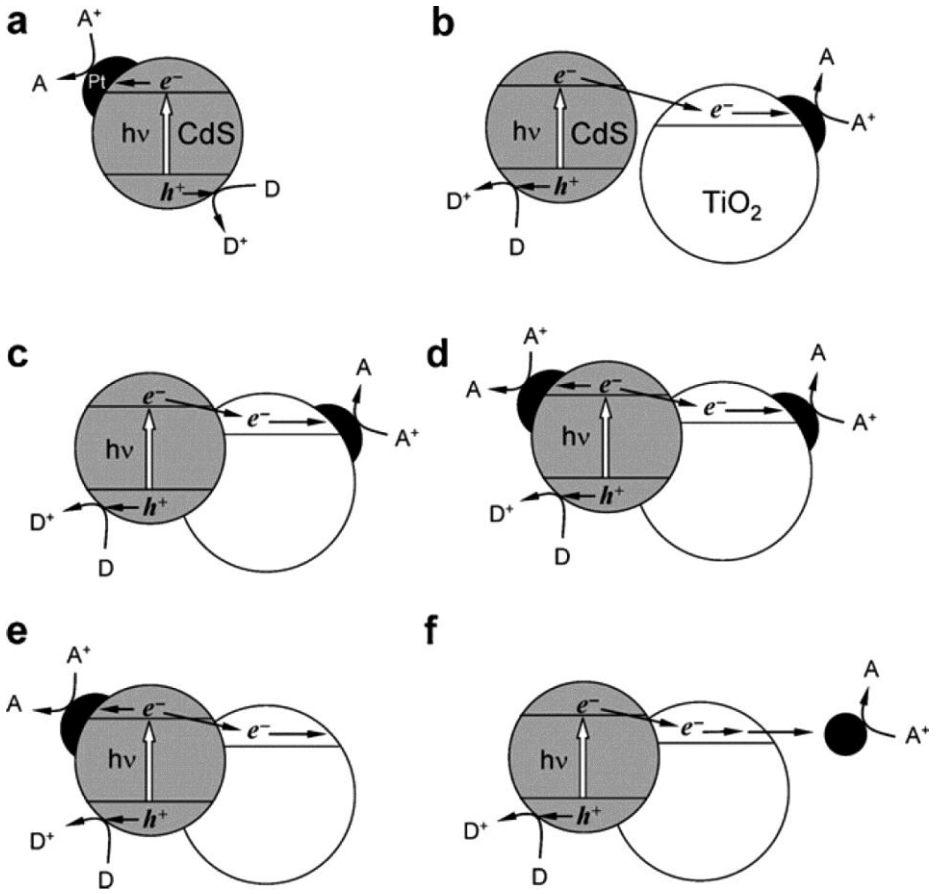


Figure 16. Illustration of charge transfer in $CdS/TiO_2$/Pt heterostructure. Reproduced with permission from ref 96. Copyright 2008 The Royal Society of Chemistry.

Zong and co-workers reported $MoS_2$ loaded CdS photocatalyst with HER activity superior to CdS/Pt.[91] $MoS_2$ has also been used as co-catalyst with CdSe photosensitizer.[92] PdS and $Ru_2S_3$ when loaded over CdS, results in a remarkable enhancement in catalytic activity.[93] Recently some metal carbides such as WC and $Mo_2C$ has been reported as an efficient HER co-catalyst.[94]

## 4.2 Semiconductor Heterostructures

Combination of the semiconductor is known to affect the photocatalytic activity due to influence on the charge carrier separation. Metal chalcogenide photocatalysts generally undergo photocorrosion because of self-oxidation by photogenerated holes, formation of semiconductor heterostructure facilitate the carrier transfer and increase the stability of such system.

CdS/$TiO_2$ combination is one of the excellent examples of semiconductor heterostructure which exhibits much superior HER activity than CdS alone. The conduction and valence band in CdS is at more negative potential than $TiO_2$, allowing electron transfer from CdS conduction band to the conduction band of $TiO_2$ whereas holes remain in the valence band of CdS, resulting in the separation of electrons and holes under visible-light (**Figure 15**).[95] Park et al. investigated the HER activity of CdS in combination with $TiO_2$ and Pt and found the notable effect of semiconductor combination wherein best activity was achieved on a system wherein $TiO_2$ and CdS form intimate heterostructure, and Pt nanoparticles are present on $TiO_2$ surface.[96] Vectorial transfer of an electron from CdS to $TiO_2$ and from $TiO_2$ to HER active site of Pt results in such remarkable catalytic activity (**Figure 16**).[96] $TiO_2$/$SnO_2$ heterostructure shows superior photocatalytic activity than $TiO_2$.[97]

One of the excellent strategies developed by Amirav and Alivisatos contains nanoheterostructure formed by CdS rod, CdSe seed, and Pt nanoparticles.[98] CdSe seed was embedded in CdS rod, and Pt nanoparticles were present on the tip of the rod. Under visible-light photoexcitation holes and electrons migrates towards CdSe seed and Pt nanoparticle respectively resulting in the efficient separation of charge carriers. Life time of charge carriers was tuned by changing the nanorod length and seed size (**Figure 17**). A quantum yield of 20 % at 450 nm has been achevied by this structure.[98]

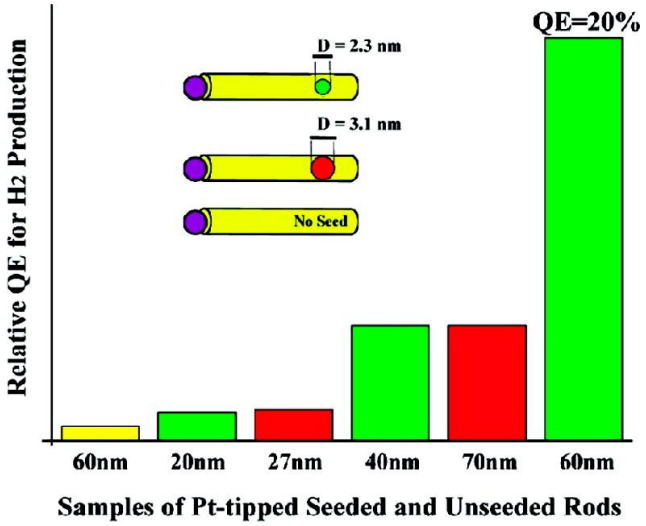


Figure 17. Relative $H_2$ quantum yield obtained from Pt-tipped unseeded CdS rod (yellow), and five different Pt-tipped rods with CdSe seed diameters of 3.1 (red), 2.3 (green). Underneath each bar is the corresponding average sample length. Reproduced with permission from ref 98. Copyright 2010 American Chemical Society.

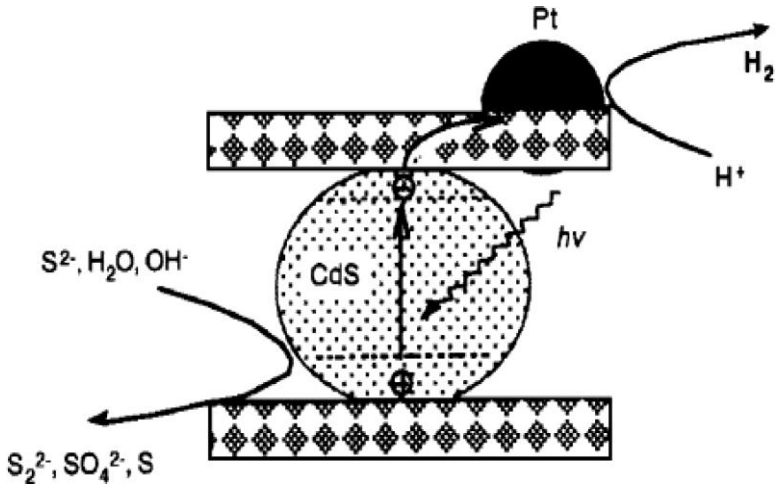


Figure 18. Illustration of the mechanism of photocatalytic $H_2$ evolution on CdS-intercalated layered composites loaded with Pt. Reproduced with permission from ref 100. Copyright 2007 IOP Publishing Ltd.

Fabrication of host-guest combination by incorporating photosensitizing semiconductor in the interlayers of the lamellar compound is an effective strategy to improve photocatalytic activity.[99] Synthesis of CdS-intercalated metal oxides is

known to perform superior to the physical mixture of two. The enhancement in the catalytic activity is attributed to the fast charge transfer from CdS to lamellar oxide layers (**Figure 18**).[100] CdS incorporated in the nanotubes of titanates ($TiO_2$ NT) also show excellent hydrogen evolution activity under visible-light irradiation in the presence of $Na_2S$-$Na_2SO_3$ sacrificial electron donors yielding a quantum yield of 43.4 % at 420 nm.[101]

## 4.3 Crystal Structure and Morphology

The life time of photogenerated charge carriers markedly depends on crystallinity, defect density, and structural features. Apart from these surface properties such as morphology, the number of active sites, the surface area of catalyst are also critical parameters affecting activity.[6]

$TiO_2$ is a typical example wherein the anatase phase exhibits superior photocatalytic activity than the rutile phase.[102] The superior performance of anatase $TiO_2$ is related to the trapping of photogenerated electrons in the oxygen vacancies whereas in the case of rutile $TiO_2$ photogenerated electrons were trapped inside intrinsic defects and de-excited by near-infrared emission.[103] A mixture of anatase and rutile $TiO_2$ exhibit much superior photocatalytic activity than anatase or rutile alone. Such improvement of catalytic activity is linked to the junction between anatase and rutile phase wherein photogenerated electrons in $TiO_2$ migrates to rutile phase causing separation of charge carriers and hence positively impacting the catalytic performance (**Figure 19**).[104] Tetragonal $In_2S_3$ with ordered In-vacancy does not show HER whereas cubic $In_2S_3$ with disordered vacancy show stable HER activity under visible-light.[105]

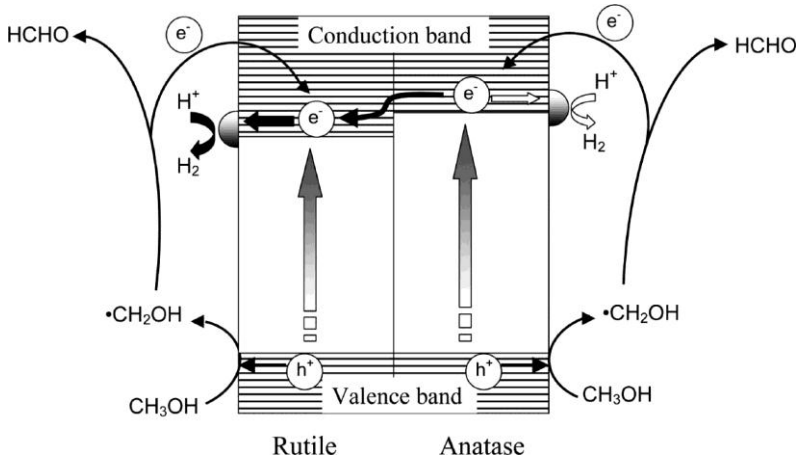


Figure 19. Mechanism of photocatalytic reaction and migration of photogenerated charge carriers in the anatase-rutile mixed phase $TiO_2$. Reproduced with permission from ref 104b. Copyright 2010 American Chemical Society.

Smaller particle size and higher surface area are required to achieve better photocatalytic activity. In the case of small particles (nanoparticles), charge carriers need to travel lesser distance (less chance of recombination) to reach the surface where redox reactions take place. A high surface area provides a large number of active sites for proton adsorption and hence are beneficial for efficient photocatalytic activities.[6]

## 5. Role of Sacrificial Electron Donors and Acceptors

Sacrificial agents are the chemicals used to either consume the photogenerated holes ( in the case of HER reaction) or photogenerated electrons (in the case of OER reaction). Since HER involve reduction of $H^+$ into $H_2$ by photogenerated electrons, hence, getting rid of holes by sacrificial electron donors reduces electron-hole recombination resulting in significant enhancement in the HER activity. In the case of OER reaction wherein photogenerated holes oxidizes $H_2O$ into $O_2$, sacrificial electron acceptors consumes the generated electrons. The basic principle of photocatalytic HER and OER reaction using electron donor and acceptor sacrificial agents is shown in **figure 20**.[106] Hole scavenging sacrificial reagents can be classified into inorganic and organic electron donors.

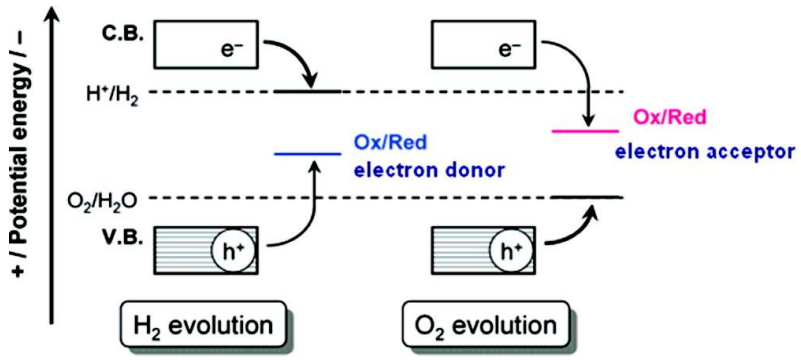


Figure 20. Photocatalytic $H_2$ and $O_2$ evolution in the presence of sacrificial agents. Reproduced with permission from 106. Copyright 2007 Ameican Chemical Society.

**Inorganic Sacrificial**

$S^{2-}/SO_3^{2-}$ is extensively used sacrificial electron donor for metal sulfides photocatalysts.[107] It significantly reduces the photocorrosion in metal sulfides by consuming holes in the valance band. $S^{2-}$ and $SO_3^{2-}$ after reacting to holes generate oxidized species $S_n^{2-}$ and $SO_4^{2-}$ respectively. It should be noted that $S_n^{2-}$ is a yellow color polysulfide which competes with the photocatalyst for light absorption and hence reduces the number of photons available for photocatalyst resulting in the HER activity reduction. In addition to the light absorption $S_n^{2-}$ competes with $H_2O$ molecules for electron reduction which further decreases $H_2$ production.[108] It is noteworthy that $SO_3^{2-}$ reacts with $S_n^{2-}$ and regenerate $S^{2-}$ which makes photocatalytic solution colorless.[108b] Therefore, $S^{2-}/SO_3^{2-}$ combination is used as a sacrificial agent. The reaction mechanism of photocatalytic $H_2$ evolution in the presence of $S^{2-}/SO_3^{2-}$ is described below.

$$\text{Photocatalyst} + h\nu \longrightarrow \text{Photocatalyst}\,(h^+, e^-)$$

$$2e^- + 2H_2O \longrightarrow H_2 + 2OH^-$$

$$SO_3^{2-} + 2OH^- + 2h^+ \longrightarrow SO_4^{2-} + 2H^+$$

$$2S^{2-} + 2h^+ \longrightarrow S_2^{2-}$$

$$S_2^{2-} + SO_3^{2-} \longrightarrow S_2O_3^{2-} + S^{2-}$$

$$SO_3^{2-} + S^{2-} + 2h^+ \longrightarrow S_2O_3^{2-}$$

Produced $S_2O_3^{2-}$ can be oxidized to $SO_3^{2-}$ and subsequently to $SO_4^{2-}$ by photogenerated holes.

Other inorganic sacrificial agents are $Fe^{2+}$, $Ce^{3+}$, $I^-$, $Br^-$, $CN^-$ get oxidized by photogenerated holes to $Fe^{3+}$, $Ce^{4+}$, $I^{3-}$, $Br_2$, and $OCN^-$ respectively.

**Hydrogen sulfide ($H_2S$) as splitting medium to produce $H_2$**

Industrial $H_2S$ and desulfurization process in petrochemical industries produce a considerable amount of $H_2S$ waste dissolved in pure water or alkaline solution. From the view of energy conservation and environmental care, production of $H_2$ by splitting such $H_2S$ system is very beneficial.[109] Fortunately, $H_2S$ in alkaline medium generates $S^{2-}$ which act as sacrificial electron donor; hence there is no requirement of external supply of sacrificial reagents. Production of $H_2$ from $H_2S$ is still thermodynamic uphill reaction which requires $\Delta G$ change of 39.3 kJ/mol; however, it is less energy demanding then splitting pure water which requires a $\Delta G$ change of 237 kJ/mol.[110] The reaction mechanism is mentioned below.

$$H_2S + OH^- \longrightarrow HS^- + H_2O$$
$$2HS^- + 2h^+ \longrightarrow S_2^{2-} + 2H^+$$
$$2H^+ + 2e^- \longrightarrow H_2$$

**Organic Sacrificial Reagents**

Organic compounds such as methanol, ethanol, benzyl alcohol, isopropanol, formaldehyde, acetaldehyde, lactic acid, Triethanolamine (TEOA) are generally used as sacrificial agents in the presence of oxide photocatalyst.[111]

The mechanism of action of organic sacrificial agents is mentioned below.

$$h^+ + H_2O \longrightarrow \bullet OH + H^+$$
$$CH_3OH + \bullet OH \longrightarrow \bullet CH_2OH + H_2O$$
$$\bullet CH_2OH \longrightarrow HCHO + H^+ + e^-$$
$$2H_2O + 2e^- \longrightarrow H_2 + 2OH^-$$

There could be further oxidation of HCHO to corresponding carboxylic acid and finally to $CO_2$ given below.

$$HCHO + H_2O \longrightarrow HCOOH + H_2$$
$$HCOOH \longrightarrow CO_2 + H_2$$

Design of photocatalytic systems wherein organic sacrificial agents are used can be envisioned as removal of organic pollutants from water along with the production of hydrogen.

## 6. Sacrificial Reagent-Free Overall water Splitting

Semiconductor photocatalyst capable of reduction as well as oxidation of water by photogenerated electrons and holes respectively does not require sacrificial assistance and produce $H_2$ and $O_2$ in stoichiometry. In the last few years, there have been several reports on semiconductor photocatalyst performing overall water splitting. Depending on the mechanism involved overall water splitting can be divided into two categories (**Figure 21**).[112]

A. Single semiconductor based overall water splitting, and B. Two semiconductor-based Z-scheme water splitting.

### A. Single semiconductor-based water splitting

Semiconductor photocatalysts with suitable CBM and VBM positions concerning water redox potential upon photoexcitation perform reduction and oxidation of $H_2O$ by conduction band electron and valence band hole respectively. In order to perform overall water splitting it is indispensable that semiconductor material should be inert towards photocorrosion. Mostly nitrides and oxynitrides semiconductors possess a potential for overall water splitting.

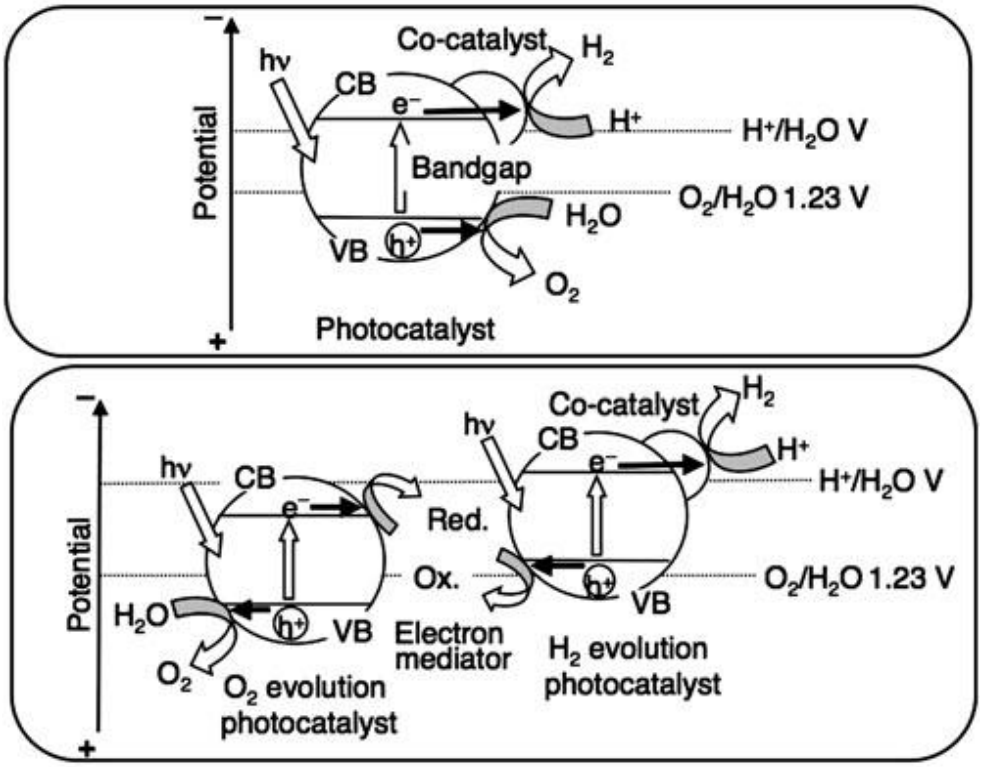


Figure 21. Overall water splitting to produce $H_2$ and $O_2$ in the presence of single and double semiconductor. Reproduced with permission from 112. Copyright 2011 Materials Research Society.

Developed by Kanazuri and co-workers $(Ga_{1-x}Zn_x)$-$(N_{1-x}O_x)$ solid solution photocatalyst perform overall water splitting when loaded with suitable co-catalyst.

A steady $H_2$ and $O_2$ evolution with a quantum yield of ~ 6% have been obtained with this photocatalyst in the range of 420-440 nm.[71a] Metal free $C_3N_4$ photocatalyst is also known to perform overall water splitting, loading of Pt and CoP as HER and OER catalyst respectively enhances their catalytic activity.[113] Kibria et al. have recently achieved a record high efficiency with a quantum yield of value 12.3 % for overall $H_2O$ splitting at pH 7, under 400-475 nm irradiation, using Mg-doped InGaN metal wires.[73]

### B. Two semiconductor based Z-scheme water splitting

Another strategy to split water into $H_2$ and $O_2$ stoichiometrically is the use of two semiconductor-based systems wherein semiconductor with suitable CBM positions performs reduction of water and semiconductor with suitable VBM positions performs oxidation of water. This approach is similar to the natural photosynthesis

wherein plants use two photosystems. $Ru/SrTiO_3$:Rh and $BiVO_4$ as $H_2$ and $O_2$ evolution

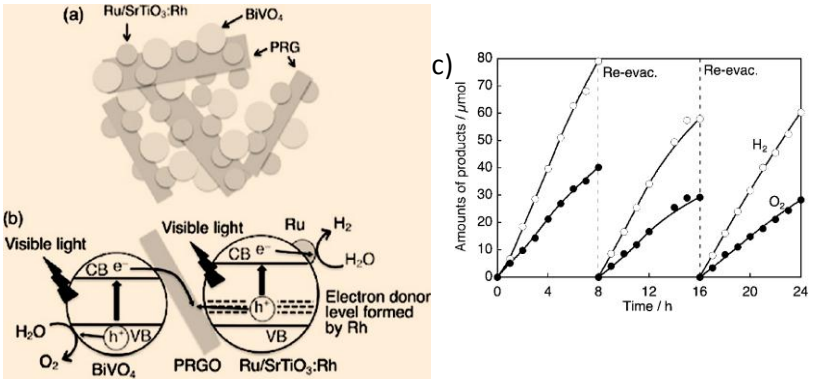


Figure 22. a) Schematic of a suspension of $Ru/SrTiO_3$ and $PRGO/BiVO_4$ in water (pH 3.5), b) Mechanism of Z-scheme water splitting under visible light using $Ru/SrTiO_3$:Rh and $PRGO/BiVO_4$, and c) Overall water splitting under visible-light irradiation using ($Ru/SrTiO_3$: Rh)-($PRGO/BiVO_4$) system. Reproduced with permission from ref 114. Copyright 2011 American Chemical Society.

photocatalyst and photoreduced graphene oxide (pRGO) has been used as an electron mediator (**Figure 22**).[114] Abe et al. reported overall water splitting in alkaline medium (pH 11) using Pt-$TiO_2$ (anatase) and $TiO_2$ (rutile) as $H_2$ and $O_2$ evolving centers in the presence of $IO_3^-/I^-$ shuttle redox mediator. Under UV irradiation a complete decomposition of water with $H_2$ and $O_2$ yield of 180 and 90 μmol/h has been achieved.[115] There are several semiconductor combinations such as (Pt/TaON)-(Pt/WO3)-($IO_3^-/I^-$), (Pt/TaON)-($RuO_2$/TaON)-($IO_3^-/I^-$), (Pt/$ATaO_2N$ (A= Ca, Sr, Ba))-(Pt/$WO_3$)-($IO_3/I^-$), etc. which have been reported for overall water splitting under visible-light.[116]

A study by Kudo et al. present overall water splitting in a system composed of ($Ru/SrTiO_3$:Rh-$BiVO_4$) wherein interparticle charge transfer occurs without the assistance of a redox-mediator (**Figure 23**). Though efficiency of the system is less but it provides a promising approach to develop Z-scheme systems without redox mediators.[117]

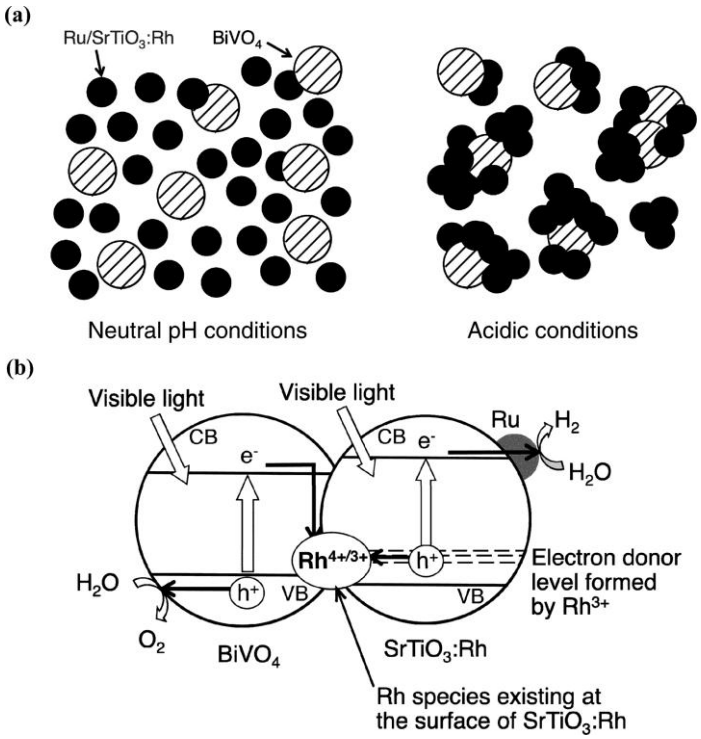


Figure 23. Z-Scheme water splitting using a) $Ru/SrTiO_3$:Rh and $BiVO_4$ suspension in neutral and acidic medium, and b) Scheme representing a process of water splitting. Reproduced with permission from ref 117. Copyright 2009 American Chemical Society.

## 7. Conclusions

Realization of the fact that energy requirements as well as environmental issues can benefit by using $H_2$ with high energy density as a clean source of fuel has evoked enormous research interest. Among the various ways to produce hydrogen the photochemical approach is attractive considering its simplicity and large-scale production possibility. Several semiconductors with suitable band positions with respect to the water redox potential have been investigated for water splitting. Sacrificial reagents assist photocatalytic reactions giving rise to high $H_2$ or $O_2$ yields because of the quenching of the other half reaction. Pt/CdS and Pt-Pd/CdS based system show a quantum yield of 60.3 and 93 % respectively in the presence of $Na_2S$-$Na_2SO_3$ as a sacrificial agent. The efficiency for overall water splitting remains very

low. $Rh_{2-y}Cr_yO_3/(Ga_{1-x}Zn_x)$-$(N_{1-x}O_x)$ is one of the best systems to perform overall water splitting with a quantum yield of ~ 6% in the wavlength range of 420-440 nm. Recently a high quantum efficiency of ~12.5 % was achieved by InGaN nanowires doped with Mg in the wavelength range of 400-475 nm. These values are still far from the quantum efficiency (30 % at 600 nm) require for practical applications. More efficient visible-light semiconductor combinations need to be investigated to achieve higher efficiency for overall water splitting. In order to harvest a significant fraction of solar radiation strategies like band gap narrowing using doping, making solid solutions, and dye-sensitization play a crucial role. Controlling life time of charge carriers is an important criteria carried out by use of co-catalyst, heterostructure formation, nanojunction giving rise to higher photocatalytic activity. Developing co-catalysts based on earth-abundant low cost materials is necessary. Morphology and crystallinity of photocatalyst also play a critical role in defining activity. Splitting sea-water using solar energy source is more relevant considering the acute shortage of clean water in coming times.

# 8. References


[1] a) S. J. Davis, K. Caldeira, *Proc. Natl. Acad. Sci. U.S.A* **2010**, *107*, 5687; b) D. Dodman, *ENVIRON URBAN* **2009**, *21*, 185-201.

[2] a) J. A. Turner, *Science* **2004**, *305*, 972; b) E. Pulido Melián, O. González Díaz, A. Ortega Méndez, C. R. López, M. Nereida Suárez, J. M. Doña Rodríguez, J. A. Navío, D. Fernández Hevia, J. Pérez Peña, *Int. J. Hydrogen Energy* **2013**, *38*, 2144-2155.

[3] a) G. L. Chiarello, M. H. Aguirre, E. Selli, *J. Catal.* **2010**, *273*, 182-190; b) K.-D. Ko, J. K. Lee, D. Park, S. H. Shin, *Korean J. Chem. Eng* **1995**, *12*, 478-480.

[4] Y. Wang, H. Suzuki, J. Xie, O. Tomita, D. J. Martin, M. Higashi, D. Kong, R. Abe, J. Tang, *Chem. Rev.* **2018**, *118*, 5201-5241.

[5] a) X. Chen, S. Shen, L. Guo, S. S. Mao, *Chem. Rev.* **2010**, *110*, 6503-6570; b) A. Fujishima, K. Honda, *Nature* **1972**, *238*, 37-38.

[6] A. Kudo, Y. Miseki, *Chem. Soc. Rev.* **2009**, *38*, 253-278.

[7] a) H. Kato, K. Asakura, A. Kudo, *J. Am. Chem. Soc* **2003**, *125*, 3082-3089; b) A. Kudo, H. Kato, S. Nakagawa, *J. Phys. Chem. B* **2000**, *104*, 571-575; c) F. Zaera, *Catal. Lett.* **2003**, *91*, 1-10; d) S. Ikeda, M. Hara, J. N. Kondo, K. Domen, H. Takahashi, T. Okubo, M. Kakihana, *Chem. Mater.* **1998**, *10*, 72-77; e) K. Maeda, N. Saito, D. Lu, Y. Inoue, K. Domen, *J. Phys. Chem. C* **2007**, *111*, 4749-4755.

[8] M. A. A. Schoonen, Y. Xu, *Am. Mineral.* **2000**, *85*, 543-556.

[9] A. L. Linsebigler, G. Lu, J. T. Yates, *Chem. Rev.* **1995**, *95*, 735-758.

[10] G. N. Schrauzer, T. D. Guth, *J. Am. Chem. Soc.* **1977**, *99*, 7189-7193.

[11] Y. Wang, J. Zhang, X. Wang, M. Antonietti, H. Li, *Angew. Chem. Int. Ed.* **2010**, *49*, 3356-3359.

[12] M. Zalas, M. Walkowiak, G. Schroeder, *J. Rare Earths* **2011**, *29*, 783-786.

[13] S. Mutsumi, K. Akihiko, T. Akira, D. Kazunari, M. Ken-ichi, O. Takaharu, *Chem. Lett.* **1987**, *16*, 1017-1018.

[14] a) J. Kim, D. W. Hwang, S. W. Bae, Y. G. Kim, J. S. Lee, *Korean J. Chem. Eng.* **2001**, *18*, 941-947; b) J. Kim, D. W. Hwang, H.-G. Kim, S. W. Bae, S. M. Ji, J. S. Lee, *Chem. Commun.* **2002**, 2488-2489; c) H. G. Kim, S. M. Ji, J. S. Jang, S. W. Bae, J. S. Lee, *Korean J. Chem. Eng.* **2004**, *21*, 970-975.

[15] K. Sayama, H. Arakawa, *J. Phys. Chem.* **1993**, *97*, 531-533.

[16] Y. Yuan, X. Zhang, L. Liu, X. Jiang, J. Lv, Z. Li, Z. Zou, *Int. J. Hydrogen Energy* **2008**, *33*, 5941-5946.

[17] Y. Yuan, Z. Zhao, J. Zheng, M. Yang, L. Qiu, Z. Li, Z. Zou, *J. Mater. Chem.* **2010**, *20*, 6772-6779.

[18] X. Chen, T. Yu, X. Fan, H. Zhang, Z. Li, J. Ye, Z. Zou, *Appl. Surf. Sci.* **2007**, *253*, 8500-8506.

[19] K. Domen, A. Kudo, M. Shibata, A. Tanaka, K.-I. Maruya, T. Onishi, *Chem. Commun.* **1986**, 1706-1707.

[20] a) D. Chen, J. Ye, *Chem. Mater.* **2009**, *21*, 2327-2333; b) Y. Miseki, H. Kato, A. Kudo, *Energy Environ. Sci.* **2009**, *2*, 306-314; c) H. G. Kim, D. W. Hwang, J. Kim, Y. G. Kim, J. S. Lee, *Chem. Commun.* **1999**, 1077-1078.

[21] H. Kato, A. Kudo, *Chem. Phys. Lett.* **1998**, *295*, 487-492.

[22] H. Kato, A. Kudo, *J. Phys. Chem. B* **2001**, *105*, 4285-4292.

[23] Y. Li, G. Chen, H. Zhang, Z. Li, *J. Phys. Chem. Solids* **2009**, *70*, 536-540.
[24] a) H. Kadowaki, N. Saito, H. Nishiyama, H. Kobayashi, Y. Shimodaira, Y. Inoue, *J. Phys. Chem. C* **2007**, *111*, 439-444; b) S. Nobuo, K. Haruhiko, K. Hisayoshi, I. Kouki, N. Hiroshi, I. Yasunobu, *Chem. Lett.* **2004**, *33*, 1452-1453.
[25] a) A. Kudo, H. Kato, *Chem. Lett.* **1997**, *26*, 421-422; b) K. Akihiko, H. Satoshi, *Chem. Lett.* **1999**, *28*, 1103-1104.
[26] Y. Wang, Z. Zhang, Y. Zhu, Z. Li, R. Vajtai, L. Ci, P. M. Ajayan, *ACS Nano* **2008**, *2*, 1492-1496.
[27] Y. Takashi, S. Yoshihisa, I. Hayao, *Chem. Lett.* **2004**, *33*, 726-727.
[28] G. R. Bamwenda, T. Uesigi, Y. Abe, K. Sayama, H. Arakawa, *Appl. Catal., A* **2001**, *205*, 117-128.
[29] K. Haruhiko, S. Nobuo, N. Hiroshi, I. Yasunobu, *Chemistry Letters* **2007**, *36*, 440-441.
[30] J. F. Reber, K. Meier, *J. Phys. Chem.* **1984**, *88*, 5903-5913.
[31] T. Ohmori, H. Mametsuka, E. Suzuki, *Int. J. Hydrogen Energy* **2000**, *25*, 953-955.
[32] M. Kazuhiko, T. Kentaro, S. Nobuo, I. Yasunobu, D. Kazunari, *Bull. Chem. Soc. Jpn.* **2007**, *80*, 1004-1010.
[33] A. Naoki, S. Nobuo, N. Hiroshi, I. Yasunobu, D. Kazunari, S. Kazunori, *Chem. Lett.* **2006**, *35*, 796-797.
[34] K. Maeda, N. Saito, Y. Inoue, K. Domen, *Chem. Mater.* **2007**, *19*, 4092-4097.
[35] a) X. Chen, S. S. Mao, *Chem. Rev.* **2007**, *107*, 2891-2959; b) D. Y. C. Leung, X. Fu, C. Wang, M. Ni, M. K. H. Leung, X. Wang, X. Fu, *ChemSusChem* **2010**, *3*, 681-694; c) H. Kato, A. Kudo, *J. Phys. Chem. B* **2002**, *106*, 5029-5034; d) A. Kudo, M. Sekizawa, *Chem. Commun.* **2000**, 1371-1372; e) E. Borgarello, J. Kiwi, M. Graetzel, E. Pelizzetti, M. Visca, *J. Am. Chem. Soc.* **1982**, *104*, 2996-3002; f) Z. Luo, Q.-H. Gao, *J. Photochem. Photobiol., A* **1992**, *63*, 367-375.
[36] Y. Cao, W. Yang, W. Zhang, G. Liu, P. Yue, *New J. Chem.* **2004**, *28*, 218-222.
[37] S. Klosek, D. Raftery, *J. Phys. Chem. B* **2001**, *105*, 2815-2819.
[38] W. Choi, A. Termin, M. R. Hoffmann, *J. Phys. Chem.* **1994**, *98*, 13669-13679.
[39] J. W. Liu, G. Chen, Z. H. Li, Z. G. Zhang, *J. Solid State Chem.* **2006**, *179*, 3704-3708.
[40] R. Konta, T. Ishii, H. Kato, A. Kudo, *J. Phys. Chem. B* **2004**, *108*, 8992-8995.
[41] H. Zhang, G. Chen, Y. Li, Y. Teng, *Int. J. Hydrogen Energy* **2010**, *35*, 2713-2716.
[42] D. W. Hwang, H. G. Kim, J. S. Jang, S. W. Bae, S. M. Ji, J. S. Lee, *Catal. Today* **2004**, *93-95*, 845-850.
[43] a) Z. Zou, J. Ye, K. Sayama, H. Arakawa, *Nature* **2001**, *414*, 625; b) Z. Zou, J. Ye, K. Sayama, H. Arakawa, *J. Photochem. Photobiol., A* **2002**, *148*, 65-69; c) Z. Zou, J. Ye, H. Arakawa, *J. Phys. Chem. B* **2002**, *106*, 13098-13101.
[44] S. Tanigawa, H. Irie, *Appl. Catal., B* **2016**, *180*, 1-5.
[45] N. Zeug, J. Buecheler, H. Kisch, *J. Am. Chem. Soc.* **1985**, *107*, 1459-1465.
[46] A. Kudo, M. Sekizawa, *Catal. Lett.* **1999**, *58*, 241-243.
[47] L. Ren, F. Yang, Y.-R. Deng, N.-N. Yan, S. Huang, D. Lei, Q. Sun, Y. Yu, *Int. J. Hydrogen Energy* **2010**, *35*, 3297-3305.
[48] K. Ikeue, S. Shiiba, M. Machida, *Chem. Mater.* **2010**, *22*, 743-745.

[49] a) W. Zhang, Z. Zhong, Y. Wang, R. Xu, *J. Phys. Chem. C* **2008**, *112*, 17635-17642; b) Y. Wang, Y. Wang, R. Xu, *Int. J. Hydrogen Energy* **2010**, *35*, 5245-5253; c) A. M. Roy, G. C. De, *J. Photochem. Photobiol., A* **2003**, *157*, 87-92.
[50] S. Shen, L. Zhao, Z. Zhou, L. Guo, *J. Phys. Chem. C* **2008**, *112*, 16148-16155.
[51] a) C. Burda, Y. Lou, X. Chen, A. C. S. Samia, J. Stout, J. L. Gole, *Nano Lett.* **2003**, *3*, 1049-1051; b) M. Shen, Z. Wu, H. Huang, Y. Du, Z. Zou, P. Yang, *Mater. Lett.* **2006**, *60*, 693-697; c) T. Tesfamichael, G. Will, J. Bell, *Appl. Surf. Sci.* **2005**, *245*, 172-178; d) Y. Zhao, X. Qiu, C. Burda, *Chem. Mater.* **2008**, *20*, 2629-2636; e) G. Zhang, X. Ding, Y. Hu, B. Huang, X. Zhang, X. Qin, J. Zhou, J. Xie, *J. Phys. Chem. C* **2008**, *112*, 17994-17997; f) X. Chen, Y.-B. Lou, A. C. S. Samia, C. Burda, J. L. Gole, *Adv. Funct. Mater.* **2005**, *15*, 41-49.
[52] K. Nishijima, T. Kamai, N. Murakami, T. Tsubota, T. Ohno, *Int. J. Photoenergy* **2008**, *2008*, 7.
[53] S. U. M. Khan, M. Al-Shahry, W. B. Ingler, *Science* **2002**, *297*, 2243-2245.
[54] a) Y. Su, X. Zhang, S. Han, X. Chen, L. Lei, *Electrochem. Commun.* **2007**, *9*, 2291-2298; b) J. Wang, W. Zhu, Y. Zhang, S. Liu, *J. Phys. Chem. C* **2007**, *111*, 1010-1014; c) D. Li, H. Haneda, S. Hishita, N. Ohashi, *Chem. Mater.* **2005**, *17*, 2588-2595; d) P. Periyat, D. E. McCormack, S. J. Hinder, S. C. Pillai, *J. Phys. Chem. C* **2009**, *113*, 3246-3253.
[55] H. Luo, T. Takata, Y. Lee, J. Zhao, K. Domen, Yan, *Chem. Mater.* **2004**, *16*, 846-849.
[56] N. Kumar, U. Maitra, V. I. Hegde, U. V. Waghmare, A. Sundaresan, C. N. R. Rao, *Inorg. Chem.* **2013**, *52*, 10512-10519.
[57] J. Fang, F. Shi, J. Bu, J. Ding, S. Xu, J. Bao, Y. Ma, Z. Jiang, W. Zhang, C. Gao, W. Huang, *J. Phys. Chem. C* **2010**, *114*, 7940-7948.
[58] Y. Li, G. Ma, S. Peng, G. Lu, S. Li, *Appl. Surf. Sci.* **2008**, *254*, 6831-6836.
[59] W.-J. Chun, A. Ishikawa, H. Fujisawa, T. Takata, J. N. Kondo, M. Hara, M. Kawai, Y. Matsumoto, K. Domen, *J. Phys. Chem. B* **2003**, *107*, 1798-1803.
[60] G. Hitoki, T. Takata, J. N. Kondo, M. Hara, H. Kobayashi, K. Domen, *Chem. Commun.* **2002**, 1698-1699.
[61] J. Wang, S. Yin, M. Komatsu, Q. Zhang, F. Saito, T. Sato, *J. Photochem. Photobiol., A* **2004**, *165*, 149-156.
[62] N. Nishimura, B. Raphael, K. Maeda, L. Le Gendre, R. Abe, J. Kubota, K. Domen, *Thin Solid Films* **2010**, *518*, 5855-5859.
[63] S. Min Ji, P. H. Borse, H. Gyu Kim, D. Won Hwang, J. Suk Jang, S. Won Bae, J. Sung Lee, *Phys. Chem. Chem. Phys.* **2005**, *7*, 1315-1321.
[64] S. Ge, H. Jia, H. Zhao, Z. Zheng, L. Zhang, *J. Mater. Chem.* **2010**, *20*, 3052-3058.
[65] L. Jiang, Q. Wang, C. Li, J. Yuan, W. Shangguan, *Int. J. Hydrogen Energy* **2010**, *35*, 7043-7050.
[66] A. Ishikawa, T. Takata, J. N. Kondo, M. Hara, H. Kobayashi, K. Domen, *J. Am. Chem. Soc.* **2002**, *124*, 13547-13553.
[67] R. Sasikala, A. R. Shirole, V. Sudarsan, Jagannath, C. Sudakar, R. Naik, R. Rao, S. R. Bharadwaj, *Appl. Catal., A* **2010**, *377*, 47-54.
[68] X. Wang, K. Maeda, A. Thomas, K. Takanabe, G. Xin, J. M. Carlsson, K. Domen, M. Antonietti, *Nat. Mater.* **2008**, *8*, 76.

[69] G. Liu, P. Niu, C. Sun, S. C. Smith, Z. Chen, G. Q. Lu, H.-M. Cheng, *J. Am. Chem. Soc.* **2010**, *132*, 11642-11648.
[70] F. Cheviré, F. Tessier, R. Marchand, *Eur. J. Inorg. Chem.* **2006**, *2006*, 1223-1230.
[71] a) K. Maeda, T. Takata, M. Hara, N. Saito, Y. Inoue, H. Kobayashi, K. Domen, *J. Am. Chem. Soc.* **2005**, *127*, 8286-8287; b) K. Maeda, K. Teramura, D. Lu, T. Takata, N. Saito, Y. Inoue, K. Domen, *Nature* **2006**, *440*, 295; c) K. Maeda, K. Teramura, T. Takata, M. Hara, N. Saito, K. Toda, Y. Inoue, H. Kobayashi, K. Domen, *J. Phys. Chem. B* **2005**, *109*, 20504-20510.
[72] K. Kamata, K. Maeda, D. Lu, Y. Kako, K. Domen, *Chem. Phys. Lett.* **2009**, *470*, 90-94.
[73] M. G. Kibria, F. A. Chowdhury, S. Zhao, B. AlOtaibi, M. L. Trudeau, H. Guo, Z. Mi, *Nat. Commun.* **2015**, *6*, 6797.
[74] N. Kakuta, K. H. Park, M. F. Finlayson, A. Ueno, A. J. Bard, A. Campion, M. A. Fox, S. E. Webber, J. M. White, *J. Phys. Chem.* **1985**, *89*, 732-734.
[75] I. Tsuji, H. Kato, H. Kobayashi, A. Kudo, *J. Am. Chem. Soc.* **2004**, *126*, 13406-13413.
[76] J. S. Jang, P. H. Borse, J. S. Lee, S. H. Choi, H. G. Kim, *J. Chem. Phys.* **2008**, *128*, 154717.
[77] U. Maitra, U. Gupta, M. De, R. Datta, A. Govindaraj, C. N. R. Rao, *Angew. Chem. Int. Ed.* **2013**, *52*, 13057-13061.
[78] U. Gupta, B. S. Naidu, U. Maitra, A. Singh, S. N. Shirodkar, U. V. Waghmare, C. N. R. Rao, *APL Mater.* **2014**, *2*, 092802.
[79] J. Ran, J. Zhang, J. Yu, M. Jaroniec, S. Z. Qiao, *Chem. Soc. Rev.* **2014**, *43*, 7787-7812.
[80] A. Iwase, H. Kato, A. Kudo, *Catal. Lett.* **2006**, *108*, 7-10.
[81] M. Hara, J. Nunoshige, T. Takata, J. N. Kondo, K. Domen, *Chem. Commun.* **2003**, 3000-3001.
[82] M. Liu, W. You, Z. Lei, G. Zhou, J. Yang, G. Wu, G. Ma, G. Luan, T. Takata, M. Hara, K. Domen, C. Li, *Chem. Commun.* **2004**, 2192-2193.
[83] G. Zhang, Z.-A. Lan, L. Lin, S. Lin, X. Wang, *Chem. Sci.* **2016**, *7*, 3062-3066.
[84] J. Sato, N. Saito, Y. Yamada, K. Maeda, T. Takata, J. N. Kondo, M. Hara, H. Kobayashi, K. Domen, Y. Inoue, *J. Am. Chem. Soc.* **2005**, *127*, 4150-4151.
[85] K. Maeda, X. Wang, Y. Nishihara, D. Lu, M. Antonietti, K. Domen, *J. Phys. Chem. C* **2009**, *113*, 4940-4947.
[86] B. Ma, J. Yang, H. Han, J. Wang, X. Zhang, C. Li, *J. Phys. Chem. C* **2010**, *114*, 12818-12822.
[87] a) K. Maeda, K. Teramura, D. Lu, T. Takata, N. Saito, Y. Inoue, K. Domen, *J. Phys. Chem. B* **2006**, *110*, 13753-13758; b) K. Maeda, D. Lu, K. Teramura, K. Domen, *J. Mater. Chem.* **2008**, *18*, 3539-3542.
[88] K. Maeda, N. Sakamoto, T. Ikeda, H. Ohtsuka, A. Xiong, D. Lu, M. Kanehara, T. Teranishi, K. Domen, *Chem. Eur. J.* **2010**, *16*, 7750-7759.
[89] a) M. Yugo, K. Hideki, K. Akihiko, *Chem. Lett.* **2005**, *34*, 54-55; b) A. Kudo, K. Sayama, A. Tanaka, K. Asakura, K. Domen, K. Maruya, T. Onishi, *J. Catal.* **1989**, *120*, 337-352.
[90] a) K. Wu, P. Wu, J. Zhu, C. Liu, X. Dong, J. Wu, G. Meng, K. Xu, J. Hou, Z. Liu, X. Guo, *Chem. Eng. J.* **2019**, *360*, 221-230; b) Z. Sun, H. Zheng, J. Li, P. Du, *Energy Environ. Sci.* **2015**, *8*, 2668-2676; c) Z. Sun, Q. Yue, J. Li, J. Xu, H. Zheng, P. Du, *J. Mater. Chem.A* **2015**, *3*, 10243-10247; d) H. Cheng, X.-J.

Lv, S. Cao, Z.-Y. Zhao, Y. Chen, W.-F. Fu, *Sci. Rep.* **2016**, *6*, 19846; e) W. Bi, L. Zhang, Z. Sun, X. Li, T. Jin, X. Wu, Q. Zhang, Y. Luo, C. Wu, Y. Xie, *ACS Catal.* **2016**, *6*, 4253-4257.
[91] X. Zong, H. Yan, G. Wu, G. Ma, F. Wen, L. Wang, C. Li, *J. Am. Chem. Soc.* **2008**, *130*, 7176-7177.
[92] F. A. Frame, F. E. Osterloh, *J. Phys. Chem. C* **2010**, *114*, 10628-10633.
[93] S. Cao, Y. Chen, C.-J. Wang, X.-J. Lv, W.-F. Fu, *Chem. Commun.* **2015**, *51*, 8708-8711.
[94] J. S. Jang, D. J. Ham, N. Lakshminarasimhan, W. y. Choi, J. S. Lee, *Appl. Catal., A* **2008**, *346*, 149-154.
[95] a) J. S. Jang, H. G. Kim, U. A. Joshi, J. W. Jang, J. S. Lee, *Int. J. Hydrogen Energy* **2008**, *33*, 5975-5980; b) J. C. Yu, L. Wu, J. Lin, P. Li, Q. Li, *Chem. Commun.* **2003**, 1552-1553; c) D. R. Baker, P. V. Kamat, *Adv. Funct. Mater.* **2009**, *19*, 805-811.
[96] H. Park, W. Choi, M. R. Hoffmann, *J. Mater. Chem.* **2008**, *18*, 2379-2385.
[97] R. Sasikala, A. Shirole, V. Sudarsan, T. Sakuntala, C. Sudakar, R. Naik, S. R. Bharadwaj, *Int. J. Hydrogen Energy* **2009**, *34*, 3621-3630.
[98] L. Amirav, A. P. Alivisatos, *J. Phys. Chem. Lett.* **2010**, *1*, 1051-1054.
[99] S. Liu, J.-H. Yang, J.-H. Choy, *J. Photochem. Photobiol., A* **2006**, *179*, 75-80.
[100] W. Shangguan, A. Yoshida, *J. Phys. Chem. B* **2002**, *106*, 12227-12230.
[101] C. Xing, D. Jing, M. Liu, L. Guo, *Mater. Res. Bull.* **2009**, *44*, 442-445.
[102] R. I. Bickley, T. Gonzalez-Carreno, J. S. Lees, L. Palmisano, R. J. D. Tilley, *J. Solid State Chem.* **1991**, *92*, 178-190.
[103] J. Shi, J. Chen, Z. Feng, T. Chen, Y. Lian, X. Wang, C. Li, *J. Phys. Chem. C* **2007**, *111*, 693-699.
[104] a) Y. K. Kho, A. Iwase, W. Y. Teoh, L. Mädler, A. Kudo, R. Amal, *J. Phys. Chem. C* **2010**, *114*, 2821-2829; b) Y. K. Kho, A. Iwase, W. Y. Teoh, L. Mädler, A. Kudo, R. Amal, *J. Phys. Chem. C* **2010**, *114*, 2821-2829.
[105] T. Li, S. Zhang, S. Meng, X. Ye, X. Fu, S. Chen, *RSC Adv.* **2017**, *7*, 6457-6466.
[106] K. Maeda, K. Domen, *J. Phys.Chem. C* **2007**, *111*, 7851-7861.
[107] a) N. Koriche, A. Bouguelia, A. Aider, M. Trari, *Int. J. Hydrogen Energy* **2005**, *30*, 693-699; b) S. Wu, Y. Sun, X. Wang, W. Wu, X. Tian, Q. Yan, Y. Luo, Q. Zhang, *Journal of Photochemistry and Photobiology A: Chemistry* **2007**, *191*, 97-103.
[108] a) S. Saadi, A. Bouguelia, M. Trari, *Renewable Energy* **2006**, *31*, 2245-2256; b) Y. Bessekhouad, M. Trari, *Int. J. Hydrogen Energy* **2002**, *27*, 357-362.
[109] a) G. Lu, S. Li, *Int. J. Hydrogen Energy* **1992**, *17*, 767-770; b) E. Subramanian, J.-O. Baeg, S. M. Lee, S.-J. Moon, K.-j. Kong, *Int. J. Hydrogen Energy* **2008**, *33*, 6586-6594.
[110] S. V. Tambwekar, M. Subrahmanyam, *Int. J. Hydrogen Energy* **1997**, *22*, 959-965.
[111] a) A. Patsoura, D. I. Kondarides, X. E. Verykios, *Catal. Today* **2007**, *124*, 94-102; b) X.-J. Zheng, L.-F. Wei, Z.-H. Zhang, Q.-J. Jiang, Y.-J. Wei, B. Xie, M.-B. Wei, *Int. J. Hydrogen Energy* **2009**, *34*, 9033-9041.
[112] A. Kudo, *MRS Bull.* **2011**, *36*, 32-38.
[113] Z. Pan, Y. Zheng, F. Guo, P. Niu, X. Wang, *ChemSusChem* **2017**, *10*, 87-90.
[114] A. Iwase, Y. H. Ng, Y. Ishiguro, A. Kudo, R. Amal, *J. Am. Chem. Soc.* **2011**, *133*, 11054-11057.

[115] R. Abe, K. Sayama, K. Domen, H. Arakawa, *Chem. Phys. Lett.* **2001**, *344*, 339-344.
[116] a) R. Abe, T. Takata, H. Sugihara, K. Domen, *Chem. Commun.* **2005**, 3829-3831; b) H. Masanobu, A. Ryu, I. Akio, T. Tsuyoshi, O. Bunsho, D. Kazunari, *Chem. Lett.* **2008**, *37*, 138-139; c) M. Higashi, R. Abe, T. Takata, K. Domen, *Chem. Mater.* **2009**, *21*, 1543-1549.
[117] Y. Sasaki, H. Nemoto, K. Saito, A. Kudo, *J. Phys.Chem C* **2009**, *113*, 17536-17542.

# Chapter 2

## Effect of Morphology and Surface Area of the Oxide Nanostructures on the Visible Light Induced Generation of Hydrogen from $ZnO(TiO_2)/Pt/Cd_{1-x}Zn_xS$


**Summary***

Hydrogen can be generated by visible light irradiation of semiconductor heterostructures of the type ZnO/Pt/CdS and $TiO_2$/Pt/CdS. In order to understand the dependence of hydrogen generation on the properties of the nanoparticles of ZnO and $TiO_2$, we have carried out systematic studies. For this purpose, we have studied photocatalytic hydrogen generation by $ZnO(TiO_2)/Cd_{1-x}Zn_xS$ and $ZnO(TiO_2)/Pt/Cd_{1-x}Zn_xS$ (x = 0.0, 0.2) heterostructures with oxide nanostructures possessing different morphologies and surface areas. In the case of $TiO_2/Pt/Cd_{0.8}Zn_{0.2}S$ heterostructures, the highest $H_2$ evolution rate up to 1.76 mmol $h^{-1}g^{-1}$ was obtained with $H_2Ti_3O_7$ nanotubes, with the least $H_2$ evolution rate (0.55 mmol $h^{-1}g^{-1}$) from $TiO_2$ powder (Degussa P25). In the case of ZnO/Pt/CdS heterostructures, the highest $H_2$ evolution rate (6.88 mmol $h^{-1}g^{-1}$) were obtained from ZnO nanorods1, whereas the least $H_2$ evolution rate (2.55 mmol $h^{-1}g^{-1}$) was obtained from ZnO nanorods3. Photocatalytic activity of heterostructures generally follows the same trend as the BET surface areas of the oxide nanostructures, with high surface area favoring good hydrogen evolution activity.


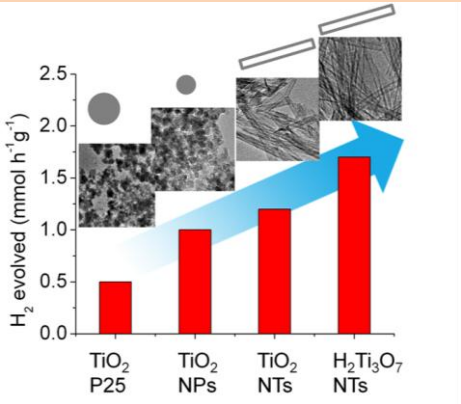


A Paper Based on this work has appeared in Chem. Phys. Lett. (2015)

# 1. Introduction

Of the strategies to produce hydrogen by splitting water, artificial photosynthesis is an attractive one due to its unique properties.[1] In particular, semiconductor heterostructures have been successfully employed to generate hydrogen under visible light irradiation.[2] Thus, Alivisatos *et al*. have employed CdSe/CdS/Pt heterostructures to obtain hydrogen with good quantum yields under visible-light irradiation.[3] Recently, solution-processed ZnO/Pt/CdS and related heterostructures have been used to produce hydrogen using visible-light irradiation in the presence of sacrificial electron donors like $Na_2S$-$Na_2SO_3$ and benzyl alcohol-acetic acid.[4] Alignment of theconduction band minima (CBM) and valence band maxima (VBM) positions of CdS and ZnO in these heterostructures result in the transfer of photogenerated electrons from CdS to the CBM of ZnO which eventually reaches to the Pt nanoparticles present on ZnO and performs the reduction of a proton into hydrogen. Such heterostructures exhibit excellent photocatalytic hydrogen evolution activity and stability due to the efficient separation of photogenerated charge carriers. Nanostructures of semiconductors are generally used in these studies to promote surface reactions, especially the reduction of protons to hydrogen. The photochemical activity of such semiconductor materials would be expected to depend on the morphology and surface area of the oxide material used.[5] For example, $TiO_2$ nanotubes are reported to exhibit superior photocatalytic activity than $TiO_2$ nanoparticles.[6] Morphology-dependent photocatalytic activities of ZnO nanostructures have also been noted.[7] We were motivated to carry out a systematic study of the dependence of surface area and morphology of oxide component in these heterostructures on the visible-light-induced hydrogen generation. In view of the excellent performance of ZnO/Pt/CdS and $TiO_2$/Pt/$Cd_{0.8}Zn_{0.2}S$ type heterostructures, we have prepared ZnO and $TiO_2$ nanostructures with different morphologies and surface areas and employed them in the heterostructures to investigate the visible-light-induced hydrogen generation by $TiO_2$/$Cd_{0.8}Zn_{0.2}S$, ZnO/CdS, $TiO_2$/Pt/$Cd_{0.8}Zn_{0.2}S$, and ZnO/Pt/CdS heterostructures. The study has revealed the major role played by the surface area of the oxide nanostructures on the hydrogen evolution activity.

## 2. Scope of the Present Investigations

Semiconductor-based heterostructures of type $TiO_2$/Pt/$Cd_{0.8}Zn_{0.2}S$ and ZnO/Pt/CdS have shown a promising activity of the conversion of solar energy into chemical energy (Hydrogen). However, the exact role of the oxide materials in these heterostructures is not clear. Present work investigates the importance of oxide nanostructures morphology and surface area on the photocatalytic activity of the heterostructures. We have employed the various morphology and surface area of $TiO_2$ and ZnO to prepare above heterostructures and measured their catalytic activity for hydrogen evolution in the presence and absence of Pt nanoparticles. It has been found that photocatalytic activity increases with the increase in the surface area of the oxide nanostructures in both the heterostructures.

## 3. Experimental Section

**Preparation of $H_2Ti_3O_7$ nanotubes:** $H_2Ti_3O_7$ nanotubes were synthesized by a hydrothermal method.[8] In a typical synthesis $TiO_2$ powder (Degussa P25) (25 mmol) was well dispersed in an aqueous solution of NaOH (10 M, 70 mL). This solution was transferred into a Teflon-lined autoclave of 100 mL capacity and placed in an oven preheated at 150 °C for 44 hours. Hydrothermal treatment was followed by natural cooling of the autoclave in the air to room temperature. The reaction product was washed several times with distilled water to get the pH of the solution close to 7. At this pH aqueous solution of HCl (0.1 M, 150 mL) was added to this compound and stirred at room temperature for 10 hours. It was followed by several times washing with distilled water to get pH close to 7. This product was dried in the open air at 65 °C.

**Preparation of $TiO_2$ nanotubes:** Calcinations of $H_2Ti_3O_7$ nanotubes prepared $TiO_2$ nanotubes at 300 °C for two hours**.**

**Preparation of $TiO_2$ nanoparticles:** $TiO_2$ nanoparticles were synthesized by sol-gel method.[9] Pluronic P 123 (2.0 g) was dissolved in aqueous sodium chloride (1 M, 50 mL) solution. Titanium isopropoxide (10 mL) was added to this solution slowly and

stirred for 10 hours at room temperature. The white product was washed and centrifuged multiple times with $H_2O$ and ethanol.

**Preparation of $TiO_2$ based heterostructures:** Preparation of the $TiO_2$/Pt/$Cd_{0.8}Zn_{0.2}S$ heterostructures consisted of two steps. In the first step, Pt nanoparticles were deposited on the surface of $TiO_2$ nanostructures, followed by the second step in which $Cd_{0.8}Zn_{0.2}S$ nanoparticles were deposited. To deposit Pt nanoparticles chloroplatinic acid was used as the precursor. $TiO_2$ (1 mmol) was dispersed in distilled water under sonication, to which chloroplatinic acid (0.5 mol %) and methanol (15 mL) were added. This dispersion was kept in UV-visible light (New Port 6279, Xe-Lamp 400W) for 1.5 hours. The brownish black colored $TiO_2$/Pt product was washed with methanol and centrifuged. Nanoparticles of $Cd_{0.8}Zn_{0.2}S$ (20 mol %) were deposited on $TiO_2$/Pt by the dropwise addition of $Cd(CH_3COO)_2.2H_2O$ (0.02 M, 10 mL), and $Na_2S$ (0.04 M, 10 mL) in methanolic solution. A solution of $Zn(CH_3COO)_2.2H_2O$ (4.5 mM, 8 mL) was added before adding $Cd^{2+}$ and $S^{2-}$ to form $Cd_{0.8}Zn_{0.2}S$ nanoparticles.

$TiO_2$/$Cd_{0.8}Zn_{0.2}S$ heterostructures were prepared by the drop-wise addition of a solution of $Cd(CH_3COO)_2.2H_2O$ and $Na_2S$ in the presence of $Zn(CH_3COO)_2.2H_2O$. In a typical synthesis, $TiO_2$ (1 mmol) was dispersed in methanol by means of sonication. Nanoparticles of $Cd_{0.8}Zn_{0.2}S$ (20 mol %) were deposited drop-wise on $TiO_2$ by adding a methanolic solution of $Cd(CH_3COO)_2$. $2H_2O$ (0.02 M, 10 mL), $Na_2S$ (0.04 M, 10 mL) and $Zn(CH_3COO)_2$. $2H_2O$ (4.5 mM, 8mL).

**Preparation of ZnO nanoparticles:** ZnO nanoparticles were synthesized by a solvothermal method.[10] In a typical synthesis, $Zn(CH_3COO)_2.2H_2O$ (4 mmol) was dissolved in methanol (60 mL) and subjected to reflux at 60 $^{\circ}$C. Potassium hydroxide pellets (13.5 mmol) were dissolved in methanol (15 mL) and added dropwise to this refluxing solution. This resulting solution was continued to reflux at 60 $^{\circ}$C for 2 hours. After the 2 hours of reflux volume of solution was reduced to half by the rotor vapor evaporation, and the remaining solution was again subjected to reflux at 60 $^{\circ}$C for 24 hours. The white product was washed and centrifuged several times with distilled water and ethanol. The product was dried at 70 $^{\circ}$C in air.

**Preparation of ZnO nanorods1:** ZnO nanorod1 was prepared by solution synthesis.[11] In a typical synthesis, $Zn(CH_3COO)_2.2H_2O$ (4 mmol) was dissolved in

ethanol (100 mL). NaOH pellets (100 mmol) were added to this solution and stirred for 2 hours. This cloudy solution was packed in a plastic container and kept at room temperature for six days. The product was washed and centrifuged several times by distilled water and ethanol and dried at 70 $^{\circ}$C in air.

**Preparation of ZnO nanorods2:** ZnO nanorod2 were prepared by the hydrothermal method.[12] In a typical synthesis, a solution of $Zn(CH_3COO)_2.2H_2O$ and NaOH were prepared separately by dissolving $Zn(CH_3COO)_2.2H_2O$ (2 mmol), and NaOH (20 mmol) in 20 and 40 mL of ethanol respectively. These two solutions were added together and packed in an autoclave of 70 mL capacity. This autoclave was placed in an oven fixed at 150 $^{\circ}$C for 24 hours. After the completion of hydrothermal reaction duration, a product was washed and centrifuged several times with distilled water and ethanol. Finally, the product was dried at 70 $^{\circ}$C in air.

**Preparation of ZnO nanorods3:** In a typical synthesis, $Zn(NO_3)_2.6H_2O$ (5 mmol) was dissolved in 10 mL of $H_2O$, NaOH (150 mmol) was added to this solution under constant stirring.[11] To this solution ethanol (100 mL) and ethylenediamine (30 mL) was added. The resulting solution was transferred into a plastic container of and kept at room temperature under constant stirring for 72 hours. The product was washed and centrifuged with distilled water and ethanol and dried at 60 $^{\circ}$C in air.

**Preparation of ZnO based heterostructures**

Synthesis of ZnO/Pt/CdS heterostructures also consisted of two steps. In the first step we prepared ZnO/Pt heterostructures, and in the second step CdS, nanoparticles were deposited on these heterostructures. ZnO (1 mmol) was dispersed in distilled water, to which chloroplatinic acid (0.5 mol %) and methanol (15 mL) were added. The mixture was sonicated, and $NaBH_4$ (0.82 mmol) solution was added drop-wise to this dispersion in order to reduce chloroplatinic acid in to Pt. The brownish-black product was washed with methanol and centrifuged.

Nanoparticles of CdS (20 mol %) were deposited on the ZnO/Pt heterostructures by drop-wise addition of a methanolic solution of $Cd(CH_3COO)_2.2H_2O$ (0.02 M, 10 mL) and $Na_2S$ (0.04 M, 10 mL). In a typical preparation of ZnO/CdS heterostructures, ZnO (0.61 mmol) was dispersed in

methanol. Nanoparticles of CdS (20 mol %) were deposited on ZnO by the drop-wise addition of a methanolic solution of $Cd(CH_3COO)_2.2H_2O$(0.012 M, 10 mL) and $Na_2S$ (0.024 M, 10 mL) .

**Characterization**

Transmission electron microscope (TEM) images were obtained with a JEOL-3010 system. X-ray diffraction (XRD) patterns were recorded with a Bruker D8 Diffraction System using a Cu Kα source (λ= 0.154178 nm). UV-Vis absorption spectra were collected by Perkin Elmer Model Lambda 900 spectrometer. Photoluminescence measurements were carried out with a Horiba Jobin Yvon Spectrometer (iHR 320) at room temperature. BET surface area measurement was done by Quantachrome, in $N_2$ gas at 77 K. Raman spectra were recorded by using the 514 nm Ar-laser with the Jobin -Yvon lab-Ran HR spectrometer.

**Photocatalytic Experiments**

Photocatalytic measurements were carried under a Xe arc lamp (New Port, 6279 NS ozone-free and working at 400 W). The amount of $H_2$ evolved was determined with a gas chromatograph (Perkin Elmer, Clarus 580). Photocatalytic measurements were carried out with 20 mg of the photocatalyst. $Na_2S$ and $Na_2SO_3$ were used as sacrificial agents.

# 4. Results and Discussion

$TiO_2$ and ZnO nanostructures with different morphologies were synthesized to prepare heterostructures based on the nanostructures, wherein $TiO_2$ and ZnO occur with Pt, and CdS or $Cd_{0.8}Zn_{0.2}S$ nanoparticles. In the case of $TiO_2$-based heterostructures, we have used (a)$TiO_2$ powder (Degussa P25) (b) nanoparticles synthesized by titanium isopropoxide hydrolysis followed by calcination at 400 $^{\circ}$C ($TiO_2$ NP), (c) nanotubes synthesized by alkaline hydrolysis of Degussa P25 nanoparticles followed by acid treatment ($H_2Ti_3O_7$ NT) and (d) nanotubes obtained by the calcination of the $H_2Ti_3O_7$ nanotubes at 300 $^{\circ}$C ($TiO_2$ NT). We show typical TEM images of the $TiO_2$ nanostructures in **Figure 1**. The diameter of Degussa P25 and the synthesized $TiO_2$ nanoparticles were in the ranges 20-30, and 7- 14 nm respectively.

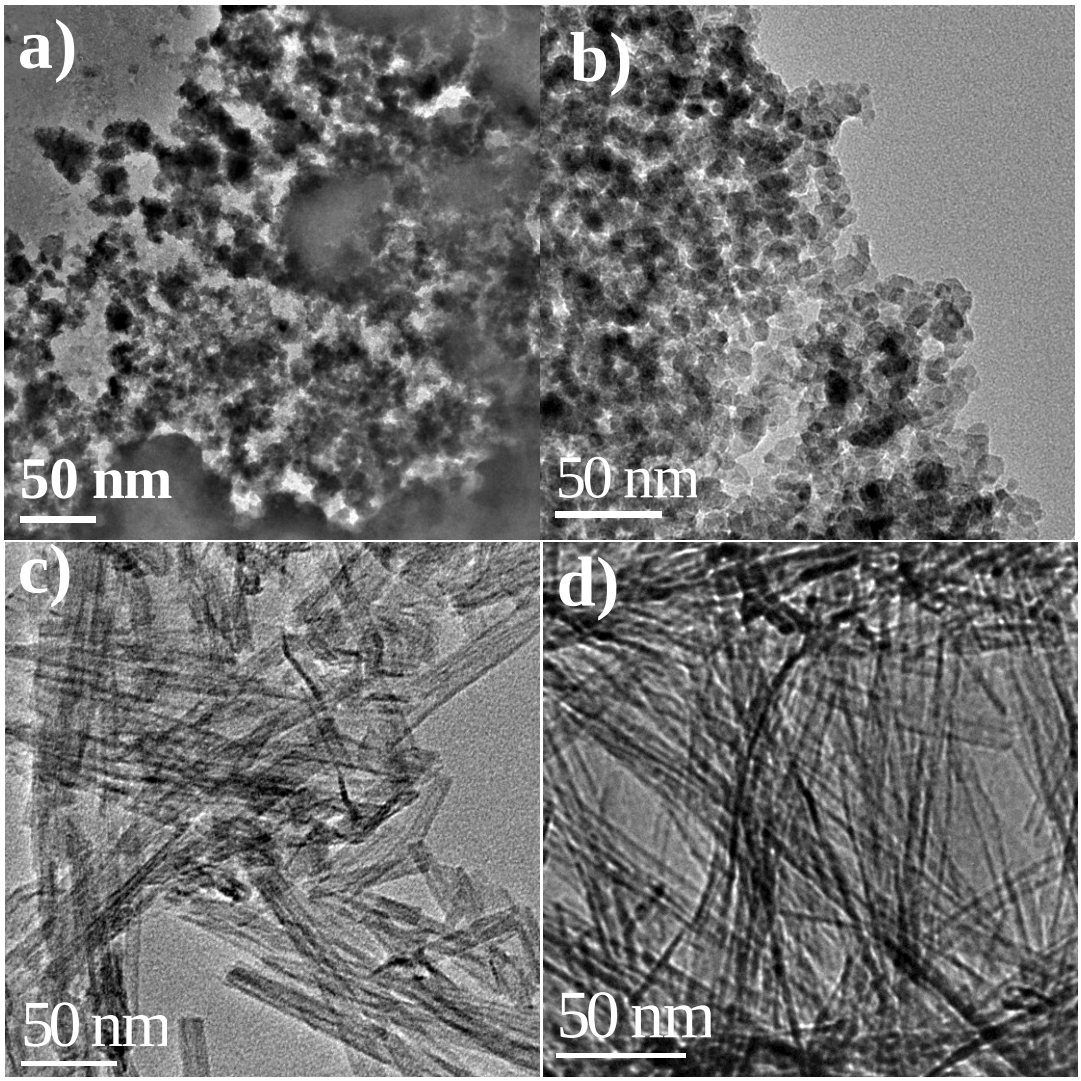


Figure 1. TEM images of a) Degussa (P25), b) $TiO_2$ NPs, c) $H_2Ti_3O_7$ NTs, and d) $TiO_2$ NTs.

The diameters of the $H_2Ti_3O_7$ and $TiO_2$ nanotubes were in the ranges 6-12 and 5-8 nm respectively. X-ray diffraction patterns of the $TiO_2$ samples were recorded at room temperature (**Figure 2a**). $TiO_2$ powder (Degussa P25) contain both anatase and rutile phases. The nanoparticles of $TiO_2$ synthesized by us crystallized in the anatase structure. The $H_2Ti_3O_7$ nanotubes had the known monoclinic structures.[13] The $TiO_2$ nanotubes obtained by calcination of $H_2Ti_3O_7$ nanotubes had the anatase structure.

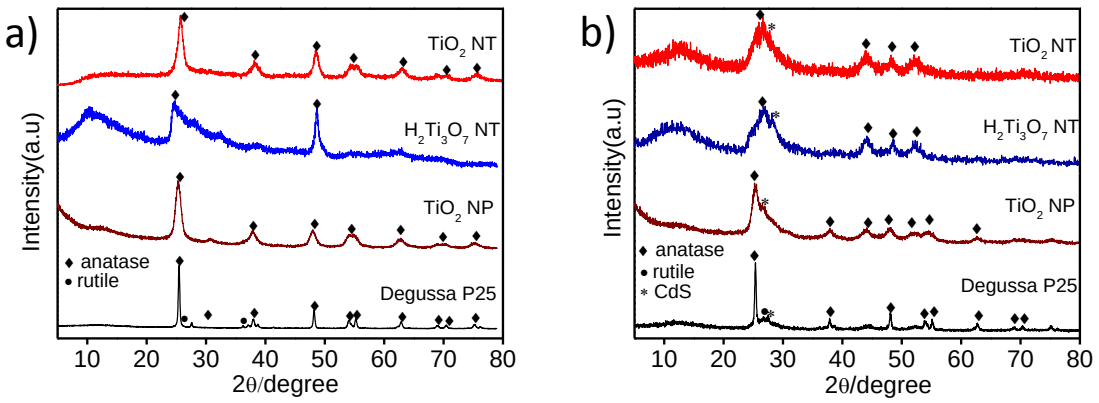


Figure 2. PXRD pattern of a) $TiO_2$ nanostructures, and b) Heterostructures synthesized by different $TiO_2$ nanostructures.

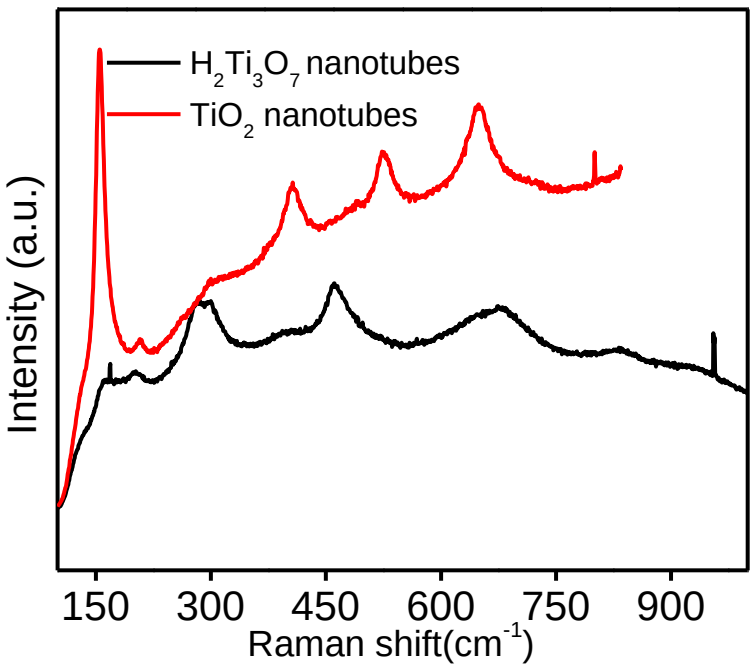


Figure 3. Raman spectra of $H_2Ti_3O_7$ and $TiO_2$ nanotubes.

XRD-diffraction patterns of $TiO_2$/Pt/$Cd_{0.8}Zn_{0.2}S$ (**Figure 2b**) show the clear presence of CdS along with $TiO_2$. The Raman spectrum of $H_2Ti_3O_7$ shows bands at 166, 203, 284, 296, 463, 675, 834, and 925 $cm^{-1}$ while $TiO_2$ nanotubes shows Raman bands at 155, 209, 405, 525, 648, and 802 $cm^{-1}$ (**Figure 3**). Raman scattering data obtained from these two compounds are consistent with the literature reports.[14] BET surface area measurements of the $TiO_2$ nanostructures were carried out with $N_2$

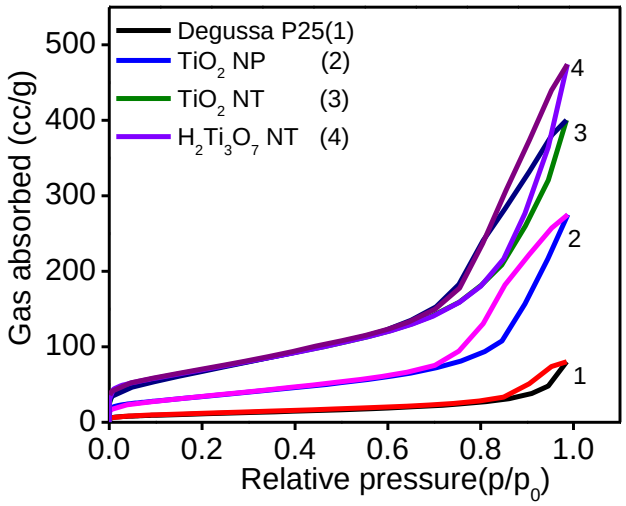


Figure 4. $N_2$ sorption profiles of different $TiO_2$ nanostructures.

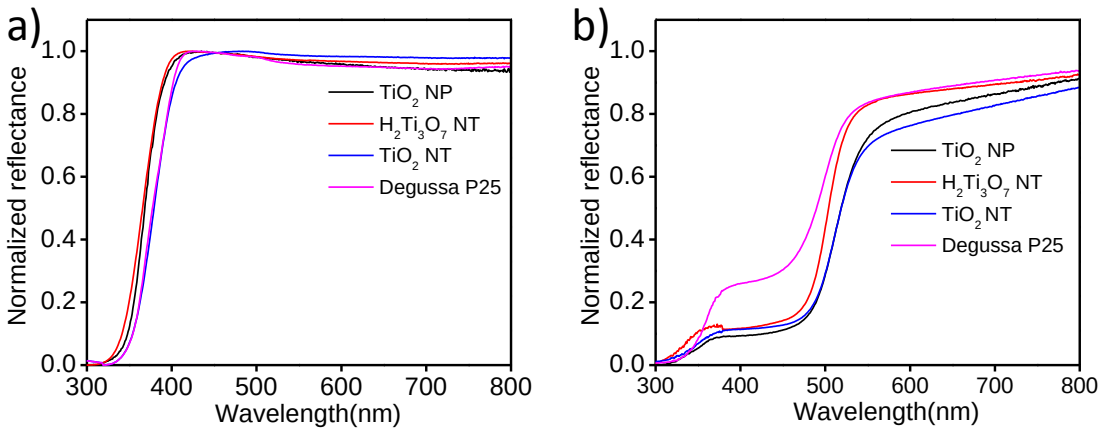


Figure 5. Reflectance spectra of a) $TiO_2$ nanostructures, and b) $TiO_2$/Pt/$Cd_{0.8}Zn_{0.2}S$.

gas at 77K (**Figure 4**). The surface areas of Degussa P25, $TiO_2$ NP, $TiO_2$ NT, and $H_2Ti_3O_7$ NT were 39.9, 123.0, 247.8, and 248.7 $m^2/g$ respectively. Diffuse reflectance spectra of the $TiO_2$ samples (**Figure 5a**) show absorption in UV region. The UV/Vis diffuse reflectance spectra of $TiO_2$/Pt/$Cd_{0.8}Zn_{0.2}S$ heterostructures (**Figure 5b**), shows absorption in visible region due to $Cd_{0.8}Zn_{0.2}S$, along with absorption in UV region related to $TiO_2$.

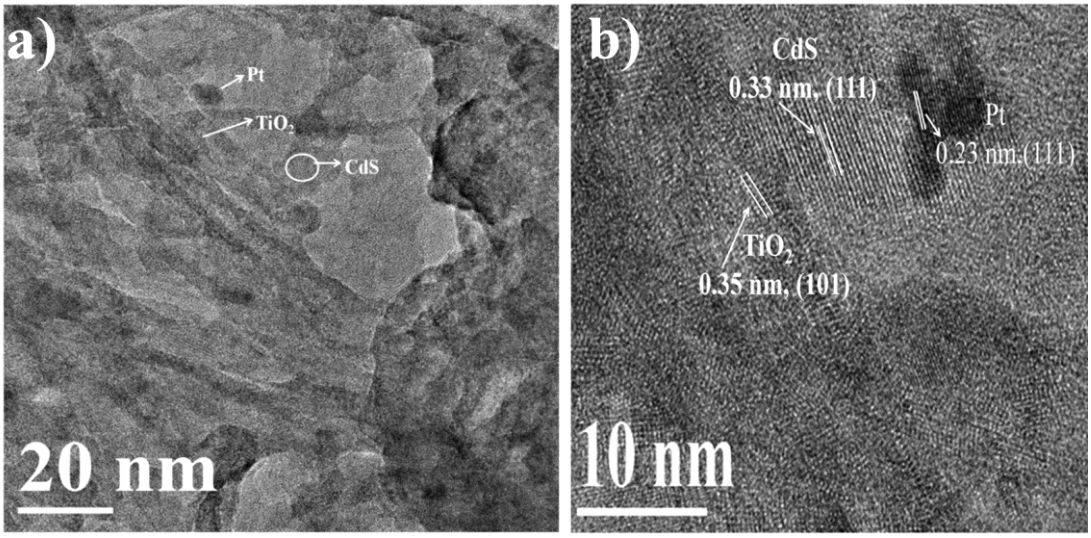


Figure 6. a) TEM, and b) HRTEM image of $TiO_2$ NT/Pt/$Cd_{0.8}Zn_{0.2}S$.

We first investigated $TiO_2$/CdS heterostructures using the different $TiO_2$ nanostructures for photocatalytic study, by measuring $H_2$ evolution in visible light in the presence of $Na_2S$ and $Na_2SO_3$ as sacrificial agents. We did not observe $H_2$ evolution from all these nanostructures except those with $H_2Ti_3O_7$ and $TiO_2$ nanotubes for two hours. Since partial substitution of Zn in CdS is known to increase the photocatalytic activity of heterostructures, we synthesized the $TiO_2$/$Cd_{0.8}Zn_{0.2}S$ as well as $TiO_2$/Pt/$Cd_{0.8}Zn_{0.2}S$ heterostructures by employing the four $TiO_2$ nanostructures.[4a] **Figure 6a** shows a typical low magnification TEM image of $TiO_2$NT/Pt/$Cd_{0.8}Zn_{0.2}S$ heterostructures. The Pt and $Cd_{0.8}Zn_{0.2}S$ nanoparticles can be seen on the surface of the $TiO_2$ nanotubes. An HRTEM image of this heterostructures further shows the lattice spacing of 0.35 nm of $TiO_2$, 0.33 nm of $Cd_{0.8}Zn_{0.2}S$ and 0.22 nm of Pt corresponding to the (101) plane of $TiO_2$, (111) plane of $Cd_{0.8}Zn_{0.2}S$ and (111) plane of Pt (**Figure 6b**).

**Photocatalytic $H_2$ evolution** activities of $TiO_2$/$Cd_{0.8}Zn_{0.2}S$ heterostructures with the different $TiO_2$ nanostructures are shown in **Figure 7a.** The photocatalytic $H_2$ evolution rate is highest in the case $H_2Ti_3O_7$ nanotubes (104 μmol $h^{-1}g^{-1}$) and least in the case of $TiO_2$ nanoparticles (18 μmol $h^{-1}g^{-1}$). The photocatalytic activity of $TiO_2$ nanotubes (93 μmol $h^{-1}g^{-1}$) is close to that of the $H_2Ti_3O_7$ nanotubes. We observe the photocatalytic activity of $TiO_2$/$Cd_{0.8}Zn_{0.2}S$ heterostructures follows the trend in the BET surface areas of $TiO_2$ nanostructures, with high surface area favoring high $H_2$

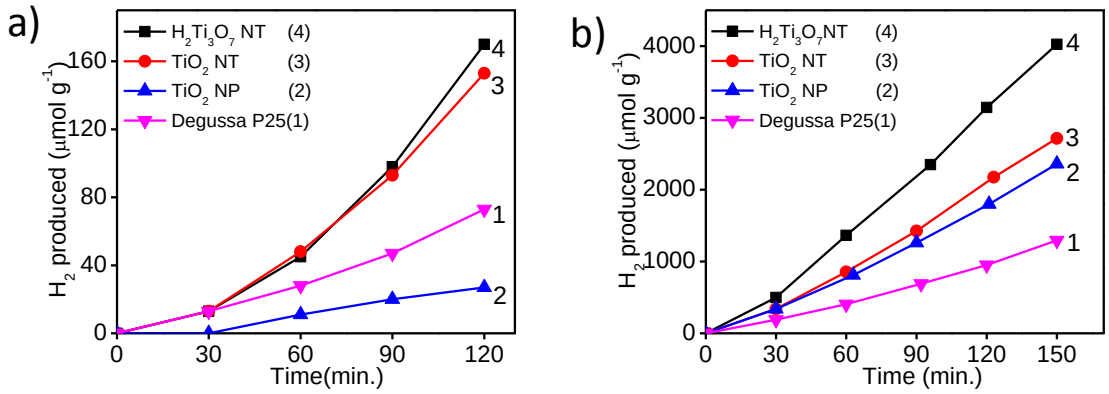


Figure 7. Photocatalytic hydrogen generation from a) $TiO_2/Cd_{0.8}Zn_{0.2}S$, and b) $TiO_2/Pt/Cd_{0.8}Zn_{0.2}S$ heterostructures employing different $TiO_2$ nanostructures.

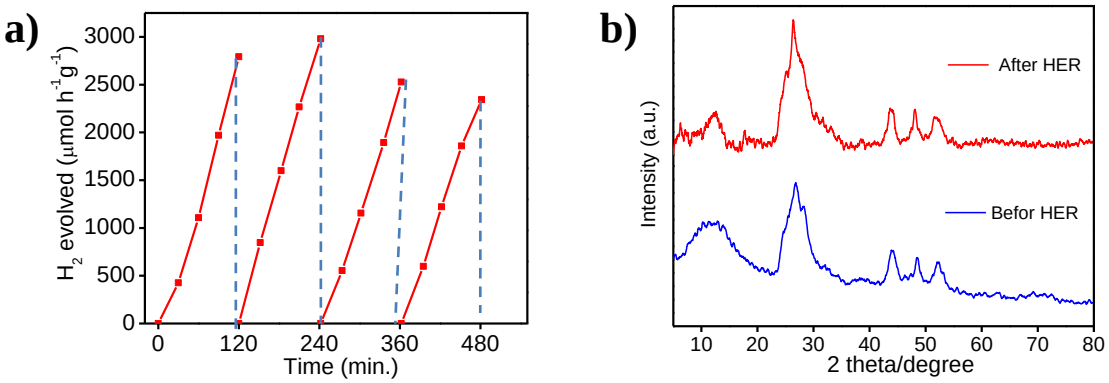


Figure 8. a) Photocatalytic activity of $H_2Ti_3O_7/Pt/Cd_{0.8}Zn_{0.2}S$ under different cycles, and b) PXRD pattern of $H_2Ti_3O_7/Pt/Cd_{0.8}Zn_{0.2}S$ before and after reaction.

evolution activity (**Table 1**). We observe a slight deviation from this trend in the case of $TiO_2$ NPS which shows lesser activity than Degussa P25. Since redox reaction in $TiO_2/Cd_{0.8}Zn_{0.2}S$ occurs at the surface of $TiO_2$ nanostructures, the smaller activity of $TiO_2$ nanoparticles is expected due to the presence of the capping agent (Pluronic P 123) used in the synthesis of the nanoparticles. The capping agent at the surface of nanoparticles can hinder the active sites for proton reduction and cause a lowering of photocatalytic activity. We have also explored the photocatalytic activity of $TiO_2/Pt/Cd_{0.8}Zn_{0.2}S$ heterostructures with the different $TiO_2$ nanostructures. **Figure 7b** shows photochemical $H_2$ evolution from $TiO_2/Pt/Cd_{0.8}Zn_{0.2}S$ heterostructures. In the presence of Pt nanoparticles, we see a significant increase in the photocatalytic activity of all the heterostructures. The highest photocatalytic $H_2$ evolution is from the

heterostructures formed with $H_2Ti_3O_7$ nanotubes (1.76 mmol $h^{-1}g^{-1}$) and least from the $TiO_2$ powder (Degussa P25) (0.55 mmol $h^{-1}g^{-1}$). The photocatalytic $H_2$ evolution from these heterostructures follows the trend in the BET surface areas of the different $TiO_2$

Table 1: Properties of $TiO_2$ nanostructures.

| Sample | Surface are ($m^2/g$) | $H_2$ ($\mu mol\ h^{-1}g^{-1}$) | AQY[c] (%) |
|---|---|---|---|
| Degussa-P25 | 39.9 | 36[a] (550)[b] | 0.88 |
| $TiO_2$ NP | 123.0 | 18 (1011) | 1.55 |
| $H_2Ti_3O_7$ NT | 248.7 | 104 (1763) | 2.69 |
| $TiO_2$ NT | 247.8 | 93 (1202) | 1.86 |

[a] Activity of $TiO_2/Cd_{0.8}Zn_{0.2}S$, [b] activity of $TiO_2/Pt/Cd_{0.8}Zn_{0.2}S$.
[c] Apparent quantum yield of $TiO_2/Pt/Cd_{0.8}Zn_{0.2}S$.

nanostructures (**Table 1**). The deviation on activity from the trend in BET surface areas found in the case of $TiO_2$ NP/$Cd_{0.8}Zn_{0.2}S$ is not observed in the presence of Pt nanoparticles. In the case of $TiO_2/Pt/Cd_{0.8}Zn_{0.2}S$ heterostructures, the $TiO_2$ nanoparticles show higher activity than Degussa P25 following the trend in surface areas. Two possible reasons for the higher activity of $TiO_2$ NPs can be the following. In the $TiO_2/Pt/Cd_{0.8}Zn_{0.2}S$ system, proton reduction occurs at the surface of Pt nanoparticles, and the presence of a capping agent probably does not hinder the rate of the redox reaction. The capping agent may also have been degraded under UV light irradiation used for the deposition of Pt on the $TiO_2$ nanoparticles. Photocatalytic hydrogen evolution activity of $H_2Ti_3O_7/Pt/Cd_{0.8}Zn_{0.2}S$ heterostructures was measured for 8 hours in four cycles (**Figure 8a**). We observe consistent hydrogen evolution activity in all the four cycles. The PXRD pattern of the photocatalyst was recorded after four cycles shows the stability of photocatalyst in the prevailing reaction condition (**Figure 8b**). The apparent quantum yield (AQY) from these heterostructures increases with the increase in photocatalytic activities as shown in

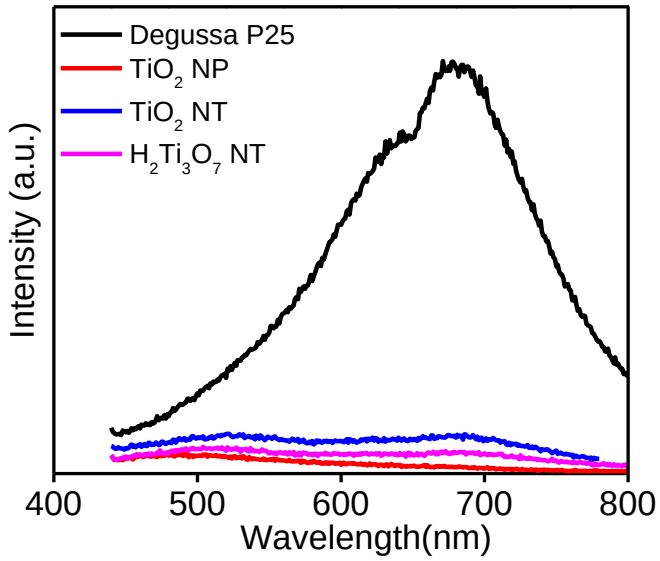


Figure 9. Photoluminescence spectra of $TiO_2/Cd_{0.8}Zn_{0.2}S$ heterostructures.

**Table 1** which summaries all the properties of the semiconductor heterostructures based on $TiO_2$.

It has been reported that a decrease in the recombination rate of photogenerated charge carriers is manifested by the lowering of the photoluminescence intensity.[15] Photoluminescence spectra (PL) of $TiO_2/Cd_{0.8}Zn_{0.2}S$ heterostructures (**Figure 9**) at room temperature (excited at 420 nm) were collected. We observe an intense broad emission centered at 680 nm from Degussa P25/$Cd_{0.8}Zn_{0.2}S$ suggesting least separation of photogenerated electrons and holes in these heterostructures. The lowest surface area and highest electron and hole recombination rate make DegussaP25/Pt/$Cd_{0.8}Zn_{0.2}S$ heterostructures least active in photocatalysis. Despite exhibiting similar photoluminescence intensity by $TiO_2$ nanoparticles and $TiO_2$ nanotubes, the later show higher photocatalytic activity due to the higher surface area.

## ZnO based heterostructures

We have also studied the effect of morphology of the various ZnO nanostructures on the photochemical $H_2$ evolution by the ZnO/CdS and ZnO/Pt/CdS heterostructures by employing the following nanostructures of ZnO: (a) ZnO nanoparticles synthesized by the hydrolysis of $Zn(CH_3COO)_2.2H_2O$, (b) ZnO NR1 synthesized by $Zn(CH_3COO)_2$ hydrolysis at room temperature, (c) ZnO NR2 synthesized by the hydrothermal method, (d) ZnO NR3 also prepared at room temperature as NR1 but with larger length and diameter. **Figure 10** shows typical low-resolution TEM images of the different zinc oxide nanostructures. The ZnO nanoparticles had the diameter in the

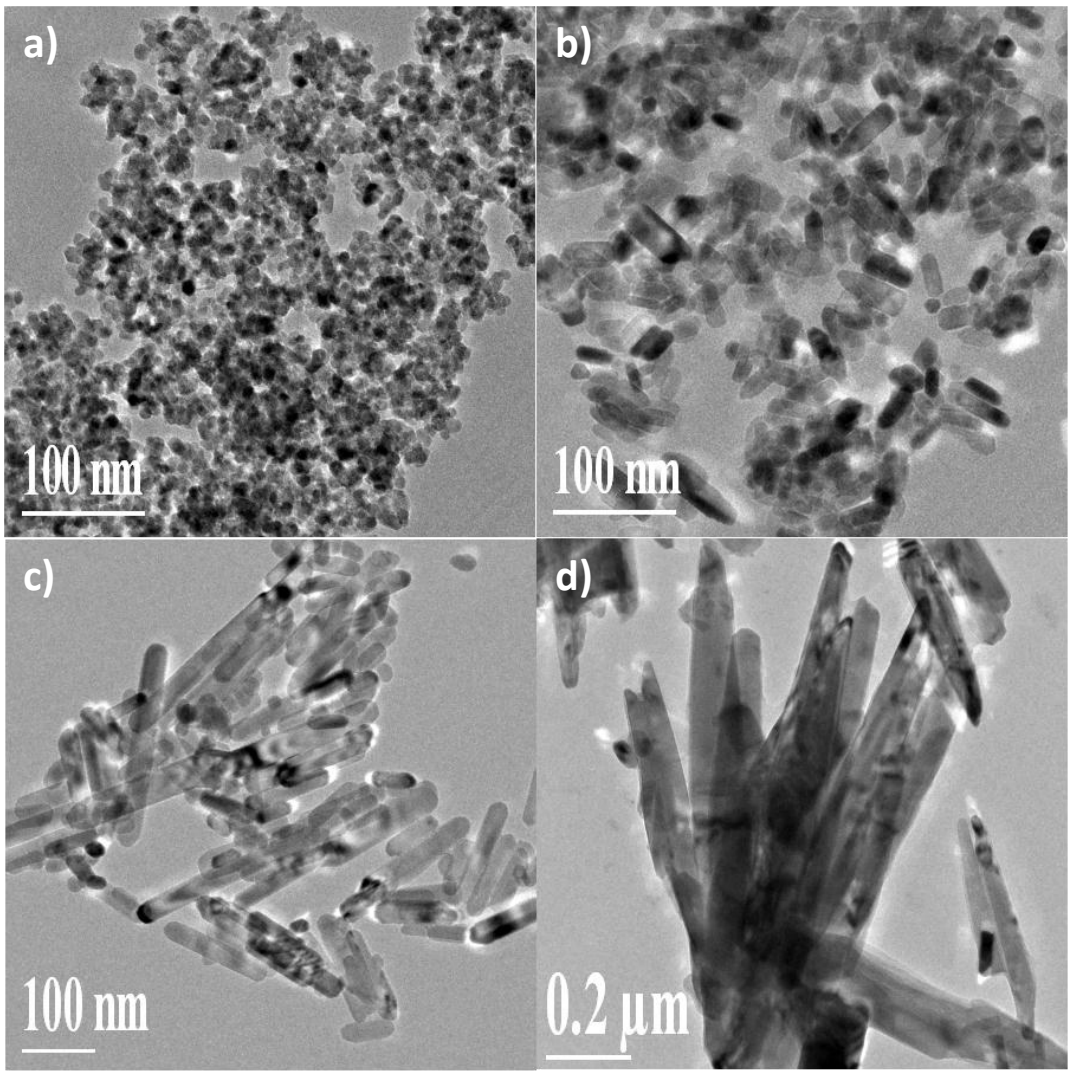


Figure 10. TEM images of a) ZnO NPs, b) ZnO NR1, c) ZnO NR2, and d) ZnO NR3.

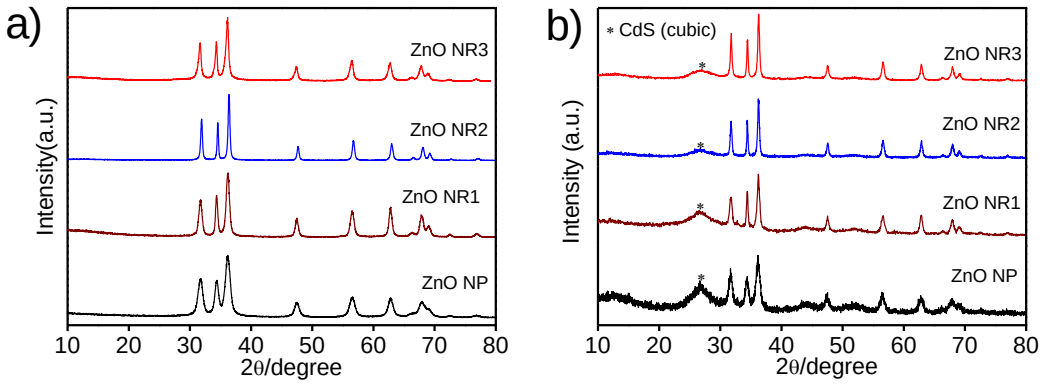


Figure 11. PXRD patterns of a) ZnO nanostructures, and b) ZnO/Pt/CdS heterostructures.

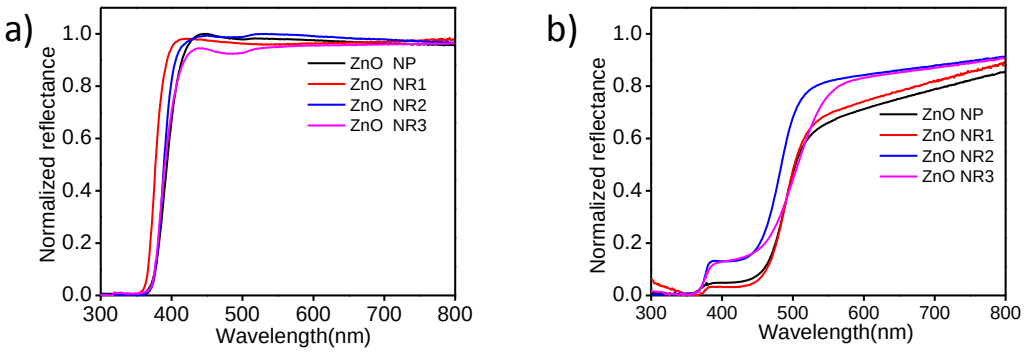


Figure 12. Reflectance spectra of a) ZnO nanostructures, and b) ZnO/Pt/CdS heterostructures.

10-20 nm range; ZnO NR1 had rods of 30-50 nm lengths and 12-20 nm diameter. ZnO NR2 had the lengths in the range 100-300 nm and diameters in the 20-35 nm range. ZnO NR3 had lengths in the range 600-800 nm and diameters in the range of 50-110 nm range. XRD-patterns of all the zinc oxide samples showed the presence of the wurtzite hexagonal phase (**Figure 11a**). The XRD-pattern of ZnO/Pt/CdS clearly shows the presence of CdS phases along with zinc oxide phases (**Figure 11b**). Diffuse reflectance spectra of the ZnO nanostructures (**Figure 12a**) show absorption in the UV region. Diffuse reflectance spectra of the ZnO/Pt/CdS heterostructures (**Figure 12b**) show absorption in visible region due to CdS along with UV absorption.BET surface areas measurements carried out with $N_2$ gas at 77 K for ZnO NP, ZnO NR1, ZnO NR2, and ZnO NR3 are 45.3, 41, 17.6, 8.7 $m^2/g$ respectively (**Figure 13**). We have prepared the ZnO/CdS and ZnO/Pt/CdS heterostructures, by employing different ZnO nanostructures along with Pt and CdS nanoparticles.

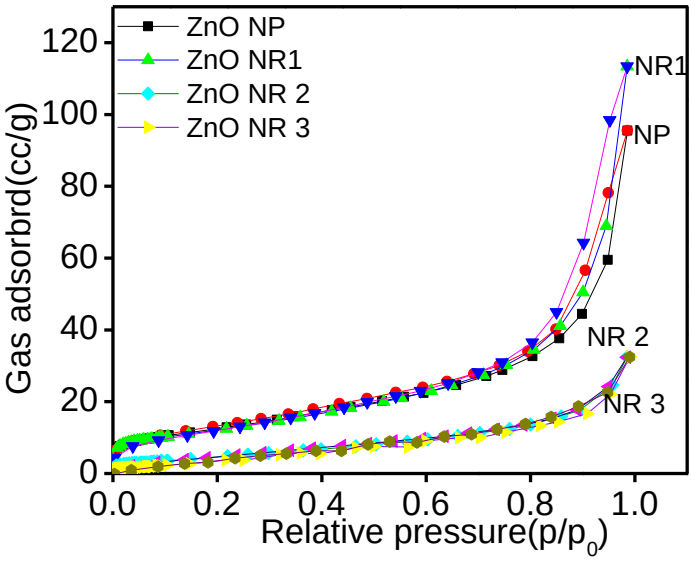


Figure 13. $N_2$ sorption profiles of ZnO nanostructures.

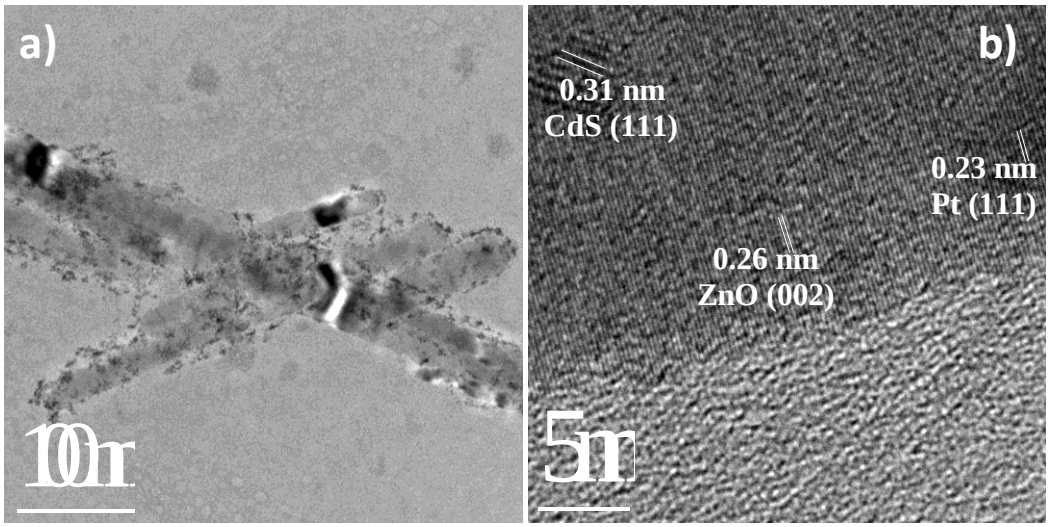


Figure 14. a) TEM image of ZnO NR2/Pt/CdS, and b) HRTEM image showing fringes.

**Figure 14a** Show the TEM image of ZnONR2/Pt/CdS heterostructures. We can see the nanoparticles of Pt, and CdS on the surface of ZnO nanorod. An HRTEM image of heterostructures (**Figure 14b**) shows lattice spacing's of 0.26, 0.33, and 0.23 nm corresponding to the (002) plane of ZnO, (111) plane of CdS and (111) plane of Pt.

We have studied the photocatalytic $H_2$ generation from ZnO/CdS as well as ZnO/Pt/CdS heterostructures in visible light in the presence of $Na_2S$ and $Na_2SO_3$ as a sacrificial agent. **Figure 15a** shows the photocatalytic activity of the ZnO/CdS heterostructures with different zinc oxide nanostructures. The photocatalytic $H_2$

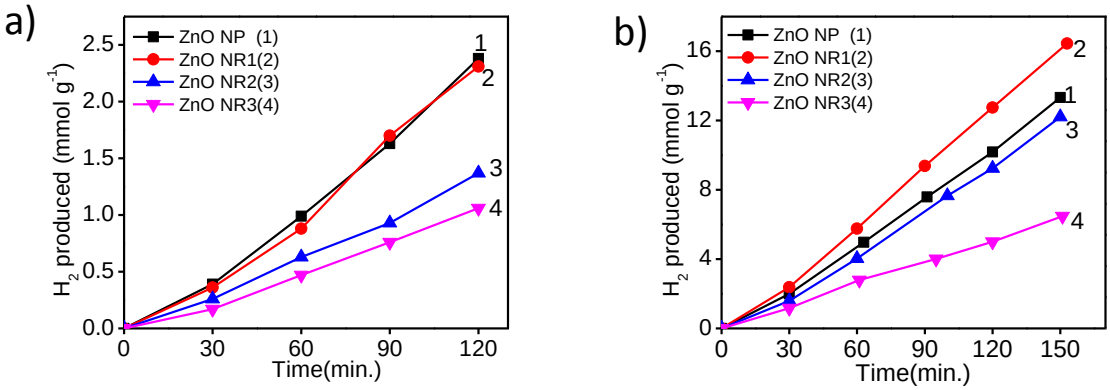


Figure 15. Photocatalytic $H_2$ generation from a) ZnO/CdS, and b) ZnO/Pt/CdS heterostructures employing different nanostructures of ZnO.

evolution activity from heterostructures with ZnO NP, ZnO NR1, ZnO NR2, and ZNO NR3 are 1.32, 1.31, 0.68, and 0.59 mmol $h^{-1}g^{-1}$ respectively. We observe that the photocatalytic $H_2$ evolution rate from these heterostructures is in the trend of the BET surface areas of the ZnO nanostructures. ZnO nanoparticles with the highest surface area (45.3 $m^2/g$) show the highest photocatalytic activity, whereas ZnO NR3 with the least surface area (8.7 $m^2/g$), shows the least photocatalytic activity. Photocatalytic activity of ZnO NR1 and ZnO NR2 are also in the order of their BET surface areas (**Table 2**).

Table 2: Properties of ZnO nanostructures.

| Samples | Surface area ($m^2/g$) | $H_2$ (mmol $h^{-1}g^{-1}$) | AQY[c] (%) |
|---|---|---|---|
| ZnO NP | 45.3 | 1.32[a] (5.36)[b] | 5.39 |
| ZnO NR1 | 41.0 | 1.34 (6.88) | 6.77 |
| ZnO NR2 | 17.6 | 0.68 (5.29) | 4.90 |
| ZnO NR3 | 8.7 | 0.59 (2.55) | 2.65 |

[a]Activity of ZnO/CdS, [b]activity of ZnO/Pt/CdS. [c]AQY of ZnO/Pt/CdS.

We have also investigated the comparative photocatalytic activity of ZnO/Pt/CdS heterostructures with different ZnO nanostructures. Like $TiO_2$ here also we observe a significant increase in the photocatalytic activity in the presence of Pt nanoparticles. **Figure 15b** shows the photocatalytic hydrogen evolution activity of ZnO/Pt/CdS heterostructures. The highest $H_2$ evolution (6.88 mmol $h^{-1}$ $g^{-1}$) is found with ZnO NR1

and the least (2.55 mmol $h^{-1}g^{-1}$) with ZnO NR3. We see that the photocatalytic $H_2$ evolution rate of these heterostructures also follows the trend in the BET surface areas of ZnO nanostructures. For the zinc oxide nanostructures with similar surface areas (ZnO NP and ZnO NR1), the heterostructure based on NR1 shows higher $H_2$ evolution activity probably due to better separation of photogenerated charge carriers. The apparent quantum yields of ZnO/Pt/CdS heterostructures are close to those reported for similar systems in the literature [6-8].[4a] In **Table 2** we present all the properties of the semiconductor heterostructures based on ZnO.

## 5. Conclusions

In summary, there is a significant effect of the morphology of oxide nanostructures on visible-light-induced hydrogen evolution from $TiO_2/Cd_{0.8}Zn_{0.2}S$, $TiO_2/Pt/Cd_{0.8}Zn_{0.2}S$, ZnO/CdS, and ZnO/Pt/CdS heterostructures. Among all the $TiO_2$ nanostructures, $H_2Ti_3O_7$ nanotubes show the highest photocatalytic hydrogen generation whereas $TiO_2$ powder (Degussa P25) shows the least photocatalytic hydrogen generation. ZnO/Pt/CdS heterostructures with ZnO nanorods1 shows the highest photocatalytic $H_2$ generation whereas those with ZnO nanorods3 show least $H_2$ generation.

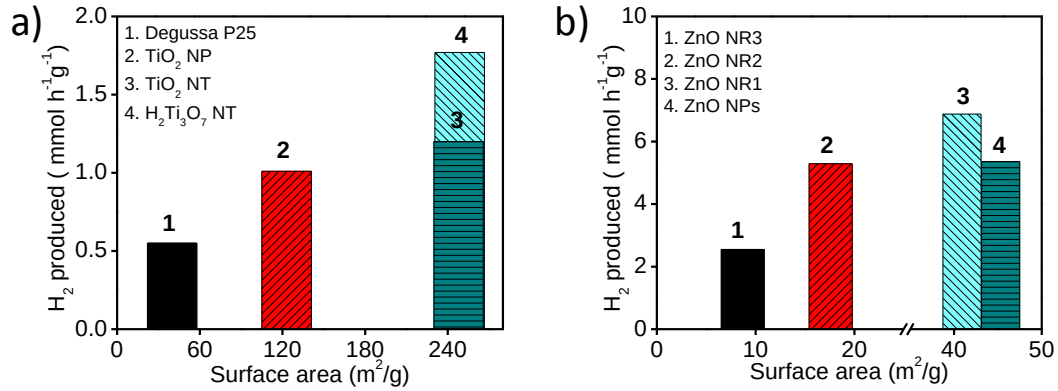


Figure 16. a) Photocatalytic $H_2$ evolution from $TiO_2/Pt/Cd_{0.8}Zn_{0.2}S$ heterostructures concerning surface areas of $TiO_2$ nanostructures, and b) Photocatalytic $H_2$ evolution from ZnO/Pt/CdS heterostructures concerning surface areas of ZnO nanostructures.

A pronounced effect of Pt is observed in the $TiO_2$ based heterostructures than those based on ZnO. Photocatalytic activities of the heterostructures generally follow the trend in the BET surface areas of the oxide nanostructures, high surface area favoring higher hydrogen evolution activity (**Figure 16**).

# 6. References


[1] a) S. Berardi, S. Drouet, L. Francàs, C. Gimbert-Suriñach, M. Guttentag, C. Richmond, T. Stoll, A. Llobet, *Chem. Soc. Rev.* **2014**, *43*, 7501-7519; b) A. J. Bard, M. A. Fox, *Acc. Chem. Res.* **1995**, *28*, 141-145.

[2] a) Z. Zou, J. Ye, K. Sayama, H. Arakawa, *Nature* **2001**, *414*, 625; b) J. S. Lee, *Catal. Surv. Asia* **2005**, *9*, 217-227.

[3] L. Amirav, A. P. Alivisatos, *J. Phys. Chem. Lett.* **2010**, *1*, 1051-1054.

[4] a) S. R. Lingampalli, U. K. Gautam, C. N. R. Rao, *Energy Environ. Sci.* **2013**, *6*, 3589-3594; b) S. R. Lingampalli, A. Roy, M. Ikram, C. N. R. Rao, *Chem. Phys. Lett.* **2014**, *610-611*, 316-320; c) S. R. Lingampalli, C. N. R. Rao, *J. Mater. Chem. A* **2014**, *2*, 7702-7705.

[5] a) H. He, C. Liu, K. D. Dubois, T. Jin, M. E. Louis, G. Li, *Ind. Eng. Chem. Res.* **2012**, *51*, 11841-11849; b) E. S. Jang, J.-H. Won, S.-J. Hwang, J.-H. Choy, *Adv. Mater.* **2006**, *18*, 3309-3312.

[6] S. K. Choi, S. Kim, S. K. Lim, H. Park, *J. Phys. Chem. C* **2010**, *114*, 16475-16480.

[7] a) A. McLaren, T. Valdes-Solis, G. Li, S. C. Tsang, *J. Am. Chem. Soc* **2009**, *131*, 12540-12541; b) H. W. Jeong, S.-Y. Choi, S. H. Hong, S. K. Lim, D. S. Han, A. Abdel-Wahab, H. Park, *J. Phys. Chem. C* **2014**, *118*, 21331-21338.

[8] T. Kasuga, M. Hiramatsu, A. Hoson, T. Sekino, K. Niihara, *Adv. Mater.* **1999**, *11*, 1307-1311.

[9] C. M. Ronconi, C. Ribeiro, L. O. S. Bulhoes, E. C. Pereira, *J. Alloys Compd.* **2008**, *466*, 435-438.

[10] C. Pacholski, A. Kornowski, H. Weller, *Angew. Chem. Int. Ed.* **2002**, *41*, 1188-1191.

[11] B. Liu, H. C. Zeng, *Langmuir* **2004**, *20*, 4196-4204.

[12] S. Solé, F. P. Gabbaï, *Chem. Commun.* **2004**, 1284-1285.

[13] N. Wang, H. Lin, J. Li, L. Zhang, C. Lin, X. Li, *J. Am. Ceram. Soc.* **2006**, *89*, 3564-3566.

[14] a) T. Gao, H. Fjellvåg, P. Norby, *Inorg. Chem.* **2009**, *48*, 1423-1432; b) R. Ma, K. Fukuda, T. Sasaki, M. Osada, Y. Bando, *J. Phys. Chem. B* **2005**, *109*, 6210-6214.

[15] a) J. Hou, Z. Wang, W. Kan, S. Jiao, H. Zhu, R. V. Kumar, *J. Mater. Chem.* **2012**, *22*, 7291-7299; b) H. R. Liu, G. X. Shao, J. F. Zhao, Z. X. Zhang, Y. Zhang, J. Liang, X. G. Liu, H. S. Jia, B. S. Xu, *J. Phys. Chem. C* **2012**, *116*, 16182-16190; c) W. Zhou, H. Liu, J. Wang, D. Liu, G. Du, J. Cui, *ACS Appl. Mater. Interfaces* **2010**, *2*, 2385-2392.

# Chapter 3

## Effectiveness of NiO in replacing Pt in the photochemical hydrogen production by $(TiO_2)_{1-x}(NiO)_xCd_{0.8}Zn_{0.2}S$ and ZnO/NiO/CdS heterostructures


**Summary***

Pt-based ZnO/Pt/CdS and $TiO_2$/Pt/CdS systems known to exhibit excellent HER rate. Considering the cost and scarcity of Pt it is important to replace it with cost effective and earth abundant cocatalyst materials. Hydrogen evolution activity of semiconductor heterostructures of the type $(TiO_2)_{1-x}(NiO)_x/Cd_{0.8}Zn_{0.2}S$ and ZnO/NiO/CdS has been investigated in detail to examine the role of NiO, used in the place of Pt in these heterostructures. $Cd_{0.8}Zn_{0.2}S$ nanoparticles act as a photosensitizer making them active in the visible-light.

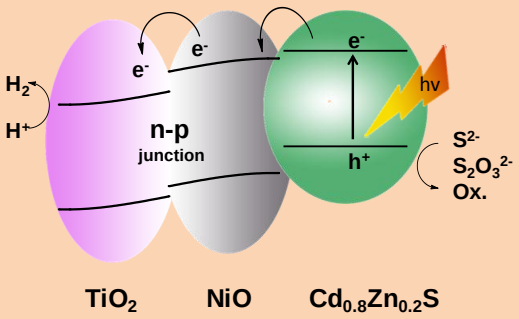


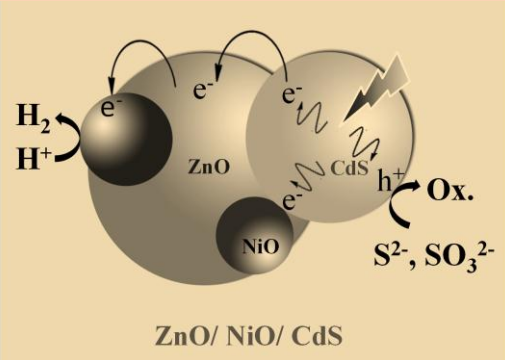


Combination of NiO with $TiO_2$ or ZnO markedly changes the photocatalytic efficiency of the heterostructures. In $(TiO_2)_{1-x}(NiO)_x/Cd_{0.8}Zn_{0.2}S$ while the $H_2$ evolution activity increases smoothly with NiO mole fraction up to x ~ 0.50, it increases further reaching a maximum at x ~ 0.83, yielding 1.6 mmol $h^{-1}g^{-1}$ (AQY ~ 2.9%) with $Na_2S$-$Na_2SO_3$ as a sacrificial agent, under visible-light irradiation, and 6.84 mmol $h^{-1}g^{-1}$ (AQY ~ 11.7%) and 13.5 mmol $h^{-1}$ $g^{-1}$ (AQY ~ 10%) with benzyl alcohol-acetic acid as a sacrificial agent under visible and UV-visible light irradiation respectively. High hydrogen evolution activity to the tune of three times that yielded by equivalent Pt containing heterostructures has been obtained, with a NiO mole fraction of 0.83 in the heterostructures. The HER activity of ZnO/NiO/CdS and ZnO/NiO/$Cd_{0.8}Zn_{0.2}S$ are 2.2 and 8.2 mmol $h^{-1}g^{-1}$ respectively. These activities values are comparable to or superior to those obtained from ZnO/Pt/$Cd_{0.8}Zn_{0.2}S$ and ZnO/Au/$Cd_{0.8}Zn_{0.2}S$ heterostructures. The ZnO/NiO heterostructure exhibit superior activity than $Zn_{1-y}Ni_yO$ solid solution.


A Paper Based on this work has appeared in Chem. Phys. Lett (2014) and Solid State Commun. (2017)

# 1. Introduction

Among the strategies to produce hydrogen, photocatalytic water splitting is an attractive one.[1] Transformation of solar energy into chemical energy could be achieved in very effective manner by photocatalytic hydrogen generation.[1a, 1b] Heterostructures of the type ZnO/Pt/CdS or $TiO_2$/Pt/CdS are known to exhibit good hydrogen evolution activity under visible as well as UV-visible light irradiation, but presence of Pt in the heterostructures is being crucial.[2] In place of CdS, $Cd_{0.8}Zn_{0.2}S$ has been used to obtain better hydrogen yields.[2a] To replace scarce and expensive Pt, NiO has been employed as a co-catalyst, under UV-light irradiation.[3] NiO is preferred co-catalyst because it does not allow the back reaction between $H_2$ and $O_2$ which occurs in the presence of Pt.[4] There are several reports where NiO has been used as a co-catalyst under UV-vis irradiation.[4] There is however only few reports where NiO has been used as a co-catalyst under visible light irradiation.[5] NiO has been used in combination with $TiO_2$ or CdS for photocatalytic $H_2$ evolution.[6] The opposite nature of the majority charge carriers in $TiO_2$ (n-type) and NiO (p-type) makes their combination purposeful in photocatalysis. Some studies have been reported on the effect of the p-n junctions on photocatalytic activity.[7] There is, however, no clear understanding of the exact role of NiO in heterostructures of the type $(TiO_2)_{1-x}(NiO)_x/Cd_{0.8}Zn_{0.2}S$, in generating hydrogen and the dependence of the mechanism of hydrogen generation on the relative proportions of NiO and $TiO_2$. For this purpose, we have prepared $(TiO_2)_{1-x}(NiO)_x$ heterostructures with different mole fractions (x~ 0.0 - 1.0) of NiO, using nanoparticles (NP) as well as nanotubes (NT) of $TiO_2$ and used them in the $(TiO_2)_{1-x}(NiO)_x/Cd_{0.8}Zn_{0.2}S$ heterostructures. Interestingly, we find that the hydrogen generation activity depends markedly on the composition of $(TiO_2)_{1-x}(NiO)_x$. Furthermore, the performance of $(TiO_2)_{1-x}(NiO)_x/Cd_{0.8}Zn_{0.2}S$ for x ~ 0.83, exceeds three times than that of shown by the Pt-containing equivalent heterostructures.[8] We have also investigated ZnO/NiO/CdS and related system where NiO substitutes Pt. A basis for expecting NiO to be a good co-catalyst in these heterostructures relates to the position of the conducton and valence band of NiO relative to those of the ZnO and CdS.[7c] The potential of conduction as well as valence band decreases in the order CdS, ZnO, and NiO favoring the vectorial transfer

of electron from CdS to NiO and holes from NiO to CdS upon illumination. Electrons on the surface of NiO involve in the redox reaction to convert $H_2O$ into $H_2$ and holes in the CdS take part in the oxidation of sacrificial agents ($Na_2S$-$Na_2SO_3$).

## 2. Scope of the Present Investigations

Semiconductor assisted photocatalytic hydrogen generation from water requires the use of noble metals nanoparticles such as Pt, Pd, Au, etc. as a co-catalyst to obtain a better conversion rate of solar to chemical energy. Considering the scarcity and cost of noble metals, it is highly desirable to explore the earth abundant materials as a potential candidate for the co-catalyst applications. Transition metal oxides based materials have the promising properties to catalyze such reactions, among them NiO is known to be very beneficial. NiO has been used as a co-catalyst for the hydrogen evolution reaction from the water under UV-light irradiation in the presence of wide band gap material such as $TiO_2$ and ZnO as a photosensitizer. However, the detailed analysis of photocatalytic activity and the exact role of NiO in these systems has not been explored. In the present work, we have used NiO nanostructure in the combination of $TiO_2$ or ZnO and $Cd_{0.8}Zn_{0.2}S$ nanostructures under visible as well as UV-light irradiation and studied their catalytic behavior in depth. The photocatalytic activity of such heterostructures exhibited almost three times higher yield of hydrogen than the Pt-based heterostructure under similar condition. The synergistic effect of $TiO_2$/NiO and probable charge separation due to the formation of multiple nano type p-n junctions between p-NiO and n-$TiO_2$ has been established. Present work reports the effectiveness of NiO as a cocatalyst in replacing expensive noble metal Pt in inorganic semiconductor based heterostructures to yield efficient hydrogen production.

# 3. Experimental Section

### Materials

$TiO_2$ nanoparticles (NP) (Degussa P25) (Sigma-Aldrich, 99.5%). $Zn(CH_3COO)_2.2H_2O$ (SD Fine Chem Ltd, India, 99.5 %), $Ni(CH_3COO)_2.4H_2O$ (SD Fine Chem Ltd, India ), $Cd(CH_3COO)_2.2H_2O$ (SD Fine Chem Ltd, India, 99.0 %), NaOH (SD Fine Chem Ltd, India, 85.5%), $H_2PtCl_6$ (Sigma Aldrich, 37.5% Pt basis) $Na_2S.xH_2O$ (SD Fine Chem Ltd, India), $Na_2SO_3$ (SD Fine Chem Ltd, India, 97%), benzyl alcohol ( SD fine Chem Ltd, Inida 99%) acetic acid (Spectrochem, India, 99.8 %) methanol (Spectrochem, India, 99.9%), water (Millipore, 18.2 MΩ.cm) are used without any further purification. KOH (SD Fine Chem Ltd, India, 85.5 %), and $NaBH_4$ (SD Fine Chem Ltd, India, 98%).

### Synthesis of NiO nanostructures

NiO nanostructures were synthesized by a modified method reported elsewhere.[9] In a typical synthesis, $Ni(CH_3COO)_2.4H_2O$ (4 mmol) and NaOH (8 mmol) were dissolved in 20 mL and 10 mL of distilled water respectively. An aqueous NaOH solution was added dropwise to the nickel acetate solution under constant stirring. This solution was maintained at 80 ˚C for three h with constant stirring. The product was washed and centrifuged with distilled water followed by ethanol and dried at 80 ˚C in air. Obtained product was calcined in the range of 400 ˚C for 2h in the air to form NiO nanostructures.

### Synthesis of $TiO_2$ nanotubes ($TiO_2$ NT)

$TiO_2$ nanotubes were prepared by adopting a method reported elsewhere.[10] In a typical synthesis, $TiO_2$ NP (Degussa P25) (25 mmol) was dispersed in an aqueous solution of NaOH (10 M, 70 mL). This dispersion was transferred to a Teflon-lined autoclave and placed in an oven at 150 ˚C for 45 h. After the reaction, the autoclave was allowed to cool down to room temperature naturally. The product was washed with distilled water until pH reaches close to 7. Afterward, an aqueous solution of HCl (0.1M, 150 mL) was added to this and stirred for 6 h at room temperature. The obtained product was further washed with distilled water and ethanol to remove

excess ions (pH~ 7) and dried at 70 ˚C. The solid product was heated at 400 ˚C for 4h in the air to obtain $TiO_2$ nanotubes.

**Synthesis of $(TiO_2NP)_{1-x}(NiO)_x$ and $(TiO_2NT)_{1-x}(NiO)_x$ heterostructures**

In a typical synthesis, $Ni(CH_3COO)_2.4H_2O$ was used as the precursor for NiO. $Ni(CH_3COO)_2.4H_2O$ and $TiO_2$ NP (or $TiO_2$ NT) were taken based on the required mole fraction. A predetermined amount of $Ni(CH_3COO)_2.4H_2O$ was dissolved in 20 mL of distilled water, $TiO_2$ NP (or $TiO_2$ NT) was added to this solution and dispersed by sonication. An aqueous solution of NaOH (2 times of $Ni(CH_3COO)_2.4H_2O$ moles) was added drop-wise to this dispersion, under constant stirring of the solution at 80 °C. The solution was maintained at 80 °C to remove the solvent. As obtained solid product was calcined in 300-500 °C range for 2h to obtain $(TiO_2)_{1-x}(NiO)_x$ heterostructures. Similarly, $(TiO_2)_{1-x}(NiO)_x$ heterostructures, with different mole fractions of NiO were prepared by changing the molar ratio of $Ni(CH_3COO)_2.4H_2O$ and $TiO_2$ NP (or $TiO_2$ NT),.

**Synthesis of $(TiO_2)_{1-x}(NiO)_x/Cd_{1-x}Zn_xS$**

$(TiO_2)_{1-x}(NiO)_x$ (85 mg) was dispersed in methanol (40 mL) by sonication. Methanolic solution of $Zn(CH_3COO)_2.2H_2O$ (8.20 mM, 5 mL) was added to the reaction solution followed by the drop-wise addition of methanolic solutions of $Cd(CH_3COO)_2.2H_2O$ (0.02 M, 10 mL) and $Na_2S$ (0.04 M, 10 mL) under constant stirring. The product was centrifuged and washed with methanol and dried at room temperature.

**Synthesis of $(TiO_2/Pt)_{1-x}(NiO)_x/Cd_{0.8}Zn_{0.2}S$**

$TiO_2$ NP (1 mmol) was dispersed in a water-methanol mixture (60 mL $H_2O$:15 mL MeOH), $H_2PtCl_6$ (558 µL, 8.95 mM) was added to this solution. The solution was irradiated by UV-visible light (New Port 6279, Xe-Lamp 400 W) for 1.5 h. The brownish-black $TiO_2$/Pt product was washed with methanol and centrifuged. For the preparation of $(TiO_2/Pt)_{1-x}(NiO)_x/Cd_{0.8}Zn_{0.2}S$ above mentioned method was employed, wherein Pt deposited $TiO_2$ NP was used at the place of $TiO_2$ NP.

**Synthesis of ZnO/NiO/$Cd_{1-x}Zn_xS$ and $Zn_{1-y}Ni_yO/Cd_{1-x}Zn_xS$**

ZnO/NiO/$Cd_{1-x}Zn_xS$ and $Zn_{1-y}Ni_yO/Cd_{1-x}Zn_xS$ heterostructures were prepared from preformed $Zn_{1-y}Ni_yO$ (method 1), or ZnO/NiO (method 2 and 3). In method 1 we synthesized $Zn_{1-y}Ni_yO$ solid solution by the decomposition of the peroxide precursor, $Zn_{1-y}Ni_yO_2$ at 250°C. In method 2, ZnO/NiO heterostructures were prepared from the decomposition of $Zn_{1-y}Ni_yO_2$ at 500 °C.

**Synthesis of Precursor $Zn_{1-y}Ni_yO_2$:**

Zinc acetate dihydrate and nickel acetate tetrahydrate were dissolved in 50 mL of water. To this solution, $H_2O_2$ (30 %, 10 mL) was added followed by the addition of aqueous solution of KOH. In few minutes the solution turned blue turbid. This sample was stirred for 30 min before separation. The sample was washed with water followed by ethanol and dried at 60 °C.

In method 3, ZnO/NiO were prepared by the impregnation of nickel salt with ZnO nanoparticles at 500 °C. ZnO nanoparticles used in this purpose was synthesized by the alkaline hydrolysis of methanolic solution of $Zn(CH_3COO)_2.2H_2O$.

ZnO/NiO heterostructures were dispersed in methanol and methanolic solution of $Cd(CH_3COO)_2$ and $Na_2S$ were simultaneously added to form ZnO/NiO/$Cd_{1-x}Zn_xS$. $Zn_{1-y}Ni_yO/Cd_{1-x}Zn_xS$ were prepared similarly. The product was washed and dried at room temperature.

**Characterization**

Powder X-ray diffraction (PXRD) patterns were recorded with a Bruker D8 Diffraction system using a Cu Kα source (λ = 0.1541 nm). UV-Vis absorption spectra were collected with Perkin Elmer Model Lambda 900 spectrometer. Photoluminescence spectra were collected by Horiba Jobin Yvon spectrometer (iHR 320). Transmission electron microscopy (TEM) images were obtained with JEOL-3010 system. Elemental mapping and EDAX spectrum were obtained using FEI-Technai microscope working at 200 kV. XPS with a MgKa (1253.6 eV) X-ray source was used to determine the composition of the sample. Photocatalytic measurements were carried out under Xe arc lamp irradiation (New Port, 6279NS ozone-free,

working at 400 watts). A 395 nm cut-off filter was used to obtain light of wavelength λ> 395 nm. The amount of $H_2$ evolved was measured by gas chromatography (Perkin Elmer, Clarus 580) equipped with TCD. Electrical measurements were done with Keithley 236 analyzer, by sandwiching the sample between FTO electrodes.

**Photocatalytic Experiments**

Photocatalytic measurements were done by dispersing 20 mg of a photocatalyst in a glass cell in 75 mL of water containing 0.1 M, $Na_2S$ and $Na_2SO_3$ each. In case of benzyl alcohol-acetic acid sacrificial agent, 5 mL of each was used. The following formula estimated apparent quantum yields (AQY). AQY (%) = (2R/I)*100 where R is the rate of evolution of hydrogen per second and I is the rate of incident photon per second. The photon flux is measured using irradiance meter, which is $3.7*10^7$ photons/s.

# 4. Results and Discussion

## 4.1 Synthesis and Properties of $(TiO_2)_{1-x}(NiO)_x/Cd_{0.8}Zn_{0.2}S$ heterostructures

Powder X-ray diffraction (PXRD) patterns of $(TiO_2)_{1-x}(NiO)_x$ prepared with the $TiO_2$ nanoparticles show reflections due to $TiO_2$ and NiO, the peak intensity of NiO depending on the mole fraction (x) (**Figure 1**). **Figure 2** shows TEM images of $TiO_2$ and NiO nanostructures along with the image of $(TiO_2NP)_{1-x}(NiO)_x$ (x ~ 0.83). The diameters of the $TiO_2$ nanoparticles are in the range of 30-40 nm, whereas the diameters of NiO nanostructures are in the range of 4-6 nm. The HRTEM image of $(TiO_2NP)_{1-x}(NiO)_x$ showed the lattice d-spacings of 0.35 and 0.23 nm corresponding to the (101) and (111) planes of $TiO_2$ and NiO respectively. Energy dispersive X-ray spectrum (EDS) and elemental mapping of $(TiO_2NP)_{1-x}(NiO)_x/Cd_{0.8}Zn_{0.2}S$ (x ~ 0.83) confirm the presence of the constituents elements in the heterostructures **(Figure 3).**

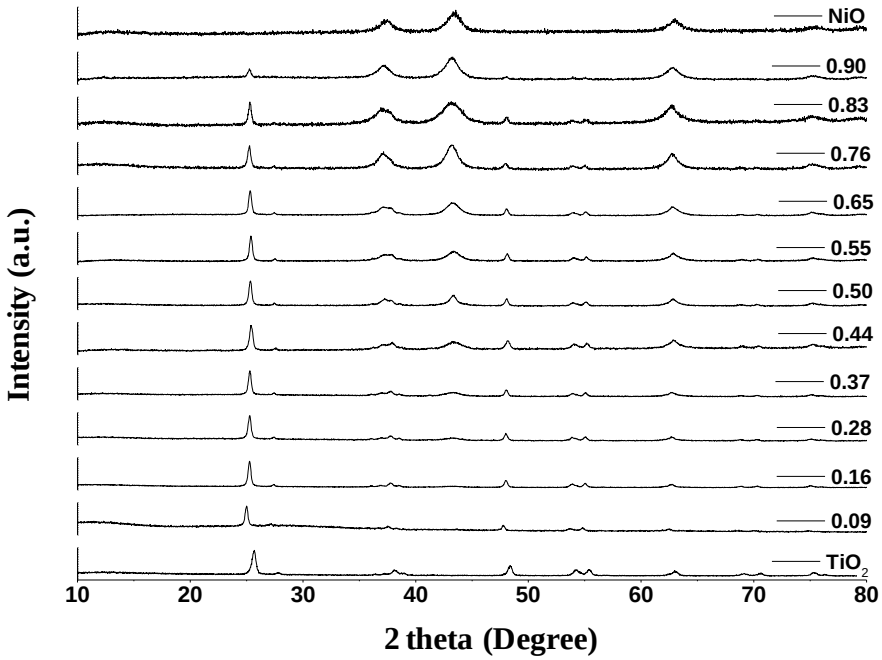


Figure 1. PXRD patterns of $TiO_2$NP, NiO and $(TiO_2)_{1-x}(NiO)_x$ heterostructures.

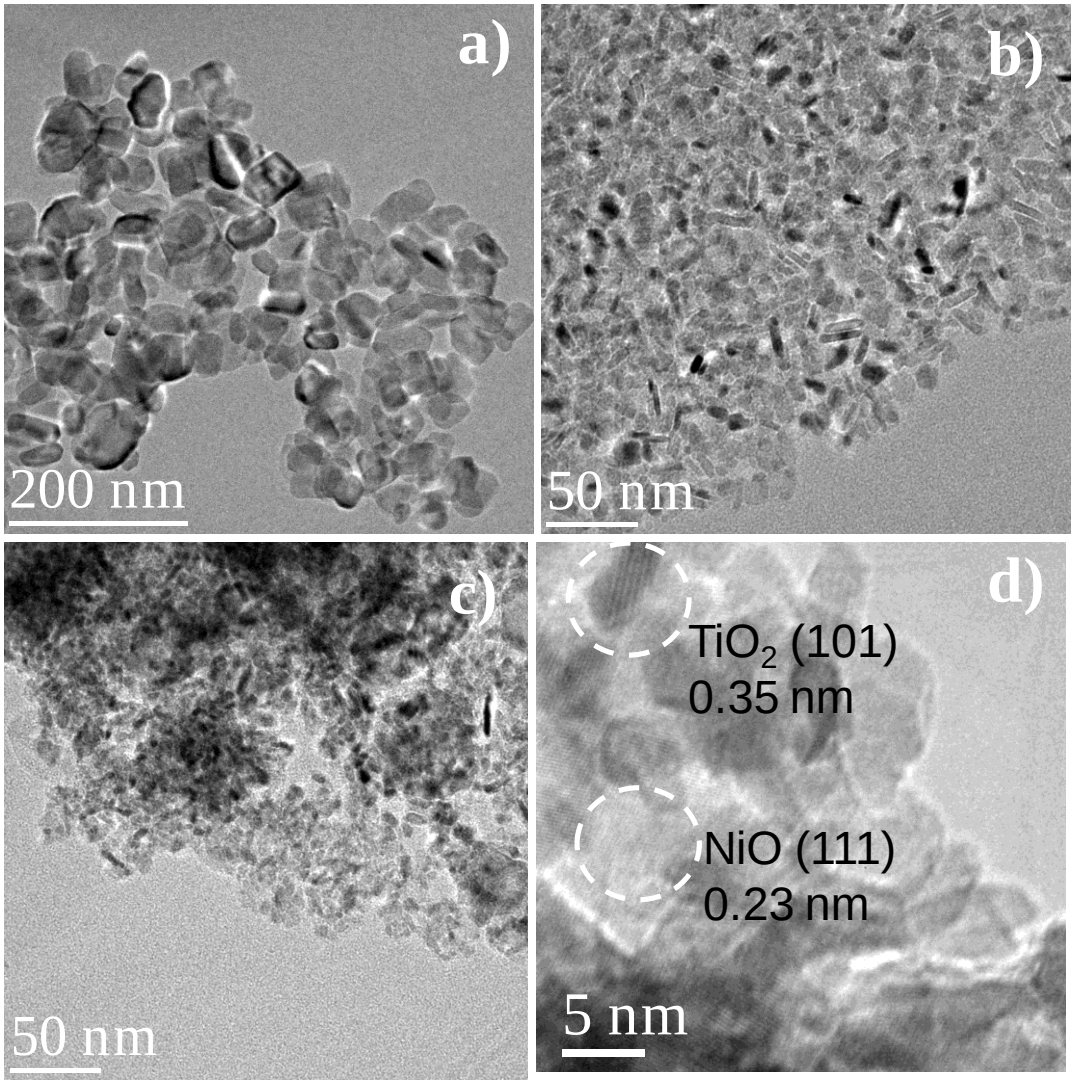


Figure 2. TEM images of a) $TiO_2$ NP, b) NiO nanorods, c) $(TiO_2)_{1-x}(NiO)_x$ heterostructures, and d) HRTEM of $(TiO_2)_{1-x}(NiO)_x$ (x~ 0.83).

The constituent elements were evenly distributed throughout the sample with Ni, Cd and Ti, atomic ratios to be 32.9, 22.7 and 6.7 % respectively**.** We have examined the effect of annealing temperature of $(TiO_2)_{1-x}(NiO)_x$ on photocatalytic activity. For this purpose, we annealed $(TiO_2)_{1-x}(NiO)_x$ samples in the temperature range of 300-500˚C and incorporated them in the $(TiO_2)_{1-x}(NiO)_x/Cd_{0.8}Zn_{0.2}S$ heterostructures. The PXRD patterns (**Figure 4a**) showed the NiO reflections to be broad at 300 ˚C becoming sharper with the increase in temperature. The sample prepared at 500 ˚C had only a small proportion of the anatase phase of $TiO_2$, possibly due to the tendency to form $NiTiO_3$.[11]

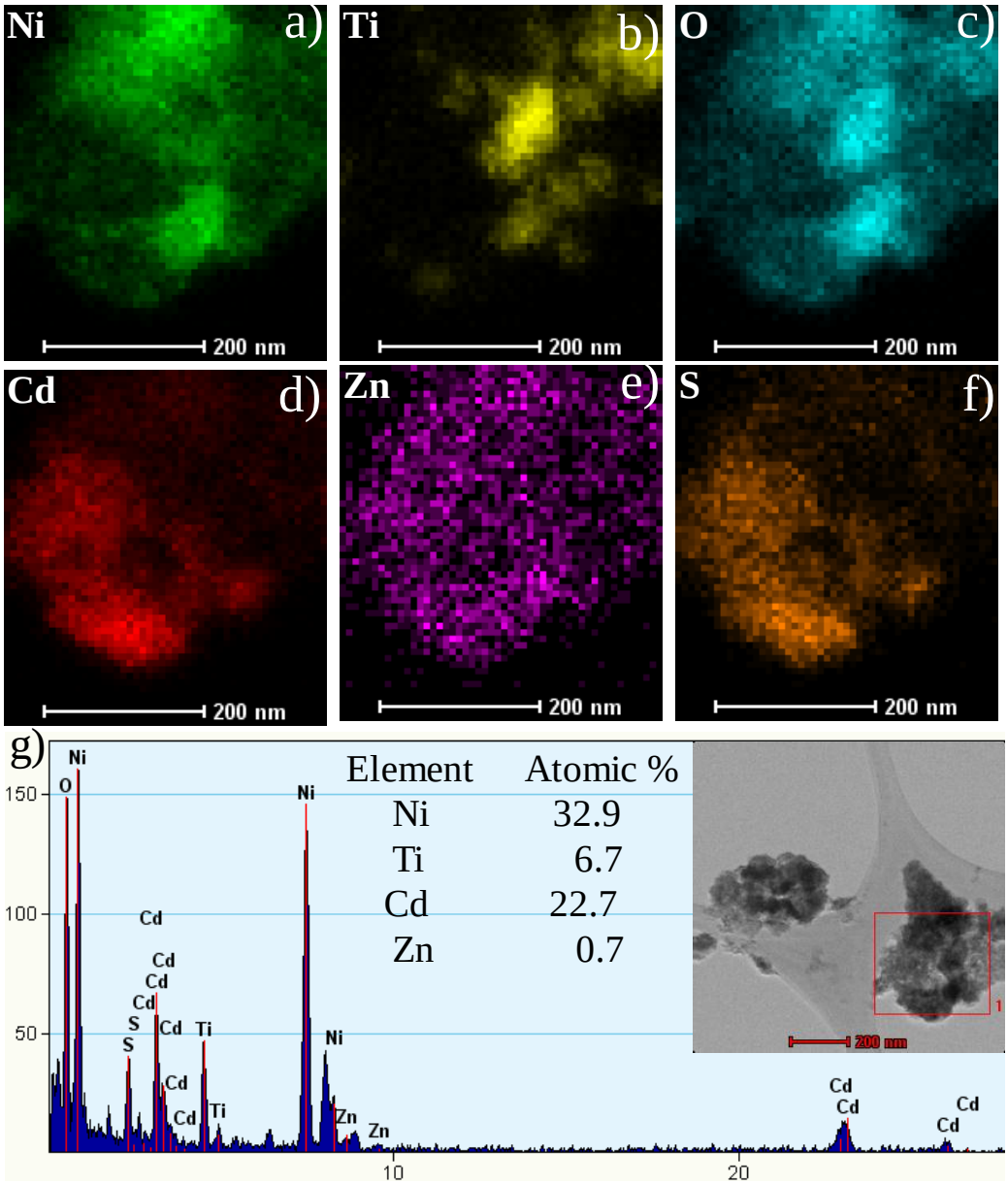


Figure 3. EDS elemental mapping of a ) Ni, b) Ti, c) O, d) Cd, e) Zn, f) S and g) spectrum of $(TiO_2)_{1-x}(NiO)_x/Cd_{0.8}Zn_{0.2}S$ (x~ 0.83) (Inset in Fig. g shows TEM image of sample analyzed).

UV-visible absorption spectra of $NiO/Cd_{0.8}Zn_{0.2}S$ and $(TiO_2)_{1-x}(NiO)_x/Cd_{0.8}Zn_{0.2}S$ (x~ 0.83) show absorption in the visible region arising due to $Cd_{0.8}Zn_{0.2}S$ nanoparticles whereas $(TiO_2)_{1-x}(NiO)_x$ absorbtion is restricted to the visible region (**Figure 4b**). $(TiO_2)_{1-x}(NiO)_x/Cd_{0.8}Zn_{0.2}S$ heterostructures incorporating $(TiO_2)_{1-x}(NiO)_x$ (x~ 0.83) samples prepared in the 300-500˚C temperature range were investigated for $H_2$ evolution.

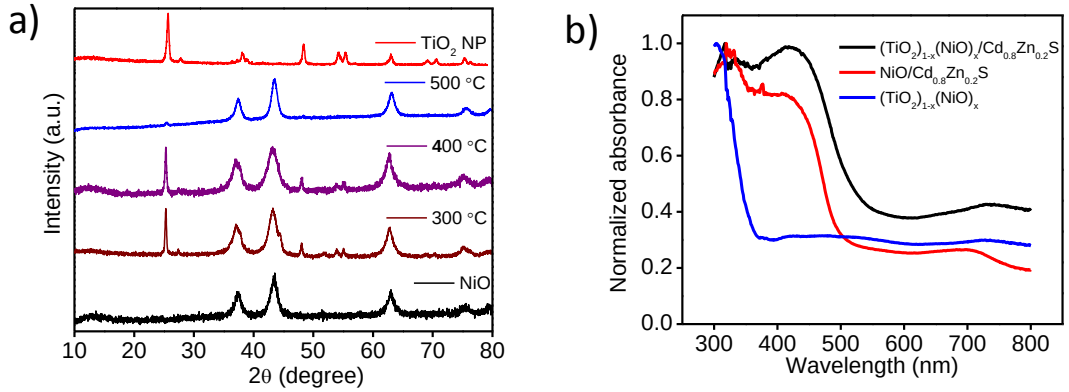


Figure 4. a) PXRD patterns of $(TiO_2)_{1-x}(NiO)_x$ (x ~ 0.83) heterostructures prepared in the temperature range of 300-500°C, and b) Normalized absorption spectra of $TiO_2$/NiO, NiO/$Cd_{0.8}Zn_{0.2}S$ and $(TiO_2)_{1-x}(NiO)_x/Cd_{0.8}Zn_{0.2}S$ (x~0.83) heterostructures.

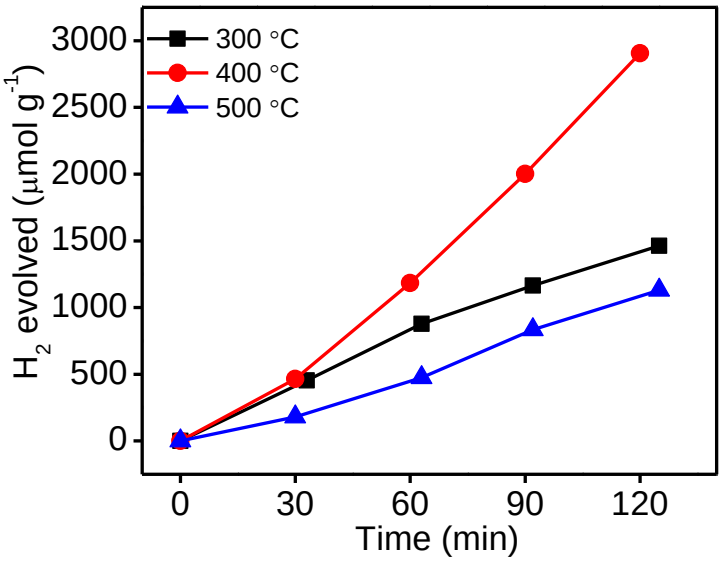


Figure 5. $H_2$ evolution from $(TiO_2)_{1-x}(NiO)_x/Cd_{0.8}Zn_{0.2}S$ heterostructures under visible-light irradiation in presence of $Na_2S$-$Na_2SO_3$ as sacrificial agents, with $(TiO_2)_{1-x}(NiO)_x$ (x ~ 0.83) prepared in the temperature range of 300-500 °C

The highest yield of $H_2$ was obtained with the structures containing $(TiO_2)_{1-x}(NiO)_x$ prepared at 400 °C (**Figure 5).** We have, therefore, used $(TiO_2)_{1-x}(NiO)_x$ samples prepared at 400 °C in all the subsequent studies.

In order to investigate the effect of the NiO content on the visible-light induced $H_2$ generation, $Cd_{0.8}Zn_{0.2}S$ nanoparticles were deposited on the $(TiO_2)_{1-}$

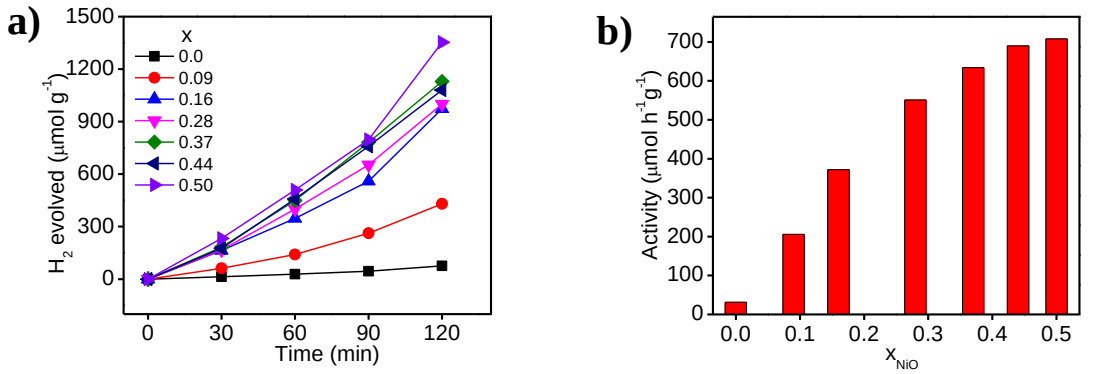


Figure 6. a) Photocatalytic $H_2$ evolution under visible-light irradiation in presence of $Na_2S$-$Na_2SO_3$ as sacrificial agent as a function of time and b) photocatalytic activity from $(TiO_2)_{1-x}(NiO)_x/Cd_{0.8}Zn_{0.2}S$ heterostructures with NiO mole fractions (x ~ 0.0-0.50).

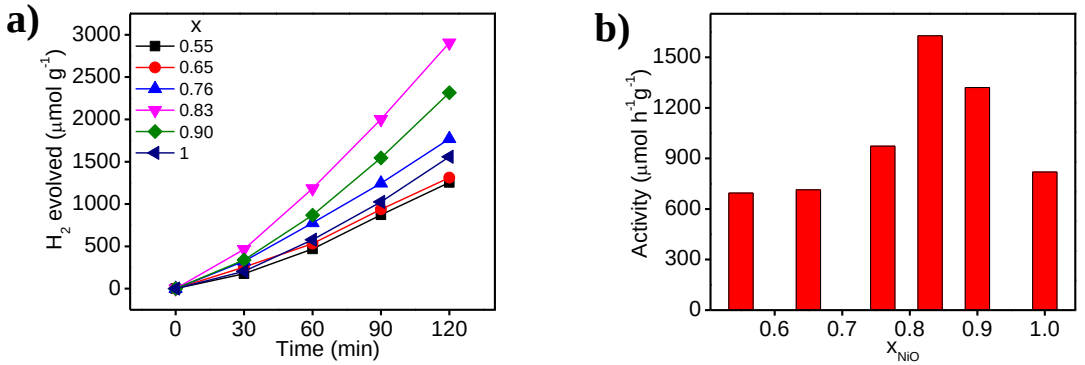


Figure 7. a) $H_2$ evolution as a function of time, and b) Photocatalytic activity from $(TiO_2)_{1-x}(NiO)_x/Cd_{0.8}Zn_{0.2}S$ heterostructures with NiO mole fractions (x~ 0.55-1.0) under visible-light irradiation in the presence of $Na_2S$-$Na_2SO_3$ as sacrificial agents.

$_x(NiO)_x$ heterostructures prepared by making use of $TiO_2$ nanoparticles. **Figure 6a** shows $H_2$ evolution from $(TiO_2)_{1-x}(NiO)_x/Cd_{0.8}Zn_{0.2}S$ for the NiO mole fraction (x) range 0.0-0.50 in the presence of $Na_2S$-$Na_2SO_3$ as sacrificial agents. The $H_2$ evolution activity increases progressively with the increasing NiO content in this mole fraction range. $TiO_2/Cd_{0.8}Zn_{0.2}S$ (x~ 0.0) shows a $H_2$ evolution rate of 32 μmol $h^{-1}g^{-1}$, whereas $(TiO_2)_{1-x}(NiO)_x/Cd_{0.8}Zn_{0.2}S$ with x ~ 0.09 shows a $H_2$ evolution rate of 205.8 μmol $h^{-1}g^{-1}$. The photocatalytic $H_2$ evolution activities increase smoothly with the mole fraction of NiO up to 0.50, which exhibits an $H_2$ evolution, a rate of 708 μmol $h^{-1}g^{-1}$. **Figure 6b** shows a histogram of the $H_2$ evolution activity of $(TiO_2)_{1-x}(NiO)_x/Cd_{0.8}Zn_{0.2}S$ heterostructures (x ~ 0.0-0.50) prepared with $TiO_2$ nanoparticles.

We have also studied the effect of NiO content beyond x ~ 0.50, going up to x ~1.0. $H_2$ evolution rates from the heterostructures in this mole fraction range (x ~ 0.55 - 1.0) are presented in **Figure 7a**. We observe that the $H_2$ evolution activity remains nearly unchanged in the range of x ~ 0.55-0.65, with further increase in NiO mole fraction resulted in the rapid increase in the $H_2$ evolution activity reaching a maximum at x~ 0.83. **Figure 7b** shows the histogram presenting the $H_2$ evolution activity from $(TiO_2)_{1-x}(NiO)_xCd_{0.8}Zn_{0.2}S$ (x ~ 0.55-1.0). We see that with an increase in the NiO content, $H_2$ evolution activity increases reaching a maximum of 1600 μmol $h^{-1}g^{-1}$ for x ~ 0.83. The $H_2$ evolution decreases when x > 0.83 reaching a value of 819 μmol $h^{-1}g^{-1}$ for x ~ 1. The apparent quantum yields (AQY) obtained from these heterostructures under visible-light irradiation in the presence of $Na_2S$-$Na_2SO_3$ sacrificial agents are presented in the **Figure 8.** The quantum yield increases smoothly with x in the 0.0 - 0.65 range. Beyond x ~ 0.65 we observe a maximum for x ~ 0.83 (AQY ~ 2.8) where also obtain the highest $H_2$ yield.

We have measured $H_2$ evolution activity of these heterostructures for x ~ 0.83 using benzyl alcohol-acetic acids (BnOH-AcOH) as sacrificial agents since they are known to be very effective.[2a] **Figure 9** compares the $H_2$ evolution from these heterostructures obtained with $Na_2S$-$Na_2SO_3$ and benzyl alcohol-acetic acid as sacrificial agents in visible as well as in UV-visible light irradiation.

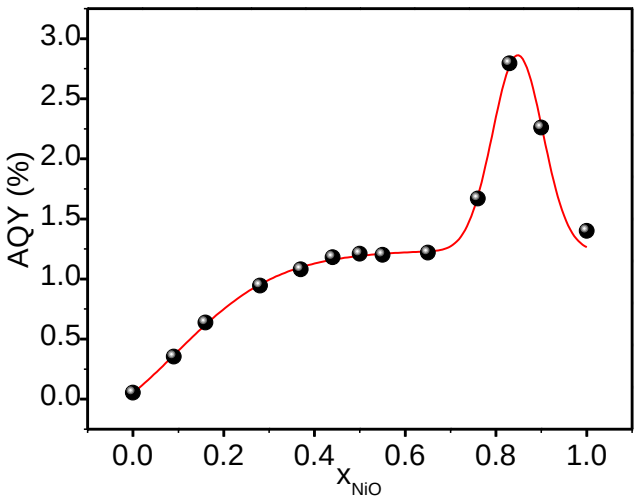


Figure 8. AQY from $(TiO_2NP)_{1-x}(NiO)_x/Cd_{0.8}Zn_{0.2}S$ heterostructures with x~ 0.0 to 1.0 under visible-light irradiation in the presence of $Na_2S$-$Na_2SO_3$ as sacrificial agents.

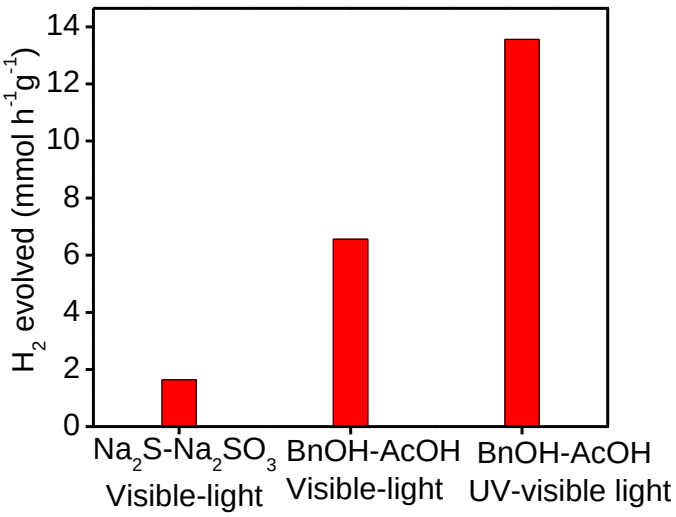


Figure 9. Photocatalytic activity of $(TiO_2NP)_{1-x}(NiO)_x/Cd_{0.8}Zn_{0.2}S$ (x~ 0.83), in the presence of $Na_2S$-$Na_2SO_3$ (visible-light irradiation) and benzyl alcohol-acetic acid (visible and UV-visible light irradiation) as sacrificial agents.

With benzyl alcohol-acetic acid, $H_2$ evolution from the heterostructures increases up to 5 times under visible-light irradiation and 8.4 times under UV-visible light irradiation, reaching values 6.84 (AQY ~ 11.7%) and 13.56 mmol $h^{-1}g^{-1}$ (AQY ~ 10%) respectively. The higher activity with benzyl alcohol-acetic acid as a sacrificial agent is due to the higher proton concentration (pH~3) in the reaction medium.[2a]

We have also investigated $H_2$ evolution from $(TiO_2NT)_{1-x}(NiO)_x/Cd_{0.8}Zn_{0.2}S$ heterostructures making use of $TiO_2$ nanotubes in place of nanoparticles. **Figure 10** represents TEM images of $TiO_2$ NT and $(TiO_2NT)_{1-x}(NiO)_x$ heterostructures (x ~ 0.83). In **Figure 11a,** we show $H_2$ evolution from the $(TiO_2NT)_{1-x}(NiO)_x/Cd_{0.8}Zn_{0.2}S$ heterostructures with x ~ 0.16-0.97, under visible-light irradiation with $Na_2S$-$Na_2SO_3$ as sacrificial agents. $H_2$ evolution from these heterostructures is again higher in the NiO rich region, with the highest value of 1333 μmol $h^{-1}g^{-1}$ for x ~ 0.95. Visible-light-induced photocatalytic activity of the heterostructures for x ~ 0.95, with benzyl alcohol-acetic acid as sacrificial agents yield a value of 8.9 mmol $h^{-1}g^{-1}$ (AQY ~ 15.3%) as shown in **Figure 11b.**

The photocatalytic activity of $(TiO_2)_{1-x}(NiO)_x/Cd_{0.8}Zn_{0.2}S$ heterostructures (0 < x < 1) is superior to the values expected from the additive contributions of

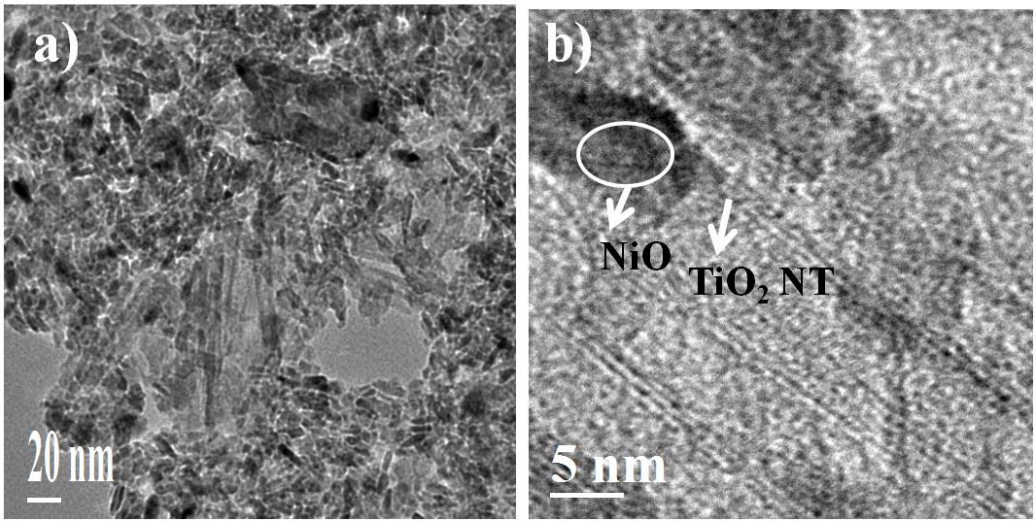


Figure 10. a) TEM, and b) HRTEM images of $(TiO_2NT)_{1-x}(NiO)_x$ (x~0.83).

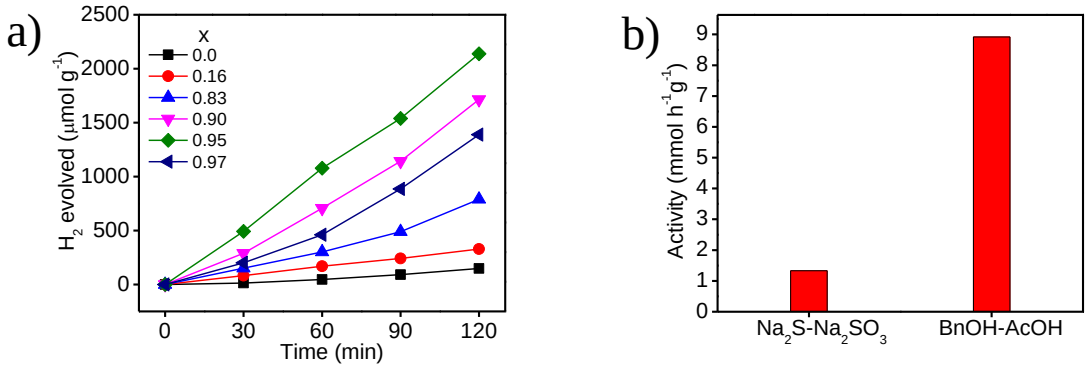


Figure 11. a) $H_2$ evolution from $(TiO_2NT)_{1-x}(NiO)_x/Cd_{0.8}Zn_{0.2}S$ heterostructures (x~0.16-0.97) as a function of time under visible-light irradiation in the presence of $Na_2S$-$Na_2SO_3$ sacrificial agents, and b) Comparison of visible-light induced photocatalytic activity obtained in the presence of $Na_2S$-$Na_2SO_3$ and benzyl alcohol-acetic acid as sacrificial agents for x~ 0.95.

$TiO_2/Cd_{0.8}Zn_{0.2}S$ and $NiO/Cd_{0.8}Zn_{0.2}S$ indicating a synergistic effect of $TiO_2$ and NiO. Several studies have explored on the catalytic activity of NiO for $H^+$ reduction where NiO act as a co-catalyst.[12] The effect of NiO mole fraction on hydrogen generation by the heterostructures $(TiO_2)_{1-x}(NiO)_x/Cd_{0.8}Zn_{0.2}S$ is likely to be affected by the p-n junction formed between p-type NiO and n-type $TiO_2$ for which there is a evidence mentioned. **Figure 12a** shows the current-voltage characteristics of $(TiO_2)_{1-x}(NiO)_x$ measured at room temperature, indicating a p-n junction behavior.[13] The exponential increase of the current with voltage suggest thermionic emission.[14] Presence of such junctions can influence the separation of charge carriers and thus enhance the

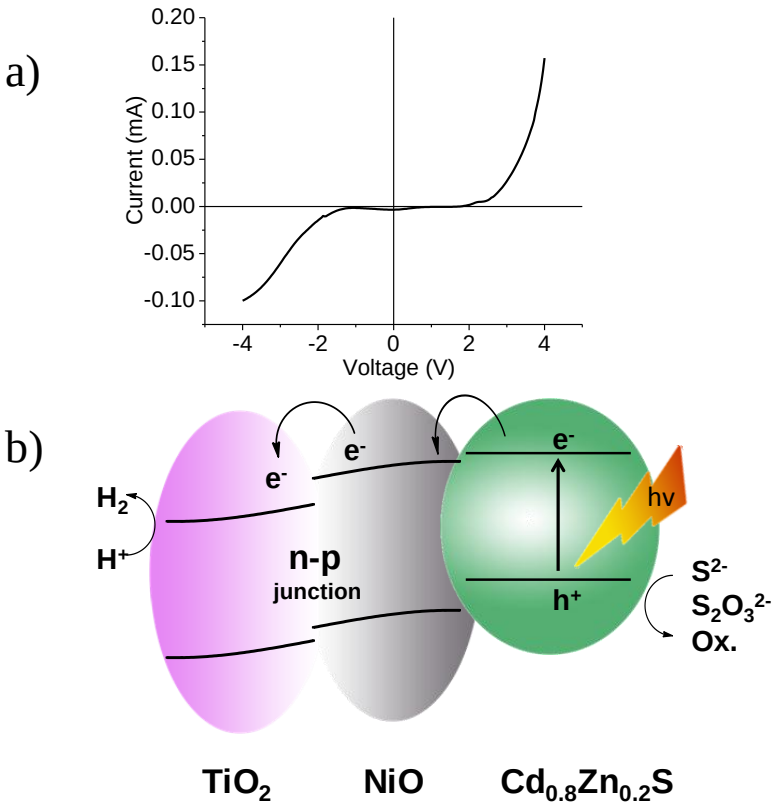


Figure 12. a) Dark I-V characteristics of $TiO_2$/NiO heterojunction, and b) Schematic representation of charge separation and photocatalytic $H_2$ evolution on $(TiO_2)_{1-x}(NiO)_x/Cd_{0.8}Zn_{0.2}S$.

photocatalytic activity.[7b, 7c] In the $(TiO_2)_{1-x}(NiO)_x/Cd_{0.8}Zn_{0.2}S$ heterostructures, $Cd_{0.8}Zn_{0.2}S$ nanoparticles absorb visible-light and generate electrons and holes. Due to the favorable band positions of NiO with respect to $Cd_{0.8}Zn_{0.2}S$, the electrons would move from the conduction band of $Cd_{0.8}Zn_{0.2}S$ to the conduction band of NiO while the holes remain in the valence band of $Cd_{0.8}Zn_{0.2}S$.[15] The p-n junctions between $(TiO_2)_{1-x}(NiO)_x$, can cause electrons to reach $TiO_2$ where proton reduction occurs (**Figure 12b**). Under UV-visible irradiation, electron-hole pairs are generated in $Cd_{0.8}Zn_{0.2}S$ as well as in $TiO_2$. The holes formed at the valence band of $TiO_2$ migrate to the NiO valence band while the electrons remain with $TiO_2$ and are involved in the reduction of protons. Since proton reduction is likely to occur at the surface of $TiO_2$ due to the presence of p-n junction between p-NiO and n-$TiO_2$. We observe the highest photocatalytic activity from $(TiO_2NP)_{1-x}(NiO)_x/Cd_{0.8}Zn_{0.2}S$ heterostructures at the optimum NiO mole fraction of 0.83. Further increase in NiO concentration reduces the $TiO_2$ concentration and hence the number of active sites available for

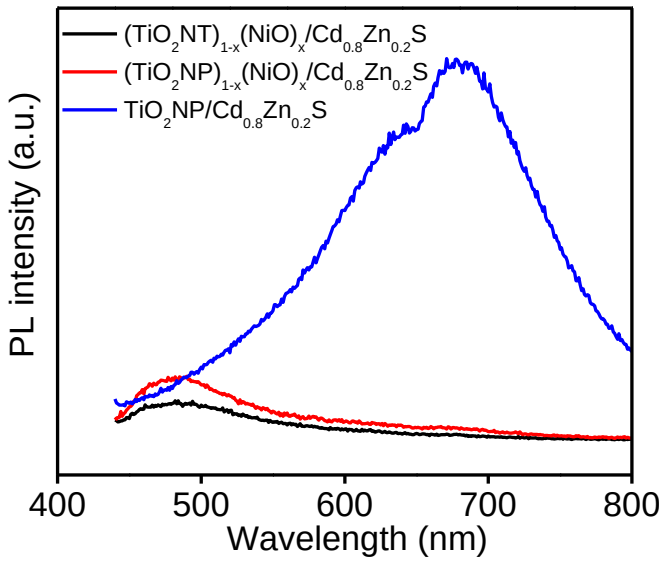


Figure 13. Steady state photoluminescence spectra of $TiO_2/Cd_{0.8}Zn_{0.2}S$ and $(TiO_2)_{1-x}(NiO)_x/Cd_{0.8}Zn_{0.2}S$ (x ~ 0.83).

proton reduction decreases. This results in a decrease in the photocatalytic activity beyond x~0.83. When x~1, there can be no p-n junction and hence the separation of photogenerated charge carriers would be less efficient, resulting in the reduction of catalytic activity. It is noteworthy that excitation of $(TiO_2)_{1-x}(NiO)_x/Cd_{0.8}Zn_{0.2}S$ heterostructures at 420 nm showed negligible photoluminescence intensity centred at 680 nm due to defect emission in $Cd_{0.8}Zn_{0.2}S$. This suggests the effective separation of the photogenerated electrons and holes and hence higher proton reduction rate (**Figure 13**).[16]

We have also examined the photocatalytic activity of $(TiO_2NP/Pt)_{1-}$

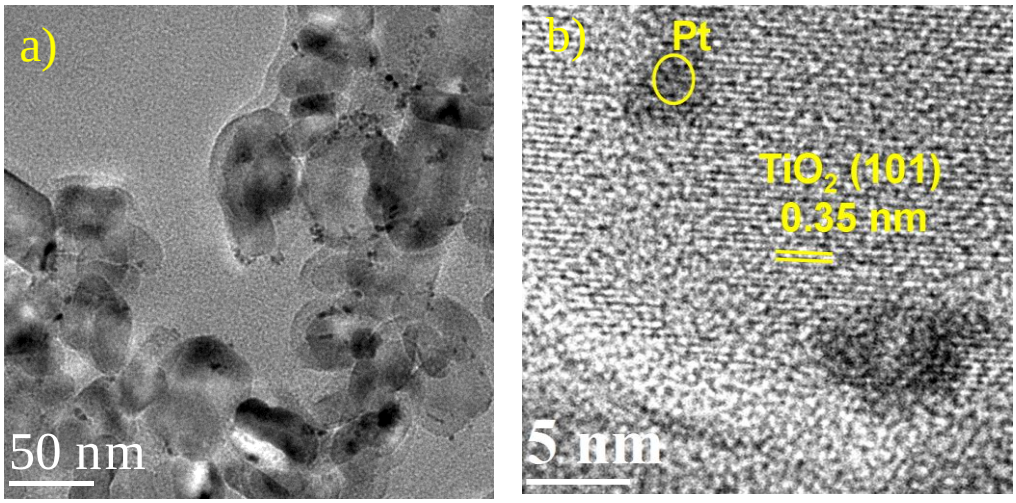


Figure 14. a) TEM, and b) HRTEM image of $TiO_2$NP/Pt heterostructures.

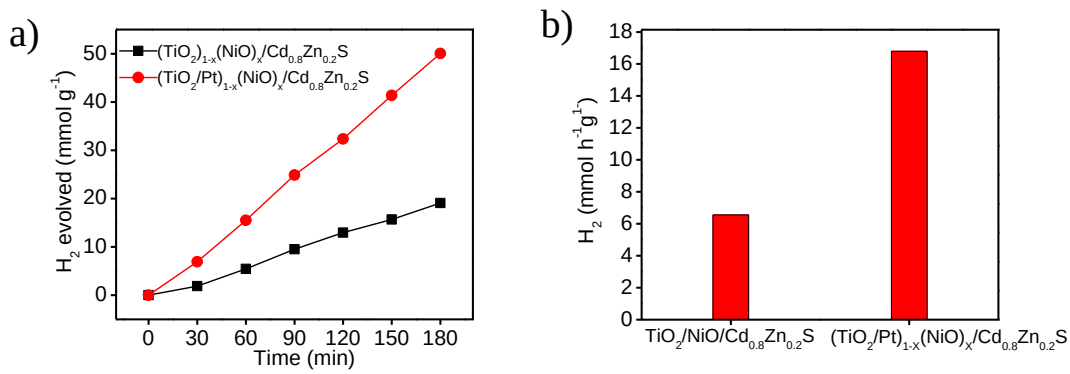


Figure 15. Comparison of photocatalytic activity of $(TiO_2NP)_{1-x}(NiO)_x/Cd_{0.8}Zn_{0.2}S$ and $(TiO_2NP/Pt)_{1-x}(NiO)_x/Cd_{0.8}Zn_{0.2}S$ (x ~ 0.83) under visible-light irradiation in the presence of benzyl alcohol-acetic acid as a sacrificial agents.

$_x(NiO)_x/Cd_{0.8}Zn_{0.2}S$ (x ~ 0.83) by selectively depositing Pt on $TiO_2$ (0.5 mol% of Pt on $TiO_2$; see **Figure 14** for TEM images of $(TiO_2NP/Pt)$. With $(TiO_2NP/Pt)_{1-x}(NiO)_x/Cd_{0.8}Zn_{0.2}S$ (x ~ 0.83) heterostructures, $H_2$ evolution increases further to 17 mmol $h^{-1}g^{-1}$ (AQY ~ 29.2%) under visible light irradiation with benzyl alcohol-acetic acid as sacrificial agents (**Figure 15**). The enhancement in activity is likely to be due to the injection of electrons to the $TiO_2$.

It would be useful to compare the present results on the generation of hydrogen with the literature reports. **Table** 1 shows such a comparison to demonstrate the effectiveness of NiO in place of Pt in the heterostructures.

**Table 1. Comparison of visible light induced hydrogen evolution by different $TiO_2$-based heterostructures.**

| Photocatalyst | $H_2$ yield (mmol $h^{-1}g^{-1}$) | AQY (%) | References |
|---|---|---|---|
| NiO/CdS | 0.74 | 6 | Ref.13 |
| $NiO/Cd_{0.8}Zn_{0.2}S$ | 0.81[a] | 1.4[a] | Present work |
| $TiO_2/Cd_{0.8}Zn_{0.2}S$ | 0.03[a] | 0.05[a] | Present work |
| $TiO_2/Pt/Cd_{0.8}Zn_{0.2}S$ | 0.55[a] | 0.9[a] | Ref.15 |
| $(TiO_2)_{0.17}(NiO)_{0.83}/Cd_{0.8}Zn_{02}S$ | 1.60[a] (6.84)[b] (13.5)[c] | 2.9[a] (11.7)[b] (10)[c] | Present work |

[a] yields in $Na_2S$-$Na_2SO_3$, [b] yields in benzyl alcohol-acetic acid (BnOH-AcOH), $TiO_2$ was in the form of nanoparticles (Degussa P25), [c]yield in UV-visible light using benzyl alcohol-acetic acid as a sacrificial agent.

## 4.2 Synthesis and Properties of ZnO/NiO/$Cd_{1-x}Zn_xS$ (x= 0.0 and 0.2) heterostructures

Phase changes in $Zn_{1-y}Ni_yO_2$ with temperature were monitored by thermo gravimetric analysis (**Figure 16**). TGA curve of $Zn_{0.9}Ni_{0.1}O_2$ recorded by heating the sample under nitrogen atmosphere with a heating rate of 3 °C/min. At the initial stage of heating, the sample showed the weight loss due to desorption of adsorbed water molecules. At the temperatures above 120 °C, the sample has shown a remarkable weight loss due the release of oxygen during the conversion of peroxides to oxides.[17] This decomposition has led to the formation Ni doped ZnO, having green or black depending on the extent of Ni. Further subjecting the sample to even high temperatures resulted in phase segregation thereby the formation of ZnO and NiO heterostructures. Based on the TGA information we have treated the samples at 200 or 500 °C for the formation of $Zn_{1-x}Ni_xO$ and ZnO/NiO heterostructures respectively.

The peroxide precursor $Zn_{1-y}Ni_yO_2$ belongs to the space group of $Pa3^-$. Ni substituted ZnO ($Zn_{1-y}Ni_yO$) obtained by the decomposition of $Zn_{1-y}Ni_yO_2$ at 250 ˚C shows broad peak corresponding to the wurtzite phase of ZnO with the space group of $P6_3mc$ (**Figure 17a**) and there is no evidence of presence of NiO. ZnO/NiO prepared by method 2 and 3 shows diffraction peaks of ZnO ($P6_3mc$) and NiO ( Fm3m). The diffraction peaks corresponding to NiO show a gradual increase in the intensity with the amount of Ni (**Figure 17b**).

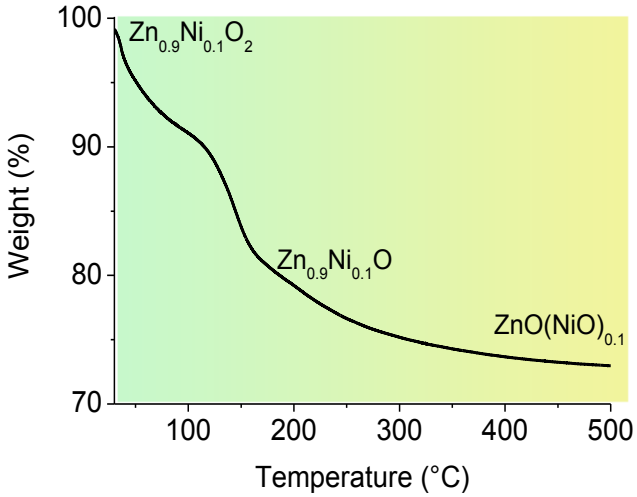


Figure 16. TGA profile depicting the formation of ZnO/NiO.

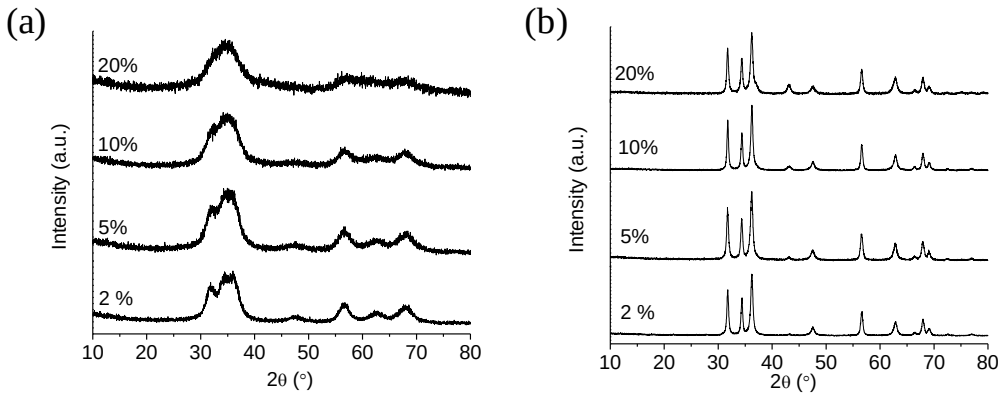


Figure 17. PXRD patterns of a) $Zn_{1-x}Ni_xO$, and b) $ZnO(NiO)_x$ with diffrent amount of Ni in the compounds.

Morphology analysis of the structures was carried out by the transmission electron microscopy. ZnO nanoparticles are having an average diameter of 20 nm. We also observed that Ni atoms form NiO nanostructures at the ZnO surfaces which are evident from the dark areas in the TEM image (**Figure 18a**). The ZnO and NiO phase can also identified by the d-spacing in the lattice fringes found in the TEM images of the ZnO/NiO heterostructures. In the case of $ZnO/NiO/Cd_{1-x}Zn_xS$ heterostructures, $Cd_{1-x}Zn_xS$ nanoparticles are located on the ZnO/NiO with slightly reduced d-spacing (**Figure 18b**). Due to wide band gaps of ZnO and NiO the extent of absorption of solar-irradiation is limited to UV regime. Visible light absorption is obtained in this system by forming heterostructures of the type ZnO/NiO/CdS. Absorption of ZnO/NiO/CdS extend to 540 nm, whereas in the case of heterostructures like $ZnO/NiO/Cd_{0.8}Zn_{0.2}S$ absorption extended up to 490 nm the blue shift in absorption is due to increase in the band gap of CdS after Zn substitution (**Figure 19**).

**Photocatalytic hydrogen generation** studied by employing $Na_2S$ and $Na_2SO_3$ as sacrificial hole scavengers. A 450 W Xe arc lamp (New Port, 6279 NS, ozone free and working at 400 W) was used as a light source in the photocatalytic hydrogen generation studies. 20 mg of photocatalyst was used for all the photocatalytic studies. Photocatalytic hydrogen evolution with ZnO/NiO/CdS heterostructures prepared by

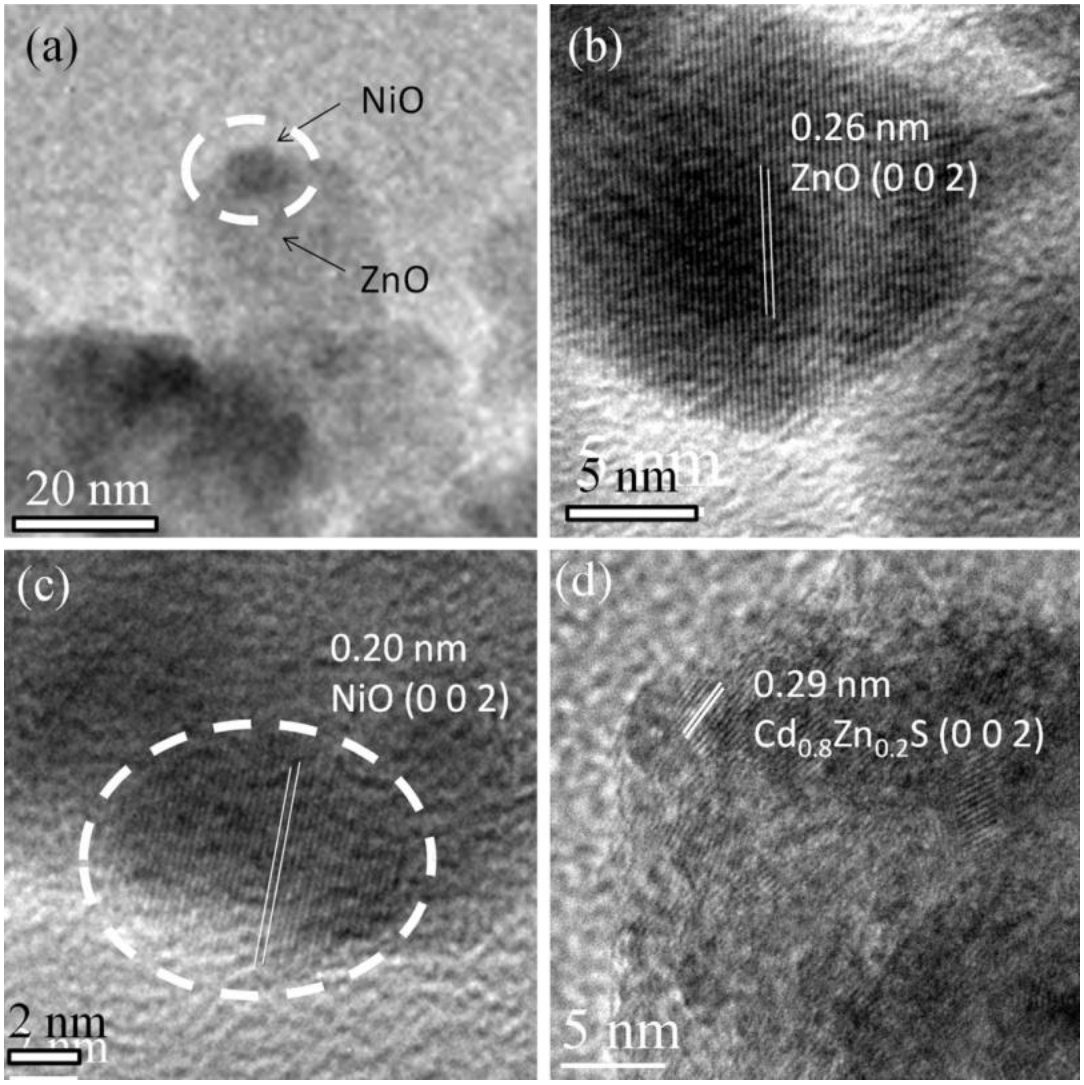


Figure 18. a) Low magnification TEM, b) HRTEM image of ZnO/NiO, C) Low magnification TEM, and d) HRTEM image of ZnO/NiO/$Cd_{0.8}Zn_{0.2}S$.

method 2 was carried out by varying the amount of NiO. With 25 mol% loading of CdS relative to ZnO, ZnO/CdS heterostructures shows hydrogen evolution rate of 1.1 mmol $h^{-1}$ $g^{-1}$ with an apparent quantum yield of 1.2 % under visible light irradiation. In the presence of NiO in heterostructures improvement in hydrogen evolution activity occurs. With 10 % loading of NiO hydrogen evolution activity was 2.2 mmol $h^{-1}g^{-1}$ with an apparent quantum yield of 2.3 % which is nearly twice than that of ZnO/CdS. Further increase in loading content of NiO lowered the activity of ZnO/NiO/CdS heterostructures (**Figure 20a**). Since it has been reported that in the heterostructures ZnO/Pt/CdS partial substitution of Zn in CdS causes improvement in photocatalytic activity.

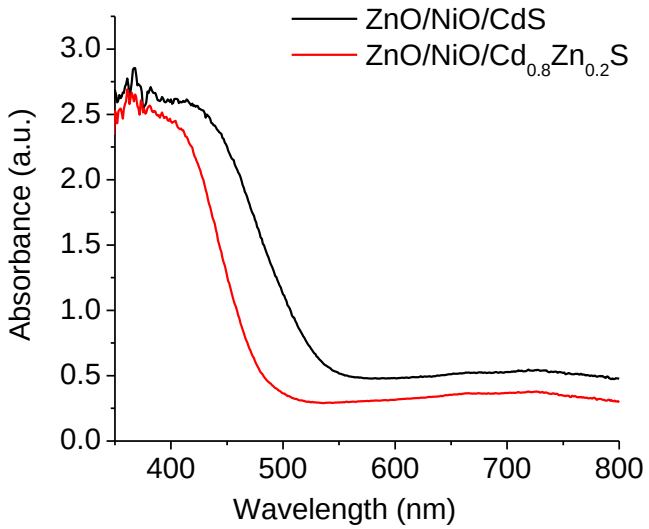


Figure 19. Absorption spectra of ZnO/NiO/CdS and ZnO/NiO/$Cd_{0.8}Zn_{0.2}S$.

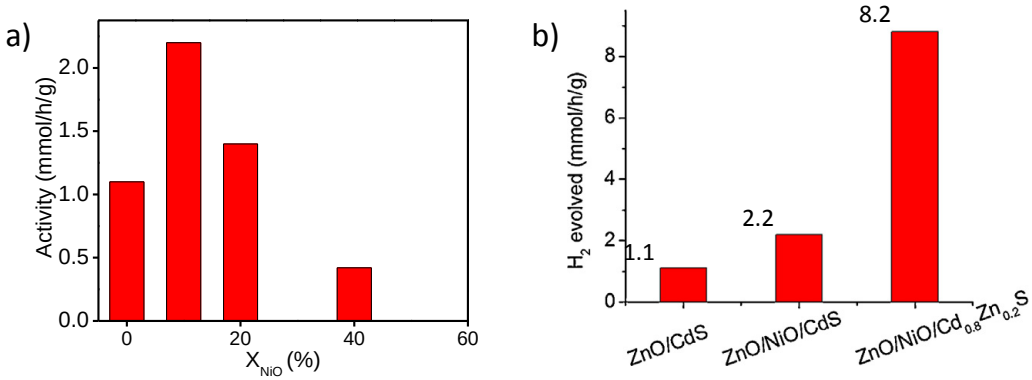


Figure 20. a) Photocatalytic hydrogen evolution activities of ZnO/NiO/CdS heterostructures with different amount of NiO and, b) Comparative activity of ZnO/CdS, ZnO/NiO/CdS, and ZnO/NiO/$Cd_{0.8}Zn_{0.2}S$.

Similar to that we prepared the heterostructures ZnO/NiO/$Cd_{0.8}Zn_{0.2}S$ and measured photocatalytic hydrogen evolution. ZnO/NiO/$Cd_{0.8}Zn_{0.2}S$ heterostructures shows significant increase in photocatalytic activity with $H_2$ evolution activity of 8.2 mmol $h^{-1}g^{-1}$, and apparent quantum yield of 14 % under visible light irradiation (**Figure 20b**).We have studied the hydrogen evolution with ZnO/NiO/$Cd_{0.8}Zn_{0.2}S$ heterostructures using ZnO/NiO heterostructures prepared by the impregnation method (method 3). These heterostructures exhibited a hydrogen evolution of 7.1 mmol $h^{-1}g^{-1}$ with apparent quantum yield of 12 % under visible light irradiation and 17 mmol $h^{-1}g^{-1}$ with apparent quantum yield of 15 % under UV-Vis light irradiation.

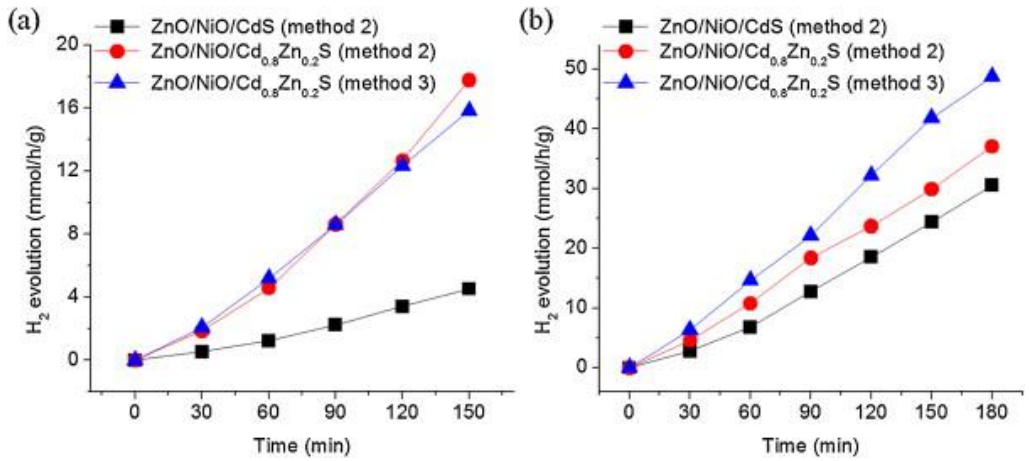


Figure 21. Comparison of a) Visible, and b) UV-vis light induced hydrogen evolution from ZnO/NiO/CdS (method 2) and ZnO/NiO/$Cd_{0.8}Zn_{0.2}S$ (method 2 and 3) in the presence of $Na_2S$ and $Na_2SO_3$.

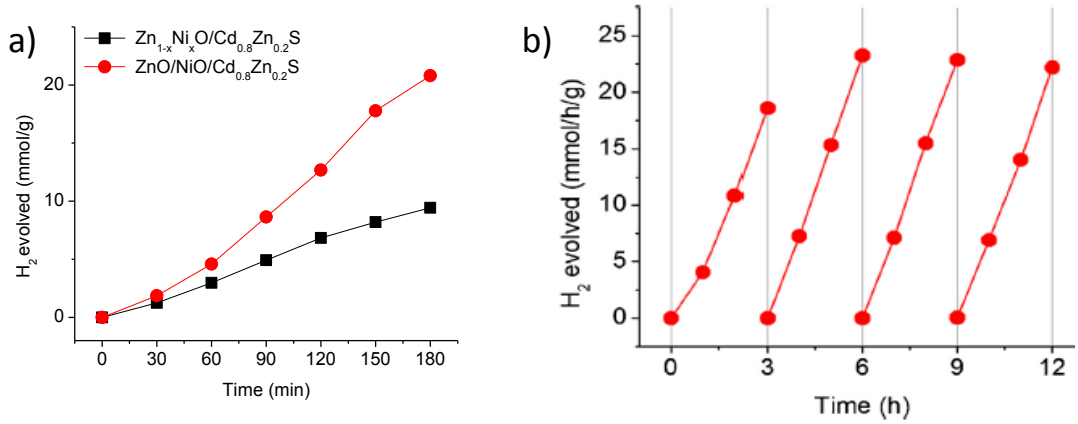


Figure 22. a) Hydrogen evolution activity of $Zn_{1-y}Ni_yO/Cd_{0.8}Zn_{0.2}S$ and ZnO/NiO/$Cd_{0.8}Zn_{0.2}S$ in visible light irradiation, and b) Recyclability and stability of visible light induced $H_2$ evolution of ZnO/NiO/$Cd_{0.8}Zn_{0.2}S$ heterostructures.

It is noteworthy to mention that ZnO/NiO prepared by method 3 shows higher activity in UV-Vis light than ZnO/NiO prepared by method 2 (**Figure 21**).

We studied hydrogen evolution activity of $Zn_{0.9}Ni_{0.1}O/Cd_{0.8}Zn_{0.2}S$ under visible light irradiation. Hydrogen evolution activity of these structures is 3.9 mmol $h^{-1}g^{-1}$ with apparent quantum yield of 7%, which is very less than the activity of ZnO/NiO/$Cd_{0.8}Zn_{0.2}S$ synthesized by method 2 (**Figure 22a)**. So, it suggests that ZnO and NiO should be present in the form of heterostructures

rather than having solid solution of the two. Photostability and recyclibity of ZnO/NiO/$Cd_{0.8}Zn_{0.2}S$ heterostructures in visible light was studied in presence of $Na_2S$ and $Na_2SO_3$ sacrificial agents. **Figure 22b** shows the photo stability of samples for the duration of 12 hour. There was no decline in the photocatalytic hydrogen evolution rate up to 12 hours, which suggest stability of these heterostructures. We compare the hydrogen evolution activity of ZnO/NiO/$Cd_{0.8}Zn_{0.2}S$ with that of heterostructures having Pt and Au at the place of NiO (**Figure 23**). Photocatalytic activity of ZnO/NiO/$Cd_{0.8}Zn_{0.2}S$ is comparable with ZnO/Pt/$Cd_{0.8}Zn_{0.2}S$ where ZnO is synthesized by the same solution method. Photocatalytic activity of ZnO/Au/$Cd_{0.8}Zn_{0.2}S$ is inferior to that of ZnO/NiO/$Cd_{0.8}Zn_{0.2}S$ for the same ZnO used in the heterostructures. ZnO/Pt/$Cd_{0.8}Zn_{0.2}S$ heterostructures having ZnO which is synthesized at 600˚C similar to we use in the case of ZnO/NiO/$Cd_{0.8}Zn_{0.2}S$ heterostructure shows lesser photocatalytic activity than ZnO/NiO/$Cd_{0.8}Zn_{0.2}S$.

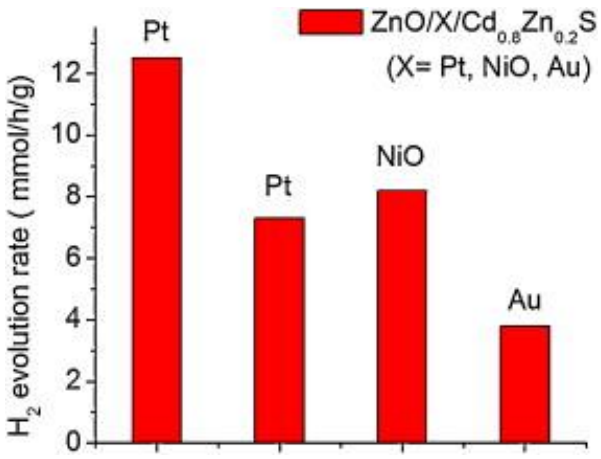


**Figure 23.** Comparison of hydrogen evolution activities of ZnO/X/$Cd_{0.8}Zn_{0.2}S$ heterostructures (X = Pt, Au, NiO) under visible light irradiation in the presence of $Na_2S$ and $Na_2SO_3$ as a sacrificial electron donor.

# 5. Conclusions

The present study establishes that NiO can be used in place of Pt in semiconductor heterostructures for the generation of hydrogen under visible-light irradiation. Thus, $H_2$ evolution from the $(TiO_2)_{1-x}(NiO)_x/Cd_{0.8}Zn_{0.2}S$ heterostructure (x~ 0.83) exhibits three times higher activity (1.6 mmol $h^{-1}g^{-1}$), compared to $TiO_2/Pt/Cd_{0.8}Zn_{0.2}S$ (0.55 mmol $h^{-1}g^{-1}$) with $Na_2S$-$Na_2SO_3$ as sacrificial agents in visible-light irradiation. Furthermore, while the photocatalytic hydrogen evolution activity increases progressively with NiO content up to x ~ 0.6, it reaches a maximum at x ~ 0.83. The $H_2$ yield obtained is superior to many other semiconductor catalysts shown in Table 1. It seems likely that p-n junction between n-$TiO_2$ and p-NiO plays an important role in determining the photocatalytic activity. ZnO/NiO/CdS and $ZnO/NiO/Cd_{0.8}Zn_{0.2}S$ heterostructures prepared by different methods have been examined for the photocatalytic hydrogen evolution activity under visible as well as UV-Vis irradiation. CdS with a band gap of 2.4 eV absorbs visible light efficiently and ZnO/CdS heterostructures enable better separation of electron and holes. Electrons at the surface of the NiO co-catalyst undergoes redox reaction to produce $H_2$ from $H_2O$. ZnO/NiO/CdS shows a two-fold higher photocatalytic activity than ZnO/CdS. Further improvement in photocatalytic activity occurs in the case of $ZnO/NiO/Cd_{1-x}Zn_xS$ heterostructures with a partial substitution of Zn in CdS. $Zn_{1-y}Ni_yO/Cd_{0.8}Zn_{0.2}S$ based photocatalyst exhibits less activity than $ZnO/NiO/Cd_{0.8}Zn_{0.2}S$.

# 6. References


[1] a) Z. Zou, J. Ye, K. Sayama, H. Arakawa, *Nature* **2001**, *414*, 625; b) M. G. Walter, E. L. Warren, J. R. McKone, S. W. Boettcher, Q. Mi, E. A. Santori, N. S. Lewis, *Chem. Rev.* **2010**, *110*, 6446-6473; c) S. Berardi, S. Drouet, L. Francàs, C. Gimbert-Suriñach, M. Guttentag, C. Richmond, T. Stoll, A. Llobet, *Chem. Soc. Rev.* **2014**, *43*, 7501-7519; d) A. J. Bard, M. A. Fox, *Acc. Chem. Res* **1995**, *28*, 141-145.

[2] a) S. R. Lingampalli, U. K. Gautam, C. N. R. Rao, *Energy Environ. Sci.* **2013**, *6*, 3589-3594; b) S. R. Lingampalli, C. N. R. Rao, *J. Mater. Chem. A* **2014**, *2*, 7702-7705.

[3] a) K. Domen, S. Naito, M. Soma, T. Onishi, K. Tamaru, *J. Chem. Soc. Chem. Commun.* **1980**, 543-544; b) H. Kato, A. Kudo, *J. Phys. Chem. B* **2001**, *105*, 4285-4292.

[4] J. Ran, J. Zhang, J. Yu, M. Jaroniec, S. Z. Qiao, *Chem. Soc. Rev.* **2014**, *43*, 7787-7812.

[5] Z. Khan, M. Khannam, N. Vinothkumar, M. De, M. Qureshi, *J. Mater. Chem.* **2012**, *22*, 12090-12095.

[6] a) T. Sreethawong, Y. Suzuki, S. Yoshikawa, *Int. J. Hydrogen Energy* **2005**, *30*, 1053-1062; b) A. Kudo, K. Domen, K.-i. Maruya, T. Onishi, *Chem. Phys. Lett.* **1987**, *133*, 517-519; c) X. Chen, W. Chen, P. Lin, Y. Yang, H. Gao, J. Yuan, W. Shangguan, *Catal. Commun.* **2013**, *36*, 104-108.

[7] a) Y. Ku, C.-N. Lin, W.-M. Hou, *J. Mol. Catal. A: Chem* **2011**, *349*, 20-27; b) J. Yu, W. Wang, B. Cheng, *Chem Asian J* **2010**, *5*, 2499-2506; c) C. Shifu, Z. Sujuan, L. Wei, Z. Wei, *J. Hazard. Mater.* **2008**, *155*, 320-326.

[8] A. Roy, S. R. Lingampalli, S. Saha, C. N. R. Rao, *Chem. Phys. Lett.* **2015**, *637*, 137-142.

[9] J. Moghaddam, E. Hashemi, *Korean J. Chem. Eng.* **2014**, *31*, 503-508.

[10] T. Kasuga, M. Hiramatsu, A. Hoson, T. Sekino, K. Niihara, *Adv. Mater.* **1999**, *11*, 1307-1311.

[11] G. Sankar, C. N. R. Rao, T. Rayment, *J. Mater. Chem.* **1991**, *1*, 299-300.

[12] a) T. Takata, Y. Furumi, K. Shinohara, A. Tanaka, M. Hara, J. N. Kondo, K. Domen, *Chem. Mater.* **1997**, *9*, 1063-1064; b) S. Ikeda, M. Hara, J. N. Kondo, K. Domen, H. Takahashi, T. Okubo, M. Kakihana, *Chem. Mater.* **1998**, *10*, 72-77; c) D. C. Lee, A. Ghezelbash, C. A. Stowell, B. A. Korgel, *J. Phys. Chem. B* **2006**, *110*, 20906-20911.

[13] A. Tataroğlu, A. G. Al-Sehemi, M. Ilhan, A. A. Al-Ghamdi, F. Yakuphanoglu, *Silicon* **2018**, *10*, 913-920.

[14] S. A. Angayarkanni, J. Philip, *J. Appl. Phys.* **2015**, *118*, 094306.

[15] H. Pan, Y.-W. Zhang, *J. Mater. Chem.* **2012**, *22*, 7280-7290.

[16] a) J. Hou, Z. Wang, W. Kan, S. Jiao, H. Zhu, R. V. Kumar, *J. Mater. Chem.* **2012**, *22*, 7291-7299; b) H. R. Liu, G. X. Shao, J. F. Zhao, Z. X. Zhang, Y. Zhang, J. Liang, X. G. Liu, H. S. Jia, B. S. Xu, *J. Phys. Chem. C* **2012**, *116*, 16182-16190.

[17] S. R. Lingampalli, U. Gupta, U. K. Gautam, C. N. R. Rao, *ChemPlusChem* **2013**, *78*, 837-842.

# Part 2

## Aliovalent Anion Substituted Inorganic Semiconductor Materials and their Novel Properties

# Chapter 1

# Introduction to the Aliovalent Anion Substitution in Inorganic Semiconductor Materials


## Summary*

There have been limited reports on anion substitution in inorganic materials compared to cation substitution. Aliovalent anion substitution involves substitution of an anion by two different anions having different valencies such as substitution of $O^{2-}$ in ZnO or $TiO_2$ by $N^{3-}$ and $F^-$ or substitution of $S^{2-}$ in CdS or ZnS by $P^{3-}$ and $Cl^-$. Aliovalent anion substitution is benefecial over isovalent anion substitution because of neutrality and elimination of defects.

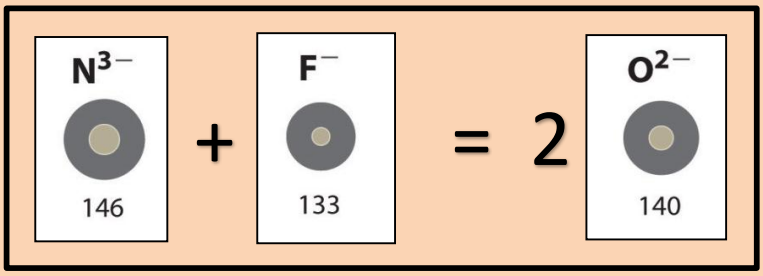


This chapter presents the result of the studies of substitution of aliovalent $N^{3-}$ and $F^-$ in ZnO and $TiO_2$. Apart from the metal oxides, effect of aliovalent anion substitution has also been studied in metal chalcogenides such as CdS and ZnS First-principles calculations have been employed to understand the electronic structures and other properties of these materials.

# 1. Introduction

In order to alter the photophysical properties of metal oxides and sulfides, a common practice is to dope metal ions which alter the conduction band related properties. Since conduction band states are mostly made up of unoccupied orbitals, hence, metal ion substitution does not create a significant change in the photophysical properties. In contrast, anion substitution in semiconductor materials alters the occupied valence band related properties and therefore have marked effect on the photophysical properties of materials. Substitution of N in ZnO is known to alter the bad gap, Raman features and the photocatalytic properties.[1] Substitution of F in ZnO affects the electrical properties.[2] There have been reports on N-substitution in $TiO_2$ wherein the absorption edge of $TiO_2$ is shifted from the UV-region to the visible-region resulting in the visible-light-induced photocatalysis.[3] F-doping in $TiO_2$ however, does not change the absorption band edge and it needs UV-radiation to work as a photocatalyst.[4] It should be noted that substitution of the only $N^{3-}$ or $F^-$ causes defects in the oxide. In the case of N-doping in ZnO, oxygen vacancy forms which give rise to weak room temperature magnetism.[5] A strategy to overcome the problem of defects formation in semiconductors host is to use the aliovalent anion substitution.[6] Substitution of $N^{3-}$ and $F^-$ in place of $O^{2-}$ results in charge neutrality. Furthermore, ionic sizes and electron counts of $N^{3-}$, $O^{2-}$ and $F^-$ are the same. There have been reports on N, F co-substituted $TiO_2$ and their photocatalytic properties under visible-light irradiation.[7] Recently, a high concentration of $N^{3-}$ and $F^-$ has been doped in ZnO and $TiO_2$ which significantly changes the electronic and photophysical properties.[8]

Apart from the anion substitution in metal oxides, metal chalcogenides such as CdS, ZnS, ZnSe also show notable changes in their electronic and photophysical properties as a result of the aliovalent anion substitution. Substitution of $Cl^-$ or $P^{3-}$ in CdS nanorods has been found to affect their optoelectronic properties.[9] Co-substitution of $P^{3-}$ and $Cl^-$ in ZnS and CdS have been studied recently.[10]

## 2. Substitution of N, F in $TiO_2$

Rao and coworkers reported codoping of $N^{3-}$ and $F^-$ in $TiO_2$, employing solid-state reaction.[8b] Synthesis of samples involved the use of urea (as a nitrogen precursor) and $NH_4F$ (as F precursor) homogenously mixed with $TiO_2$ nanoparticles and annealed at 600 ºC under $N_2$ atmosphere. In the same work authors report the use of $(NH_4)_2TiF_6$ complex to obtain N, F co-substituted $TiO_2$ when annealed at 550 ºC under open atmosphere condition. N, F doped $TiO_2$ crystallized in the anatase structure with a slight reduction in the lattice parameters (**Figure 1**). XPS measurements were employed to qualitatively and quantitatively analyze the doped sample, and the analysis showed the presence of N(1s) and F(1s) signals with the amount in percentage close to 15 % (**Figure 2**). UV-vis absorption spectra of N, F co-doped samples show absorption in the visible region with an absorption edge close to ~550 nm (**Figure 3a**). The band gaps of samples obtained employing two different methodologies (use of urea and $NH_4F$ or use of $(NH_4)_2TiF_6$ complex) have values 2.2 and 2.5 eV respectively. Noteworthy to mention that a defect band at 600 nm in N doped $TiO_2$ samples vanished in the case of N, F co-doped samples indicating defect free system (**Figure 3b**).

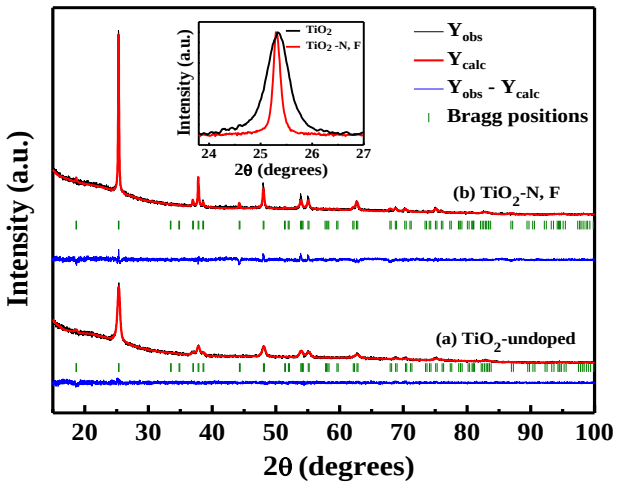


Figure 1. X-ray diffraction patterns of undoped and N, F co-doped $TiO_2$ samples. Reproduced with Permission from ref. 8b. Copyright 2013 American Chemical Society.

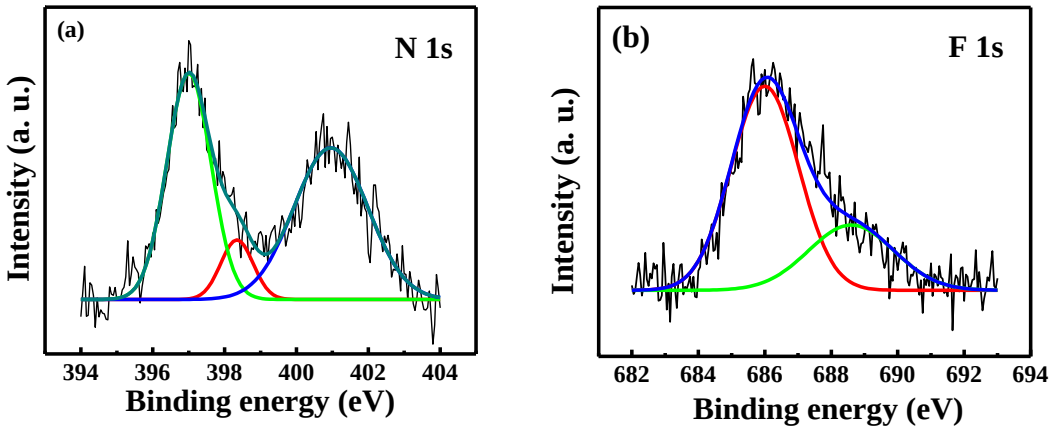


Figure 2. XPS core-level spectra of N, F co-substituted $TiO_2$, a) N1s, and b) F1s. Reproduced with Permission from ref. 8b. Copyright 2013 American Chemical Society.

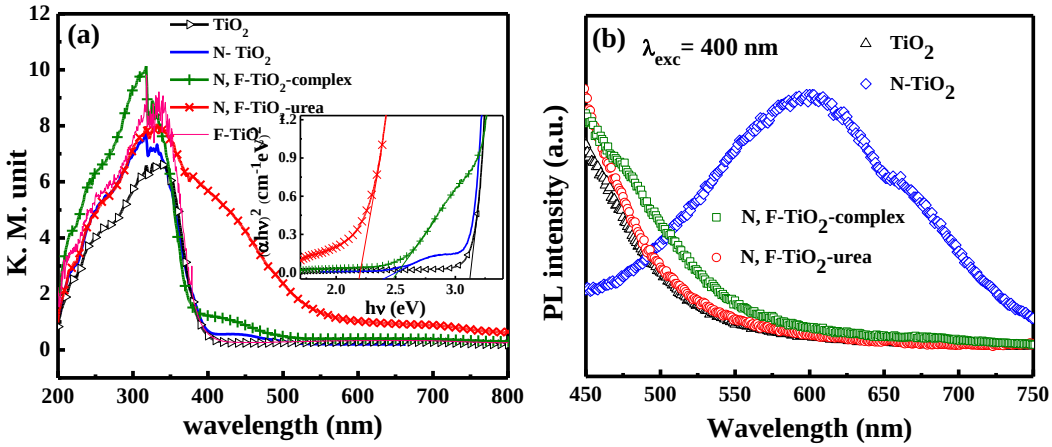


Figure 3. a) UV-vis absorption spectra, and b) Steady-state photoluminescence spectra of undoped and N, F co-doped $TiO_2$ samples. Reproduced with Permission from ref. 8b. Copyright 2013 American Chemical Society.

First-principles calculations revealed a change in the lattice parameters and bond length as a result of N, F co-substitution in $TiO_2$. It was found that co-substitution of $N^{3-}$ and $F^-$ is energetically more favored than the isovalent substitution of $N^{3-}$ or $F^-$ in $TiO_2$. In pristine $TiO_2$, top of the valence band is majorly contributed by O 2p orbitals and bottom of the conduction band is contributed by Ti 3d. Upon N,F substitution an isolated band appeared at the top of the valance band, the density of states analysis confirmed it to be N 2p states (**Figure 4**). F 2p orbitals were found deep down in the valence band. Reduction in the band gap of $TiO_2$ is linked with the N 2p states at the

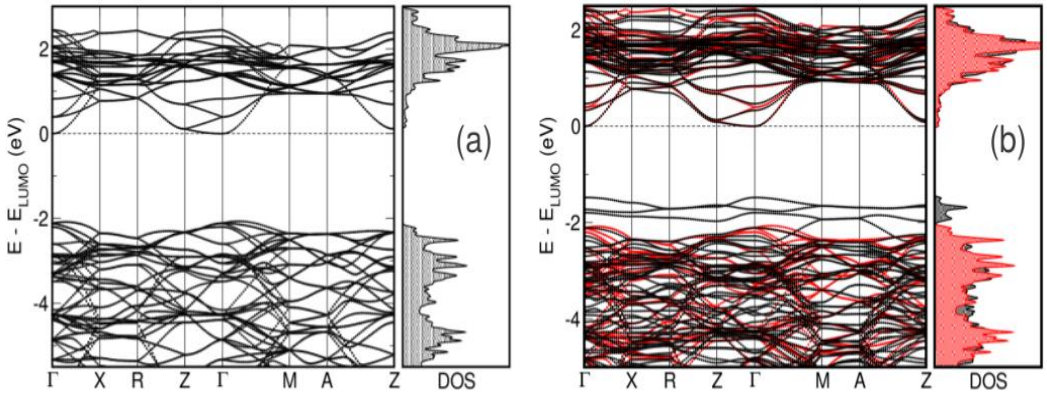


Figure 4. Electronic structure and density of states of a) undoped, and b) N, F co-doped $TiO_2$. Reproduced with Permission from ref. 8b. Copyright 2013 American Chemical Society.

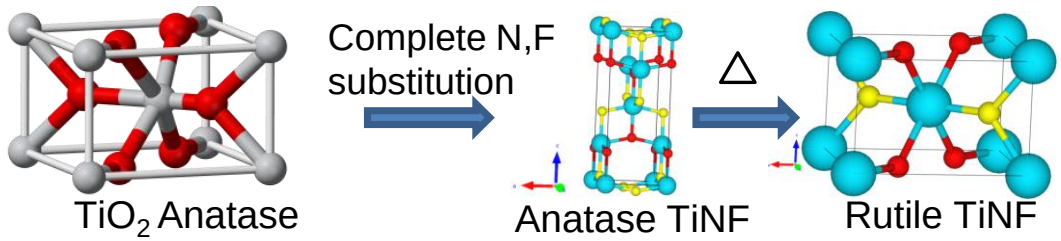


Figure 5. Schematic representation of the formation of anatase and rutile TiNF. Reproduced with Permission from ref. 11. Copyright 2018 Wiley-VCH Verlag GmbH & co. kGaA, Weinheim.

top of the valence band. Such N, F co-doped $TiO_2$ samples performs visible-light induced hydrogen generation from water without any co-catalyst assistance.

Recently there has been a report on the complete substitution of $O^{2-}$ in $TiO_2$ by aliovalent anions, $N^{3-}$ and $F^-$ which yielded a compound of composition TiNF (**Figure 5**).[11] A reaction between TiN and $TiF_4$ under inert atmosphere resulted in the formation of anatase TiNF ($I4_1/amd$) which was converted into the rutile phase ($P4_2/mnm$) by further heating (**Figure 6**). XPS was employed to analyze the composition of TiNF. Anatase and rutile phase TiNF exhibit the absorption edge at 315 and 365 nm respectively (**Figure 7**).

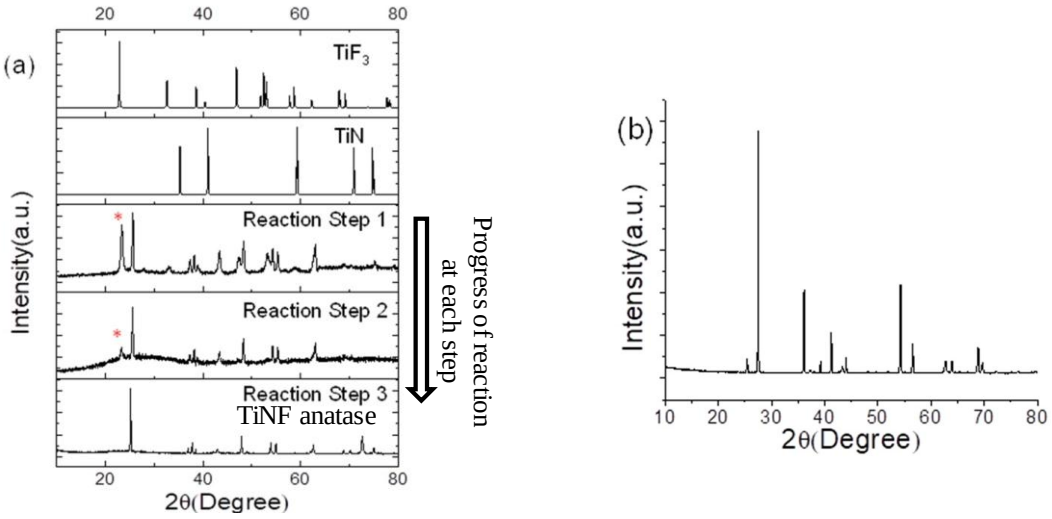


Figure 6. PXRD pattern of a) reactants, reaction intermediates and anatase TiNF, b) rutile TiNF. Reproduced with Permission from ref. 11. Copyright 2018 Wiley-VCH Verlag GmbH & co. kGaA, Weinheim.

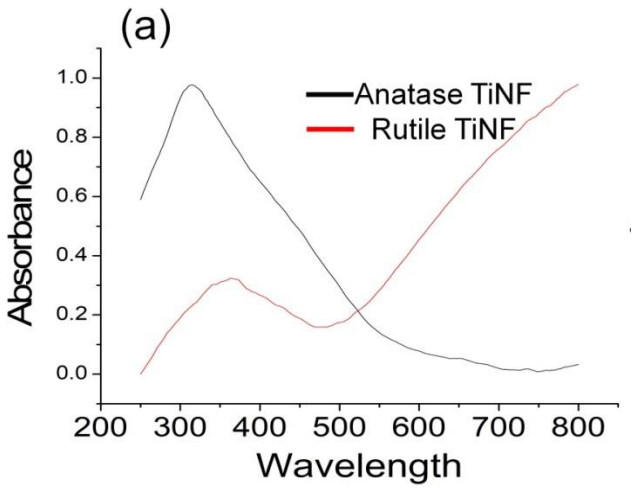


Figure 7. UV-vis absorption spectra of rutile and anatase phase of TiNF. Reproduced with Permission from ref. 11. Copyright 2018 Wiley-VCH Verlag GmbH & co. kGaA, Weinheim.

## 3. Substitution of N, F in ZnO

Co-substitution of $N^{3-}$ and $F^-$ at the place of $O^{2-}$ in ZnO can be achieved by the solid-state reaction wherein $NH_4F$ act as $F^-$ precursor and $NH_3$ gas or urea act as $N^{3-}$ precursor.[8a] Annealing of $NH_4ZnF_3$ complex under controlled $NH_3$ atmosphere also produces N, F co-substituted ZnO.[8a] N-doped ZnO can be prepared by heating ZnO nanoparticles in $NH_3$ atmosphere. Co-doped samples can be represented by the formula $ZnO_{1-x-}yN_xF_y$, and qualitative and quantitive presence of N and F can be achieved by the XPS-analysis. Co-substituted ZnO samples crystallize in the wurtzite structure and possesses slightly reduced lattice parameters. The most striking feature of N, F co-substituted ZnO is

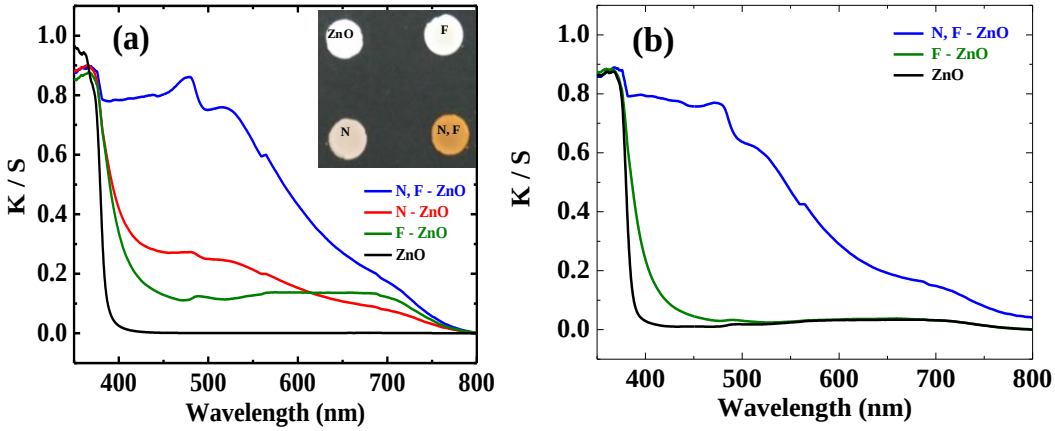


Figure 8. UV-vis absorption spectra of N, F co-doped ZnO obtained by a) nanoparticle route, and b) complex route. Reproduced with the Permission from ref. 8a. Copyright 2013 Wiley-VCH Verlag GmbH & co. kGaA, Weinheim.

their UV-vis absorption spectrum, wherein a significant broadening of the absorption spectrum extending up to 750 nm has been achieved (**Figure 8**).[8a]

Results of the first-principles calculations predicted the energetics favors co-substitution of $N^{3-}$ and $F^-$ in ZnO over the isovalent substitution of $N^{3-}$ or $F^-$ ions.[8a] The energetics of different orientation of N, F co-substitutes ZnO suggest that N and F like to be as a near neighbor in the lattice. Electronic structure of N, F co-substituted ZnO exhibits a subband at the top of the valance band (**Figure 9**). The density of states analysis confirmed the top band is majorly constituted by N2p states resulting in the broadning

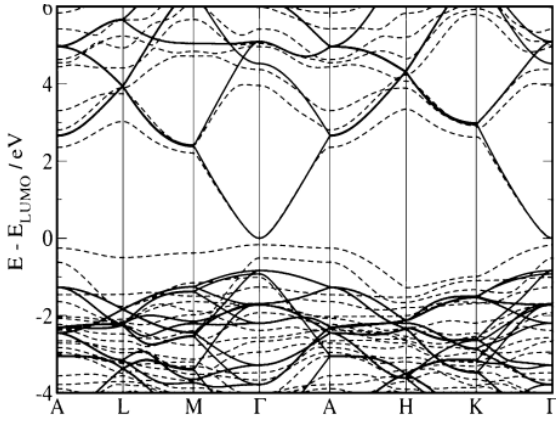


Figure 9. Electronic structure of N, F co-substituted ZnO. Reproduced with the Permission from ref. 8a. Copyright 2013 Wiley-VCH Verlag GmbH & co. kGaA, Weinheim.

of the absorption spectrum and hence lowering of the band gap. F2p orbitals occupy the deep states in the valance band hence did not directly affect the band gap tuning; however, it was found that the presence of F enhances the contribution of N states. $ZnO_{1-x-y}N_xF_y$, were used in the heterostructure with Pt and CdS nanoparticles to perform photochemical hydrogen evolution from water in the presence of $Na_2S$-$Na_2SO_3$ sacrificial electron donors. Interestingly, such heterostructure exhibited remarkable photochemical hydrogen evolution activity.[12]

Similar to TiNF, Rao and coworkers have reported a compound of formula $Zn_2NF$ obtained by the complete substitution of $O^{2-}$ by $N^{3-}$ and $F^-$ in ZnO.[13] $Zn_2NF$ was prepared by a solid-state reaction between $Zn_3N_2$ and $ZnF_2$ at an optimum reaction temperature. Resulting $Zn_2NF$ product crystallizes in the tetragonal ($P4_12_12$) and orthorhombic ($P2_12_12_1$) structure, however an excessive N, F co-doped ZnO remained in the hexagonal structure (**Figure 10**). Optical properties of both the form of $Zn_2NF$ and hexagonal N, F co-doped ZnO exhibit absorption in the visible-region with their band gaps 2.77, 2.72 and 2.84 eV for tetragonal, orthorhombic and hexagonal phases respectively (**Figure 11**). In the same work, authors have reported optical absorption features of a series of N, F co-doped ZnO samples along with $Zn_2NF$, wherein a band gap of ZnO varies from 3.2 eV to 2.0 eV (**Figure 12**).

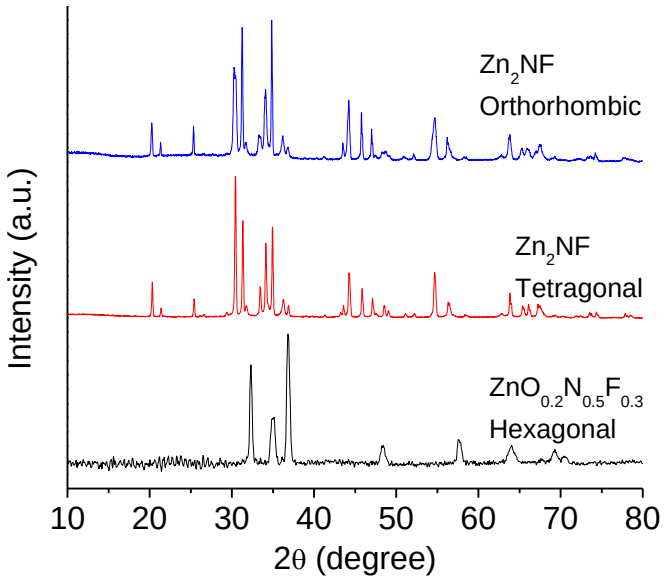


Figure 10. PXRD patterns of samples obtained by complete and substantial substitution of $O^{2-}$ by $N^{3-}$ and $F^{-}$ in ZnO. Reproduced with Permission from ref. 13. Copyright 2016 American Chemical Society.

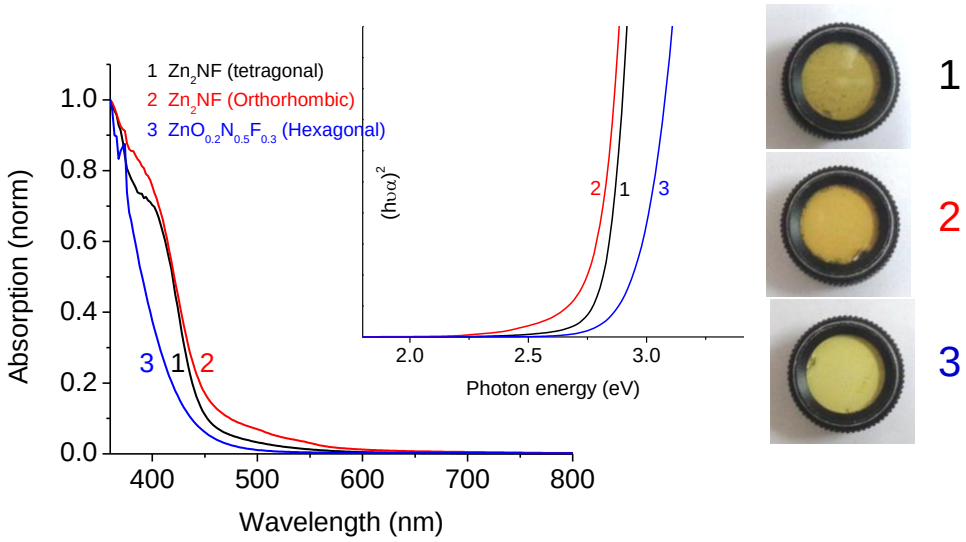


Figure 11. Optical absorption spectra of $Zn_2NF$ tetragonal, $Zn_2NF$ orthorhombic and hexagonal $ZnO_{0.2}N_{0.5}F_{0.3}$ along with the color of samples. Reproduced with Permission from ref. 13. Copyright 2016 American Chemical Society.

It is remarkable that concentration of N3- creats such marked effect on the absoprtion properties of ZNO.

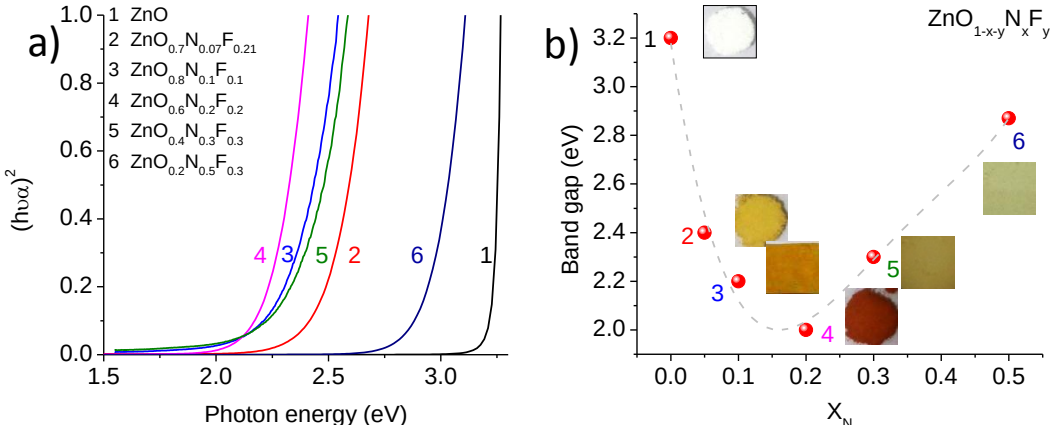


Figure 12. a) Tauc plots for various compositions of N, F co-doped ZnO samples, and b) band gaps of samples concerning the N-content. Reproduced with Permission from ref. 13. Copyright 2016 American Chemical Society.

Similar to the analogs of ZnO and $TiO_2$ recently analogs of CdO and HgO has also been reported.[14]

## 4. Substitution of P, Cl or N, F in ZnS

P, Cl co-substituted ZnS has been prepared using ZnS in a solid state reaction with $Zn_3P_2$ and $NH_4Cl$ as P and Cl precursors.[15] N, F substituted ZnS was prepared by a mixture of ZnS and $NH_4F$ in $NH_3$ atmosphere.[15] Valence band of metal chalcogenides are majorly contributed by the anions (S-3p in the case of CdS and ZnS) whereas conduction band has major contribution from the metal s-orbtals. First-principles calculations on P, Cl co-substituted ZnS system revealed the presence of the band on the top of S 3p states which has major contribution from P 3p robitals. Similarly, in the case of N, F substituted CdS system an solated band at the top of the valence band was revealed it to have major contribution from N 1s-states (**Figure 13**). X-ray photoeelctron spectroscopy (XPS) was used to confirm the oxidation states and concentration of the dopants ZnS lattice. UV/vis absorption spectra showed a significant reduction in the band gap of ZnS as a result of P, Cl or N, F substitution (**Figure 14**). Noteworthy to mention that unlike the limited UV absorption of pristine ZnS compound, aliovalent anions substituted samples possess absorption in the visible-region of spectrum which can be benefecial.

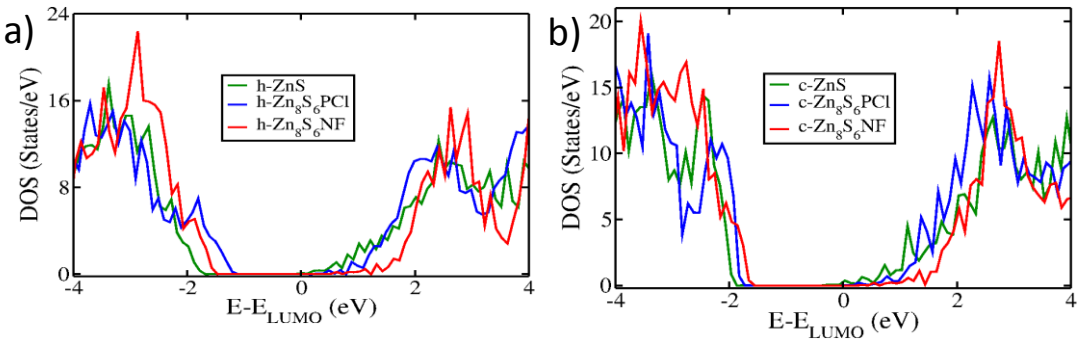


Figure 13. The density of states related to the P, Cl, and N, F substituted a) hexagonal ZnS, and b) cubic ZnS. Reproduced with Permission from ref. 15. Copyright 2015 Wiley-VCH Verlag GmbH & co. kGaA, Weinheim.

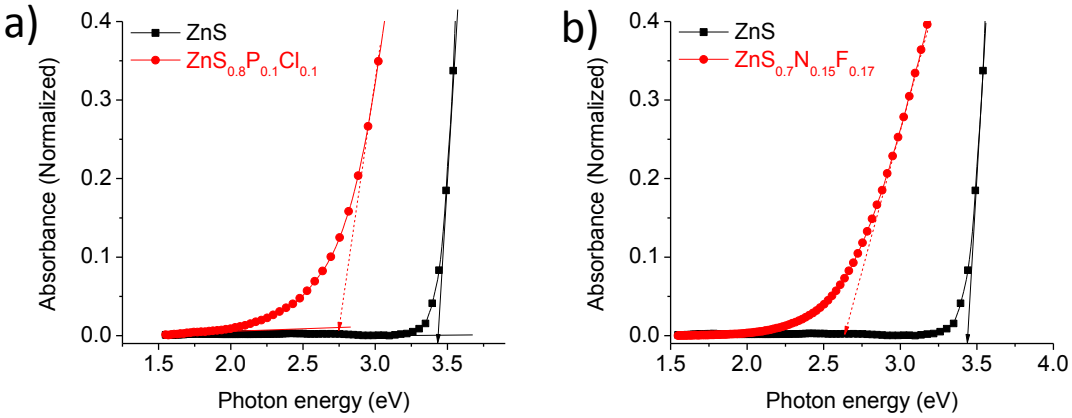


Figure 14. Absorption spectra of a) P, Cl substituted ZnS, and b) N, F substituted ZnS. Reproduced with Permission from ref. 15. Copyright 2015 Wiley-VCH Verlag GmbH & co. kGaA, Weinheim.

## 5. Conclusions

In summary, aliovalent anion substitution in metal oxides and sulfides brings about extraordinary changes in their electronic structure and photophysical properties. Co-substituion is enegetically more favored than the single anion substitution. Co-substitution of $N^{3-}$ and $F^{-}$ in ZnO and $TiO_2$ causes a significant shift in the absorption band resulting in visible-light absorption. In sulfides such as ZnS, substitution of $P^{3-}$ and $Cl^{-}$ brings about significant change in band gap and absorption spectra. It is

noteworthy that $N^{3-}$ and $P^{3-}$ form new states at the top of the valence bands in metal oxides and metal sulfides respectively. States related to $F^-$ and $Cl^-$ lies deep in the valence band, hence do not affect the absorption features. However, the presence of $F^-$ and $Cl^-$ makes doping of $N^{3-}$ and $P^{3-}$ energetically favorable. Compounds obtained by the complete substitution of $O^{2-}$ in ZnO and $TiO_2$ by $N^{3-}$ and $F^-$ have formula $Zn_2NF$ and TiNF and possess unique properties.

# 6. References


[1] a) A. Kaschner, U. Haboeck, M. Strassburg, M. Strassburg, G. Kaczmarczyk, A. Hoffmann, C. Thomsen, A. Zeuner, H. R. Alves, D. M. Hofmann, B. K. Meyer, *Appl. Phys. Lett.* **2002**, *80*, 1909-1911; b) N. Varghese, L. S. Panchakarla, M. Hanapi, A. Govindaraj, C. N. R. Rao, *Mater. Res. Bull.* **2007**, *42*, 2117-2124.

[2] a) H. Y. Xu, Y. C. Liu, R. Mu, C. L. Shao, Y. M. Lu, D. Z. Shen, X. W. Fan, *Appl. Phys. Lett.* **2005**, *86*, 123107; b) R. Gonzalez-Hernandez, A. I. Martinez, C. Falcony, A. A. Lopez, M. I. Pech-Canul, H. M. Hdz-Garcia, *Mater. Lett.* **2010**, *64*, 1493-1495.

[3] Z. Zhang, Z. Luo, Z. Yang, S. Zhang, Y. Zhang, Y. Zhou, X. Wang, X. Fu, *RSC Adv.* **2013**, *3*, 7215-7218.

[4] a) J. H. Pan, Z. Cai, Y. Yu, X. S. Zhao, *J. Mater. Chem.* **2011**, *21*, 11430-11438; b) J. Yu, Q. Xiang, J. Ran, S. Mann, *CrystEngComm* **2010**, *12*, 872-879.

[5] A. Sundaresan, C. N. R. Rao, *Nano Today* **2009**, *4*, 96-106.

[6] C. N. R. Rao, *J. Phys. Chem. Lett.* **2015**, *6*, 3303-3308.

[7] a) Q. Wang, C. Chen, W. Ma, H. Zhu, J. Zhao, *Chem. – Eur. J.* **2009**, *15*, 4765-4769; b) G. Liu, H. G. Yang, X. Wang, L. Cheng, J. Pan, G. Q. Lu, H.-M. Cheng, *J. Am. Chem. Soc.* **2009**, *131*, 12868-12869; c) D. Li, H. Haneda, S. Hishita, N. Ohashi, *Chem. Mater.* **2005**, *17*, 2596-2602.

[8] a) R. Saha, S. Revoju, V. I. Hegde, U. V. Waghmare, A. Sundaresan, C. N. R. Rao, *ChemPhysChem* **2013**, *14*, 2672-2677; b) N. Kumar, U. Maitra, V. I. Hegde, U. V. Waghmare, A. Sundaresan, C. N. R. Rao, *Inorg. Chem.* **2013**, *52*, 10512-10519.

[9] a) C. Wu, J. Jie, L. Wang, Y. Yu, Q. Peng, X. Zhang, J. Cai, H. Guo, D. Wu, Y. Jiang, *Nanotechnol.* **2010**, *21*, 505203; b) Y. Zeng, S. Li, R. Xie, Y. Huang, A. Lu, C. Y. Fong, X. Chen, H. Xing, D.-x. Yao, *Phys. Status Solidi B* **2018**, *255*, 1800294.

[10] S. Kouser, S. R. Lingampalli, P. Chithaiah, A. Roy, S. Saha, U. V. Waghmare, C. N. R. Rao, *Angew. Chem., International Edition* **2015**, *54*, 8149-8153.

[11] M. M. Ayyub, S. Prasad, S. R. Lingampalli, K. Manjunath, U. V. Waghmare, C. N. R. Rao, *ChemPhysChem* **2018**, *19*, 3410-3417.

[12] S. R. Lingampalli, C. N. R. Rao, *J. Mater. Chem. A* **2014**, *2*, 7702-7705.

[13] S. R. Lingampalli, K. Manjunath, S. Shenoy, U. V. Waghmare, C. N. R. Rao, *J. Am. Chem. Soc.* **2016**, *138*, 8228-8234.

[14] K. Manjunath, S. Prasad, U. V. Waghmare, C. N. R. Rao, *Dalton Trans.* **2018**, *47*, 9303-9309.

[15] S. Kouser, S. R. Lingampalli, P. Chithaiah, A. Roy, S. Saha, U. V. Waghmare, C. N. R. Rao, *Angew. Chem. Int. Ed.* **2015**, *54*, 8149-8153.

# Chapter 2

# Extraordinary Changes in the Electronic Structure and Properties of CdS by Aliovalent Anion Substitution


## Summary*

Unlike cation substitution, anion substitution in inorganic materials such as metal oxides and sulfides would be expected to bring about major changes in the electronic structure and properties. Experimentally, it has been possible to substitute P and Cl in hexagonal CdS and ZnS. The doping reduces the band gap significantly as predicted by theory. A similar decrease in the band gap is observed in N and F cosubstituted in cubic ZnS. Such anionic substitution helps to improve hydrogen evolution from CdS semiconductor structures and may give rise to other applications as well. We have carried out first-principles DFT calculations to determine the effects of substitution of P and Cl on the properties of CdS and ZnS in hexagonal and cubic structures and show that a sub-band of the trivalent phosphorus with strong bonding with the cation appears in the gap just above the valence band, causing a reduction in the gap and enhancement of dielectric properties.



A Paper Based on this work has appeared in Angew. Wandte Chemie. Int. Ed. (2015)

# 1. Introduction

Changes in the electronic structures and properties of materials brought about by the substitution of metal ions are comparatively less marked than the substitution of the anions. Substitution of anions brings more effective change in the electronic structures of materials related to its valance band. It has been reported that partial substitution of oxygen with nitrogen in ZnO and $TiO_2$ changes the optical properties of these oxide materials.[1] The problem with substitution of a single anion ($N^{3-}$ or $F^-$) is that it creates point defects such as oxygen vacancies and this can be avoided by the strategy of co-substitution of $N^{3-}$ and $F^-$ in the place of $O^{2-}$.[2] N, F co-substituted ZnO, and $TiO_2$ show absorption in the visible region due to a reduction in band gap and hence visible light induced photocatalysis.[3] Inspired by this knowledge we have explored the effects of anion substitution in metal sulfides. Among the metal chalcogenides, CdS is well explored due to its unique capability to absorb visible light and ease of synthesis. CdS posseses a band gap of 2.4 eV, and exhibit visible light induced photocatalysis. It also find use in solar cells, gas sensors and optoelectronic devices. We have carried out co-substitution of phosphorus and chlorine alone in the place of sulfur in CdS. Partial substitution of only phosphorus or chlorine in CdS creates defects in the CdS lattice, whereas co-doping of phosphorus and chlorine is expected to give a defect free products due to charge neutrality.

# 2. Scope of the Present Investigations

There have been reports on the isovalent cation and anion substitution in CdS, however, to the best of our knowledge there have been no reports on aliovalent anion substitution in CdS. In the present work we have synthesized the aliovalent substitututed CdS wherein partial amount of $S^{2-}$ is replaced by the $P^{3-}$ and $Cl^-$ ions. Electronic structure and properties of P, Cl substituted CdS has been investigated in detail using first-principles calculations. It is noteworthy that co-substituted CdS show a remarkable change in the electronic structure and properties.

Present work opens the door for the investigation of the synthesis and properties of various aliovalent anionic substituted metal chalcogenides.

## 3. Experimental Section

**Synthesis of CdS**

$Cd(CH_3COO)_2.2H_2O$ (1.33 g) was dissolved in distilled water ( 50 mL) to make 0.1 M solution. $Na_2S$ solution (0.1 M) was made separately by dissolving $Na_2S$ (0.39 g) in distilled water (50 mL). $Na_2S$ solution was added drop-wise to the $Cd(CH_3COO)_2$ solution under constant stirring. Formation of CdS was seen as the yellow coloration of the solution after the immediate addition of $Na_2S$ solution. This resulting yellow color solution was left for one hour under stirring. Solution was washed with distilled water and ethanol and centrifuged at 4000 rpm to remove soluble impurities. Product was dried at 80 ºC and collected.

**Preparation of Cl doped CdS**

CdS (1.87 mmol) and $NH_4Cl$ (0.187 mmol, 10 mol % of CdS) was ground for 15 minutes. Ground sample was kept in a ceramic boat and placed in a furnace under $N_2$ atmosphere under 0.5 h of purging at room temperature followed by ramping at the rate of 5˚/min to achieve the temperature 330 ˚C and furnace was fixed at this temperature for 4 h, finally temperature was lowered down to the room temperature. Sample was collected, and ground. To observe the effect of Cl concentration in CdS, 20 and 30 mol % of $NH_4Cl$ precursors was also treated in the similar condition.

**Preparation of P, Cl co-doped CdS**

CdS (2 mmol), red-P (2 mmol), and $NH_4Cl$ (1 mmol) was ground to get uniform mixture and converted in to a pellet. This pellet was taken in a boat and kept under a tube furnace and heated at 350 ºC for 2 hours in $N_2$ atmosphere. After the heating of 2 hours sample was allowed to cool to room temperature. This sample was again ground well and heated at 400 ºC for 1h in $N_2$ atmosphere. Finally product was allowed to come down to room temperature and used for characterizations.

**Characterization**

The X-ray diffraction patterns of the products were recorded with Bruker D8 Diffraction system using a Cu Kα source (λ = 0.154 nm). UV-Vis absorption spectra were taken with Perkin Elmer Model Lambda 750 spectrometer. For photocatalytic measurements 450 W Xe arc lamp (working at 400 W) (New Port, 6279NS, Ozone-free) was used. The $H_2$ evolved was quantified using gas chromatography (Perkin Elmer, Clarus 580 GC) equipped with TCD detector.

## 4. Results and Discussion

We first carried out first-principles density functional theoretical (DFT) calculations as implemented in the Quantum Espresso package[4] with interaction between ionic cores and valence electrons represented by means of ultrasoft pseudopotentials.[5] We have used two flavors of exchange correlation energy functionals: 1) generalized gradient approximation (GGA) of Perdew Burke–Ernzehof (PBE) and 2) local density approximation (LDA) of Perdew–Zunger (PZ) parameterized form, respectively.[6] A few calculations for estimation of band gap were carried out with a hybrid (HSE) functional, though it does not give very accurate estimates of band gaps. Crystalline CdS occurs in cubic (c-CdS) and hexagonal wurtzite (h-CdS) structures belonging to F43m (T2d) and P63mc (C4 6v) space groups, respectively, and the wurtzite phase is found to be more stable than c-CdS (DE=2 meV) in our calculations. Our estimates of the lattice constant obtained within GGA and LDA are within the typical DFT errors.[7] The electronic structures obtained within LDA and GGA are quite similar, and h-CdS exhibits a direct band gap of about 1.1 eV. Band gaps are typically underestimated in LDA or GGA-based DFT calculations. An improved estimate of band gap using HSE functionals is 2.35 eV, in agreement with experimental value of 2.3 eV.[8] From the projected density of states (PDOS), we find that the energy bands immediately below the gap are constituted of p-orbitals of S and valence bands deeper in energy (about -8.5 to -7.5 eV) arise from d-orbitals of Cd. Conduction bands (just above the gap) are primarily contributed by s-orbitals of Cd, while the bands around 2–3 eV arise from p-orbitals of Cd. Phonon spectrum of CdS confirms that the local structural stability of h-CdS.

We have considered three different kinds of anionic substitutions in h-CdS: 1) A, P substituted CdS (h-$CdS_{1-x}P_x$), 2) B, Cl substituted CdS (h-$CdS_{1-x}Cl_x$), and 3) A, B, with P, Cl co substituted CdS (h-$CdS_{1-x-y}P_xCl_y$). To correlate our results with experiment, we have considered a 2×1×1 periodic supercell containing 16 atoms: $Cd_8S_8$ with substitution of 1) one of the sulfur atoms with A amounting to 6.25%, 2) one of the sulfur atoms with B (6.25%), and 3) two of the sulfur atoms with A and B (12.5%). In the case of individual substitution of a p-type or a n-type atom at 6.25%, we have only one inequivalent configuration.[9] For co-substitution, there are many possible configurations corresponding to different of the ordering of A-and B-type atoms. We have employed the site occupancy disorder (SOD) technique which uses symmetry of the crystal to determine the inequivalent configurations.[9] We find three inequivalent configurations: A, B atoms present in different atomic planes and bonded to the same Cd atom (I), A, B atoms present in the same atomic plane and bonded to the same Cd atom (II) and A, B atoms bonded to different Cd atoms. From their energies, we find that the configuration with A and B atoms occupying sites bonding to the same Cd atom but present in different planes to be the most stable one. We first consider P and Cl for p-type and n-type doping, respectively. The change in the lattice parameters upon substitution with phosphorus and chlorine for sulfur is small (within about 1–2%). On the other hand, there are pronounced local structural distortions in the vicinity of the substitutional sites in the co-substituted CdS. The energetics of h-$Cd_8S_7P$, h-$Cd_8S_7Cl$, and h-$Cd_8S_6PCl$ reveal that cosubstitution with P and Cl is preferred over individual dopant substitutions with a lowering of energy by EC = -1.94 eV per (P, Cl) pair, where EC defines its relative stability

[Eq. (1)].

$$E_c = E_{h\text{-}CdS1\text{-}x\text{-}yAxBy} + E_{h\text{-}CdS} - E_{h\text{-}CdS1\text{-}xAx} - E_{h\text{-}CdS1\text{-}yBy}$$

Here, Eα (with α =h-$CdS_{1-x-y}A_xB_y$, h-CdS, h-$CdS_{1-x}A_x$ and h-$CdS_{1-y}B_y$) represents the total energy of the corresponding complex (**Table 1**). It is the relative energy of bulk CdS and cosubstituted CdS with respect to individually anion substituted CdS. For example, its negative value implies that co-substitution of P and Cl is energetically more favorable to P and Cl separately substituted in CdS. From bond valence analysis,

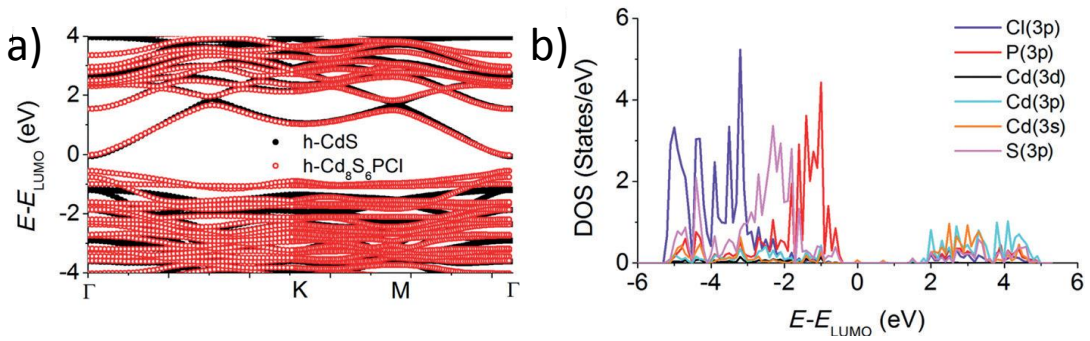


Figure 1. a) Electronic structure, and b) Projected density of states of h-$Cd_8S_6PCl$ clearly reveal an isolated band emerging from 3p orbital of P at the top of the valance band.

Table 1. Comparison of the energetics of different configurations of h-$Cd_8S_6PCl$

| Configuration (n) | $\Delta E=E_n-E_{stabl}$(eV) h-$Cd_8S_6PCl$ |
|---|---|
| I | 0 |
| II | 0.01 |
| III | 0.16 |

Cd-P and Cd-Cl bond lengths are 2.49 and 2.98 Å, respectively, in $Cd_8S_6PCl$. Notably, these are 3% shorter and 9% in $Cd_8S_6PCl$. Notably, these are 3% shorter and 9% longer, respectively, than the Cd-S bonds (2.57 Å) of bulk h-CdS, leading to a decrease in effective coordination number of Cd bonded with P and Cl in h-Cd8S6PCl to 3.31. These bond lengths are 4.2% shorter and 11.6% longer than average bond lengths of Cd-P (2.6 Å) and Cd-Cl (2.67 Å), respectively, in other Cd-P and Cd-Cl compounds reported in literature.[10]

The electronic structure of h-$Cd_8S_6PCl$ shows an isolated occupied band split from the rest of the valence bands (**Figure 1a**), leading to a drastic decrease in band gap ($\Delta Eg$= 0.58 eV, $E_g^{h\text{-}Cd_8S_6PCl}$ = 0.53 eV). To understand the nature of this isolated sub-band at the top of the valence band, we analyzed the density of electronic states of h-$Cd_8S_6PCl$ by projecting them onto atomic orbitals and compared with bulk h-CdS. In bulk h-CdS, the valence band is constituted primarily of p-orbitals of S with a little mixing of d-orbitals of Cd. The uppermost valence band is most affected by phosphorus 3p states emerging as a sub-band with a bandwidth of about 0.64 eV (**Figure 1b**) in the

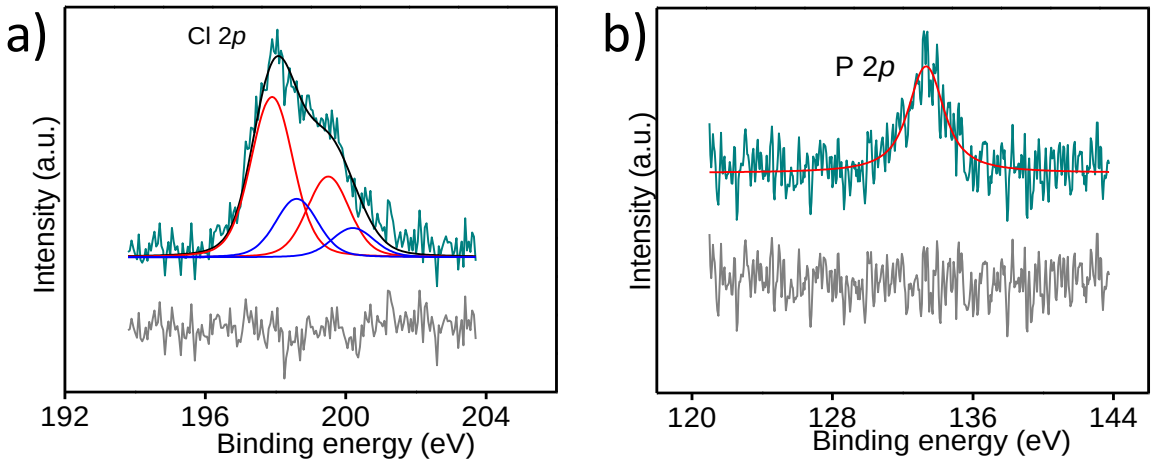


Figure 2. High-resolution XPS spectra of a) Cl 2p, and b) P 2p in P, Cl co-doped CdS sample.

gap. Analysis of the density of electronic states of h-$Cd_8S_7P$, h-$Cd_8S_7Cl$, and h-$Cd_8S_6PCl$ reveals that 1) 3p states of strongly electronegative Cl atoms are deep-lying in energy (about -5 to -2 eV) while those of the less electronegative P is concentrated at the top of the valence band, and 2) isolation of the sub-band of 3p states of P atom (in h-$CdS_{1-x-y}P_xCl_y$) from the rest of valence band becomes even more prominent on co-substitution with chlorine. The lowest energy conduction bands are essentially unaffected by P, Cl co-substitution and retain their Cd(3s) character.

We have been able to prepare CdS co-substituted with P and Cl by two methods. In the first method, CdS was treated with $Cd_3P_2$ and $NH_4Cl$ at 400ºC in a nitrogen atmosphere. In the second method, CdS was heated with red phosphorus and $NH_4Cl$ in two-steps. The resulting products show the presence of P and Cl as determined by X-ray photoelectron spectroscopy (XPS). We show typical core level P 2p (133.3 eV) and Cl 2p (198.2 eV) spectra of a sample prepared by method 1 in **Figure 2**. The Cl 2p signal can be deconvoluted to four peaks corresponding to 2p 3/2 and 2p 1/2 (corresponding to substituted and interstitial Cl) with a spacing of 1.6 eV. The composition of this sample obtained was $CdS_{0.7}P_{0.14}Cl_{0.15}$. After P, Cl co-substitution, CdS assumes a brown color, unlike pristine CdS which is yellow. The crystal structure of the undoped and doped CdS samples was hexagonal with unit cell parameters a=4.09 Å, c=6.67 Å, and a=4.12 Å, c=6.69 Å, respectively.

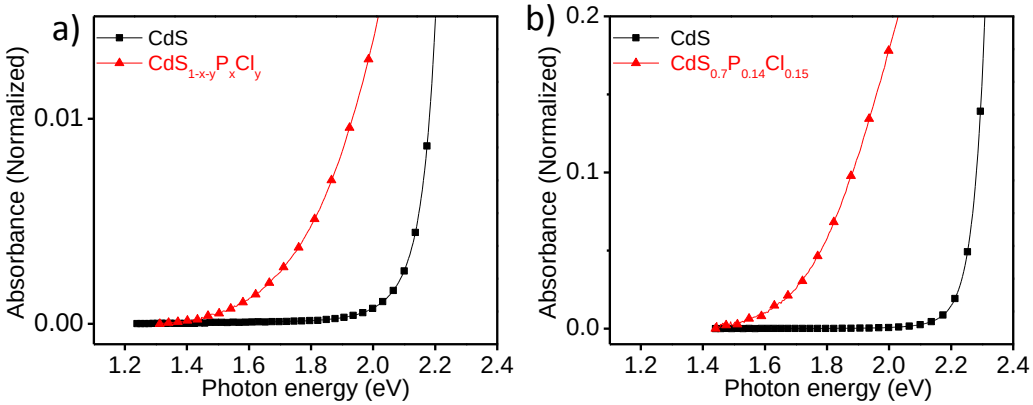


Figure 3. Comparison of UV-vis absorption spectra of pristine CdS and P, Cl co-doped CdS synthesized employing two different methodologies.

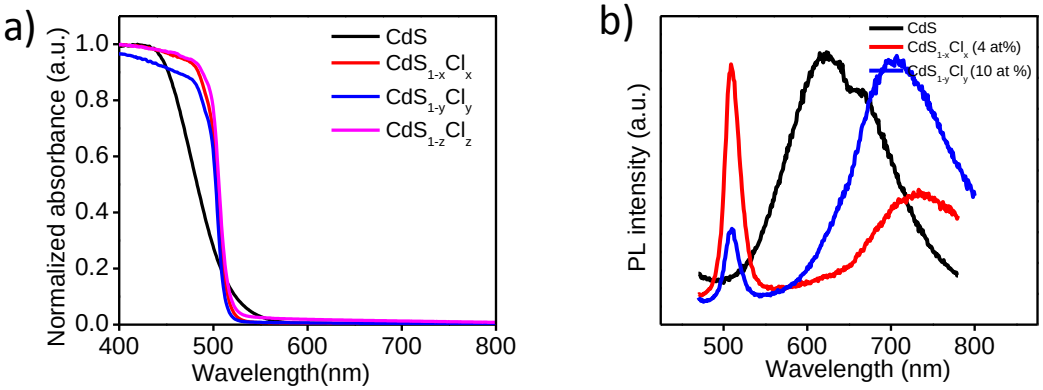


Figure 4. a) Absorption spectra, and b) photoluminescence spectra of pure and chlorine doped CdS samples.

The electronic absorption spectrum of the P, Cl co-substituted CdS shows an extension of the absorption band edge to longer wavelengths. In **Figure 3a** we compare typical absorption spectra of CdS and P, Cl co-substituted CdS. Pristine CdS shows a band gap of 2.3 eV whereas the P, Cl co-substituted CdS sample show the band gap of 1.8 eV. This significant decrease in the band gap agrees with the theoretical prediction (.0.5 eV). The sample of P, Cl co-substituted CdS prepared by the second method also had hexagonal structure (a=4.13 Å, c=6.71 Å). We show the electronic absorption spectrum of this sample with that of pristine CdS in **Figure 3b**. We clearly see a decrease in the band gap.

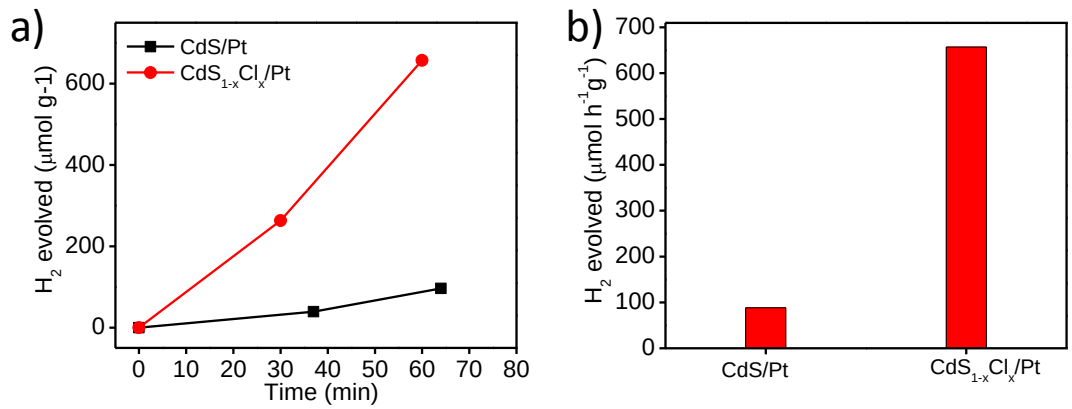


Figure 5. a) Time course of hydrogen evolution activity of pristine and Cl-substituted CdS, and b) Rate of hydrogen evolution reaction of pristine and chlorine substituted CdS samples.

We have also studied the effect of the isovalent substitution of $Cl^-$ in CdS **Figure 4a** shows the UV-visible absorption spectra of pristine CdS along with the 10, 20, and 30 mol % $NH_4Cl$ (used as a source of chloride ion) treated sample. As we can see $Cl^-$ doped samples did not exhibit any considerable change in the absorption edge of CdS which can be understood from electronic structures of these compound obtained by first-principles calculations indicating Cl-orbitals to be at the deep energy states in the valence band (**Figure 1**). Photoluminescence spectra of prisitine and Cl-doped CdS samples was collected at room temperature and 450 nm excitation wavelength (**Figure 4b**). CdS nanoparticles prepared in the absence of capping agents did not show any band edge emission and a broad emission peak related to surface trap state is present at 620 nm. However, Cl-substituted samples showed sharp emission peak corresponding to band edge emission which is sensative to Cl-concentration in samples. Occurance of band edge emission in Cl-substituted samples indicates avaliability of exciton pairs which was trapped in pristine CdS samples. Photochemical hydrogen evolution properties of pristine and Cl-substituted samples were investigated (**Figure 5**). Noteworthy to mention that Cl-substituted samples exhibited significantly higher HER activity than the pristine CdS due to the avaliability of photogenerated electrons which was trapped by the surface states in the case of pristine CdS.

## 5. Conclusions

Anionic co-substitution is energetically preferred over individual substitutions by more than 1.5 eV/atom, and P, Cl atoms preferentially occupy sites bonding to Cd in the lowest energy configuration. The reduction in band gap in P, Cl co-substituted CdS arises from the emergence of an isolated sub-band at the top of the valence band which is primarily contributed by the less electronegative trivalent anion like. Band of the more electronegative Cl anion lie deep in an energy well below the valence band. Changes in the electronic band gap are predicted to be more pronounced in the hexagonal crystal structure for P, and Cl co substituted CdS. Effects of anionic co-substitution on the electronic structure are sensitive to the crystal structure as well as to the dopants. We have been able to prepare P, Cl co-substituted CdS in hexagonal structures and characterized it adequately. They both show a marked decrease in band gaps, close to the shifts predicted by theory. We believe that properties of P, Cl co-substituted CdS may be useful in many applications.

# 6. References


[1] a) H. Qin, W. Li, Y. Xia, T. He, *ACS Appl. Mater. Interfaces* **2011**, *3*, 3152-3156; b) Z. Zhang, Z. Luo, Z. Yang, S. Zhang, Y. Zhang, Y. Zhou, X. Wang, X. Fu, *RSC Adv.* **2013**, *3*, 7215-7218.

[2] R. Saha, S. Revoju, V. I. Hegde, U. V. Waghmare, A. Sundaresan, C. N. R. Rao, *ChemPhysChem* **2013**, *14*, 2672-2677.

[3] a) S. R. Lingampalli, C. N. R. Rao, *J. Mater. Chem. A* **2014**, *2*, 7702-7705; b) N. Kumar, U. Maitra, V. I. Hegde, U. V. Waghmare, A. Sundaresan, C. N. R. Rao, *Inorg. Chem.* **2013**, *52*, 10512-10519.

[4] P. Giannozzi, S. Baroni, N. Bonini, M. Calandra, R. Car, C. Cavazzoni, D. Ceresoli, G. L. Chiarotti, M. Cococcioni, I. Dabo, A. Dal Corso, S. de Gironcoli, S. Fabris, G. Fratesi, R. Gebauer, U. Gerstmann, C. Gougoussis, A. Kokalj, M. Lazzeri, L. Martin-Samos, N. Marzari, F. Mauri, R. Mazzarello, S. Paolini, A. Pasquarello, L. Paulatto, C. Sbraccia, S. Scandolo, G. Sclauzero, A. P. Seitsonen, A. Smogunov, P. Umari, R. M. Wentzcovitch, *J. Phys. Condens. Matter* **2009**, *21*, 395502.

[5] D. Vanderbilt, *Phys. Rev. B* **1990**, *41*, 7892-7895.

[6] J. P. Perdew, A. Zunger, *Phys. Rev. B* **1981**, *23*, 5048-5079.

[7] S.-H. Wei, S. B. Zhang, *Phys. Rev. B* **2000**, *62*, 6944-6947.

[8] L. A. Silva, S. Y. Ryu, J. Choi, W. Choi, M. R. Hoffmann, *J. Phys. Chem. C* **2008**, *112*, 12069-12073.

[9] R. Grau-Crespo, S. Hamad, C. R. A. Catlow, N. H. d. Leeuw, *J. Phys. Condens. Matter* **2007**, *19*, 256201.

[10] M. S. Bharara, C. H. Kim, S. Parkin, D. A. Atwood, *Polyhedron* **2005**, *24*, 865-871.

# Chapter 3

## Electronic Structures and Properties of $Cd_4P_2Cl_3$, $Cd_4As_2Br_3$, and $Cd_4Sb_2I_3$ : Analogues of CdS, CdSe, and CdTe


**Summary***

Substitution of aliovalent anions in metal oxides and chalcogenides significantly affects the electronic structure and properties of the materials. Thus, substitution of $P^{3-}$ and $Cl^-$ in CdS decreases the band gap and favorably influences the photocatalytic activity. Complete substitution of a trivalent ($A^{3-}$) and a monovalent ($B^-$) anions in a cadmium chalcogenides, CdX, should give rise to a material of the composition $CdA_{0.5}B_{0.5}$ or $Cd_2AB$, but a compound with the composition $Cd_4A_2B_3$ (or $Cd_2AB_{1.5}$) is obtained experimentally. We have investigated the structure and properties of $Cd_4P_2Cl_3$, $Cd_4As_2Br_3$ and $Cd_4Sb_2I_3$.

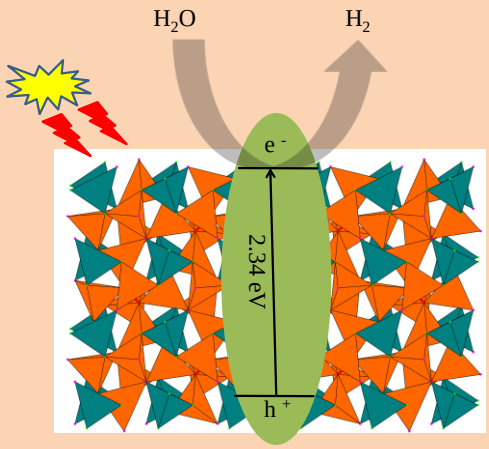


All the three compounds crystallize in the cubic structure, where two kinds of cadmium atoms are bound differently with the anions in the crystals. These compounds are direct gap semiconductor with band gaps of 2.3, 1.9 and 1.8 eV in the case of $Cd_4P_2Cl_3$, $Cd_4As_2Br_3$ and $Cd_4Sb_2I_3$ respectively. These band gaps are comparable to the gaps of their analogues CdS, CdSe, and CdTe respectively. All the compounds exhibit a photoluminescence band in the visible-region. First-principles calculations suggest appropriate alingment of conduction band postions of all the three compounds with respect to the water redox potential a prerequisite to perform HER. $Cd_4P_2Cl_3$ exhibits much superior HER activity than the other two compounds. $Cd_4As_2Br_3$ exhibits superior activity than $Cd_4Sb_2I_3$ as predicted by theory. Hydrogen evolution in the absence of any sacrificial agent and the absence of photocorrosion seems to be unique features of $Cd_4P_2Cl_3$.



A Paper Based on this work has appeared in J. Phys. Chem. C (2017) and Solid State Commun. (2017).

# 1. Introduction

CdS is one of the most explored metal sulfide semiconductors due to its unique optical and electronic properties.[1] Visible-light-harvesting ability and photoluminescence in the visible region makes it useful in light emitting diodes, solar cells, and other devices.[2] CdS has received attention in solar water splitting to produce molecular hydrogen, because of the favorable conduction and valence band positions with respect to the water redox potential.[3] Metal sulfides including CdS suffer from the problem of photocorrosion wherein $S^{2-}$ ions get oxidized by the photo-generated holes, resulting in the elution of $Cd^{2+}$ and hence metal sulfide cannot produce hydrogen from water without a sacrificial agent.[4] A possible strategy to overcome the photocorrosion problem of metal sulfides, is to make use of valence band engineering by anion substitution.[5] Substitution of aliovalent anions in metal oxides and sulfides brings about marked changes in the electronic structures and properties, unlike substitution of isovalent anion.[5-6] Thus, substitution of $P^{3-}$ and $Cl^-$ in place of the $S^{2-}$ ions in CdS causes a change in the electronic properties along with a significant decrease in the band gap.[5a] Such changes are not brought about by substitution of $S^{2-}$ ions by $Se^{2-}$ ions.[7] Substitution of $S^{2-}$ by either $P^{3-}$ or $Cl^-$ alone also affects optoelectronic properties of CdS but is accompanied by creation of defects.[2a, 8] Anionic substitution in CdSe has been reported.[9] Co-doping of arsenic and chlorine in CdTe is known to modulate its photovoltaic efficiencies.[10] Doping of Sb on the performance of the CdTe solar cells has also been examined.[11] Doping of iodine in CdTe has also been reported.[12] In all these cases the dopant concentration varies in the range of 2-15 %. To the best of our knowledge it has not been able to prepare compounds of compositions $Cd_2PCl$, $Cd_2AsBr$, and $Cd_2SbI$ by the complete substitution of $S^{2-}$, $Se^{2-}$, and $Te^{2-}$ in CdS, CdSe, and CdTe by the corresponding aliovalent anions respectively. However, compounds of the compositions $Cd_4P_2Cl_3$, $Cd_4As_2Br_3$, and $Cd_4Sb_2I_3$ are reported in a US patent. Crystal structures of these compounds have been reported, but little is known about their electronic structures and properties.[13]

In this chapter, we report the electronic structures and properties of $Cd_4P_2Cl_3$, $Cd_4As_2Br_3$ and $Cd_4Sb_2I_3$ which crystallize in the cubic structure with the space group

Pa-3. These compounds are direct band gap semiconductors with band gap in the range of 2.3 to 1.8 eV and exhibit photoluminescence band in the visible region. First-principles calculations have been carried out to understand the structural features and electronic structure of these compounds. First-principles calculations indicate that the band positions of these compounds are suitable with respect to water redox potential, for the generation of molecular hydrogen by photocatalytic water splitting. We have examined the photochemical hydrogen evolution activities (HER) of these compounds experimentally. Among all $Cd_4P_2Cl_3$ is an effective and stable photocatalyst. $Cd_4P_2Cl_3$ produces hydrogen from water in the absence of sacrificial agents unlike its analogue CdS which requires sacrificial agents to perform HER. Use of sacrificial agents is economically and environmentally not favorable and to the best of our knowledge, this is the first report of photochemical hydrogen generation by these semiconductors with and without the use of a sacrificial agent.[14] Both $Cd_4As_2Br_3$ and $Cd_4Sb_2I_3$ are also capable of producing hydrogen under visible-light irradiation. HER activity and photochemical stability of $Cd_4P_2Cl_3$ is superior to that of $Cd_4As_2Br_3$ and $Cd_4Sb_2I_3$.

## 2. Scope of the Present Investigations

Substitution of the cation alters the conduction band properties whereas substitution of anion alters the valence band properties in the inorganic semiconductor compounds. Anion substitution in inorganic materials known to have a great impact on the electronic structure and properties. There have been reports on the study of electronic and optoelectronic of the isovalent substituted CdS, wherein $S^{2-}$ is being substituted by $P^{3-}$ or $Cl^-$. Effect of aliovalent substitution of $P^{3-}$ and $Cl^-$ in the place of $S^{2-}$ in CdS and ZnS has also been reported in recent years. However, complete substitution of $X^{2-}$ by $P^{3-}$ and $Cl^-$ in metal chalcogenides have not been achieved till date. Present work explores the synthesis, electronic structure and properties of the compounds of composition $Cd_4P_2Cl_3$, $Cd_4As_2Br_3$ and $Cd_4Sb_2I_3$ which can be considered as analogous of CdS, CdSe and CdTe respectively and would obtain by the complete substituion of $S^{2-}$, $Se^{2-}$, and $Te^{2-}$ in these compounds. Since all the ternary compounds reported here exhibit visible-light absorption, it would be interesting to explore the applications of these materials in the photovoltaics and other semiconductor based devices.

# 3. Experimental Section

## Materials

Cd-powder (99.5 % metal basis), $CdCl_2$ (99.9 % trace metal basis), and $H_2PtCl_6.6H_2O$ (37.5 % metal basis) was purchased from sigma Aldrich, P-red was purchased from spectrochem (97-98 % assay), $NH_4Cl$ (AR grade, 99.5%), $Cd(CH_3COO)_2.2H_2O$ (SD Fine Chem Ltd, India, 99.0 %), $Na_2S.xH_2O$ (SD Fine Chem Ltd, India, 55-60 %), NaOH (SD Fine Chem Ltd, India, 85.5 %), $Na_2SO_3$ (SD Fine Chem Ltd, India, 97 %), De-ionized water was used for the experiments.

## Synthesis

$Cd_4P_2Cl_3$ was prepared by three different methods. In method 1, $Cd_4P_2Cl_3$ ($Cd_4P_2Cl_3$-1) was synthesized by heating $Cd_3P_2$ and $CdCl_2$ in a sealed ampoule. Pure $Cd_3P_2$ was first prepared. A mixture of $Cd_3P_2$ and $CdCl_2$ (1:1 mole ratio) was ground inside a glove box for 30 min. The homogeneous mixture was sealed inside a quartz ampoule in vacuum and heated at 500 ˚C for 20 h, with the ramp rate of 2.3˚/min and allowed to cool down at the same rate. Along with yellow polycrystalline powder product, we obtained needle shaped crystals at the cooler end of the ampoule (yield; 83%). In method 2, a mixture of $Cd_3P_2$, $CdCl_2$ and $NH_4Cl$ (1:1:1 mole ratio) was ground inside a glove-box for 30 min, the mixture was sealed in a quartz ampoule under vacuum and heated in a muffle furnace at 500 ˚C for 20 h (yield 85%). In method 3, a mixture of Cd-powder, red-P, and $NH_4Cl$ (mole ratio of 2:1:1.5) was ground inside a glove box for 30 min. The mixture was sealed in a quartz ampoule under vacuum and heated in a muffle furnace at 500 ˚C for 72 h, with the ramp rate of 2.3˚/min and allowed to cool down with the same rate (yield; 82%). CdS was synthesized under similar condition by solid state reaction. In a typical synthesis 1:1 mole ratio of $Cd(CH_3COO)_2$. $2H_2O$ and $CS(NH_2)_2$ was ground for 15 min. This homogenous mixture was heated under $N_2$ atmosphere at 500 ˚C for 4 h inside a tube furnace. In order to prepare $Cd_4P_2Cl_3$/Pt and CdS/Pt, Pt deposition was carried out by the reported literature where an aqueous solution of $H_2PtCl_6$ was used as a precursor of Pt.[15] In a typical synthesis 1 wt% of Pt was photodeposited on the photocatalyst in 1 M NaOH solution under UV-Visible irradiation for 1.5 h.

$Cd_4As_2Br_3$ was synthesized by a procedure different from that reported elsewhere.[16] In a typical synthesis, a mixture of Cd, As, and $CdI_2$ in the molar ratio of 2.5:2:1.5 was ground inside a glove-box for 20 min, and the homogenous mixture was taken in a quartz tube which was evacuated and sealed in vacuum ($2x10^{-5}$ mbar). The quartz tube was placed in a muffle furnace and heated at 550 °C for 12 h with a ramp rate of 2.3°/min, and allowed to cool to room temperature at the same rate. Along with dark red crystalline powder, we obtained shiny crystals at the cooler end of the tube. $Cd_4Sb_2I_3$ was prepared by a similar procedure.[17] In a typical synthesis, a mixture of Cd, Sb and $CdI_2$ in the molar ratio of 2.5:2:1.5 was ground inside the glove box and the mixture taken in a quartz tube was evacuated and heated at 480 °C for 12 h. Deposition of Pt on $Cd_4As_2Br_3$ and $Cd_4Sb_2I_3$ was done using a modified method reported elsewhere, wherein an aqueous solution of $H_2PtCl_6$ (1 wt %) was used as a Pt precursor under the UV-light irradiation for 1.5 h.[15]

**Characterization**

X-ray diffraction (XRD) patterns were recorded with a Bruker D8 Diffraction system using a Cu Kα source (λ = 0.1541 nm). Single crystal XRD data were collected at room temperature on a Bruker Smart diffractometer equipped with a normal focus 2.4 kW sealed tube X-ray source with graphite monochromatized Mo Kα radiation (λ = 0.710 Å) operating at 50 kV and 30 mA in ω scan mode. UV-Vis absorption spectra were collected with Perkin Elmer Model Lambda 900 spectrometer. Photoluminescence spectra were collected by Horiba JobinYvon spectrometer (iHR 320). Solid state $^{31}P$ magic angle spinning NMR spectrum was collected with a Bruker AVANCE 400 MHz spectrometer. Raman spectra were collected using a 514.5 nm Ar+laser with a HORIBA LabRam HR800 spectrometer.

**Photocatalytic Experiments**

Photocatalytic $H_2$ evolution measurements were carried out by dispersing 20 mg of the semiconductor photocatalyst in 75 mL of water containing 0.18 M $Na_2S$ and 0. 24 M $Na_2SO_3$ in a 135 mL glass cell. A Xe arc lamp (New Port, 6279NS ozone-free, working at 400 watt) with a 395 nm cut-off filter was used to obtain light of wavelength λ> 395 nm. The amount of $H_2$ evolved was measured by gas

chromatography (Perkin Elmer, Clarus 580) equipped with TCD. Apparent quantum yields (AQY) were estimated by the formula, AQY (%) = (2R/I) *100 where, R is the rate of evolution of hydrogen per second and I is the rate of incident photon per second. The photon flux ($6.3*10^{17}$ photons/s) was measured using an irradiance meter.

**Computational Details**

For bulk $Cd_4P_2Cl_3$ we used the Quantum Espresso package for first-principles calculations based on Density functional theory (DFT) to determine electronic structure and stability of $Cd_4P_2Cl_3$.[18]Scalar relativistic Vanderbilt ultra-soft pseudopotentials and a gradient corrected exchange-correlation energy functional of Perdew-Burke-Ernzerhof (PBE) were employed in these calculations.[19] Valence electrons of Cd, P and Cl in $4d^{10}\ 5s^2$, $3s^23p^3$ and $3s^23p^5$ configurations respectively were simulated using pseudopotentials. $Cd_4P_2Cl_3$ crystallizes in the cubic structure containing 72 atoms, with symmetry of the space group 205 (Pa-3) [with unit cell parameter of 12.13 Å]. Plane wave basis representing the wavefunctions was truncated with an energy cutoff of 50 Ry and that representing charge density with a cut off of 400 Ry. A uniform mesh of 4X4X4 of k points was used to sample integrations over the Brilloiun zone. Structure was relaxed through minimization of energy until the Hellman-Feynman forces on each of the atoms was 0.01 eV/°A or less, and the stresses within 1 kbar. The difference in the theoretical estimates of band gap and its experimental value is typically due to the approximation used in the calculations. DFT-GGA gives underestimation of band gap up to 40%. Such underestimation of the band gap by GGA is due to the existence of a discontinuity in the derivative of energy with respect to number of electron.[20] On the other hand, HSE uses error function screened Coloumb potential to treat the exact exchange portion of the energy[21] and hence gaps obtained from HSE calculation are typically higher than the GGA ones and are closer to experiment. Hence, Heyd-Scuseria-Ernzerhof (HSE-06) hybrid functional was used to obtain more accurate estimates of the gap. We used Vienna ab-initio simulation package (VASP) with projector augmented wave method (PAW)[22] for these calculations based on a generalized gradient approximation (GGA)-based energy functional of Perdew, Burke, and Erzenhoff (PBE).[18b, 19b] The structure was optimized to minimize energy using conjugate-gradients algorithm.

For bulk $Cd_4As_2Br_3$ and $Cd_4Sb_2I_3$ First-principles calculations based on density functional theory (DFT) have been performed using Quantum Espresso treating exchange correlation energy within a Generalized Gradient approximation parameterized by Perdew Burke Ernzerhof (PBE) ultrasoft pseudopotentials We used the periodic unit cell in calculations of the electronic structure. We considered valence electrons with configurations $4d^{10}5s^2$, $4s^24p^3$, $4s^24p^5$, $5s^25p^3$, and $5s^25p^5$ of Cd, As, Br, Sb and I respectively. The kinetic energy cut off of 55 Ry is used to truncate the plane wave basis. Uniform mesh of 4x4x4 k-points is used for sampling integration of the Brillouin Zone. The structure has been relaxed to minimize energy until the Hellmann-Feynmann forces on each atom are less than 0.02 eV/Å. To achieve convergence of self-consistency in the Kohn-Sham solution, we used a tolerance criterion of $10^{-6}$ eV.

# 4. Results and Discussion

## 4.1 Structure and Properties of $Cd_4P_2Cl_3$

In **Figure 1a**, we show powder X-ray diffraction patterns of CdS and as prepared $Cd_4P_2Cl_3$ compounds by different routes. The PXRD patterns of all the $Cd_4P_2Cl_3$ samples are identical and could be indexed in the cubic structure with a space group; Pa-3 (a = 12.13). The sharp diffraction peaks suggest the highly crystalline nature of $Cd_4P_2Cl_3$ compounds. The experimental PXRD pattern match well with that simulated from single crystal X-ray diffraction data (**Figure 1b**). The crystallite size of $Cd_4P_2Cl_3$ was generally around 70 nm. Our single crystal study gave a structure (**Figure 2**) identical to that reported in the literature. [15, 16] Essentials of the structure of $Cd_4P_2Cl_3$

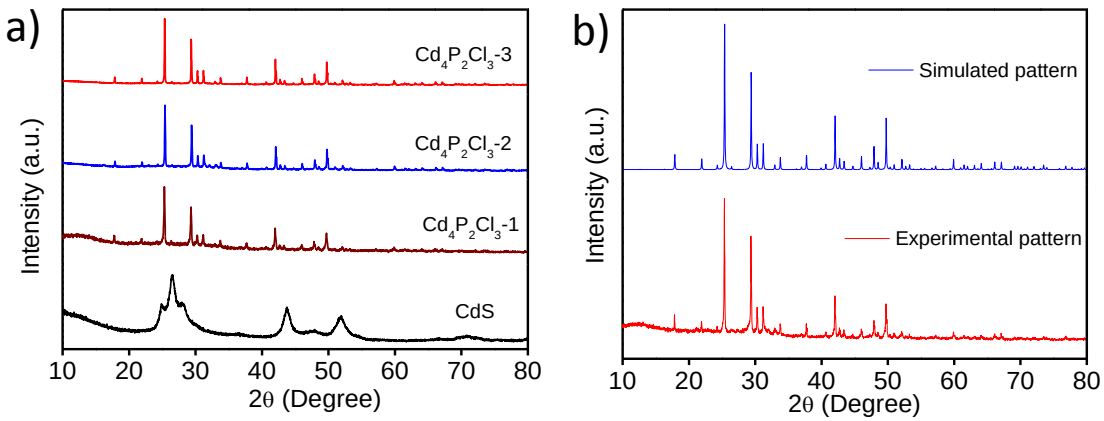


Figure 1. a) PXRD patterns of $Cd_4P_2Cl_3$ samples prepared by different methods, and b) Comparison of experimental and simulated XRD patterns of $Cd_4P_2Cl_3$.

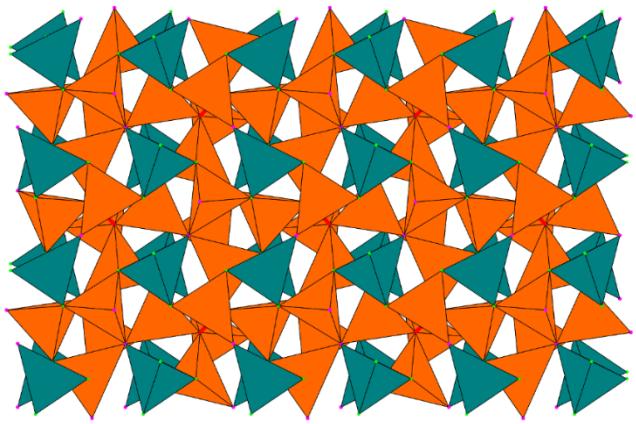

Figure 2. Structure of $Cd_4P_2Cl_3$-1 showing different polyhedra (orange $CdP_2Cl_2$ and blue $CdPCl_3$).

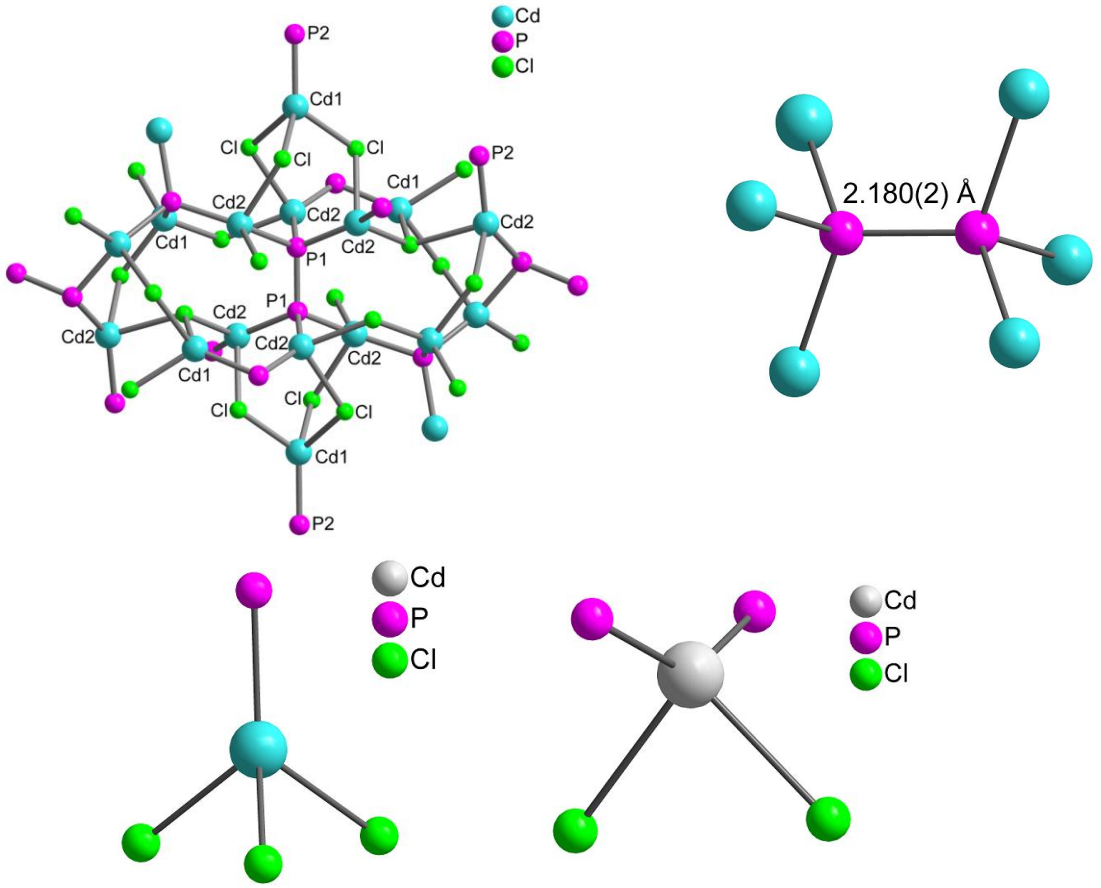


Figure 3. Representation of bonding in $Cd_4P_2Cl_3$ compound using ball-stick model.

are as follows. The Cd atoms are distorted face centered cubic (fcc) packed with octahedral and tetrahedral interstices.[13a] The arrangement of P and Cl atoms bestows a tetrahedral coordination to the Cd atoms, wherein Cd (1) is coordinated by one P and three Cl, and Cd (2) is coordinated by two P and two Cl atoms. The P (1) atoms form P-P pairs ($d_{p-p}$ = 2.18 Å), and involved in $[P_2Cd_6]$ octahedra, whereas the P (2) atoms form $[PCd_4]$ tetrahedron. These two polyhedra form the 3-D structure of $Cd_4P_2Cl_3$ (**Figure 3**).

The presence of two different types of P atoms in $Cd_4P_2Cl_3$ was further confirmed by $^{31}P$ solid state NMR. $^{31}P$ solid state NMR spectra of $Cd_4P_2Cl_3$ collected at 162.01 MHz shows the presence of two $^{31}P$ signals corresponding to P-P bonded and non- bonded P atoms (**Figure 4a**).

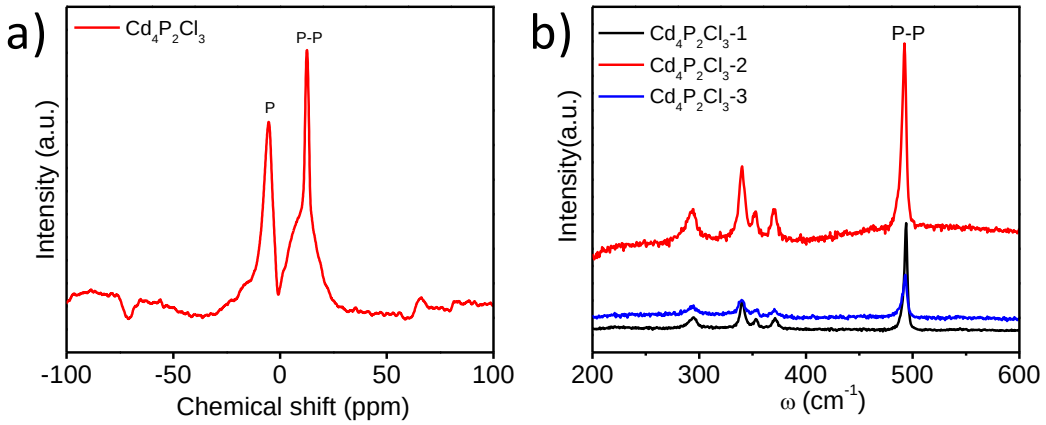


Figure 4. a) $^{31}P$ NMR spectra of $Cd_4P_2Cl_3$, and b) Raman spectra of $Cd_4P_2Cl_3$ compounds prepared by different method.

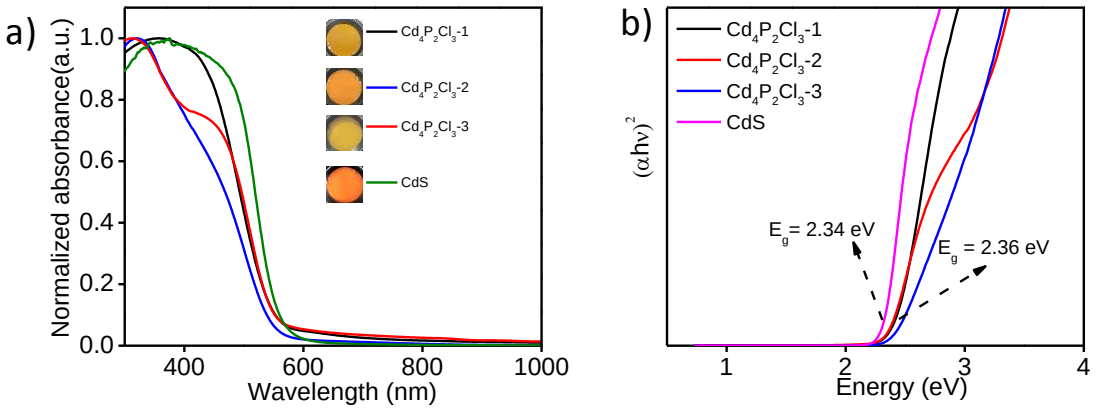


Figure 5. a) UV-Vis absorption spectra, and b) Tauc plot of, CdS and $Cd_4P_2Cl_3$ compounds.

We have characterized $Cd_4P_2Cl_3$ using Raman spectral studies (**Figure 4b**). The band at 493 $cm^{-1}$ is due to P-P bond whereas bands at 353, 371 and 294, 340 $cm^{-1}$ are likely to be due to two different Cd-P and Cd-Cl bonds respectively described in the crystal structure discussion.[23]

UV-Visible diffuse reflectance spectrum of $Cd_4P_2Cl_3$ is shown in **Figure 5a**. $Cd_4P_2Cl_3$ exhibits a semiconductor-like characteristic absorption in the visible region similar to CdS. It has a direct band gap of 2.36 eV as obtained by the Kubelka-Munk method. This band gap is comparable to that of CdS (2.34 eV) (**Figure 5b**).

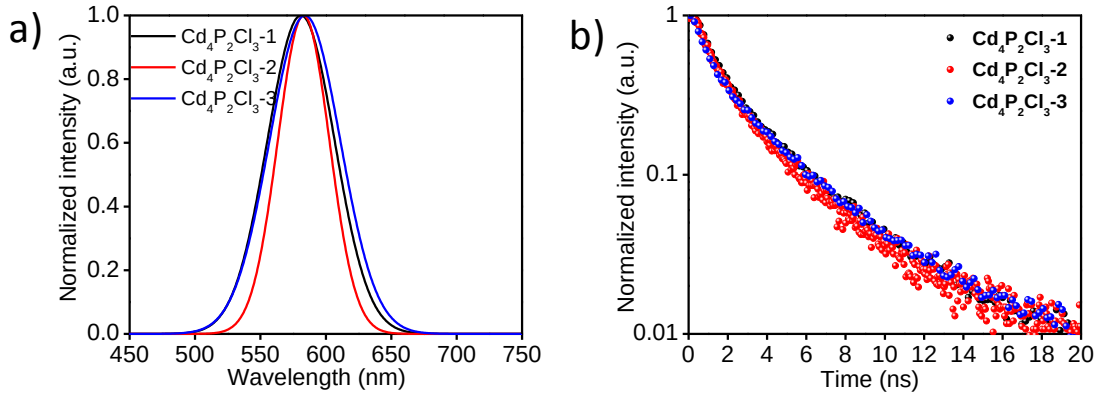


Figure 6. a) Steady state PL spectra of $Cd_4P_2Cl_3$ samples, and b) time- resolved PL spectra of $Cd_4P_2Cl_3$ samples.

The photoluminescence spectrum of all the $Cd_4P_2Cl_3$ samples collected at 400 nm excitation (**Figure 6a**) show a band at the 580 nm originating from the recombination of electrons and holes generated by band edge excitation. Note that CdS exhibits a photoluminescence band close to 510 nm.[24] The life time of charge carriers decides their probability of involvement in photocatalytic reactions before their recombination with a longer life time suggesting a greater probability of involvement of charge carriers in photocatalytic reaction.[25] In order to find out the lifetime of photogenerated charge carriers in $Cd_4P_2Cl_3$ compounds, we recorded the time-resolved photoluminescence spectra (**Figure 6b**). $Cd_4P_2Cl_3$ samples prepared by different methods exhibit almost identical life times. The life time is found to be 3 ns which is higher than that of bulk CdS.

**Theoritical Results**

We have examined the electronic structure of $Cd_4P_2Cl_3$ along the path Γ-X-M-Γ-R-X (**Figure 7a**) in the Brillouin Zone, by employing GGA based calculations. The calculations reveal a band gap of 0.61 eV, which is an underestimate, as this is typical of DFT-based calculations. In order to understand the orbital character of the bands, we have analyzed the density of states by projecting them onto the atomic orbitals. The valence band is constituted primarily of P 3p-orbitals with some mixing with Cd 5s-orbitals, while the lowest energy conduction band has a predominant character of P 3p-orbitals (**Figure 7b**). The P atoms contributing the 3p-orbitals to the valence band

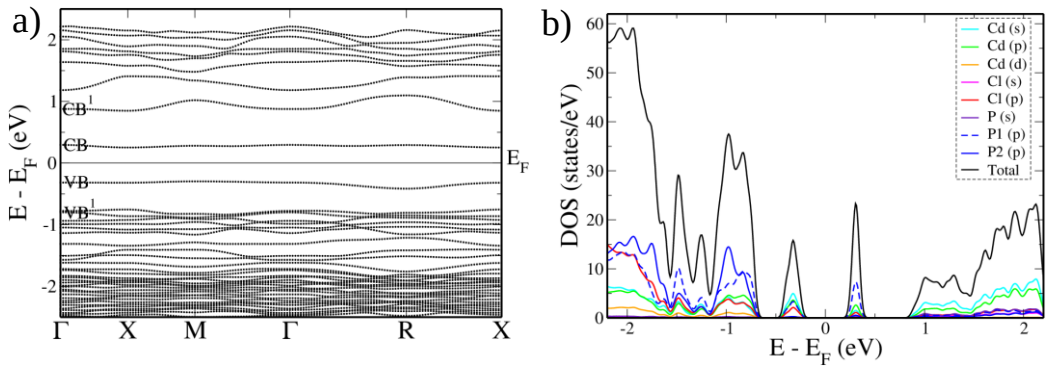


Figure 7. a) Electronic structure, and b) Density of electronic states of, $Cd_4P_2Cl_3$ obtained by GGA based calculations. The energy is shifted with respect to Fermi energy which is set to zero.

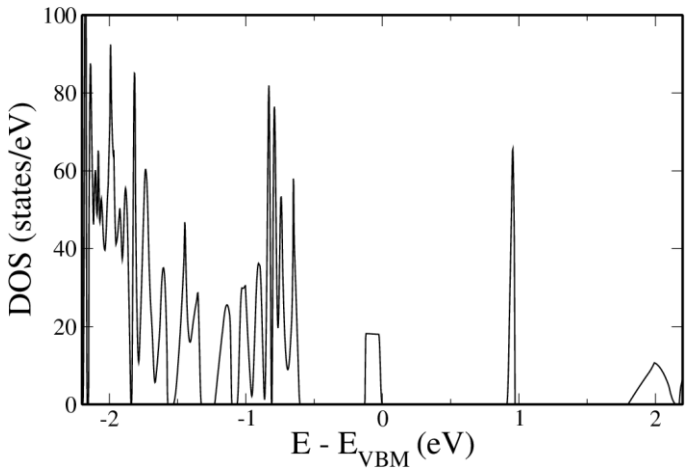


Figure 8. The density of state of $Cd_4P_2Cl_3$ obtained using VASP calculations based on the HSE functional. The energies are shifted with respect to the valence band maximum which is set to zero.

possess a $3^-$ charge (denoted as P2 in the **Figure 7b**) and the ones contributing to the conduction band are the ones with $2^-$ charge (denoted as P1 in the **Figure 7b**), forming P-P bonds (with bond length of ~2.1 Å), connected to the cadmium atom coordinated to two other Cl atoms. To overcome the under estimation of the band gap in the calculations, we have used the HSE functional as implemented in VASP. From the total density of states, we note that the band gap is 0.91 eV (**Figure 8**). However, this is not the gap relevant to optical absorption. Visualization of the wavefunctions of states at the Γ-point and of the energy around the Fermi level (**Figure 9**) shows that

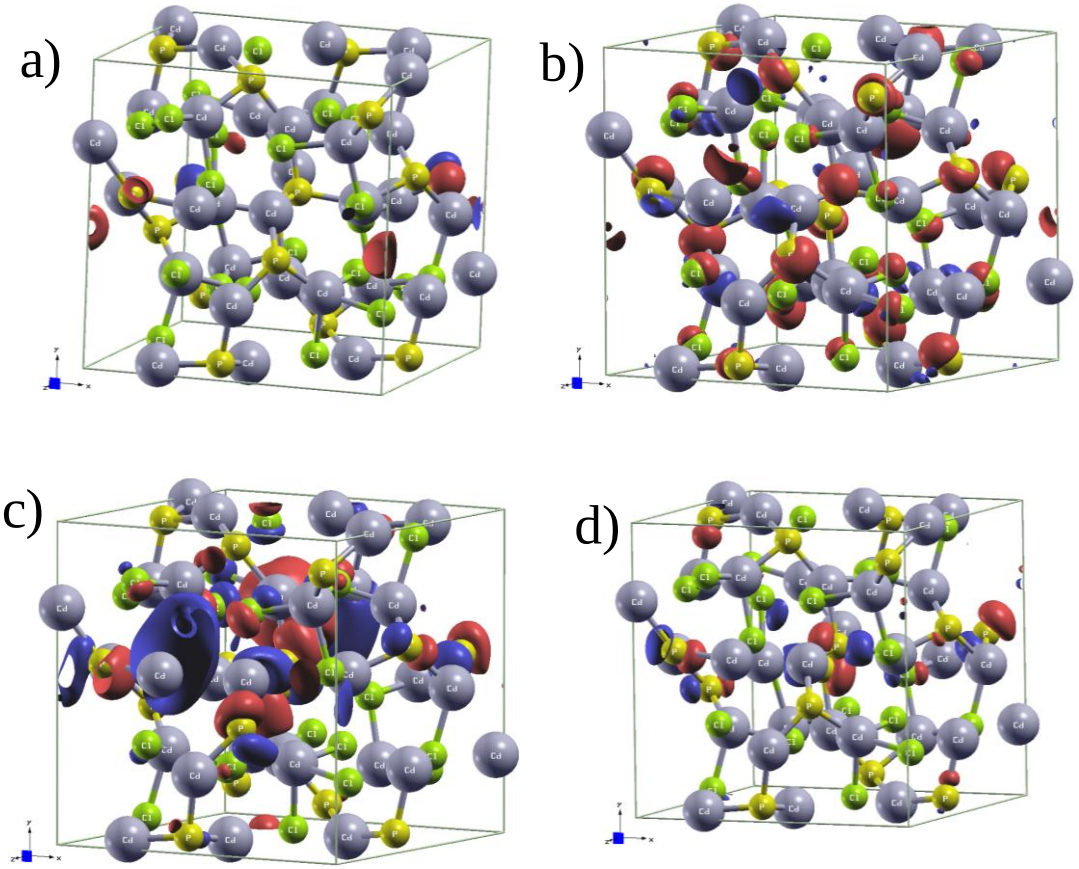


Figure 9. Visualization of the wavefunctions of states at the Γ point of a) CB, b) $CB^1$, c) VB, and d) $VB^1$ (Color code: grey-Cd, Yellow-P, and Green-Cl).

$VB^1$ (penultimate valence band) and VB (topmost valence band) have major contributions from the 3p-orbitals of phosphorus, resulting in odd parity. The conduction band (CB, lowest energy conduction band) has contributions from the phosphorus 3p-orbitals and is odd under inversion Hence, a dipole-mediated transition from VB to CB is forbidden. $CB^1$ (second higher energy conduction band) has contributions mainly from the s-orbitals of Cd, resulting in even parity. Thus, a transition from VB to $CB^1$ is an allowed transition according to the dipole selection rule. Thus, the optical band gap in the GGA-based electronic structure is 1.19 eV, while it is 1.8 eV in the electronic structure obtained with the HSE functional, which is closer to the observed experimental band gap.

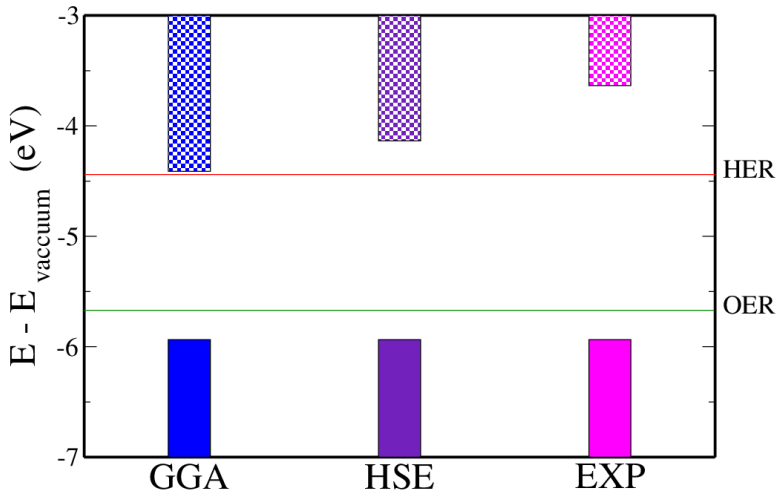


Figure 10**.** Alignment of valence and conduction band of $Cd_4P_2Cl_3$ obtained from calculations based on GGA functional (blue), HSE functional (Indigo) and experimental band gap (magenta) to position the conduction band.

To determine the potential of $Cd_4P_2Cl_3$ for use in photocatalytic water splitting, we aligned its valence and conduction band edges with respect to vacuum and compared with the redox potentials of water splitting. Though our calculations with the HSE functional give a better estimate of the band gap than the GGA, the improvement is not quite complete. To this end, we use a scissor correction in aligning the conduction band by taking experimental band gap in shifting it. We find that the valence band and the conduction band edges straddle the redox potentials of hydrogen evolution reaction (HER) and oxygen evolution reaction (OER) (**Figure 10**). We therefore expect, $Cd_4P_2Cl_3$ to be suitable for use as a photo-catalyst for water splitting.

**Photocatalytic $H_2$ generation**

In the light of the above theoretical predictions we have studied photocatalytic water splitting from $Cd_4P_2Cl_3$ samples under visible-light irradiation. **Figure 11a** shows $H_2$ generation from $Cd_4P_2Cl_3$/Pt and CdS/Pt under visible-light irradiation with $Na_2S$-$Na_2SO_3$ as the sacrificial agent. CdS synthesized at the same temperature by solid state reaction shows much less activity than all the $Cd_4P_2Cl_3$ samples. A $H_2$ evolution rate of 285 (±11), 555(±25) and 336(±9) μmol $h^{-1}g^{-1}$ was exhibited by $Cd_4P_2Cl_3$-1, $Cd_4P_2Cl_3$-2 and $Cd_4P_2Cl_3$-3 respectively. $Cd_4P_2Cl_3$-2 exhibits a hydrogen

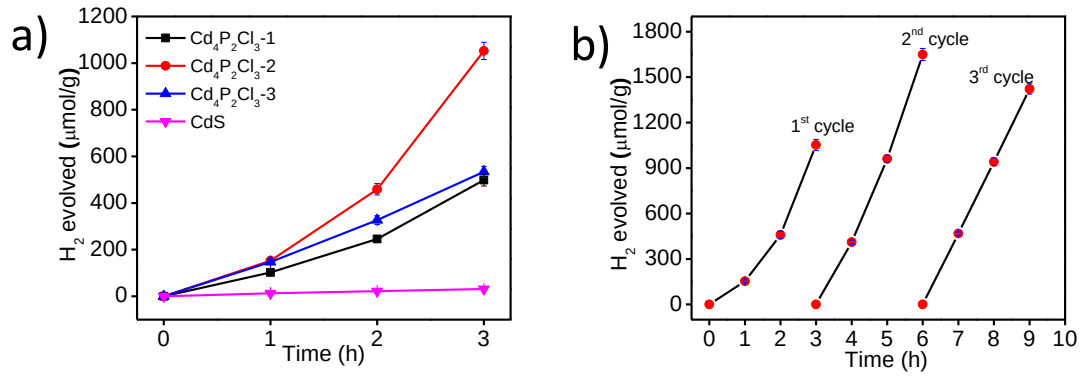


Figure 11. a) Photocatalytic $H_2$ generation from CdS/Pt and $Cd_4P_2Cl_3$ /Pt, and b) Cyclic HER activity of $Cd_4P_2Cl_3$-2/Pt under visible-light irradiation with $Na_2S$-$Na_2SO_3$ as sacrificial agent.

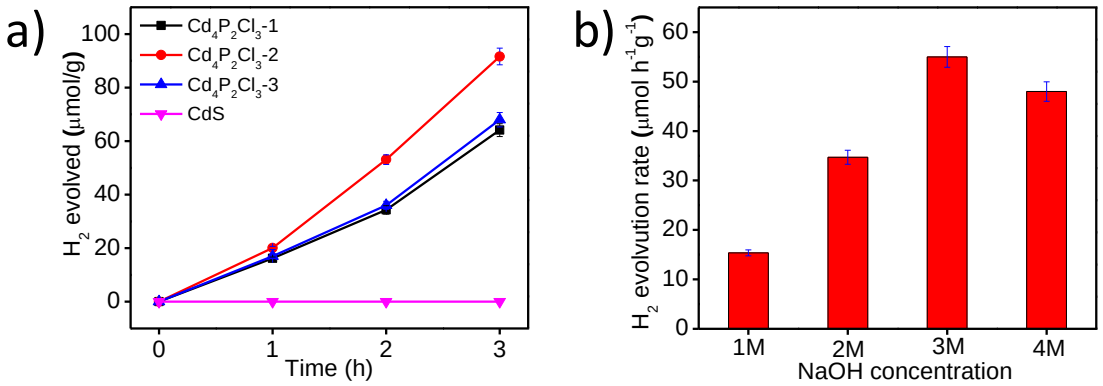


Figure 12. a) Visible-light induced $H_2$ evolution from CdS/Pt and $Cd_4P_2Cl_3$/Pt in alkaline medium without any sacrificial agent, and b) Effect of NaOH concentration on $H_2$ evolution from $Cd_4P_2Cl_3$-2/Pt.

evolution rate of 555 (±25) µmol $h^{-1}g^{-1}$, which is 25 times higher than the $H_2$ evolution rate from CdS (22.0±9 µmol $h^{-1}g^{-1}$). An enhancement of nearly two times in the catalytic activity of all $Cd_4P_2Cl_3$ samples was observed after an induction period of 3h. $Cd_4P_2Cl_3$-2 shows an enhancement in the photocatalytic $H_2$ generation activity from 555 to 1007 (± 26) µmol $h^{-1}g^{-1}$ after an induction period of 3h and remains nearly constant afterwards. Differences in the HER activity of the three samples needs to be examined further, and it is possible that surface properties could be an important factor. The apparent quantum yield (AQY) obtained from $Cd_4P_2Cl_3$-2 under visible-light is ~1.07 (± 0.04) which is higher than that of CdS (AQY~ 0.023). We have

examined the catalytic performance of $Cd_4P_2Cl_3$-2/Pt over 9 h in 3 cycles. **Figure 11b** shows recyclability of these photocatalyst for hydrogen production under visible-light irradiation with $Na_2S$-$Na_2SO_3$ as the sacrificial agent. $Cd_4P_2Cl_3$-2/Pt exhibits a $H_2$ evolution rate of rate of 555(±25), 1007(± 26), and 993(±23) μmol $h^{-1}g^{-1}$ in first, second and third cycle, respectively. We did not observe any decline in the photocatalytic activity of samples up to 9 h.

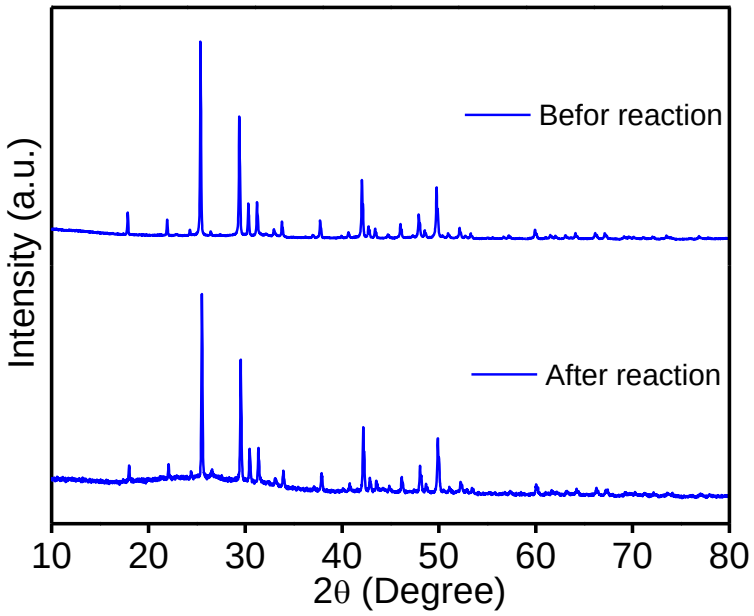


Figure 13. PXRD patterns of $Cd_4P_2Cl_3$-2 before and after photocatalytic reaction.

We have studied hydrogen evolution in alkaline medium from $Cd_4P_2Cl_3$/Pt under visible-light irradiation without any sacrificial agent. **Figure 12a** shows visible-light induced hydrogen evolution from $Cd_4P_2Cl_3$/Pt samples along with CdS/Pt (without any sacrificial agent). It is noteworthy that $Cd_4P_2Cl_3$ shows hydrogen evolution even without any sacrificial agent, unlike CdS which requires a sacrificial agent to produce hydrogen. The $Cd_4P_2Cl_3$/Pt samples under visible-light irradiation shows a linear variation in the hydrogen evolution activity with time, suggesting stability of $Cd_4P_2Cl_3$ against photocorrosion. This is probably linked with the fact that the lowest energy conduction band is flat in this compound (**See Figure 7a**).[26] A hydrogen evolution rate of 54(±4) μmol $h^{-1}g^{-1}$ is exhibited by $Cd_4P_2Cl_3$-2/Pt in alkaline medium without any sacrificial agent. **Figure 12b** shows the effect of NaOH concentration on the hydrogen evolution from $Cd_4P_2Cl_3$-2/Pt sample under visible-

light irradiation. With increase in NaOH concentration hydrogen evolution activity of the photocatalyst increases up to an optimum concentration of 3M. The cause of this is yet to be understood. This finding suggests that $Cd_4P_2Cl_3$ can be used in place of CdS to avoid photocorrosion. In order to examine the stability of $Cd_4P_2Cl_3$ under reaction conditions, we have collected the powder X-ray diffraction pattern after the full course of photocatalytic reaction. **Figure 13** shows the PXRD patterns of the $Cd_4P_2Cl_3$-2 photocatalyst before and after reaction. We see no change in the PXRD pattern of the photocatalyst indicating its stability.

## 4.2 Structure and Properties of $Cd_4As_2Br_3$ and $Cd_4Sb_2I_3$

**Figure 14.** shows the PXRD patterns of $Cd_4As_2Br_3$ and $Cd_4Sb_2I_3$ compounds which is in the good agreement with simulated pattern obtained from single crystal data. Both the compounds crystallize in the cubic structure with the space group Pa-3. The lattice parameters, for $Cd_4As_2Br_3$ and $Cd_4Sb_2I_3$ are 12.61 and 13.48 Å respectively. The sharp diffraction peaks reflect the crystalline nature of samples. The crystallite sizes of these compounds estimated using the Scherrer formula are 0.52 and 0.74 µm in the case of $Cd_4As_2Br_3$ and $Cd_4Sb_2I_3$ respectively.

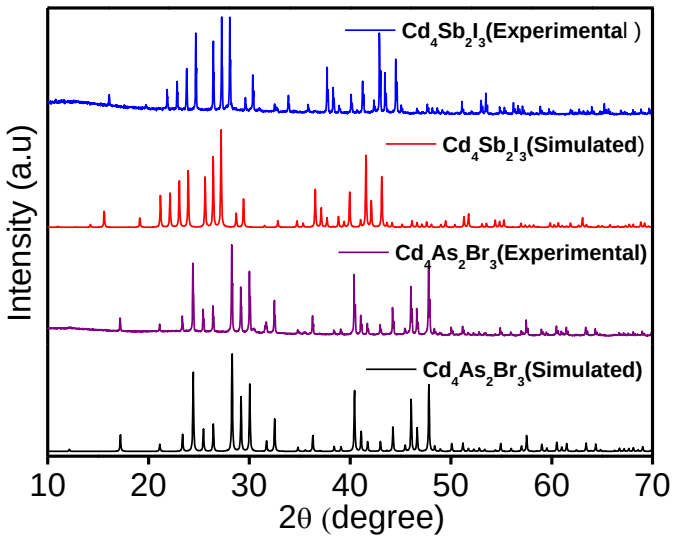


Figure 14. PXRD patterns of $Cd_4As_2Br_3$ and $Cd_4Sb_2I_3$ along with simulated pattern.

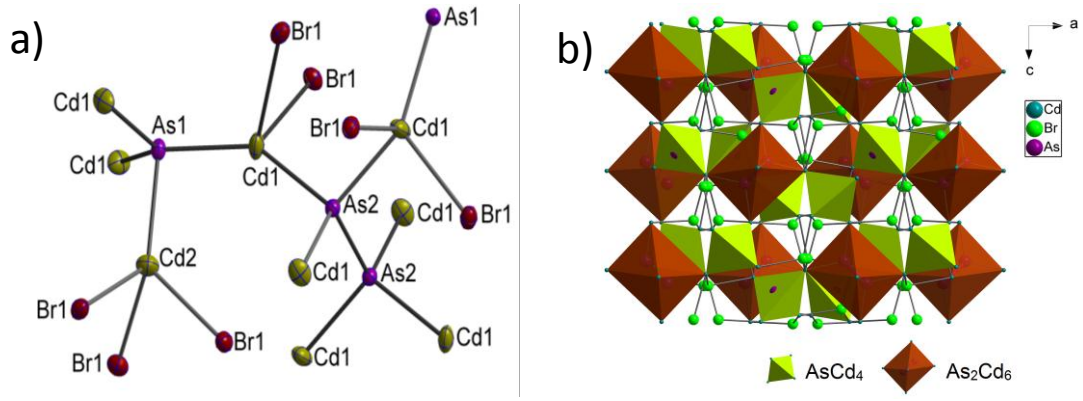


Figure 15. a) Ball and stick model showing bonding in $Cd_4As_2Br_3$, and b) Crystal structure of $Cd_4As_2Br_3$ showing of $AsCd_4$ and $As_2Cd_6$ polyhedra.

The crystal structure of $Cd_4As_2Br_3$ obtained by us using single crystal XRD matches with that reported in the literature.[27] The structure has two independent Cd and As atoms labelled as Cd(1), Cd(2) and As(1), As(2) (**Figure 15a**). Bonding of the As and Br atoms around the Cd centres gives rise to a tetrahedral environment wherein Cd(1) is surrounded by two As and two Br atoms and Cd(2) is surrounded by one As and three Br atoms respectively. As(1) possessing $3^-$ charge forms $AsCd_4$ tetrahedra, whereas As(2)with $2^-$ charge and forms $As_2Cd_6$ octahedra with a As(2)-As(2) dumbbells in the centre (As-As bond length, 2.390 Å). These two polyhedra give rise to the three-dimensional structure to $Cd_4As_2Br_3$, which is linked with the Br located in the voids of the three-dimensional structure (**Figure 15b**). $Cd_4Sb_2I_3$ is isostructural with $Cd_4As_2Br_3$ wherein the Cd(1) atoms are coordinated by two Sb and two I atoms whereas Cd(2) atoms are coordinated by three I atoms and one Sb atom. Sb (1) ($3^-$ charge) forms $Cd_4Sb$ units and Sb(2) ($2^-$ charge) is part of the $Sb_2Cd_6$ polyhedra wherein Sb(2)-Sb(2) bond exist (Sb(2)-Sb(2) bond length 2.83 Å) (**Figure 16**). X-ray photoelectron spectra (XPS) of these compounds were recorded to further ascertain the nature of As, Br and Sb, I in these compounds. **Figure 17a** shows As core level spectrum, As signal is split in to two peaks due

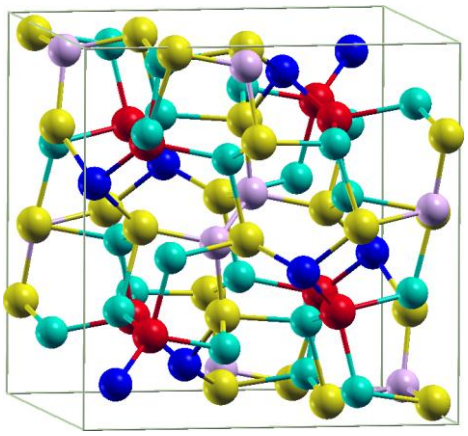

Figure 16. Crystal structure of $Cd_4Sb_2I_3$. Cd1: Yellow, Cd2: Red, I: Green, Sb1: Blue, Sb2: Pink.

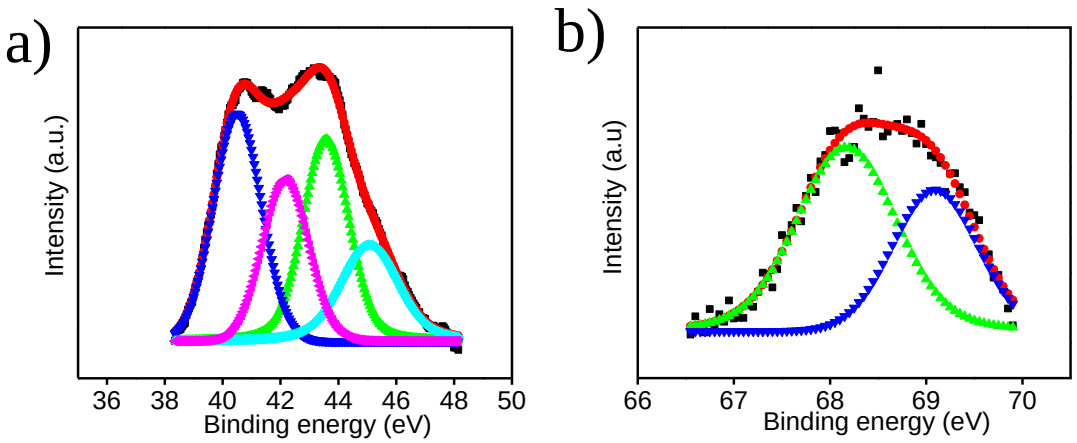


Figure 17. Core level XP spectra of $Cd_4As_2Br_3$; state of a) As, and b) Br

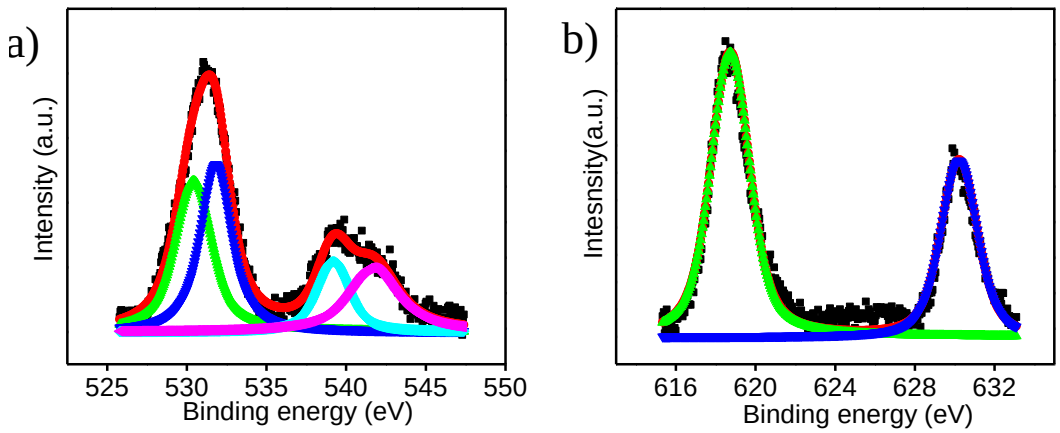


Figure 18. Core level XP spectra of $Cd_4Sb_2I_3$ state of; a) Sb, and b) I

to the presence of two different As atoms in the compound. These peaks can be deconvoluted into two peaks, at 40.5 and 42.1 eV due to the $3d_{5/2}$ and $3d_{3/2}$ states of As(1) ($3^-$ charge) in $AsCd_4$, and at 43.5 and 45.0 eV is the core of $3d_{5/2}$ and $3d_{3/2}$ states of As(2) ($2^-$ charge) in $As_2Cd_6$. **Figure 17b** shows the Br core level spectrum in $Cd_4As_2Br_3$, signal at 68.5 eV can be deconvoluted into two peaks at 68.14 and 69.10 eV due to Br $3d_{5/2}$ and $3d_{3/2}$ states respectively. **Figure 18a** shows the XP spectrum of Sb, with signals at 531.33 and 540.11 due to $3d_{5/2}$ and $3d_{3/2}$ states respectively. These peaks can be further deconvoluted into two peaks due to two different Sb atoms. The peaks at 530.4 and 539.23 are due to the $3d_{5/2}$ and $3d_{3/2}$ states of $Sb^{3-}$ in $SbCd_4$ and the peaks at 531.82 and 541.7 due to be $3d_{5/2}$ and $3d_{3/2}$ states, of $Sb^{2-}$ in $Sb_2Cd_6$. **Figure 18b** shows the iodine signal in $Cd_4Sb_2I_3$, with peaks at 618.8 and 630.25 corresponding to $3d_{5/2}$ and $3d_{3/2}$ states.

UV-Visible diffuse reflectance spectra of $Cd_4As_2Br_3$ and $Cd_4Sb_2I_3$ show characteristic absorption bands in the visible region with the absorption edges at 673 and 691 nm for $Cd_4As_2Br_3$ and $Cd_4Sb_2I_3$ respectively. The colors of samples are also shown in the figures (**Figures 19a and 19b**). $Cd_4As_2Br_3$ shows an optical band gap of 1.93 eV, acquired by Kubelka-Munk method whereas $Cd_4Sb_2I_3$ shows a band gap of 1.83 eV. It is noteworthy to mention that the band gaps in bulk CdSe and CdTe are 1.74 and 1.5 eV respectively. Photoluminescence spectra of these compounds were recorded at the room temperature. Excitation at 400 nm gives a photoluminescence band at 590 nm in the case of $Cd_4As_2Br_3$ (**Figure 20a)**, and a band centred at 700 nm in the case of $Cd_4Sb_2I_3$ (**Figure 20b**) due to the recombination of photogenerated charge carriers.

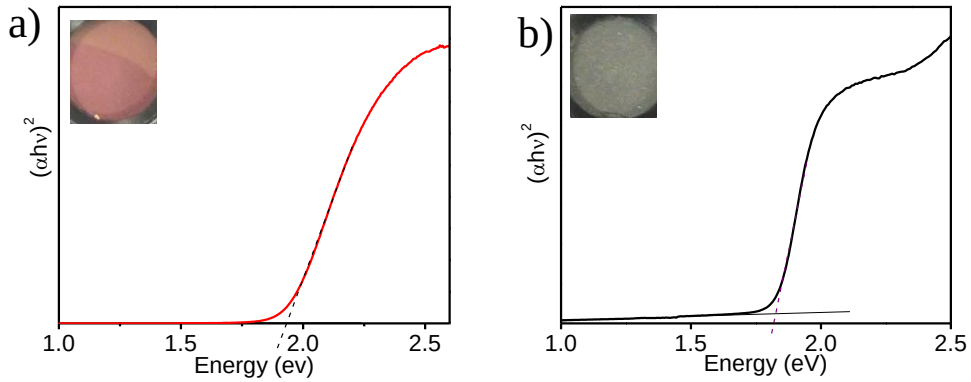


Figure 19. Tauc plot showing band gap in a) $Cd_4As_2Br_3$, and b) $Cd_4Sb_2I_3$.

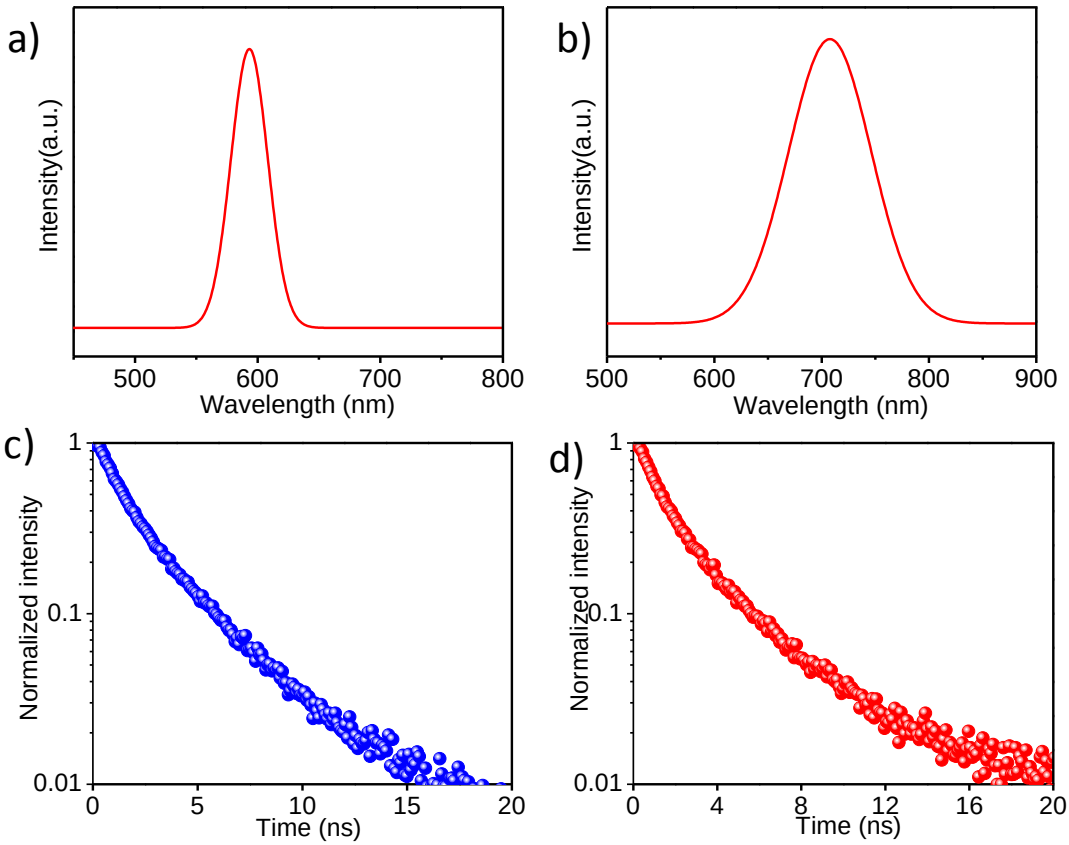


Figure 20. Steady state photoluminescence spectra of a) $Cd_4As_2Br_3$, and b) $Cd_4Sb_2I_3$. Time resolved photoluminescence spectra of c) $Cd_4As_2Br_3$, and d) $Cd_4Sb_2I_3$.

It is known that life time of photogenerated charge carriers have the notable impact on catalytic activity.[25a,28] Longer life-time of photogenerated electrons and holes suggests higher photocatalytic efficiency due to the higher probability of involvement in the surface catalytic reactions. The life-time of photogenerated charge carriers in $Cd_4As_2Br_3$ and $Cd_4Sb_2I_3$ were obtained by

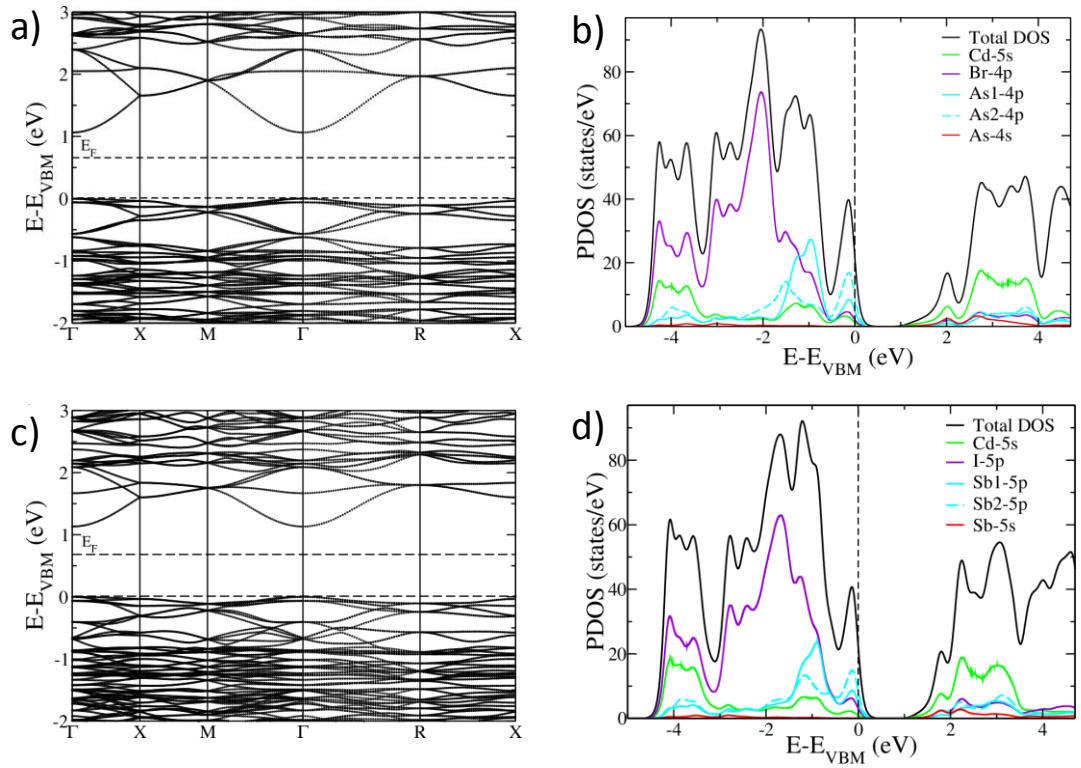


Figure 21. Electronic structures of (a) $Cd_4As_2Br_3$, and (c) $Cd_4Sb_2I_3$. Density of states of (b) $Cd_4As_2Br_3$, and (d) $Cd_4Sb_2I_3$ projected on various atomic orbitals.

time-resolved photoluminescence spectrum. Excitation at 400 nm laser shows an exponential decay of photogenerated charge carriers which could be fitted to a double exponential function. An average life time of charge carriers was found to be 2 ns in both the compounds (**Figures 20c and 20d**).

Our theoretical estimates based on first-principles calculation yield lattice constants are 12.92 and 13.85 Å for $Cd_4As_2Br_3$ and $Cd_4Sb_2I_3$ respectively. These are within the typical errors of GGA calculations. The electronic structure of $Cd_4As_2Br_3$ (**Figure 21a**) has a direct band gap of 1.06 eV at Γ-point, which is underestimated with respect to the experimental gap of 1.93 eV. Our HSE calculations predict a band gap of 1.72 eV, which is closer to the experimental value. From the projected density of states (**Figure 21b**), it is evident that the states at VBM and CBM are predominantly comprised of As-4p and Cd-5s orbitals respectively. The maximum contribution to the valence band is from $As^{2-}$ forming the As-As (denoted by As2) bond. $As^{3-}$ (denoted by As1) constitutes the higher energy valence band state. $Cd_4Sb_2I_3$ also has a direct band gap of 1.13 eV (**Figure 21c**), with Cd-5s orbitals contributing to the states near

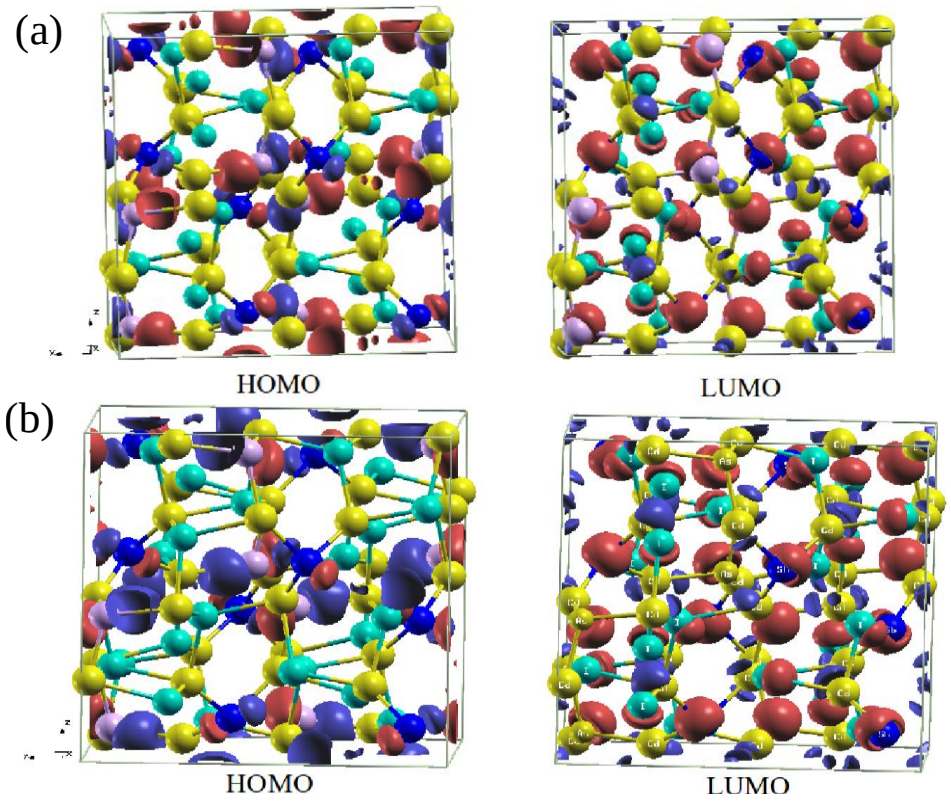


Figure 22. Visualization of wavefunctions of HOMO and LUMO at Γ-point of (a) $Cd_4As_2Br_3$, and (b) $Cd_4Sb_2I_3$. Red and blue colors of the isosurfaces of wavefunctionsindicate positive and negative signs respectively. Cd: yellow, Br and I: Green, As1 and Sb1: Blue, As2 and Sb2: Pink.

CBM and Sb-5p contributing to the states near VBM (**Figure 21d**). Here also, $Sb^{2-}$ (denoted by Sb2) contributes to the VBM, and high energy valence band state has major contribution from $Sb^{3-}$ (denoted by Sb1). From HSE calculations, the band gap of $Cd_4Sb_2I_3$ is expected to be around 1.79 eV. We noticed that the theoretical estimates of the band gaps of $Cd_4As_2Br_3$ and $Cd_4Sb_2I_3$ obtained using VASP in combination with the PBE functional are 0.98 eV and 1.13 eV respectively, which agree well with the estimates of 1.06 eV and 1.13 eV obtained using Quantum-Espresso calculations. We have used xcrysden to visualize HOMO-LUMO of the bulk configuration obtained from Quantum-Espresso calculations. Visualization of the wave functions state near the band gap at Γ-point show that the VBM has a major contribution from As-4p orbitals and CBM has contribution from S orbitals of Cd, As and Br (**Figure**

**22a**). In $Cd_4Sb_2I_3$, Sb-5p orbitals constitute the VBM, and the CBM is contributed from s orbitals of Cd, Sb and I (**Figure 22b**).

To assess the potential of $Cd_4As_2Br_3$ and $Cd_4Sb_2I_3$ as photocatalysts for the hydrogen evolution reaction (HER), we have aligned their valence and conduction band edges with respect to vacuum potential. Their positions relative to hydrogen redox potential allow us to discuss their suitability for catalytic behaviour. Since it is not straightforward to assign the vacuum potential in calculations of bulk compounds, we performed calculations on (001) slabs consisting of two unit cells of $Cd_4As_2Br_3$ and $Cd_4Sb_2I_3$ amounting to thickness of 26 Å and 28 Å respectively. The structure of the slab has been constructed using the relaxed bulk positions of the compounds. The bulk band edge energies are aligned with respect to vacuum using ΔV, defined as the difference between the potential in vacuum and macroscopically averaged potential deep inside the slab. We also simulated slabs with 5 unit cells thickness, and found that the bulk-vacuum potential difference of the 2 unit-cell thick slab is within 5 meV of that obtained with the thicker slab.

For catalysing the hydrogen evolution reaction, the CBM of semiconductors should ideally be above the HER potential. The band alignment of these compounds (**Figure 23**) clearly suggests their suitability for photocatalysis of HER. Since, their VBMs are above the oxygen evolution reaction (OER) potential they are not suitable for the OER. The conduction band in $Cd_4As_2Br_3$ is more dispersed along Γ-M than in $Cd_4Sb_2I_3$, indicating its lower electronic effective mass and higher mobility. This could lead to the better catalytic activity of this compound towards the HER.

**Photocatalytic $H_2$ generation**

Since first-principles calculations suggest that these semiconductors materials can be useful for the photocatalytic water splitting to generate molecular hydrogen, we have investigated the hydrogen evolution from these semiconductors materials under visible-light irradiation in the presence of $Na_2S$-$Na_2SO_3$ as the sacrificial agent. $Cd_4As_2Br_3$ exhibits a hydrogen evolution rate of 138 and 164 μmol $h^{-1}g^{-1}$ in the first and the second cycle respectively (**Figure 24a**).

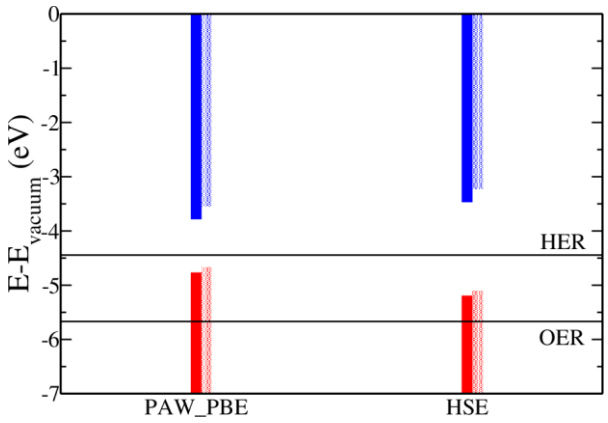


Figure 23. Alignment of valence and conduction bands obtained with GGA and HSE calculations. Solid and shaded bars show the VBM and CBM positions of $Cd_4As_2Br_3$ and $Cd_4Sb_2I_3$ respectively.

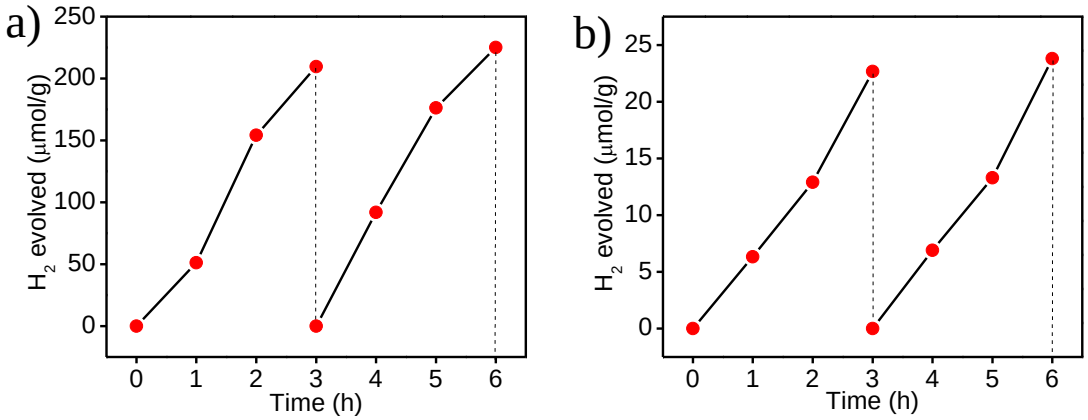


Figure 24. Photochemical $H_2$ evolution from a) $Cd_4As_2$ $Br_3$, and b) $Cd_4Sb_2I_3$ under visible light irradiation in the presence of $Na_2S$-$Na_2SO_3$ as a sacrificial agent.

It is noteworthy that bulk CdSe does not show hydrogen evolution, whereas its analogue $Cd_4As_2Br_3$ does. The HER activity remains almost same for multiple cycles. The HER activity of $Cd_4Sb_2I_3$ is lower than that of $Cd_4As_2Br_3$ (**Figure 24b**) in agreement with the theoretical prediction. The PXRD pattern of photocatalyst after multiple cycles does not show any change suggesting the stability of the photocatalyst under reaction conditions (**Figure 25**). To further confirm the stability of the photocatalyst, time dependence measurement of $Cd^{2+}$ concentration in the reaction solution was done by ICP which shows absence of $Cd^{2+}$ ions up to 6h. Although the HER activity of these compounds are not high it is still interesting that these ternary

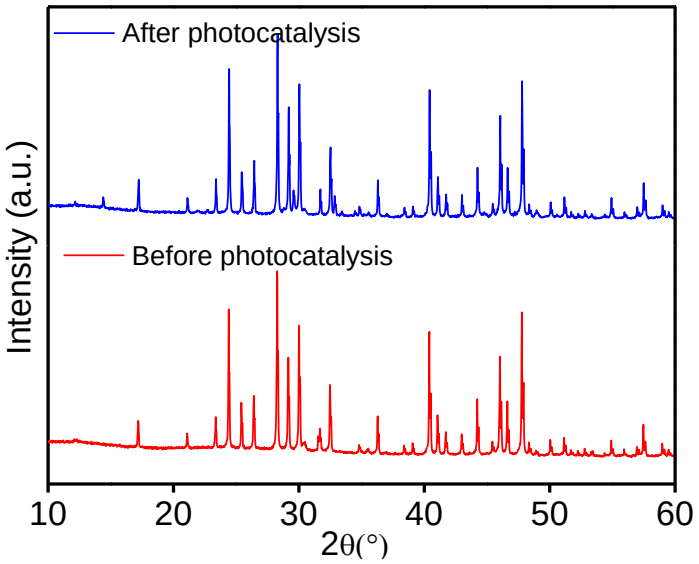


Figure 25. PXRD patterns of $Cd_4As_2Br_3$ before and after photocatalytic reaction.

semiconductors produces hydrogen in visible light and shows the photostability under the reaction condition. We believe further optimizations can enhance the HER activity of these compounds.

# 5. Conclusions

We have been able to examine the electronic structure of $Cd_4P_2Cl_3$, $Cd_4As_2Br_3$ and $Cd_4Sb_2I_3$ compounds which are close to $Cd_2PCl$, $Cd_2AsBr$, and $Cd_2SbI$ which would have been obtained by the complete substitution of $X^{2-}$ (X= S, Se, and Te) by the corresponding aliovalent anions in the cadmium chalcogenides (CdX). All the three compounds crystallize in the cubic structure with space group Pa-3. The direct band gaps in $Cd_4P_2Cl_3$, $Cd_4As_2Br_3$ and $Cd_4Sb_2I_3$ are comparable to the band gaps of the analogous CdS, CdSe, and CdTe respectively. The life-times of photogenerated charge carriers are found to be in the range of 2-3 ns. First principles calculations enable us to understand the experimental results clearly. Among three compounds, $Cd_4P_2Cl_3$ exhibit excellent hydrogen generation activity under visible-light irradiation and possess unique photostability even in the absence of sacrificial electron donors.

# 6. References


[1] a) A. Mews, A. Eychmueller, M. Giersig, D. Schooss, H. Weller, *J. Phys. Chem.* **1994**, *98*, 934-941; b) N. Chestnoy, T. D. Harris, R. Hull, L. E. Brus, *J. Phys. Chem.* **1986**, *90*, 3393-3399; c) T. Shanmugapriya, P. Ramamurthy, *J. Phys. Chem. C* **2013**, *117*, 12272-12278.

[2] a) C. Wu, J. Jie, L. Wang, Y. Yu, Q. Peng, X. Zhang, J. Cai, H. Guo, D. Wu, Y. Jiang, *Nanotechnol.* **2010**, *21*, 505203; b) X. Duan, Y. Huang, R. Agarwal, C. M. Lieber, *Nature* **2003**, *421*, 241; c) Y. Ye, L. Dai, P. C. Wu, C. Liu, T. Sun, R. M. Ma, G. G. Qin, *Nanotechnol.* **2009**, *20*, 375202; d) O. Stroyuk, A. Raevskaya, N. Gaponik, *Chem. Soc. Rev.* **2018**, *47*, 5354-5422.

[3] a) K. Zhang, L. Guo, *Catal. Sci. Technol.* **2013**, *3*, 1672-1690; b) L. A. Silva, S. Y. Ryu, J. Choi, W. Choi, M. R. Hoffmann, *J. Phys. Chem. C* **2008**, *112*, 12069-12073.

[4] A. Kudo, Y. Miseki, *Chem. Soc. Rev.* **2009**, *38*, 253-278.

[5] a) S. Kouser, S. R. Lingampalli, P. Chithaiah, A. Roy, S. Saha, U. V. Waghmare, C. N. R. Rao, *Angew. Chem. Int. Ed.* **2015**, *54*, 8149-8153; b) C. N. R. Rao, *J. Phys. Chem. Lett.* **2015**, *6*, 3303-3308.

[6] a) N. Kumar, U. Maitra, V. I. Hegde, U. V. Waghmare, A. Sundaresan, C. N. R. Rao, *Inorg. Chem.* **2013**, *52*, 10512-10519; b) C. N. R. Rao, *J. Phys. Chem. Lett.* **2015**, *6*, 3303-3308.

[7] W. Witte, S. Spiering, D. Hariskos, *Vak. Forsch. Prax.* **2014**, *26*, 23-27.

[8] R. Shi, H.-F. Ye, F. Liang, Z. Wang, K. Li, Y. Weng, Z. Lin, W.-F. Fu, C.-M. Che, Y. Chen, *Adv. Mater.* **2018**, *30*, 1705941.

[9] H. Luo, C. Tuinenga, E. B. Guidez, C. Lewis, J. Shipman, S. Roy, C. M. Aikens, V. Chikan, *J. Phys. Chem. C* **2015**, *119*, 10749-10757.

[10] Y. Y. Proskuryakov, K. Durose, J. D. Major, M. K. Al Turkestani, V. Barrioz, S. J. C. Irvine, E. W. Jones, *Sol. Energ. Mat. Sol. Cells* **2009**, *93*, 1572-1581.

[11] a) S. Shanmugan, S. Balaji, D. Mutharasu, *Mater. Lett.* **2009**, *63*, 1189-1191; b) T. Okamoto, S. Ikeda, S. Nagatsuka, R. Hayashi, K. Yoshino, Y. Kanda, A. Noda, R. Hirano, *Jpn. J. Appl. Phys.* **2012**, *51*, 10NC12.

[12] O. S. Ogedengbe, C. H. Swartz, P. A. R. D. Jayathilaka, J. E. Petersen, S. Sohal, E. G. LeBlanc, M. Edirisooriya, K. N. Zaunbrecher, A. Wang, T. M. Barnes, T. H. Myers, *J. Electron. Mater.* **2017**, *46*, 5424-5429.

[13] a) A. V. Shevelkov, L. N. Reshetova, B. A. Popovkin, *J. Solid State Chem.* **1998**, *137*, 138-142; b) A. V. Shevelkov, M. M. Shatruk, *Russ. Chem. Bull.* **2001**, *50*, 337-352.

[14] C.-H. Liao, C.-W. Huang, J. C. S. Wu, *Catal.* **2012**, *2*, 490.

[15] Y. Wang, Y. Wang, R. Xu, *J. Phys. Chem. C* **2013**, *117*, 783-790.

[16] M. Kars, T. Roisnel, V. Dorcet, A. Rebbah, L. C. Otero-Diaz, *ActaCryst., E.* **2014**, *70*, i15.

[17] A. V. Shevelkov, E. V. Dikarev, B. A. Popovkin, *J. Solid State Chem.* **1991**, *93*, 331-335.

[18] a) P. Hohenberg, W. Kohn, *Phys. Rev.* **1964**, *136*, B864-B871; b) W. Kohn, L. J. Sham, *Phys. Rev.* **1965**, *140*, A1133-A1138; c) P. Giannozzi, S. Baroni, N. Bonini, M. Calandra, R. Car, C. Cavazzoni, D. Ceresoli, G. L. Chiarotti, M. Cococcioni, I. Dabo, A. Dal Corso, S. de Gironcoli, S. Fabris, G. Fratesi, R. Gebauer, U. Gerstmann, C. Gougoussis, A. Kokalj, M. Lazzeri, L. Martin-

Samos, N. Marzari, F. Mauri, R. Mazzarello, S. Paolini, A. Pasquarello, L. Paulatto, C. Sbraccia, S. Scandolo, G. Sclauzero, A. P. Seitsonen, A. Smogunov, P. Umari, R. M. Wentzcovitch, *J. Phys. Condens. Matter*. **2009**, *21*, 395502.

[19] a) D. Vanderbilt, *Phys. Rev. B* **1990**, *41*, 7892-7895; b) J. P. Perdew, K. Burke, M. Ernzerhof, *Phys. Rev. Lett.* **1996**, *77*, 3865-3868.

[20] J. P. Perdew, M. Levy, *Phys. Rev. Lett.* **1983**, *51*, 1884-1887.

[21] J. Heyd, G. E. Scuseria, M. Ernzerhof, *J. Chem. Phys.* **2003**, *118*, 8207-8215.

[22] a) G. Kresse, J. Furthmüller, *Phys. Rev. B* **1996**, *54*, 11169-11186; b) P. E. Blöchl, *Phys. Rev. B* **1994**, *50*, 17953-17979.

[23] a) M. Ceppatelli, S. Fanetti, R. Bini, M. Caporali, M. Peruzzini, *J. Phys. Conf. Ser.* **2014**, *500*, 022008; b) S. Wei, J. Lu, W. Yu, H. Zhang, Y. Qian, *Cryst. Growth Des.* **2006**, *6*, 849-853; c) D. J. Lockwood, *J. Opt. Soc. Am.* **1973**, *63*, 374-382.

[24] T. B. Hoang, L. V. Titova, H. E. Jackson, L. M. Smith, J. M. Yarrison-Rice, J. L. Lensch, L. J. Lauhon, *App. Phys. Lett.* **2006**, *89*, 123123.

[25] a) P. Niu, L. Zhang, G. Liu, H.-M. Cheng, *Adv. Funct. Mater.* **2012**, *22*, 4763-4770; b) X. Zhang, L. Yu, C. Zhuang, T. Peng, R. Li, X. Li, *ACS Catal.* **2014**, *4*, 162-170.

[26] D. Meissner, R. Memming, B. Kastening, *J. Phys. Chem.* **1988**, *92*, 3476-3483.

[27] M. Kars, T. Roisnel, V. Dorcet, A. Rebbah, L. C. Otero-Diaz, *Acta Crystallogr., Sect. E: Struct. Rep.* **2014**, *70*, i15.

[28] J. D. Benck, T. R. Hellstern, J. Kibsgaard, P. Chakthranont, T. F. Jaramillo, *ACS Catal.* **2014**, *4*, 3957-3971.

# Chapter 4

# Cadmium Phosphohalides with Novel Structural Features, Exhibiting HER activity and other Properties


## Summary*

We have carried out a combined experimental and theoretical investigation of the structures and properties of a family of cadmium phosphochlorides of members, $Cd_2P_3Cl$, $Cd_4P_2Cl_3$, $Cd_3PCl_3$, and $Cd_7P_4Cl_6$, with varying Cl/Cd and P/Cd ratios. The phosphochlorides possess optical band gaps in the visible-region which is sensitive to Cl/Cd and P/Cd ratios, the band gap showing an increase with increasing Cl/Cd ratio and the P/Cd ratio having the opposite effect. First-principles calculations have been employed to understand the bonding and electronic structures. Except for $Cd_2P_3Cl$, the other phosphochlorides possess direct band gaps.

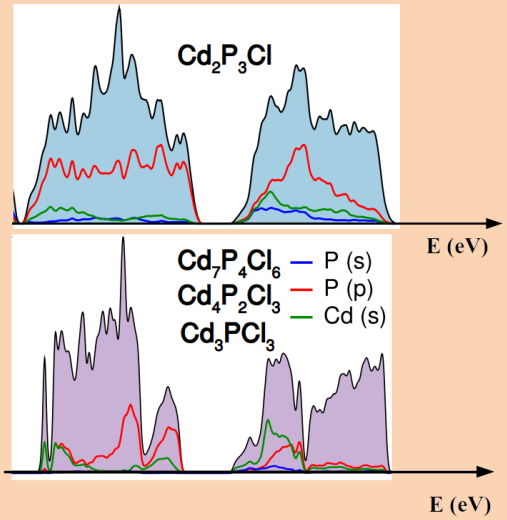


Dielectric constants and Born effective charges from first-principles calculations illustrate the bonding, hybridization and ionic character in these compounds. The band positions of these compounds are appropriate with respect to $H_2O$ redox potental for performing the water splitting reaction. All cadmium phosphochlorides do indeed exhibit hydrogen evolution reaction (HER) with $Cd_7P_4Cl_6$ showing best activity whereas $Cd_3PCl_3$ with least activity. The apparent quantum yield (20.1%) is highest in $Cd_7P_4Cl_6$ even without the assistance of a co-catalyst. The HER activity can be understood on the basis of photoelectrochemical measurements.



A Paper Based on this work has appeared in Angew. Chem. Int. Ed. 2019

# 1. Introduction

Aliovalent anion substitution in inorganic materials brings about profound changes in the electronic structure and properties.[1] Thus, in the case of $N^{3-}$ and $F^{-}$ substituted ZnO and $TiO_2$, complete substitution of $O^{2-}$ yields $Zn_2NF$ and TiNF respectively with unique properties.[2] Aliovalent substitution of P and Cl in place of S in CdS, modified the electronic structure and properties,[3] but, it has not been possible to obtain a compound of the composition $Cd_2PCl$ by the complete substitution of $S^{2-}$, by $P^{3-}$ and $Cl^{-}$. Instead, the simplest composition obtained is $Cd_4P_2Cl_3$.[4] Interestingly, there are several Cd compounds with a variety of compositions or varied Cd/P and Cd/Cl ratios.[5] Notable members of this family are $Cd_3PCl_3$, $Cd_7P_4Cl_6$, $Cd_4P_2Cl_3$, $Cd_2P_3Cl$ and $Cd_2PCl_2$. It was interesting to us to investigate how the structures and properties of these compounds vary with the P/Cd and Cl/Cd ratios. For this purpose, we have synthesized the low-temperature phases of $Cd_3PCl_3$ and $Cd_7P_4Cl_6$ in pure form along with the high-temperature forms, $Cd_4P_2Cl_3$ and $Cd_2P_3Cl$. We have investigated the electronic structures and photocatalytic properties of these compounds experimentally as well as by extensive first-principles calculations. The band gap decreases with increasing P/Cd ratio and increases with increasing Cl/Cd ratio. Interestingly, the conduction band minima (CBM) and valence band maxima (VBM) of these compounds straddle between the oxidation and reduction potentials of $H_2O$, rendering them thermodynamically favorable to perform water splitting. They exhibit hydrogen evolution reaction (HER) activity, and the activity is affected by the presence of P-P bonds. DFT calculations throw light on the dependence of the properties on the structure and bonding in these compounds.

# 2. Scope of the Present Investigations

Cadmium phosphochlorides form a family of compounds with various Cl/Cd and P/Cd ratios. Notable members of this family are $Cd_2P_3Cl$, $Cd_4P_2Cl_3$, $Cd_7P_4Cl_6$ and $Cd_3PCl_3$. Structures of some of the cadmium phosphochlorides are known to some extent, but little is known about their electronic and photophysical properties. In the present work, we have synthesized various cadmium phosphochlorides in pure form and investigated their structural features, electronic and photophysical properties in

depth. Intrestingly, we have found a remarkable effect of structure and bonding on the photocatalytic HER activity of these compounds.

## 3. Experimental Section

**Materials:** All the materials involved in the synthesis have bought from Sigma-Aldrich and have been used as received without further purification.

**Synthesis of $Cd_3PCl_3$**

In a typical synthesis of $Cd_3PCl_3$ compound, a stoichiometric quantity of Cd, red-P, and $CdCl_2$ was ground in the form of a homogenous mixture. This homogenous mixture was sealed inside a quartz ampule under vacuum and heated to 350°C (heating rate 2.5°/min) and maintained at this temperature for 48 h, followed by the cooling of the sample to the room temperature with the same rate.

**Synthesis of $Cd_7P_4Cl_6$**

In a typical synthesis of $Cd_7P_4Cl_6$ compound, a stoichiometric quantity of Cd, red-P, and $CdCl_2$ was ground in the form of a homogenous mixture. This homogenous mixture was sealed inside a quartz ampule under vacuum and heated to 450 ºC (heating rate 2.5°/min) and maintained at this temperature for 72 h, followed by the cooling down of the sample to the room temperature with the same rate.

**Synthesis of $Cd_4P_2Cl_3$**

In a typical synthesis of $Cd_4P_2Cl_3$ compound, a stoichiometric quantity of $Cd_3P_2$, red-P, and $CdCl_2$ was ground in the form of a homogenous mixture. This homogenous mixture was sealed inside a quartz ampule under vacuum and heated to 500 °C (heating rate 2.5°/min) and maintained at this temperature for 24 h, followed by the cooling of the sample to the room temperature with the same rate.

**Synthesis of $Cd_2P_3Cl$**

In a typical synthesis of $Cd_2P_3Cl$ compound, a stoichiometric quantity of Cd, red-P, and $CdCl_2$ was ground in the form of a homogenous mixture. This homogenous mixture was sealed inside a quartz ampule under vacuum and kept under a tube furnace with a natural temperature gradient. End of the tube containing the reactant mixture was heated to 740 ºC with the rate of 2.5°/min whereas the other end of the

tube was maintained at 300 ºC for 72 h. The cooling of the sample followed this at the same rate.

**Synthesis of $Cd_2P_3Br$ and $Cd_2P_3I$**

Synthesis of $Cd_2P_3Br$ and $Cd_2P_3I$ was carried out with a slight modification of reported literature, in a heavy wall silica tube (16 mm o.d., 12 mm i.d., 6-7 inch length) wherein a stoichiometric amount of Cd, red-P, $PBr_3$ and Cd, red-P, $I_2$ was sealed under vacuum.[6] The sealed ampule containing precursor was heated to 740 ºC (heating rate of 2.5º/min) and maintained at this temperature for 48 h, whereas another end of the ampule was maintained at 300 ºC. The cooling of the tube followed this at the same rate; a dark red product was obtained at the cooler end of the tube.

It should be noted that the use of $PCl_3$ as a precursor for $Cd_2P_3Cl$ resulted in the formation of $CdP_2$ as major impurity phase with a small proportion of desired compound $Cd_2P_3Cl$. To avoid $CdP_2$ which is extremely difficult to remove, we used the precursors Cd, red-P and $CdCl_2$. Thereby obtained the desired product, $Cd_2P_3Cl$, only with a trace amount of $CdP_2$ impurities. In the case of $Cd_2P_3Br$ and $Cd_2P_3I$, we observe small impurity peaks corresponding to $CdBr_2$ and $CdI_2$ which could be removed by washing with an ethanol-water mixture.

**Charcterization**

X-ray diffraction (XRD) patterns were recorded with a Bruker D8 Diffraction system using a Cu Kα source (λ = 0.1541 nm). UV-Vis absorption spectra were collected with Perkin Elmer Model Lambda 900 spectrometer. Energy dispersive X-ray analysis and elemental mapping was done using EDAX genesis instrument attached to SEM. Inductiveley coupled plasma-optical emission spectroscopy (ICP-OES) was carried out using Pekin Elmer Optima 7000 DV machine (minimum detection limit 0.05 ppm).

**Photocatalytic Experiments**

Photocatalytic hydrogen evolution measurements were carried at ambient condition under constant stirring in a cylindrical glass reactor (140 mL) with head space closed by high quality septa. A Xe-arc lamp (New Port, 6279NS ozone-free, working at 400 watt) with UV cut-off filter (λ> 395 nm) was used as light source. In a typical experiment 20 mg of the photocatalyst was dispersed in 75 mL of Di-$H_2O$ containing

0.18 M $Na_2S$ and 0.24 M $Na_2SO_3$ as hole scavengers. Before light irradiation photocatalyst solution was purged with pure $N_2$ gas for 30 min to remove dissolved air. The quantity of evolved $H_2$ gas was measured by manual injection of gas sample into a gas chromatography (Perkin Elmer, Clarus 580) equipped with TCD detector. To study the effect of different sacrificial electron donor we have used 10 volume% of methanol, ethanol, benzyl alcohol, and triethanol amine (TEOA).

Apparent quantum yield calculation:

$$\text{AQY (\%)} = 2 \times \frac{\text{Number of evolved Hydrogen molecules}}{\text{Number of incident photons}} \times 100$$

**Photoelectrochemical (PEC) Measurements**

Photocurrent measurements were carried out on a CHI 1760E electrochemical work station (CH instrument Inc.) in a conventional three-electrode set-up. Spin-coated samples on FTO served as the working electrode, with a platinum wire as the counter electrode and an Ag/AgCl (saturated KCl) electrode as the reference electrode. The working electrode was prepared by spin coating. First, the catalyst slurry was prepared by ultrasonicating 20-25 mg photocatalyst in 50 µL Nafion (5.0 wt%, Sigma Aldrich) and 250 µL of ethanol for 20-30 minutes. Fluorine-doped tin oxide (FTO) (2x1$cm^2$ pieces) which was used as the substrate was cleaned and dried at 100 ºC. An area of 1$cm^2$ of the substrate was masked by scotch tape and spin coating (750 rpm, 60 seconds) was performed by collecting 15 µL of slurry each time. The electrode films were then dried under vacuum at 100ºC for 1 hour and Cu wire connections were made with the help of Ag paste. The portion of electrode, except the photocatalyst part, was electronically sealed by transparent epoxy coating and left overnight. A 0.5 M $Na_2SO_4$ aqueous solution was used as the electrolyte. A 300 W Xenon lamp, with a calibrated intensity of 100 mW/$cm^2$ was used as the light source. Mott-Schottky measurements were carried out on working electrodes in a 0.5 M $Na_2SO_4$ aqueous electrolytes solution (pH 7) at various operating frequencies and an amplitude of 0.005 V.

**Computational Methods**

We have carried out first-principles calculations within density functional theory (DFT) employing Quantum Espresso (QE)[7] and VASP[8] software packages. The exchange correlation energy is treated within a Generalized Gradient Approximation through a functional parameterized by the Perdew BurkeErzwehof (PBE)[9]. We used projected augmented wave[10] method to describe the interaction between the valence electrons and ionic cores. We used kinetic energy cut-off of 40 Ry to truncate the plane wave basis for representing Kohn-Sham wavefunctions and a uniform mesh of 4x4x4 k-points to sample integrations over Brillouin zone (BZ). Valence electron configurations used in the PAW potentials of Cd, Cl and P are $4d^{10}\ 5s^{2.0}$, $3s^2\ 3p^5$ and $3s^2\ 3p^3$ respectively. We relaxed structures to minimize energy such that Hellmann-Feynman force acting on each atom is less than 0.02 eV/Å. Self-consistency in the Kohn-Sham solution was achieved with a convergence tolerance of $10^{-7}$Ry. Dielectric properties were calculated using Density functional theory-linear response as implemented in QE. In calculations of the density of states, a uniform mesh of 16x16x16 k-points in the BZ was employed. Since DFT typically underestimates the electronic bandgap, we have used HSE functional[11] to estimate gaps accurately. In this work, we determined structure and electronic properties of four compounds: $Cd_7P_4Cl_6$, $Cd_4P_2Cl_3$, $Cd_3PCl_3$ and $Cd_2P_3Cl$.

To assess the suitability of these cadmium phosphohalides as photocatalysts for the hydrogen evolution reaction (HER), we aligned their valence and conduction band edges w.r.t. vacuum potential (see supporting information), and that their energies relative to the redox potential of HER make it suitable catalytic activity. Here, the vacuum potential in reference to energies of electronic bands was determined with simulations of (001) surface terminated slab with a vacuum of 15 Å, relaxing the structure. We subtracted the macroscopic potential of bulk from VBM and CBM of compounds and aligned the energies of band edges with respect to vacuum using $\Delta V$: the difference between average potential in the vacuum and average potential deep inside the slab.

# 4. Results and Discussion

We have prepared different cadmium phosphohalides by employing suitable reaction temperatures.We show the powder XRD patterns of the four phosphochlorides in **Figure 1a**. Pure forms of some of these ternary compounds, are not reported in the literature. For example, Shevelkov *et al.* obtained a mixture in an attempt to synthesize $Cd_7P_4Cl_6$.[12] A reaction temperature of 350 ºC results in the formation almost entirely of $Cd_3PCl_3$ (Orthorhombic; Pmna, a= 13.0, b= 7.95 and c= 7.0 Å) with small proportion of hexagonal phase. Increase in the reaction temperature to 400 ºC gives rise to $Cd_7P_4Cl_6$ along with the small proportion of orthorhombic $Cd_3PCl_3$ (**Figure 1b**). Pure $Cd_7P_4Cl_6$ (cubic; Pa-3, a =11.93 Å) is obtained at a temperature of

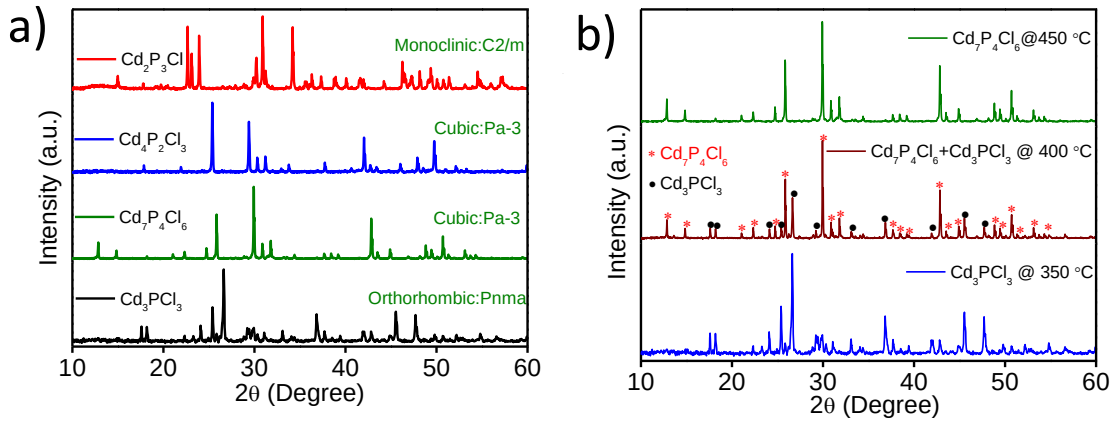


Figure 1. PXRD patterns of a) Pure cadmium phosphochlorides, and b) Role of temperature on product selectivity and purity.

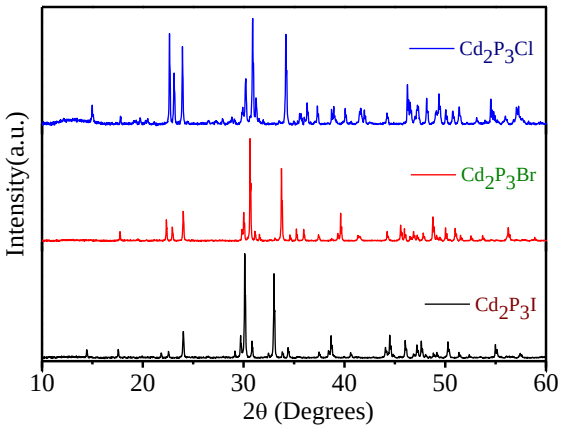


Figure 2. PXRD patterns of $Cd_2P_3X$ compounds (X=Cl, Br and I).

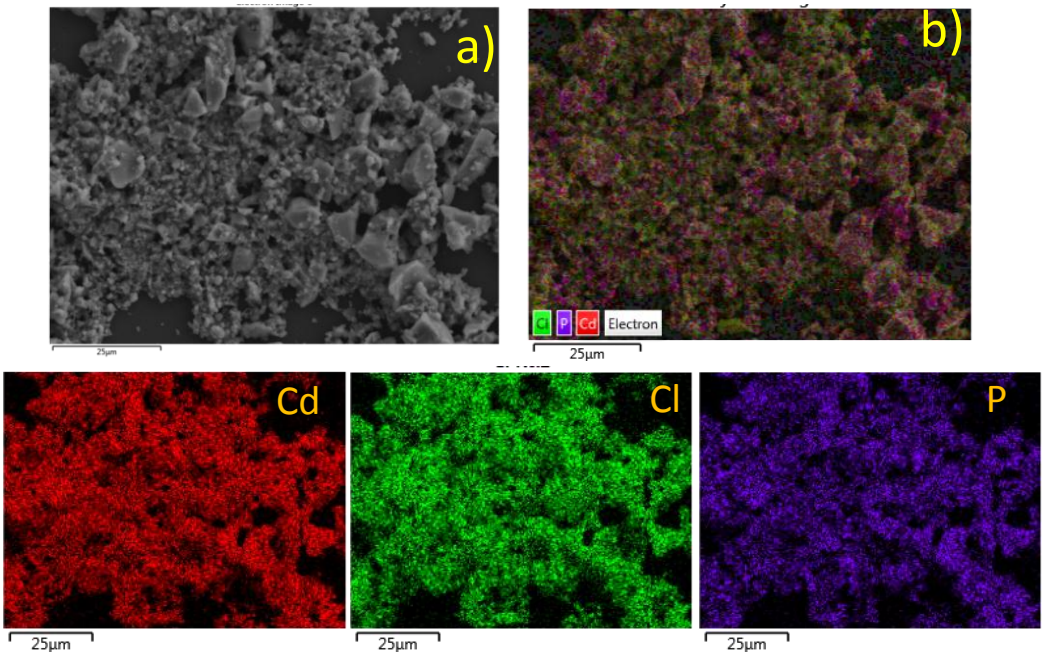


Figure 3. a) SEM image of $Cd_7P_4Cl_6$ sample, b) elemental mapping image showing presence of Cd, P, and Cl in sample. Individual mapping for Cd, Cl, and P in $Cd_7P_4Cl_6$.

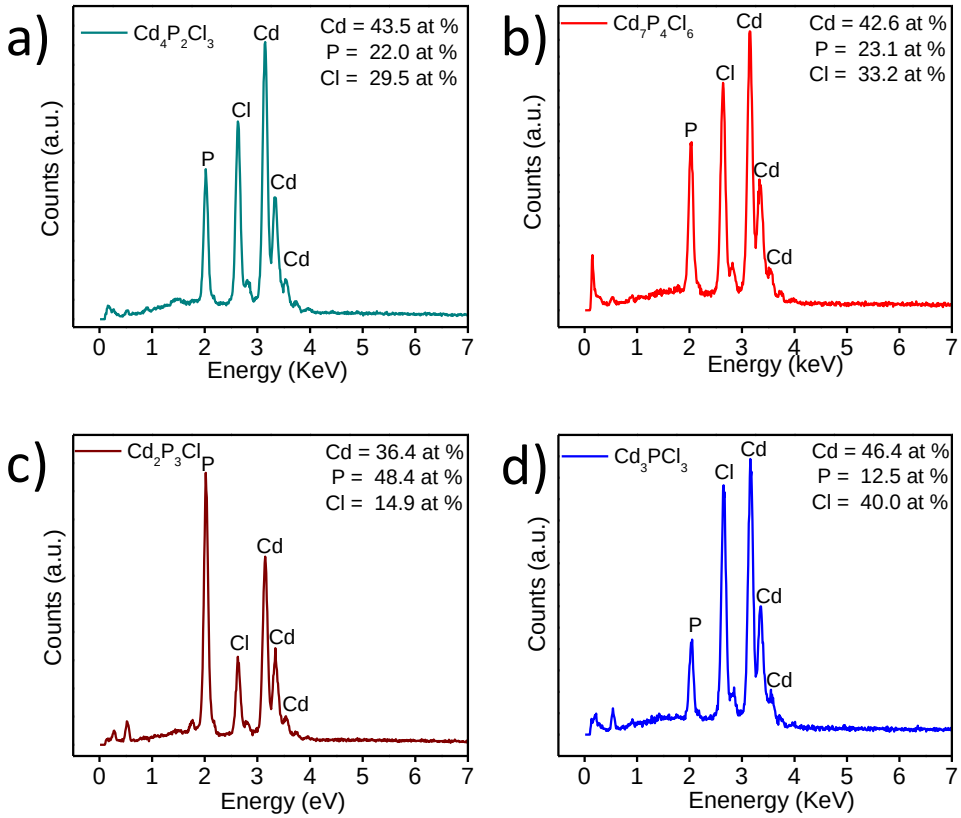


Figure 4. EDAX spectra of a) $Cd_4P_2Cl_3$, b) $Cd_7P_4Cl_6$, c) $Cd_2P_3Cl$, and d) $Cd_3PCl_3$ compounds.

450 ºC and pure $Cd_4P_2Cl_3$ (cubic; Pa-3, a = 12.13 Å) at 500 ºC. Unlike the above-mentioned Cd-P-Cl compounds, $Cd_2P_3Cl$ requires a temperature gradient to yield the product by the chemical vapor transport of the reactants. $Cd_2P_3Cl$ has the monoclinic structure (C2/c, a= 7.98, b= 8.98 and c= 7.55 Å).[6] The bromo and iodo analogues of $Cd_2P_3Cl$ also possess the monoclinic structure (C2/c) (**Figure 2**) (**Table 1**). Energy dispersive X-ray analysis (EDAX) along with the elemental mapping revealed the relative Cd/P and Cd/Cl ratios confirming the stoichiometry of the compounds to be close to the chemical formula (**Figure 3 and 4**).

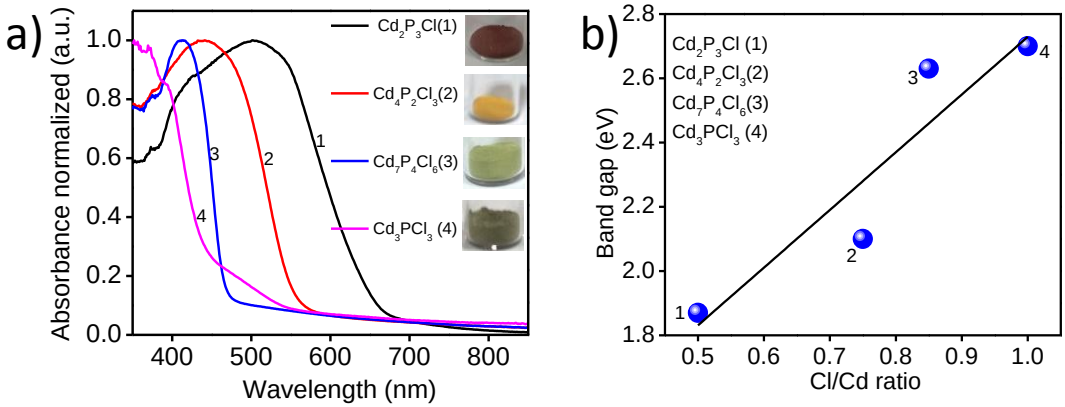


Figure 5. a) UV-vis absorption spectra of cadmium phosphochlorides, and b) Band gap of compounds with respect to Cl/Cd ratio.

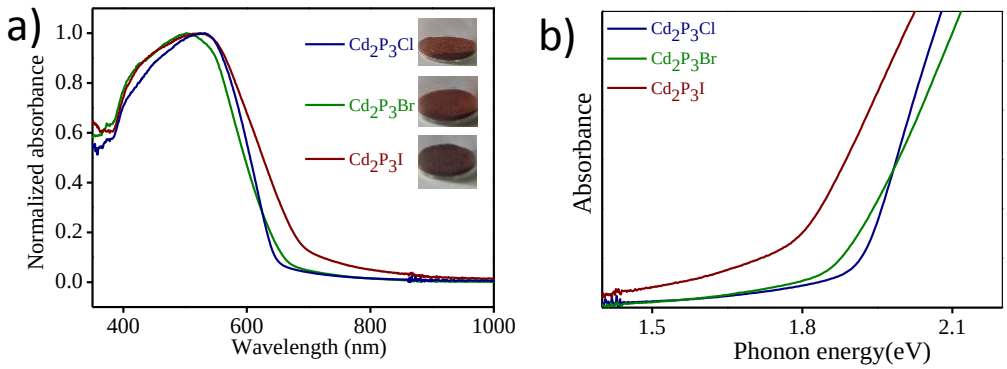


Figure 6. UV-vis absorption spectra of $Cd_2P_3X$ compounds (X= Cl, Br, and I).

The UV/visible spectra of the cadmium phosphochlorides are shown in **Figure 5a** along with the colors of the samples. The band gaps are 2.70, 2.63, 2.21 and 1.87 eV for $Cd_3PCl_3$, $Cd_7P_4Cl_6$, $Cd_4P_2Cl_3$, and $Cd_2P_3Cl$ respectively. The band gaps of $Cd_4P_2Cl_3$ and $Cd_7P_4Cl_6$ are quite different although they crystallize in the cubic

structures. It is noteworthy to mention that the band gap increases with the increase in the Cl/Cd ratio of these compounds (**Figure 5b**), whereas gap decreases with the increase in the P/Cd ratio. Compounds of formula, $Cd_2P_3X$ have band gaps of 1.87, 1.86 and 1.74 eV respectively for X= Cl, Br and I (**Figure 6**). There is negligible change in the band gap with X as in $Cd_4P_2X_3$.[13]

**Theoretical Results**

We now discuss the structural aspects along with the electronic properties, as revealed by first-principles calculations. Structures of $Cd_4P_2Cl_3$ and $Cd_7P_4Cl_6$ obtained from calculations agrees well with the experimental ones (**Figure 7 and 8**).[12] Crystal structure of $Cd_4P_2Cl_3$ can be best described in terms of distorted face-centered cubic packing of Cd atoms (**Figure 7a**). There are two distinct Cd and P atoms and one Cl atom. P atoms occur in pair with bond length of 2.19 Å, and P1 atom occupy 1/8 octahedral voids whereas P2 atoms fill 1/8 tetrahedral voids. Cl atoms occupy 3/4 of

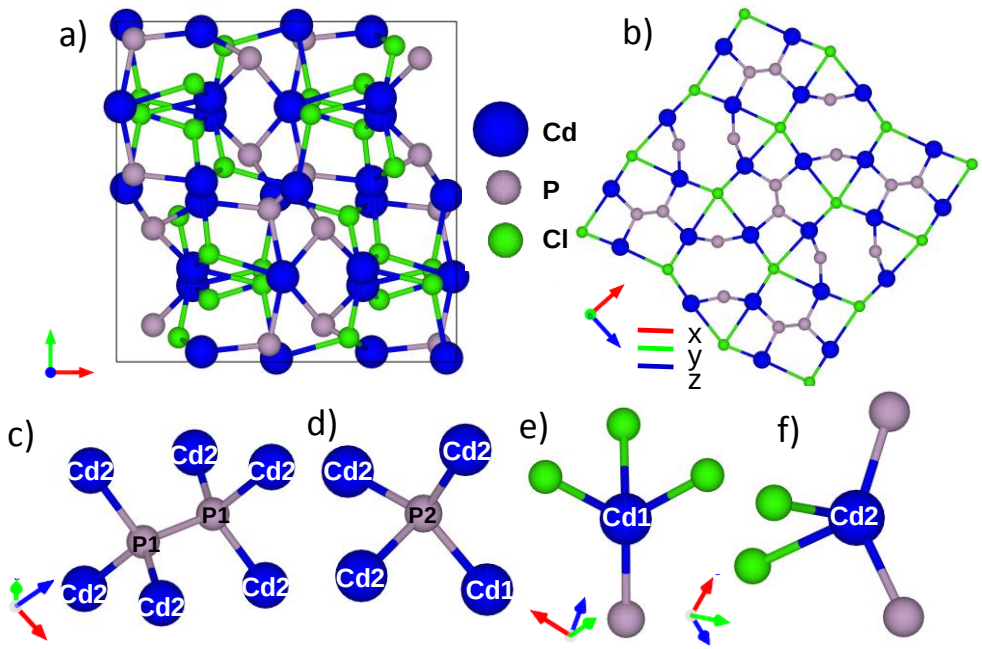


Figure 7. a) Crystal structure of $Cd_4P_2Cl_3$, b) 4 P-P bonds are at an angle of 90º with the P-P bond at center in the xz plane, c) P-P bonding pair coordinated by 6 Cd2 atoms, d) coordination of P2 atom, e) Cd1 is coordinated tetrahedrally by 3 Cl and 1 P atoms, and f) Cd2 coordinated tetrahedrally by 2P and 2Cl atoms.

the octahedral voids and are shifted from the octahedral center towards one of its faces. Each P atom in P-P pair is connected with 3 Cd2 atoms.

The crystal structure of $Cd_7P_4Cl_6$ consists of an octahedral anionic complex $[CdCl6]^{4-}$ and a three-dimensional cationic network, $[Cd_3P_2]^{2+}$, as shown in **Figure 8a**. The 3D network, $[Cd_3P_2]^{2+}$, consists of 3 Cd1, P-P bonds and the P-P bond length is 2.19 Å (**Figure 8b**). The Cd-Cl bond length in the octahedral $[CdCl_6]^{4-}$ is 2.66 Å (refer **Figure 8c**). These paired P atoms constitute the $P_2^{4-}$ anions. A slightly distorted tetrahedron is further formed by the bonding of each P atom to the three Cd (1) atoms

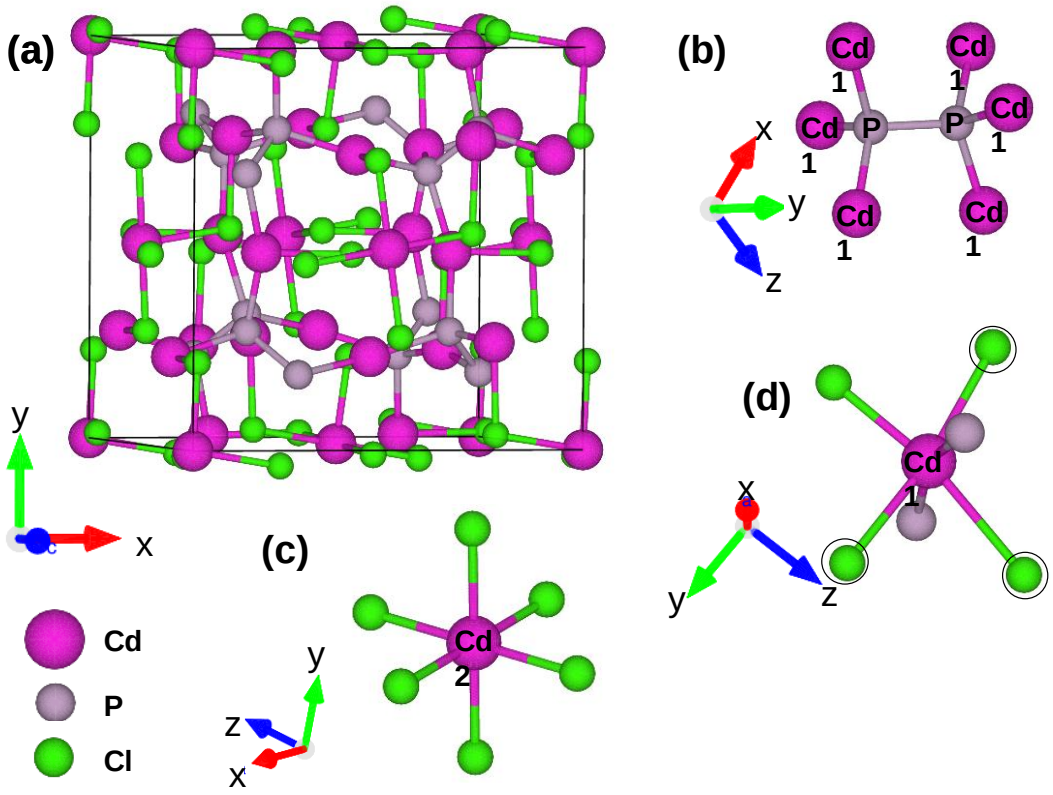


Figure 8. a) Crystal structure of $Cd_7P_4Cl_6$: there are two types of Cd atoms in the unit cell based on bonding, which are marked as Cd1 and Cd2, b) bonding of P-P pair with Cd1 atoms, c) Cd2 is octahedrally coordinated by Cl atoms, and d) Coordination of Cd1:Cd1 is octahedrally coordinated by two P and four Cl atoms, note that black circles around Cl atoms in figure c indicate Cd-Cl bond of lengths more than 3Å.

(**Figure 8d**). In $Cd_7P_4Cl_6$, Cd1 has a very peculiar bonding arrangement: it is closely bonded to two P atoms at a distance of 2.48 Å and is further bonded to one Cl atom with bond length 2.76 Å. Three more Cl atoms are bonded to this Cd1 at Cd-Cl distances of 3.03, 3.08, and 3.28 Å; however, these exceed the sum of ionic radii of Cd and Cl and are perceived to be too long for Cd1 and Cl to be bonded. It can be

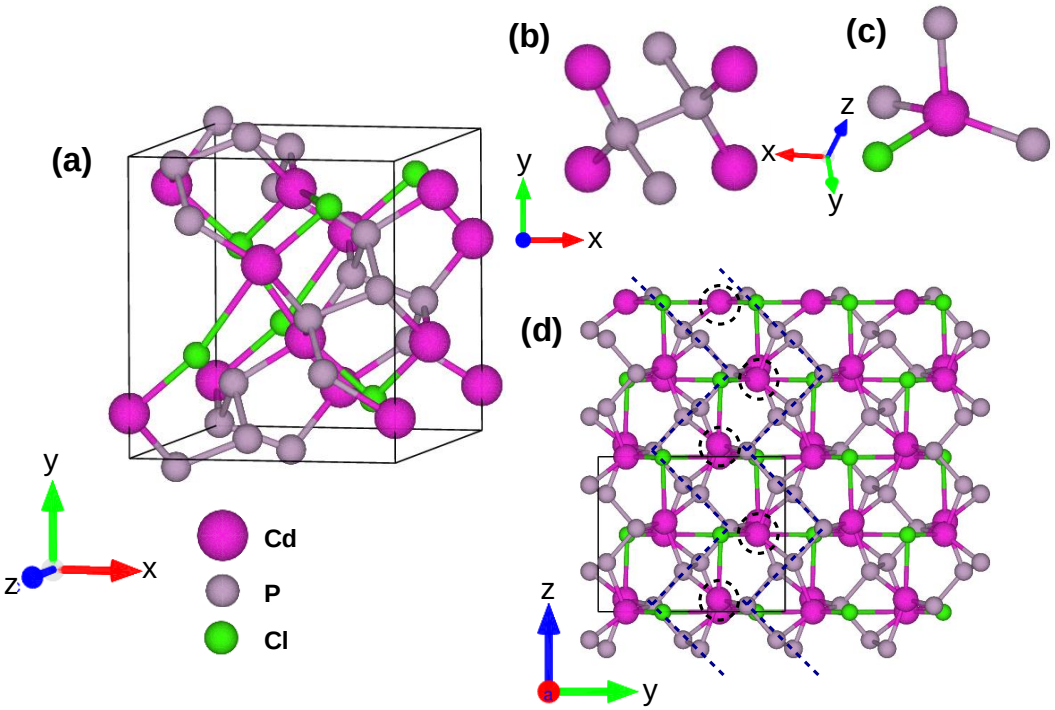


Figure 9. a) Crystal structure of $Cd_2P_3Cl$, b) Local structure of P-P pair in $Cd_2P_3Cl$ where each P is connected with 2 Cd and 1P atom, c) tetrahedrally bounded Cd atom with 3P and 1 Cl atom in $Cd_2P_3Cl$, and d) zigzag chain of P atoms (in ZY plane) (dotted lines) and neighbouring chains are connected by Cd atoms (dotted circles) with bond inperpendicular direction (dashed line) of this chain.

seen that six Cd (1) atoms enclose each $P_2^{4-}$ dumbbell. A perovskite-like framework is formed by the octahedra units ($[Cd_6P_2]^{8+}$) having the P-P bond at its center and shares all vertices with adjacent octahedra ($[CdCl_6]^{4-}$).

The structure of $Cd_2P_3Cl$ consists of poly-anionic P atoms forming a zigzag chain running along the c axis (**Figure 9a**), and two Cd atoms bridging the neighboring zigzag chains $(P)_n$ (**Figure 9d**). In the zigzag chain of P atoms, two P-P bonds of 2.21 Å are at 103.2º, and this $P_3^{6-}$ is connected to another by P-P bond of 2.20 Å at an angle of 98.8º. Each P-P pair is connected to 4 Cd and 2 P atoms (**Figure 9b**). The Cd atoms are coordinated tetrahedrally to one Cl and three P atoms (**Figure 9c**). The bond lengths of Cd-Cl, Cd-P1, Cd-P2, and Cd-P3 bonds are 2.71 Å, 2.56 Å, 2.65 Å and 2.59 Å respectively. The optimized lattice parameters are a = 8.08 Å, b = 9.12 Å and c = 7.64 Å, comparable to the experimental values.

The orthorhombic structure of $Cd_3PCl_3$ (**Figure 10a**) is based on a distorted two-layer stacking of chlorine and cadmium atoms, in which half of the octahedral sites

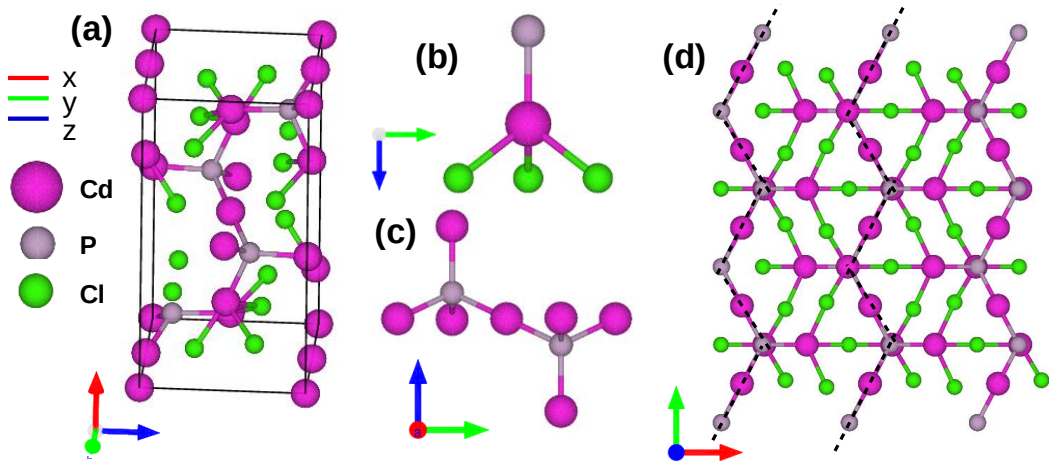


Figure 10. a) Crystal structure of $Cd_3PCl_3$, b) tetrahedrally bounded Cd atom in $Cd_3PCl_3$ with 3 Cl and 1 P atom, c) Cd atom bounded to 2P atoms making P-Cd-P angle 180º, where each P atom is bounded with 3 Cd atoms in $Cd_3PCl_3$, d) zigzag chain of Cd and P atoms in the xy plane highlighted by dashed lines (neighbouring zigzag chain are connected by Cd-Cl bond in the xy plane in $Cd_3PCl_3$.

and 1/8 of the tetrahedral sites are occupied by cadmium atoms. Cd is bonded to 3 Cl atoms and 1 P atom (**Figure 10b**). Two P atoms are bonded to Cd forming the P-Cd-P motif with Cd-P bonds of 2.47 Å at an angle of 180º, where each P atom is connected with another 3 Cd atoms. Each P is bonded to 4 Cd atoms tetrahedrally, of which Cd-P bonds are of 2.47 Å, and one Cd-P bond is 2.49 Å (**Figure 10c**). The zigzag chain structure of Cd and P atoms is highlighted in **Figure 10d**. Neighboring zigzag chains are connected by Cd and Cl bonds along the x-direction. Optimized lattice parameters of $Cd_3PCl_3$ are a = 13.26 Å, b = 8.08 Å and c = 7.08 Å, within the GGA errors of experimental values.

We have investigated the electronic structures of the optimized structures of $Cd_4P_2Cl_3$ and $Cd_7P_4Cl_6$ (having intermediate P/Cd and Cl/Cd ratios) along with those of $Cd_2P_3Cl$ and $Cd_3PCl_3$ with the highest P/Cd and Cl/Cd ratios respectively. $Cd_4P_2Cl_3$ and $Cd_7P_4Cl_6$ possess similar electronic structures. We find that $Cd_4P_2Cl_3$ has a direct band gap of 1.41 eV at Γ-point (**Figure 11a**). Our estimate of its band gap with HSE calculation is 3.09 eV, which is overestimated by 40% w.r.t. experimental band gap of 2.2 eV. From density of states, we find that the VBM is constituted of p orbitals of Cd and P atoms and CBM is constituted of s orbitals of P and Cd atoms (**Figure 11b**).

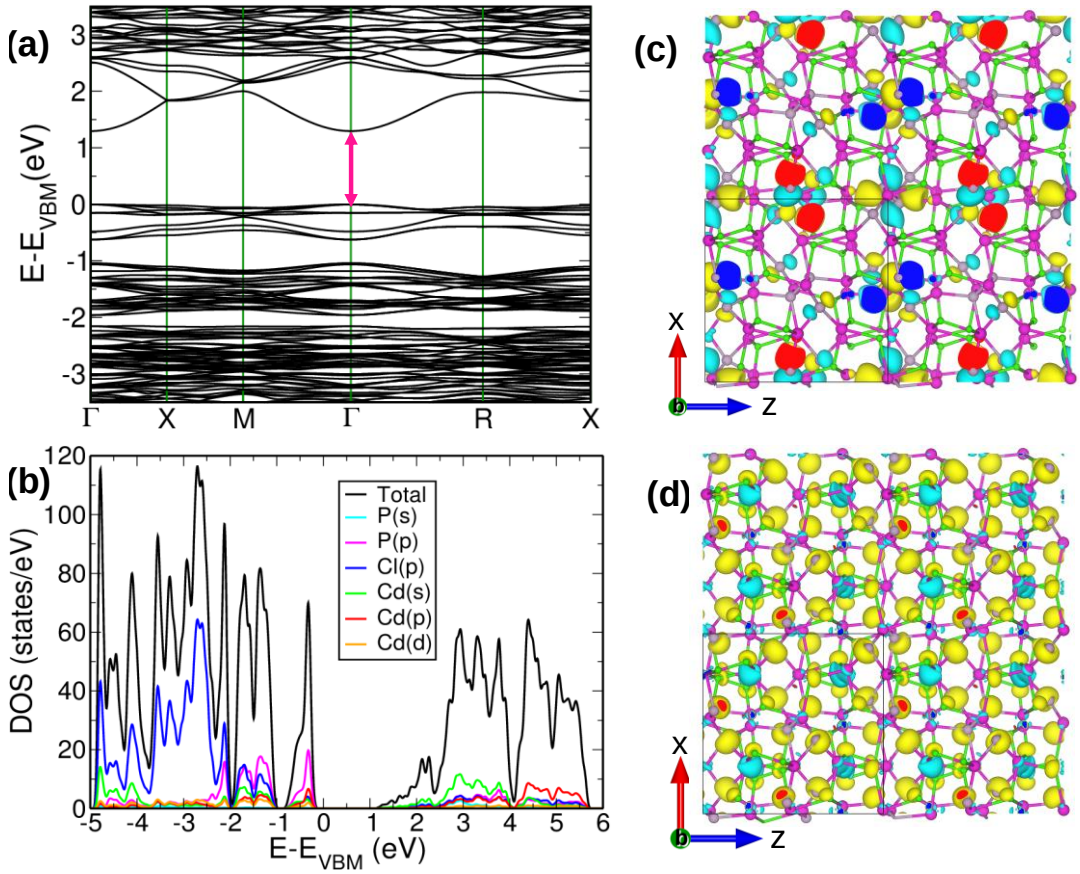


Figure 11. $Cd_4P_2Cl_3$: a) Electronic structure, b) projected density of states, and isosurfaces of wavefunctions at c) VBM, and d) CBM at Γ point. VBM isosuraface show л antibonding of P atom with bond length 2.20 Å. CBM isosurface show σ antibonding of P atoms along P-P bonds and hybradization of p-orbital of Cd and P atoms. Yellow and cyan colors of the isosurface of wavefunction indicate positive and negative sign respectively.

Isosurface of VBM show л antibonding of P atoms whereas CBM isosurfaces show hybridization of s orbitals P and Cd atoms (**Figure 11c, 11d**). GGA based calculations on $Cd_7P_4Cl_6$ yield direct band gap of 1.8 eV at Γ-point (**Figure 12a**) which is in the range of typical DFT based underestimation. HSE-based estimate of the band gaps for this compound is 3.2 eV which is overestimated by 23 % w.r.t to the experimental band gap. The projected density of states (PDOS) reveals that the states at the VBM are constituted of the p-orbitals of P (dominant contribution) and Cd and CBM has contribution from the s-orbital of Cd along with some hybridization with the p-orbital of P (**Figure 12b**).

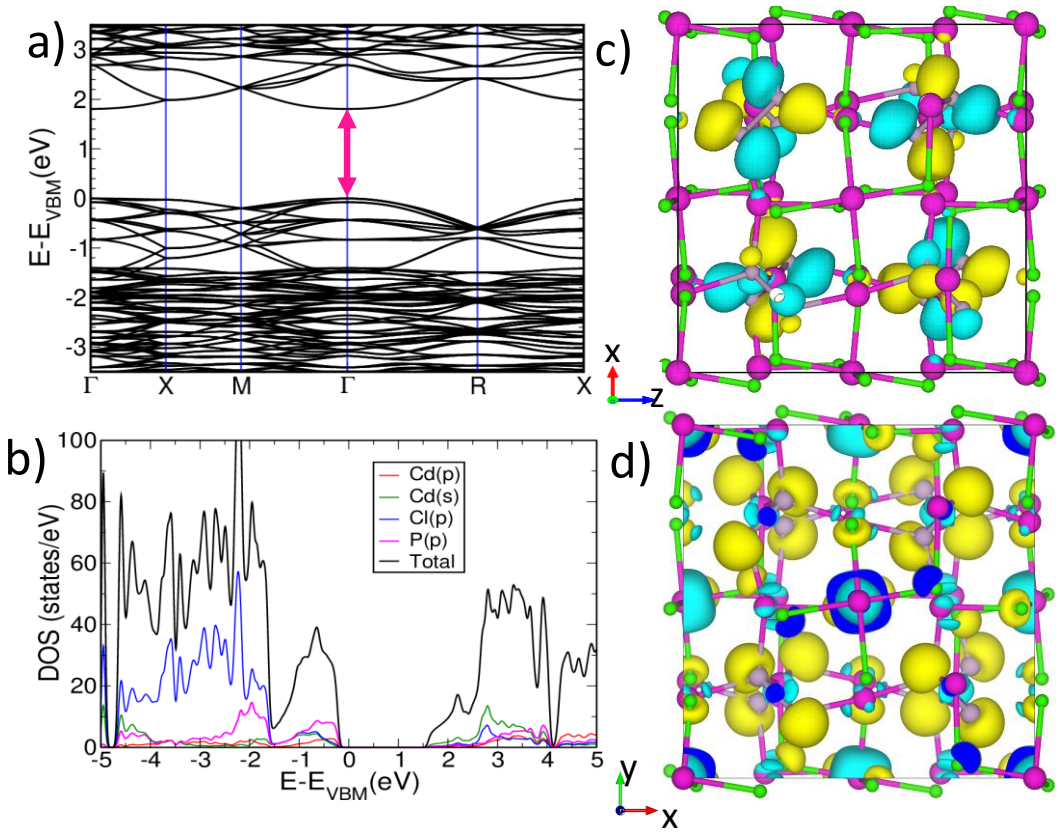


Figure 12. $Cd_7P_4Cl_6$: a) Electronic structure, b) projected density of states, and isosurfaces of wavefunction at c) VBM, and d) CBM at Γ-point.Yellow and cyan colors of the isosurface of wavefunction indicate positive and negative sign respectively.

Isosurfaces of states at VBM and CBM of electronic structure at Γ- point gives a clear idea of the electronic frontier states (**Figure 12c, 12d**). The VBM in this compound is primarily made up of л-antibonding orbitals of P-atoms from the P-P pairs. The states at the CBM are constituted primarily of the σ-antibonding orbital of P also involving hybridization of Cd p-orbitals. The next two states (VBM2 and VBM3) are degenerate with the VBM in involving other P-P pairs.

$Cd_3PCl_3$ with the highest Cl/Cd ratio shows a direct band gap of 1.82 eV at the Γ-point (**Figure 13a**), while HSE calculations estimate the band gap to be 3.86 eV, which is overestimated by 42 % w.r.t experimental value of 2.7 eV. Analysis of DOS and charge densities show that the VBM has almost equal contribution from the p-orbitals of P and Cl along with a slight contribution of Cd p-orbitals, while the CBM is made from the s, p, and d orbitals of P, Cl and Cd respectively (**Figure 13b to 13d**).

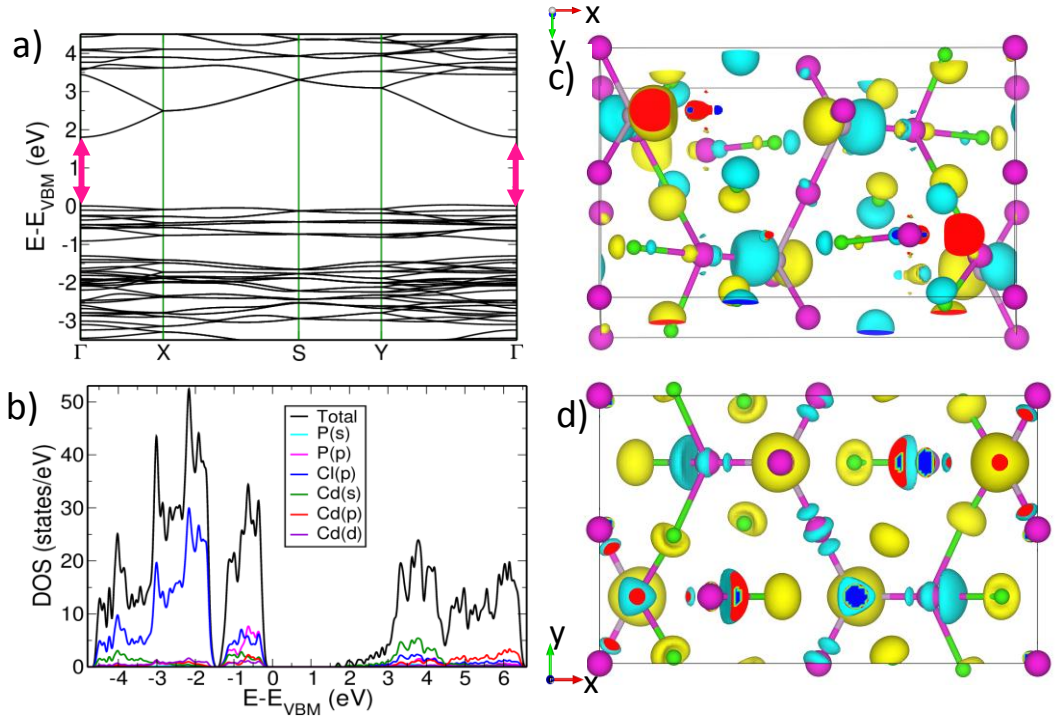


Figure 13. $Cd_3PCl_3$: a) Electronic structure, b) projected density of states and isosurfaces of wavefunctions at c) VBM, and d) CBM at the Γ-point. Yellow and cyan colors of the isosurface of wavefunction indicate positive and negative sign respectively.

The VBM and CBM states in $Cd_3PCl_3$ possess a dominant contribution from the Cl-orbitals, unlike other cadmium phosphochlorides.

Unlike that of other cadmium phosphochlorides, the electronic structure of $Cd_2P_3Cl$, reveals it to be an indirect band gap semiconductor, with its VBM at the mid-point of the M-Y path and the CBM at the Y-point (**Figure 14a**). The value of the band gap obtained by GGA based calculations is 1.57 eV; the experimental bandgap is 1.87 eV and our estimate from HSE calculations is 2.24 eV, overestimated by 20% relative to the experimental value. The density of states of $Cd_2P_3Cl$ reveals VBM to be essentially constituted of the p orbitals of P and Cd atoms, while the s and p orbitals of Cd and P make contributions to the CBM respectively (**Figure 14b**). We can understand the bonding better by visualizing the isosurfaces of the VBM and CBM. The VBM is essentially P (л) bonding orbital of P-P pairs. The states at CBM show л-antibonding character of p-orbitals of P in P-P pairs (**Figure 14c, 14d**), with some hybridization with p-orbitals of Cl and Cd atoms.

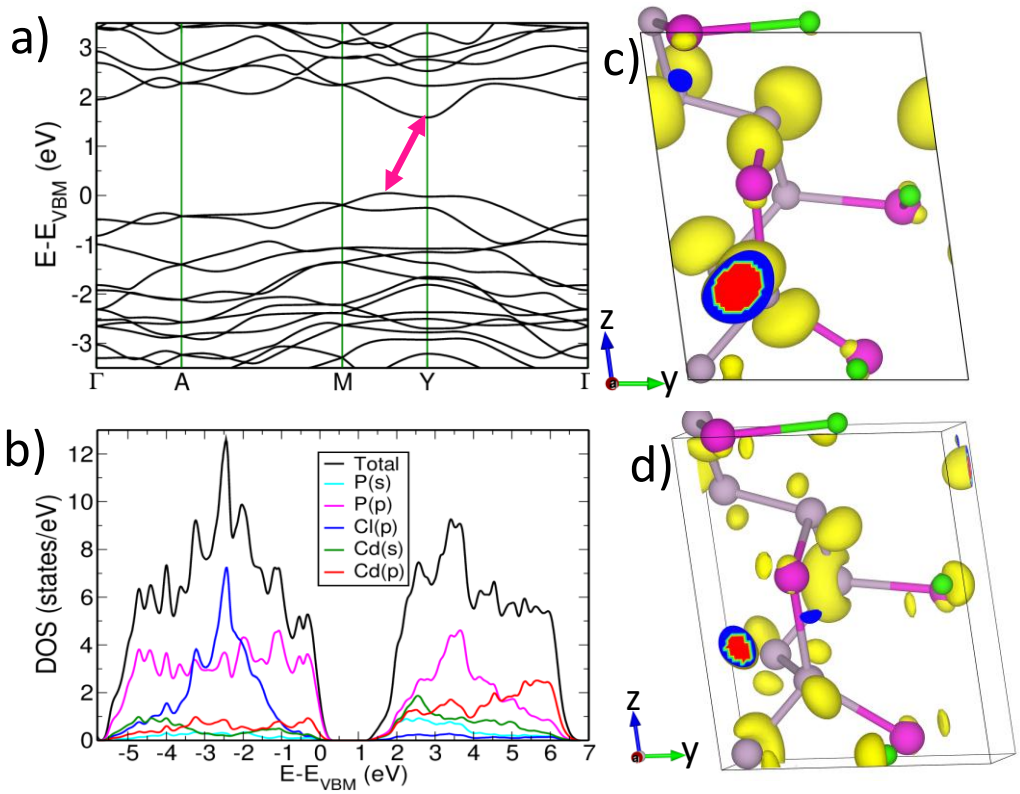


Figure 14. $Cd_2P_3Cl$: a) Electronic structure, b) projected density of states, and isosurfaces of wavefunction at c) VBM and d) CBM.

$Cd_2P_3Cl$ with the highest P/Cd ratio possesses VBM and CBM states exclusively contributed by л bonding and antibonding orbitals of P-P pairs (**Table 2**).

To get an idea about hybridization, bonding and ionic character we determined the Born charge tensors (Z*) which describe the forces exerted on an ion in response by electric field. We also obtain estimates of the electronic contribution of dielectric constant. Estimates of the Born charges and the electronic contribution to the dielectric constant of all the four compounds are shown in **Table 1**. Z* values indicate that covalency is stronger in P-rich compounds. $Cd_2P_3Cl$ is the only compound with both valence and conduction bands made of orbitals of P (see Table I). Despite having different band gaps the magnitude of dielectric constant (ε) of all compounds are comparable except for $Cd_2P_3Cl$. Notably higher ε of $Cd_2P_3Cl$ is because of its high polarizability arising from л-bonding and л-antibonding frontier states made of p-orbitals of P atoms (**Table 2**). We have also calculated the valance electron count (Lowdin charges) of Cd, P, and Cl atoms in cadmium phosphochlorides (**Table 3**).

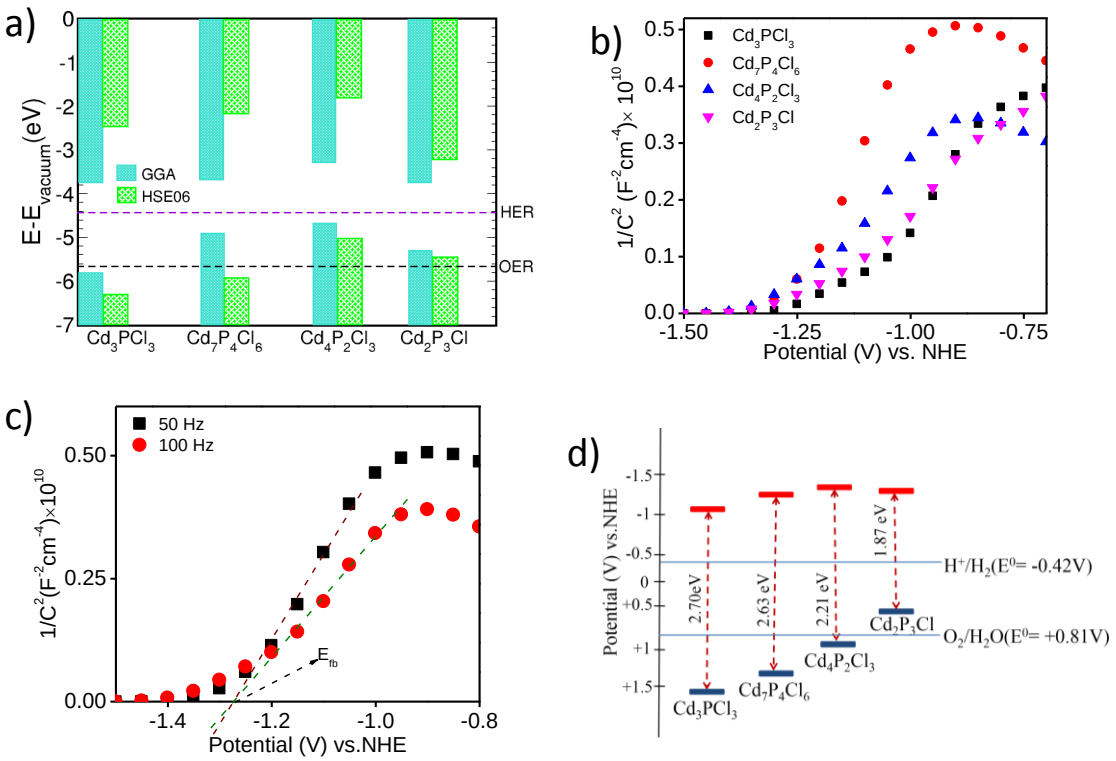


Figure 15. a) Band gaps and band edge positions of cadmium phosphochlorides calculated with the GGA and HSE06 functional with respect to vacuum potential, b) Mott-Schottkey plot for cadmium phosphochloride compounds at an opertaing frequencey of 50 Hz, c) Mott-Schottkey plot for $Cd_7P_4Cl_6$ electrode at operating frequencies of 50 and 100 Hz in 0.5 M $Na_2SO_4$ electrodes, and d) Conduction and valence band edges of the compounds obtained from MS measurements along with the alignment of bands with respects to $H_2O$ redox potentials at pH 7.

To assess the suitability of these cadmium phosphohalides as photocatalysts for the hydrogen evolution reaction (HER), we aligned their valence and conduction band edges w.r.t. vacuum potential, and that their energies relative to the redox potential of $H_2O$ make it suitable for $H_2O$ splitting. Our calculations reveal that all the cadmium phosphochloride compounds possess CBM position suitable for performing HER. $Cd_7P_4Cl_6$ and $Cd_3PCl_3$ also possess suitable VBM positions for performing OER (**Figure 15a**). In the light of the theoretical predictions, we have estimated the CBM and VBM positions of the phosphohalides by Mott-Schottky measurements at pH 7 in 0.5 M $Na_2SO_4$ electrolyte under various operating frequencies.

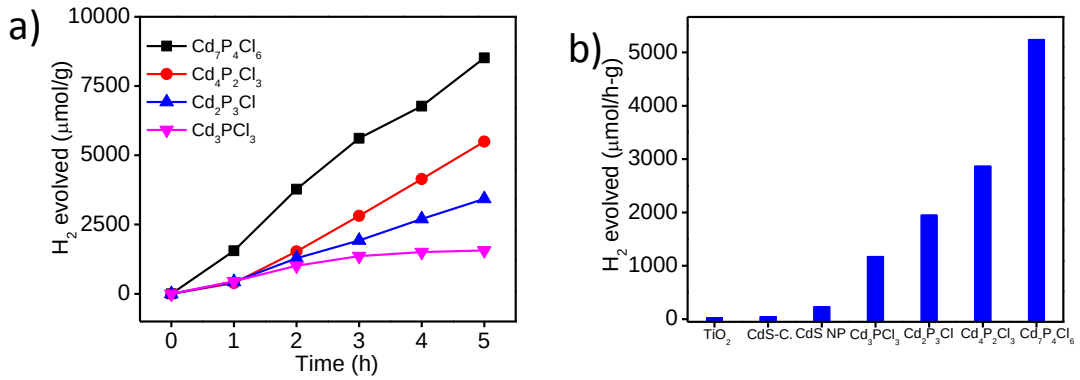


Figure 16. a) Time course of hydrogen evolution, and b) Comparative HER activity of cadmium phosphochlorides along with the HER activity of CdS and $TiO_2$.

Presence of a positive slope of MS plot suggests n-type conductivity in these compounds (**Figure 15b**).[14] The flat band potentials ($E_{fb}$) for $Cd_3PCl_3$, $Cd_7P_4Cl_6$, $Cd_4P_2Cl_3$ and $Cd_2P_3Cl$ are -1.15, -1.25, -1.30 and -1.28 V vs. NHE respectively. The flat band potentials vary almost in the same direction as the band gaps. Measurements at various operating frequencies shown that flat band potentials obtained at different operating frequencies remain the same (**Figure 15c**). Provided that these compounds are n-type, and the Fermi level lies close to the conduction band minima (CBM), the flat band potential gives an approximate position of CBM in these compounds.[14-15] The VBM of the compounds could be estimated from a knowledge of the band gap and the position of the CBM. There is no significant change in the CBM of the compounds, but the VBM position shifts downwards with an increase in the Cl/Cd ratio similar to the observation found in the case of first-principles calculations (**Figure 15d)**. The alignment of CBM and VBM positions with respect to the water redox potential shows thermodynamic suitability of these compounds for water splitting to generate hydrogen (**Figure 15d**).

**Photocatalytic $H_2$ evolution**

In the light of the above findings, we have investigated the photochemical hydrogen generation (HER) properties of these cadmium phosphohalides under visible-light irradiation. All the phosphochlorides compounds exhibit the hydrogen evolution reaction (HER) even without the assistance of any co-catalyst. Interestingly the HER rate and stability vary with the composition, $Cd_7P_4Cl_6$ exhibiting the highest activity of 5246.7 μmol/h-g, followed by $Cd_4P_2Cl_3$ (2870 μmol/h-g) and $Cd_2P_3Cl$

(1953.4 µmol/h-g) (**Figure 16a**). $Cd_3PCl_3$ exhibits the least activity (1178 µmol/h-g). It is noteworthy that HER activity is exhibited by these compounds in the absence of any co-catalyst, unlike metal chalcogenides wherein a co-catalyst is very crucial to obtain good activity. Such remarkable HER activity without any co-catalyst suggests high mobility and less recombination rate of charge carriers in these compounds.[16] **Figure 16b** compares the HER activity of these compounds with the well-explored state-of-the-art materials such as CdS, commercial (CdS-C.), CdS nanoparticles (CdS-NP) $TiO_2$-P25. $Cd_7P_4Cl_6$ and $Cd_4P_2Cl_3$ exhibit significantly higher HER activity than CdS and $TiO_2$ based photocatalysts under visible-light irradiation. PXRD patterns of all the compounds after catalysis show almost negligible change except $Cd_3PCl_3$ (**Figure 17**). In the case of $Cd_3PCl_3$ a significant broadening of the peaks suggesting photocorrosion due to leaching of Cd ions. More importantly, the concentrations of the released $Cd^{2+}$ ions in solution after the photochemical reaction were 0.40 and 0.19 ppm for $Cd_3PCl_3$ and $Cd_2P_3Cl$ samples respectively whereas, we did not observe any detectable amount of $Cd^{2+}$ ions in the case of $Cd_4P_2Cl_3$ and $Cd_7P_4Cl_6$ demonstrating

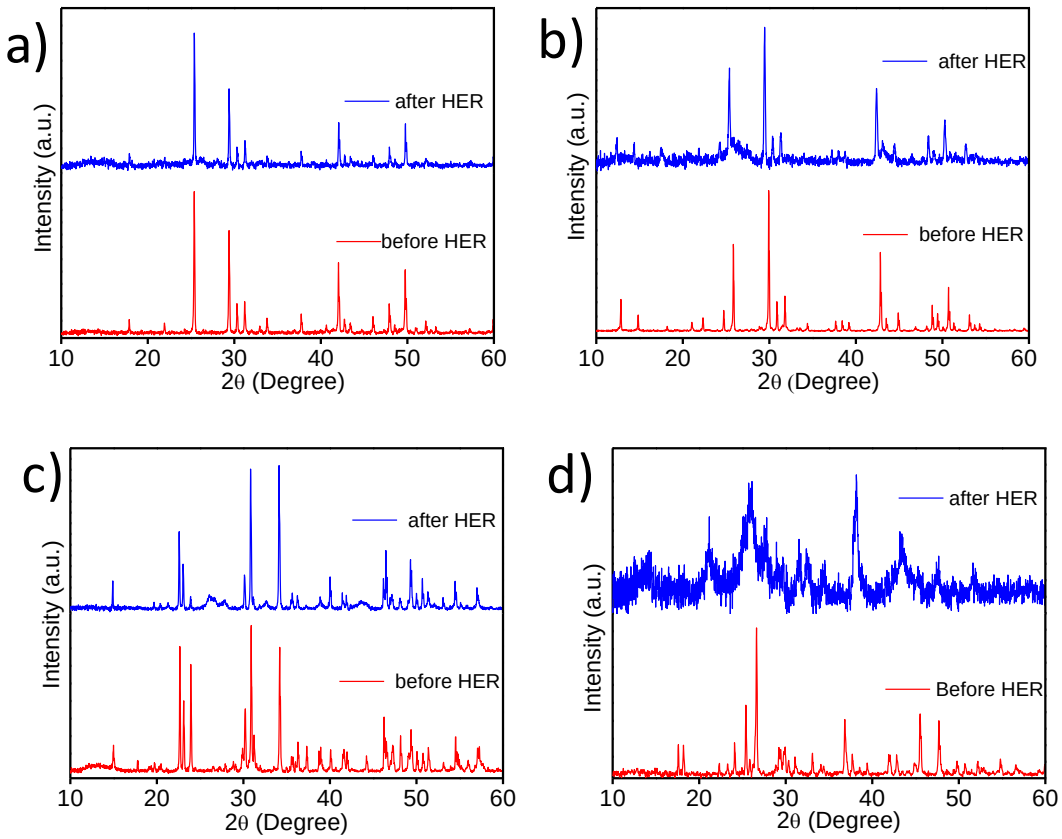


Figure 17. PXRD patterns of the compounds before and after their use in hydrogen evolution reaction for a) $Cd_4P_2Cl_3$, b) $Cd_7P_4Cl_6$, c) $Cd_2P_3Cl$, and d) $Cd_3PCl_3$.

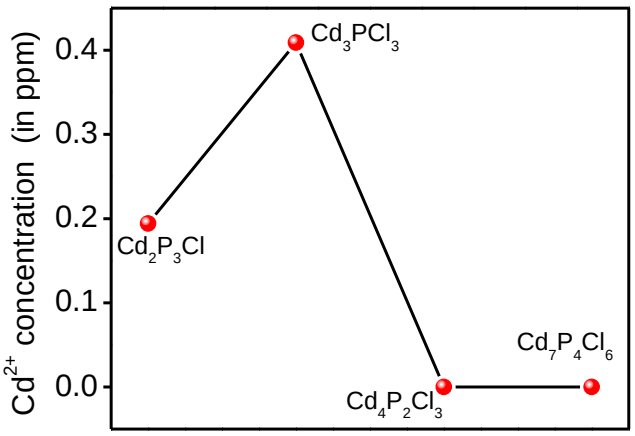


Figure 18. Concentration of $Cd^{2+}$ ions in solutions after the photochemical (PC) studies, obtained by ICP-OES measurements.

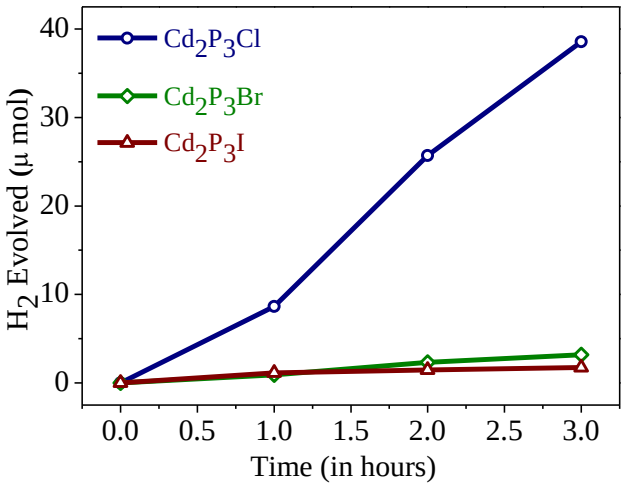


Figure 19. Time course of photochemical HER from $Cd_2P_3X$ compounds (X= Cl, Br, or I).

their better photostability (**Figure 18**). Loading of the co-catalyst on the surface or making heterostructures with oxide materials could farther increase the photostability of the semiconductor photosensitizers. Among $Cd_2P_3X$ compounds $Cd_2P_3Cl$ exhibits significantly superior activity than the $Cd_2P_3Br$ and $Cd_2P_3I$ (**Figure 19**).

To understand the HER activity and stability of the compounds, we have examined the lifetime of charge carriers employing photoelectrochemical techniques. $Cd_4P_2Cl_3$ and $Cd_2P_3Cl$ photoelectrodes exhibit rapid decay of the open circuit voltage ($V_{oc}$) whereas, $Cd_7P_4Cl_6$ exhibits slow $V_{oc}$ decay which suggests slow recombination

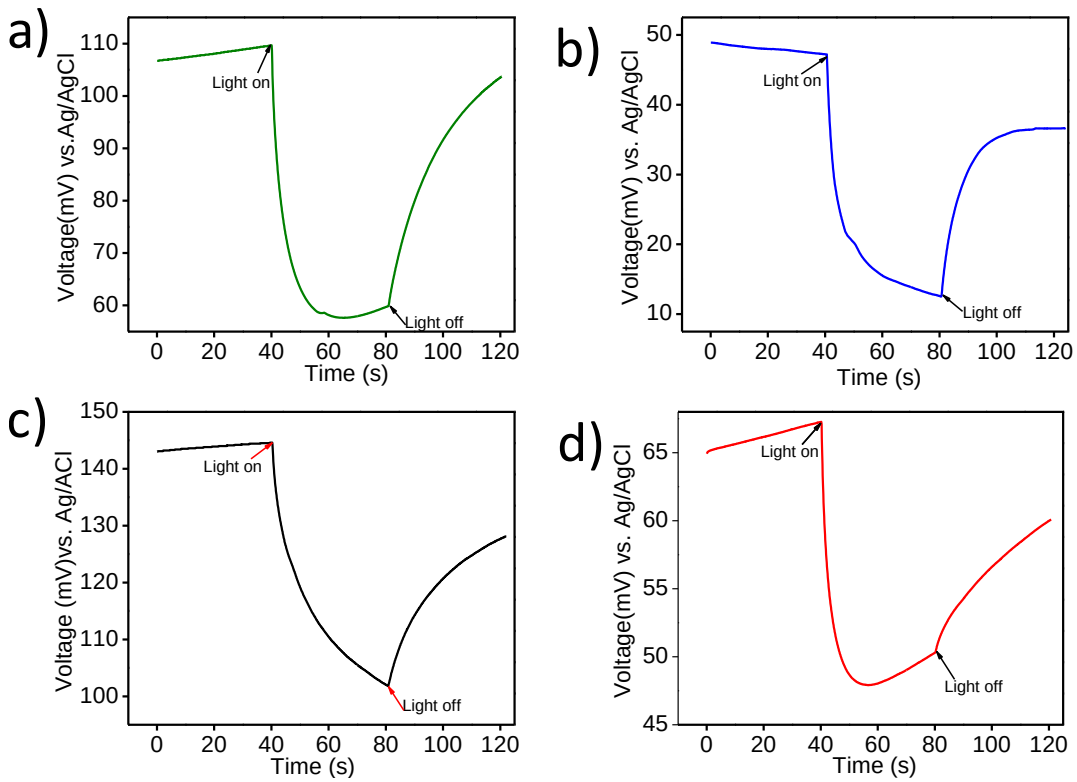


Figure 20. Open circuit potential plots of a) $Cd_4P_2Cl_3$, b) $Cd_2P_3Cl$, c) $Cd_3PCl_3$, and d) $Cd_7P_4Cl_6$ photoelectrodes, obtained at pH 7 in 0.5 M $Na_2SO_4$ electrolyte.

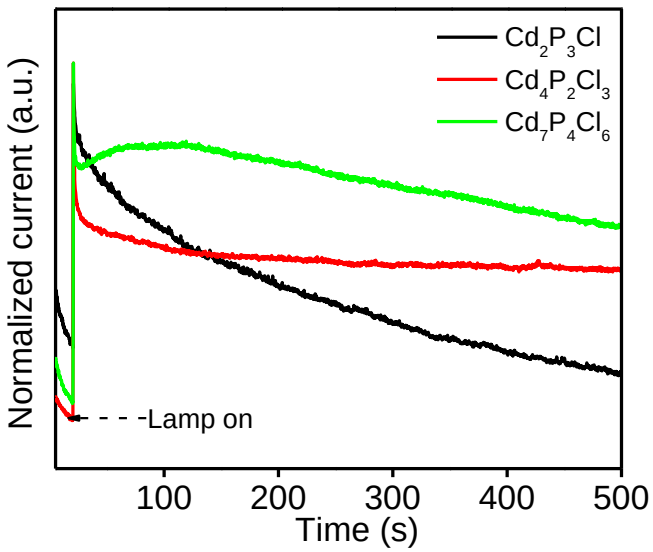


Figure 21. Transient photocurrent obtained from cadmium phosphochlorides under continuous light irradiation in 0.5 M $Na_2SO_4$ electrolyte.

rate and hence better activity in this compound (**Figure 20**).[17] An extremely slow $V_{oc}$ build-up with fast $V_{oc}$ decay of $Cd_3PCl_3$ suggests its poor HER activity and stability.

Photocurrent measurements over a longer time scale (500 s) under continuous light-irradiation revealed significant loss (~50 %) of photocurrent in the case of $Cd_2P_3Cl$ whereas $Cd_4P_2Cl_3$ and $Cd_7P_4Cl_6$ exhibited only 12 and 14 % decrease in the photocurrent, demonstrating their better photochemical performance (**Figure 21**). Transient photocurrent measurements show the highest photocurrent in the case of $Cd_7P_4Cl_6$ followed by $Cd_4P_2Cl_3$ and $Cd_2P_3Cl$ which is in the line with the HER performance (**Figure 22a**).[18] $Cd_3PCl_3$ with a rapid decay of photocurrent suggest speedy recombination of charge carriers and hence least activity and stability. The apparent quantum yields (AQY) are plotted against the absorption edge wavelengths of compounds. (**Figure 22b**). $Cd_2P_3Cl$ and $Cd_4P_2Cl_3$ with longer absorption edge wavelength exhibit low quantum yields of 3.6 and 6.6 % respectively, whereas $Cd_7P_4Cl_6$ with a shorter absorption edge wavelength (472 nm) exhibits the highest quantum yield of 20.1%. This observation suggests that charge carrier lifetime determines the HER activity of these compounds, rather than the number of photons involved in the generation of charge carriers which is in the line with our photoelectrochemical findings. $Cd_3PCl_3$ exhibits superior AQY (8.3 %) than $Cd_4P_2Cl_3$, but the lack of stability is the problem of the former. To the best of our knowledge, AQY obtained with $Cd_7P_4Cl_6$ is the highest known of any single inorganic semiconductor based photocatalyst in the bare form.

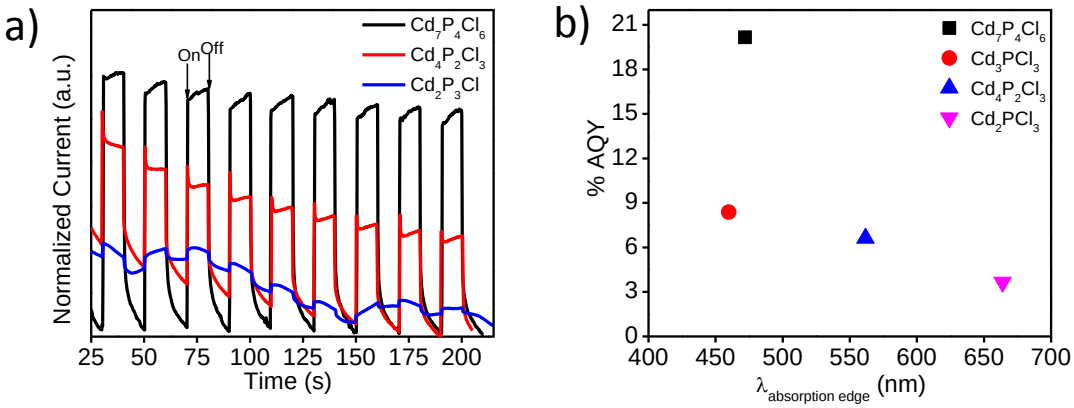


Figure 22. a) Transient photocurrent obtained from cadmium phosphochlorides electrodes in 0.5 M $Na_2SO_4$ aqueous electrolyte, and b) Apparent quantum yields with respect to their absorption edge wavelength.

**T**able 1. Crystal structure details and optical properties of $Cd_2P_3X$ compounds (X= Cl, Br, and I)

| Compound | Crystal System | Space group | a (Å) | b (Å) | c (Å) | Band gap (eV) |
|---|---|---|---|---|---|---|
| $Cd_2P_3Cl$ | Monoclinic | C2/c | 7.98 | 8.98 | 7.55 | 1.87 |
| $Cd_2P_3Br$ | Monoclinic | C2/c | 8.08 | 9.08 | 7.53 | 1.86 |
| $Cd_2P_3I$ | Monoclinic | C2/c | 8.25 | 9.30 | 7.51 | 1.74 |

**Table 2.** Structural features, electronic frontier states, Born charges and electronic dielectric constants ($\varepsilon^{\infty}$) of cadmium phosphochloride compounds. Note $O_h$: octahedral, $T_d$: Tetrahedral, $Z_1^*$: Digonal, $Z_2^*$: Off-digonal, [a]Space group, [b]Optical band gaps.

| Compound | Str. Features | VBM | CBM | Z | | $\varepsilon^{\infty}$ |
|---|---|---|---|---|---|---|
| | | | | Atom $Z_1^*$ | $Z_2^*$ | |
| $Cd_2P_3Cl$ (C2/c)[a] [b]1.87 eV | $[P_2Cd_4P_2]o_{h.}$ $[CdP_3Cl]_{Td.}$ Zig-Zag P-P | л-bonding P-P pairs | л-antibonding P-P pairs | Cd 2.0 to 2.16<br>P -0.68 to -1.41<br>Cl -1.22 to -2.23 | 0.0 to 0.55<br>-0.09 to-0.36<br>0.0 to -0.18 | $\varepsilon^{\infty}_{xx}$=7.96<br>$\varepsilon^{\infty}_{yy}$=8.05<br>$\varepsilon^{\infty}_{zz}$=9.45 |
| $Cd_7P_4Cl_6$ (Pa-3)[a] [b]2.63 eV | $[P_2Cd_6]O_{h.}$ $[CdCl_4P_2]O_{h.}$ $[CdCl_6]_{Oh.}$ P-P pairs | л -bonding P-P pairs | σ-antibonding P-P pairs, Cd s-orbital | Cd 1.56 to 2.39<br>P -0.94<br>Cl -1.15to -2.0 | -0.49 to 0.52<br>0.13 to 0.32<br>-0.12 to 0.06 | $\varepsilon^{\infty}_{xx}$=5.64<br>$\varepsilon^{\infty}_{yy}$=5.64<br>$\varepsilon^{\infty}_{zz}$=5.64 |
| $Cd_3PCl_3$ (Pnma)[a] [b]2.70 eV | $[PCdP.Cd_6]O_{h.}$ $[CdPCl_3]_{Td.}$ | Cl, P and Cd p-orbitals | p and s of Cl and Cd | Cd 1.59 to 2.66<br>P -0.94 to-1.19<br>Cl -1.80 to -2.05 | -0.08 to 0.06<br>-0.08 to 0.0<br>-0.21 to 0.0 | $\varepsilon^{\infty}_{xx}$=5.08<br>$\varepsilon^{\infty}_{yy}$=5.36<br>$\varepsilon^{\infty}_{zz}$=5.24 |
| $Cd_4P_2Cl_3$ (Pa-3)[a] [b]2.21 eV | $[P_2Cd_6]O_{h.}$ $[CdPCl_3]_{Td.}$ $[CdP_2Cl_2]_{Td.}$ P-P pairs | л-antibonding P1-P1pair and p-orbitals of P2 | σ-antibonding of P1-P1 pair and s-orbital of Cd | Cd 1.57 to2.05<br>P -1.32 to -1.50<br>Cl -1.69 to -1.89 | -0.06 to 0.47<br>-0.05 to 0.30<br>-0.42 to 0.30 | $\varepsilon^{\infty}_{xx}$=5.92<br>$\varepsilon^{\infty}_{yy}$=5.92<br>$\varepsilon^{\infty}_{zz}$=5.92 |

Table 3. Estimate of the Lowdin charges of Cd, P and Cl atoms in $Cd_2P_3Cl$, $Cd_7P_4Cl_6$, $Cd_3PCl_3$, and $Cd_4P_2Cl_3$ compounds.

| Compound | Atom | Number of valence electrons | | | Total number of valence electrons |
|---|---|---|---|---|---|
| | | s | p | d | |
| $Cd_2P_3Cl$ | Cd | 0.78 | 1.16 | 9.95 | 11.89 |
| | P | 1.43 | 3.48 | 0.00 | 4.91 |
| | Cl | 1.84 | 5.41 | 0.00 | 7.25 |
| $Cd_7P_4Cl_6$ | Cd1 | 0.83 | 0.98 | 9.95 | 11.76 |
| | Cd2 | 0.60 | 1.00 | 9.98 | 11.58 |
| | P | 1.41 | 3.67 | 0.00 | 5.08 |
| | Cl | 1.83 | 5.38 | 0.00 | 7.21 |
| $Cd_3PCl_3$ | Cd1 | 0.73 | 0.95 | 9.96 | 11.64 |
| | Cd2 | 0.84 | 0.94 | 9.95 | 11.73 |
| | P | 1.39 | 3.87 | 0.00 | 5.26 |
| | Cl | 1.82 | 5.39 | 0.00 | 7.21 |
| | | | | | |
| $Cd_4P_2Cl_3$ | Cd1 | 0.74 | 0.97 | 9.96 | 11.67 |
| | Cd2 | 0.80 | 1.00 | 9.95 | 11.75 |
| | P1 | 1.40 | 3.69 | 0.00 | 5.09 |
| | P2 | 1.39 | 3.85 | 0.00 | 5.24 |
| | Cl | 1.82 | 5.38 | 0.00 | 7.20 |

Lowdin charges are estimated by summing up the projections of all the occupied electronic bands onto orbitals of a given atom. These projections also include its electron that participate in covalent bonding. This is why the total number does not change much from one compound to another. Lowdin charge of Cl does not change much and is ~ 7.2; we can assume its character does not change much (partly ionic Cl). Lowdin charge of Cd is ($s<1$, $p>1$), which means it participate into sp-hybridized covalent bonding, in addition to being partly ionic. Also there are two types of Cd atoms ($p = 1.16$, reflecting stronger covalency in P rich compound $Cd_2P_3Cl$). Lowdin charges of P: count of electron in p-orbitals is smallest in P-rich compound. Thus the compounds are quite covalent and it is hard to assign charges to each ion.

**Apparent quantum Yield Calculations**

In the case of $Cd_7P_4Cl_6$ with a band gap of 2.63 eV, corresponding to the absorption edge wavelength 472 nm, the number of photons were obtained integrating photons available from 395 nm (λ >395 nm, UV cut-off filter used to allow only visible-light photons) to 472 nm (absorption edge or cut-off wavelength of $Cd_7P_4Cl_6$ beyond which there will not be any absorption). From the lamp spectra number of photons

Number of photons entering cylindrical sample cell (diameter = 4.5 cm) = $\int_{395}^{472} F d\lambda$= $1.7359\times10^{17}$ photons/second

HER activity of $Cd_7P_4Cl_6$ = 104.92 μmol/h = $0.175\times10^{17}$ hydrogen molecules/second

$$AQY\ (\%) = 2 \times \frac{Number\ of\ evolved\ hydrogen}{Number\ of\ incident\ photons} \times 100 = 2 \times \frac{0.175\times10\text{^}17}{1.735\times10\text{^}17} \times 100 = 20.17\ \%$$

$Cd_4P_2Cl_3$ with band gap 2.21 corresponding to absorption edge 561.7 nm, number of photons used from 395 nm to 561.7 nm are $2.898\times10^{17}$ photons/second.

HER activity of $Cd_4P_2Cl_3$ = 57.4 μmol/h = $0.0960\times10^{17}$ hydrogen molecules/second

$$AQY\ (\%) = 2 \times \frac{0.096 \times 10\text{^}17}{2.898 \times 10\text{^}17} \times 100 = 6.62\ \%$$

$Cd_3PCl_3$ with band gap of 2.70 eV corresponding to absorption edge 459.8 nm, number of photons used from 395 nm to 459.8 nm are $0.930\times10^{17}$.

HER activity of Cd3PCl3 = 23.5 μmol/h = $0.039 \times 10^{17}$ hydrogen molecules/second

$$AQY\ (\%) = 2 \times \frac{0.039 \times 10\text{^}17}{0.930 \times 10\text{^}17} \times 100 = 8.38\ \%$$

$Cd_2P_3Cl$ with band gap of 1.87 eV corresponding to the absorption edge 663.9 nm, number of photons used from 395 nm to 663.9 nm are $3.549 \times 10^{17}$ photons/second.

HER acticity of $Cd_2P_3Cl$ = 39.06 μmol/h = $0.065 \times 10^{17}$ hydrogen molecules/second

$$AQY\ (\%) = 2 \times \frac{0.065 \times 10\text{^}17}{3.549 \times 10\text{^}17} \times 100 = 3.66\ \%$$

# 5. Conclusions

In summary, cadmium phosphochlorides constitute a family of compounds with different P/Cd and Cl/Cd ratios exhibiting band gaps in the range of 1.87-2.70 eV. The flat band potentials of these compounds vary in the same direction as the band gap. The density of states reveals that in the case of $Cd_4P_2Cl_3$ and $Cd_7P_4Cl_6$ the P p-orbitals and Cd s-orbitals are the main contributors to the VBM and CBM respectively. VBM and CBM in $Cd_3PCl_3$ have a major contribution from the p-orbitals of Cl. Unlike other phosphochlorides both VBM and CBM in $Cd_2P_3Cl$ have a dominant contribution from the p-orbitals of P involved in P-P bonding. Dielectric constants of these compounds are comparable and follow the trend in the electronic band gaps, except in $Cd_2P_3Cl$ with a unique electronic structure. The cadmium phosphochlorides exhibit excellent HER activity with $Cd_7P_4Cl_6$ showing the highest activity of 5246.7 µmol/h-g corresponding to an AQY of 20.1%. HER activity follows the orders $Cd_7P_4Cl_6$>$Cd_4P_2Cl_3$>$Cd_2P_3Cl$>$Cd_3PCl_3$. The lifetimes of photogenerated charge carriers obtained from photoelectrochemical measurements explains the HER activity of these compounds. It is noteworthy that these ternary semiconductor compounds exhibit such remarkable HER activity even in the absence of any co-catalyst, unlike metal chalcogenides.

# 6. References


[1] C. N. R. Rao, The *Journal of Physical Chemistry Letters* **2015**, *6*, 3303-3308.

[2] a) S. R. Lingampalli, K. Manjunath, S. Shenoy, U. V. Waghmare, C. N. R. Rao, *Journal of the American Chemical Society* **2016**, *138*, 8228-8234; b) M. M. Ayyub, S. Prasad, S. R. Lingampalli, K. Manjunath, U. V. Waghmare, C. N. R. Rao, *ChemPhysChem* **2018**, *19*, 3410-3417.

[3] S. Kouser, S. R. Lingampalli, P. Chithaiah, A. Roy, S. Saha, U. V. Waghmare, C. N. R. Rao, *Angewandte Chemie* **2015**, *127*, 8267-8271.

[4] A. Roy, U. S. Shenoy, K. Manjunath, P. Vishnoi, U. V. Waghmare, C. N. R. Rao, *The Journal of Physical Chemistry C* **2016**, *120*, 15063-15069.

[5] H. Rebbah, A. Rebbah, *Journal of Solid State Chemistry* **1994**, *113*, 1-8.

[6] P. C. Donohue, *Journal of Solid State Chemistry* **1972**, *5*, 71-74.

[7] P. Giannozzi, S. Baroni, N. Bonini, M. Calandra, R. Car, C. Cavazzoni, D. Ceresoli, G. L. Chiarotti, M. Cococcioni, I. Dabo, A. Dal Corso, S. de Gironcoli, S. Fabris, G. Fratesi, R. Gebauer, U. Gerstmann, C. Gougoussis, A. Kokalj, M. Lazzeri, L. Martin-Samos, N. Marzari, F. Mauri, R. Mazzarello, S. Paolini, A. Pasquarello, L. Paulatto, C. Sbraccia, S. Scandolo, G. Sclauzero, A. P. Seitsonen, A. Smogunov, P. Umari, R. M. Wentzcovitch, *Journal of Physics: Condensed Matter* **2009**, *21*, 395502.

[8] a) G. Kresse, J. Furthmüller, *Computational Materials Science* **1996**, *6*, 15-50; b) G. Kresse, J. Furthmüller, *Physical Review B* **1996**, *54*, 11169-11186.

[9] J. P. Perdew, K. Burke, M. Ernzerhof, *Physical Review Letters* **1996**, *77*, 3865-3868.

[10] a) P. E. Blöchl, *Physical Review B* **1994**, *50*, 17953-17979; b) G. Kresse, D. Joubert, *Physical Review B* **1999**, *59*, 1758-1775.

[11] J. Heyd, G. E. Scuseria, M. Ernzerhof, *The Journal of Chemical Physics* **2003**, *118*, 8207-8215.

[12] A. V. Shevelkov, L. N. Reshetova, B. A. Popovkin, *J. Solid State Chem.* **1998**, *137*, 138-142.

[13] A. Roy, M. Chhetri, S. Prasad, U. V. Waghmare, C. N. R. Rao, *ACS Applied Materials & Interfaces* **2018**, *10*, 2526-2536.

[14] Z. Chen, T. F. Jaramillo, T. G. Deutsch, A. Kleiman-Shwarsctein, A. J. Forman, N. Gaillard, R. Garland, K. Takanabe, C. Heske, M. Sunkara, E. W. McFarland, K. Domen, E. L. Miller, J. A. Turner, H. N. Dinh, *Journal of Materials Research* **2011**, *25*, 3-16.

[15] A. Pareek, P. Paik, P. H. Borse, *Electroanalysis* **2014**, *26*, 2403-2407.

[16] A. Kudo, Y. Miseki, *Chemical Society Reviews* **2009**, *38*, 253-278.

[17] Y. Zhang, D. Wang, X. Zhang, Y. Chen, L. Kong, P. Chen, Y. Wang, C. Wang, L. Wang, Y. Liu, *Electrochimica Acta* **2016**, *195*, 51-58.

[18] S. Cao, Y. Chen, C.-J. Wang, P. He, W.-F. Fu, *Chem. Commun.* **2014**, *50*, 10427-10429.

# Chapter 5

# Photocatalytic Reduction of $H_2O$ and $CO_2$ by the New Catalysts, $Cd_4P_2X_3$ (X= Cl, Br, or I)

## Summary*


Photochemical reduction of $H_2O$ and $CO_2$ has been investigated with a new family of catalysts of the formula $Cd_4P_2X_3$ (X= Cl, Br, or I), obtained by the complete aliovalent substitution of the $S^{2-}$ ions in CdS by $P^{3-}$ and $X^-$ (X= Cl, Br, or I). Unlike CdS, the $Cd_4P_2X_3$ compounds exhibit hydrogen evolution and $CO_2$ reduction from water in the absence of a sacrificial agent or a co-catalyst. Loading of $Ni_xP_y$ as the co-catalyst, enhances hydrogen evolution, reaching 3870 (AQY= 4.11) and 9258 $\mu molh^{-1}g^{-1}$ respectively under artificial and sunlight irradiation, in the case of $Cd_4P_2Br_3/Ni_xP_y$. Electrochemical and spectroscopic studies have been carried out to understand the photocatalytic activity of this family of compounds.

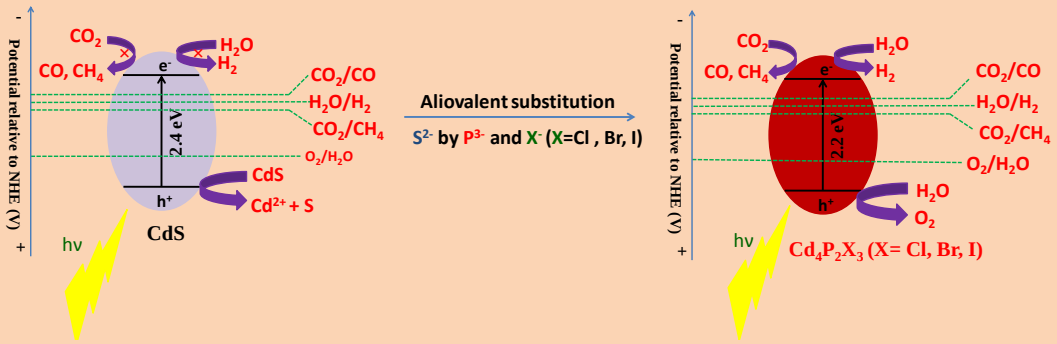


Unlike most semiconductor-based photocatalysts, $Cd_4P_2X_3$ catalysts reduces $CO_2$ to CO and $CH_4$ in the absence of any sacrificial-agent or co-catalyst using water as the electron source. CO, $CH_4$, and $H_2$ are obtained with these catalysts under irradiation by artificial light as well as sun-light. First-principles calculations have been carried out to understand the electronic structure and catalytic properties.



A Paper Based on this work has appeared in ACS. Appl. Mater. Interfaces (2018)

# 1. Introduction

Use of solar energy to generate chemical fuels has become indispensable in the present scenario.[1] Photoreduction of $H_2O$ and $CO_2$ to produce $H_2$, CO, $CH_4$ and $CH_3OH$ are the relevant reactions in this context.[2] Since the early work of Honda and Fujishima, several photocatalysts have been reported of which metal sulfides such as CdS have received significant attention due to their visible-light harvesting capacity and suitable band alignment.[3] However, the serious drawback with metal sulfide photocatalysts is that their use requires sacrificial agents, due to photocorrosion wherein $S^{2-}$ is oxidized by photogenerated holes.[4] There have been recent reports on visible-light based photocatalysts such as $CuGaS_2$, $Cu_{1-x}Ag_xGaS_2$ and $CuInS_2$, wherein Cd is replaced by different metal ions.[5] These photocatalysts show good hydrogen evolution reaction (HER) activity under visible-light irradiation in the presence of hole-scavenger. To the best of our knowledge, there is no report of hydrogen evolution from these sulfide-based photocatalysts in the absence of a sacrificial agent. It is therefore desirable to explore sulfide-free materials as visible-light photocatalysts. Aliovalent substitution of $S^{2-}$ ions in metal sulfides provides a possible strategy. Complete substitution of $S^{2-}$ in CdS by aliovalent $P^{3-}$ and $Cl^-$ ions yields a compound of the composition $Cd_4P_2Cl_3$.[6] Structure and properties of such a ternary compound has been examined, but despite its visible-light absorption (band gap~2.2 eV), it has not been explored for photocatalysis.[7]

In the present study, we have investigated the photocatalytic properties of $Cd_4P_2Cl_3$ as well as $Cd_4P_2Br_3$ and $Cd_4P_2I_3$ for water splitting as well as $CO_2$ reduction. First-principles calculations revealed that in contrast to $Cd_4P_2Cl_3$ and $Cd_4P_2Br_3$ where the top of the valence band has the major contribution from P 3p-orbitals, the valence band in $Cd_4P_2I_3$ has an equal contribution of P 3p and I 5p-orbitals. The calculations show that the conduction band minima (CBM) of the $Cd_4P_2X_3$ compounds are aligned with respect to the redox potentials of $H_2O$ and $CO_2$, which is a prerequisite for the photoreduction process. We have examined the photochemical HER activity of $Cd_4P_2X_3$ composites with nickel phosphide, $Ni_xP_y$, containing $Ni_2P$, $Ni_5P_4$ and $NiP_2$ phases which is an efficient electrocatalyst for water splitting.[8] We have also

investigated the potential of $Cd_4P_2X_3$ compounds for the photocatalytic reduction of $CO_2$, using water as the sole electron donor. The selectivity of $Cd_4P_2X_3$ photocatalysts for $CO_2$ reduction is superior to many of the reported catalysts in the literature.[9] It is noteworthy that $Cd_4P_2X_3$ photocatalysts show excellent activity and stability for water splitting as well as for $CO_2$ reduction without a sacrificial agent or a co-catalyst under artificial or direct sunlight irradiation unlike most semiconductor materials which cannot reduce $H_2O$ and $CO_2$ without a co-catalyst or a sacrificial agent[10],. First-principles calculations throw light on the electronic properties of $Cd_4P_2X_3$ compounds.

## 2. Scope of the Present Investigations

In the present work, we have synthesized a family of a compounds of the composition $Cd_4P_2X_3$ (X= Cl, Br, or I) and studied their electronic and photophysical properties. Interestingly, band gaps of these compounds are in the range of 2.21-2.23 eV and they show photoluminescence in the visible region corresponding to the band edge emission. Alignment of the CBM and VBM positions of these ternary compounds with respect to $H_2O$ and $CO_2$ reduction potentials make them suitable for performing the reduction of these molecules. Photocatalytic splitting of $H_2O$ and $CO_2$ has been examined in the absence of any sacrificial electron donors or a co-catalyst.

## 3. Experimental Section

Synthesis of $Cd_4P_2X_3$ compounds (X= Cl, Br, or I)

$Cd_4P_2X_3$ compounds were synthesized by using a modified procedure reported elsewhere. $Cd_3P_2$ precursor was first synthesized by standard ampoule synthesis method wherein 3.0:2.5 molar ratio of Cd and red-P powder was ground to get homogenous mixture was sealed in a quartz ampoule under vacuum. This ampoule was heated to 400 °C and kept at this temperature for 4h, followed by the colling of the tube to the room temperature. Black powder sample was characterized as $Cd_3P_2$. In a typical synthesis of $Cd_4P_2X_3$ compounds, 1.1:2.0:0.5 molar ratio of $Cd_3P_2$:$CdX_2$: red-P was ground inside a glove-box and homogenous mixture was transfered into a quartz ampoule which was flame sealed under vacuum ($2\times10^{-5}$ mbar).

Synthesis of $Cd_4P_2Cl_3$ was done by heating the sealed ampoule to 500 °C (heating rate 2.5 ºC/min.) for 24 h, followed by the cooling of the tube with the same rate. Synthesis of $Cd_4P_2Br_3$ and $Cd_4P_2I_3$ were done by heating the reaction mixture at 525 °C, and 550 °C for 16 h and 3h respectively employing same heating and cooling rate as mentioned in the case of $Cd_4P_2Cl_3$.

**Synthesis of nickel phosphide ($Ni_xP_y$) NPs**

$Ni_xP_y$ was synthesized by a modification of reported method.[8] In a typical synthesis $Ni(OH)_2$ was first synthesized by drop-wise addition of $Ni(NO_3)_2.6H_2O$ aqueous solution (0.1M, 20 mL) into aqueous solution of NaOH (20 mL, 8.0 M) followed by the hydrothermal treatment of reaction solution at 100 °C for 24 h. Product was centrifuged and washed with Di-water and ethanol, and dried at 80 °C under vacuum. $Ni_xP_y$ was obtained by a solid state reaction between $Ni(OH)_2$ and $NaH_2PO_2.H_2O$ (1:5 molar ratio) at 300 °C (heating rate of 5°C/min) for 2 h under the protection of $N_2$ gas. Obtained powder product was washed thoroughly with Di-water and ethanol to remove unreacted salts followed by centrifugation and drying at 60 °C under vacuum.

**Synthesis of $Cd_4P_2X_3/Ni_xP_y$ composites**

200 mg of $Cd_4P_2X_3$ powder was dispersed in 30 mL of methanol, different weight percentage of $Ni_xP_y$ powder (pre-synthesized) was added to this dispersion and a fine dispersion was achieved by ultrasonication. This dispersion was heated at 65 °C under constant magnetic stirring to evaporate the methanol. To get the intimate contact between $Cd_4P_2X_3$ and $Ni_xP_y$, obtained product was ground homogenously and annealed at 200 °C for 2 h under the $N_2$ gas protection. Obtained powder sample was used as photocatalyst.

**Characterization**

Powder X-ray diffraction (PXRD) patterns were recorded with a Bruker D8 Diffraction system using a Cu Kα source (λ = 0.1541 nm). UV-Vis absorption spectra were collected with Perkin Elmer Lambda 900 spectrophotometer. Photoluminescence spectra were collected by Horiba JobinYvon spectrometer (iHR 320). Transmission electron microscope (TEM) images were collected with a JEOL-3010 TEM microscope with an accelerating voltage of 300 kV. Energy dispersive spectroscopy

(EDS) and elemental mapping analysis were carried out with an EDAX Genesis instrument attached to the SEM instrument. X-ray photoelectron spectra (XPS) were recorded with an Omicron Nanotechnology spectrometer using Al-K α (1486.6 eV) as the X-ray source. Inductively coupled plasma atomic emission spectroscopy (ICP-AES) was done using a Perkin-Elmer Optima 7000 DV machine.

**Photocatalytic Experiments**

Photocatalytic hydrogen evolution measurements were carried at ambient condition under constant stirring in a cylindrical glass reactor (140 mL) with head space closed by high quality septa. A Xe-arc lamp (New Port, 6279NS ozone-free, working at 400 watt) with UV cut-off filter (λ> 395 nm) was used as light source. In a typical experiment 20 mg of the photocatalyst was dispersed in 75 mL of Di-$H_2O$ containing 0.18 M $Na_2S$ and 0. 24 M $Na_2SO_3$ as hole scavengers. Before light irradiation photocatalyst solution was purged with pure $N_2$ gas for 30 min to remove dissolved air. The quantity of evolved $H_2$ gas was measured by manual injection of gas sample into a gas chromatography (Perkin Elmer, Clarus 580) equipped with TCD detector. Photocatalytic $H_2$ evolution for sacrificial free system was done in same cylindrical cell with 75 mL, 3M NaOH aqueous solution. For the hydrogen evolution experiment under direct sun-light irradiation reactor was placed on terrace without any stirring.

Apparent quantum yield calculation:

AQY (%) = $\frac{Number\ of\ reacted\ electrons}{Number\ of\ incident\ photons}$*100 = ($\frac{2\times R}{I}$)*100, where R= Rate of hydrogen evolution in molecules/sec, I = Rate of Incident photon in photons/sec.

The band gap of $Cd_4P_2Br_3$ is 2.2 eV which is equivalent to the absorption cut-off wavelength of 565 nm. Since the HER studies were carried out with visible irradiation using a UV cut-off filter (λ >395 nm), the number of incident photons was calculated by using the irradiance meter from the following formula

No. of photons (I) = $\int_{395}^{565} F d\lambda$= $6.3\times10^{17}$ photons/sec; here F is the photon flux.

Photon flux entering our reaction cell is derived from the data provided by the 'Newport' radiative irradiance at different wavelengths and by use of the irradiance meter. The intensity of incident light at the sample cell was 150 mW/$cm^2$.

**Photocatalytic $CO_2$ reduction** was carried at ambient condition under constant magnetic stirring in a cylindrical quartz reactor cell (130 mL) with head space closed by high quality septa. Same light source mentioned above has been used for irradiation. In a typical experiment 40 mg of photocatalyst was dispersed in 60 mL of Di-$H_2O$, and high pure $CO_2$ gas (99.999 %) was purged for 30 min under constant stirring. $CO_2$ reduction products was measured by injecting 3 mL of gaseous sample from reactor head-space into the Perkin Elmer clarus 580 GC equipped with flame ionized detector (FID) and methanizer. Selectivity for $CO_2$ reduction product was obtained using following formula:

CO selectivity = $CO/(CO+H_2+ CH_4)$.

Oxygen ($O_2$) evolution measurements were carried out using an ocean-optics fluorescence sensor (Neofox, FOSPOR-R 1/16”). In a typical measurements sensor was fixed in the head space of cylindrical glass cell having 40 mg of photocatalyst suspended in 60 mL of Di-water closed by air tight septa. Prior to any measurements sensor was calibrated using two point calibration techniques wherein two known amount of oxygen (0.0 % $O_2$ and 20.9 % $O_2$) was used. The evolved oxygen with respect to time was recorded in the unit of µmol/L.

**Photoelectrochemical (PEC) Measurements**

Photocurrent measurements were performed on a CHI 1760E electrochemical work station (CH instrument Inc.) in a conventional three-electrode set up. The resultant electrode served as the working electrode, with a platinum wire as the counter electrode and an Ag/AgCl (saturated KCl) electrode as the reference electrode. For the purpose of PEC measurements, 300 W Xenon lamp, with a calibrated intensity of 100 $mW/cm^2$ was used as the light source. A 0.5 M $Na_2SO_4$ aqueous solution was used as the electrolyte. The working electrode was prepared by spin coating. First, the catalyst slurry was prepared by ultrasonicating 20 mg photocatalyst in 30 µL Nafion (5.0 wt%, Sigma Aldrich) and 300 µL of ethanol for 20-30 minutes. Fluorine-doped tin oxide (FTO) ($2x1cm^2$ pieces) which was used as the substrate was cleaned, using soap solution and ultrasonication in deionized water. This was followed by the same procedure in ethanol+acetone (1:1) mixture for 30 minutes and drying at 100$^oC$ for 1h. An area of $1cm^2$ of the substrate was masked by scotch tape and spin coating (1800 rpm, 30 seconds) was performed by collecting 100 µL of slurry each time. The

electrode films were then dried at 100°C for 1 hour and Cu wire connections were made with the help of Ag paste. The portion of electrode, except the photocatalyst part, was electronically sealed by transparent epoxy coating and left overnight.

**Computational details**

We used the quantum-espresso packag in our first-principles calculations carried out within density functional theory (DFT), with ultra-soft pseudopotentials (USPP) to model the interaction between ionic cores and valence electrons.[11] We treated the exchange-correlation energy within a generalized-gradient approximation (GGA)and functional parameterized by Perdew, Burke, and Ernzerhof.[12] We used plane-wave basis truncated with a kinetic energy cut-off of 55 Ry in representation of Kohn-Sham wave-functions, and 4x4x4 uniform mesh of k-points for sampling the integrations over the Brillouin zone (BZ). Since DFT calculations underestimate band gaps, we used Heyd-Scuseria-Ernzerhof (HSE) hybrid functional based on a screened Coulomb potential in Hartree-Fock exchange interaction in estimation of gaps.[13] Crystal structures were internally relaxedto minimize total energy keeping the experimental lattice constants until the Hellman-Feynman forces on each atom are less than 0.02 eV/Å. For alignment of energies of band edges (e.g. energy of the conduction band minimum (CBM)), we simulated a slab of crystals with (001) orientation and thickness of two units separated by a vacuum of about 15 Å along the z-direction in the periodic supercell. Brillouin zone integrations in these slab calculations were sampled on a 4x4x1mesh of k-points.

# 4. Results and Discussion

$Cd_4P_2Cl_3$ and $Cd_4P_2Br_3$ crystallize in the cubic structure (Pa-3) with lattice parameters of 12.13 and 12.36 Å respectively (PCPDF 89-4687 and 82-1419) whereas $Cd_4P_2I_3$ crystallizes in the orthorhombic structure (Pcab) with a=12.85, b= 12.69 and c= 12.62 Å (PDF00-045-0317) (**Figure 1a**).[14] $Cd_4P_2X_3$ compounds show absorption in visible-region with a direct band gap in the range of 2.21-2.23 eV calculated from Tauc's plot (**Figure 1b**). $Ni_xP_y$, synthesized by a solid-state between $Ni(OH)_2$ and $NaH_2PO_2.H_2O$, was loaded on the $Cd_4P_2X_3$ compounds by the impregnation method.

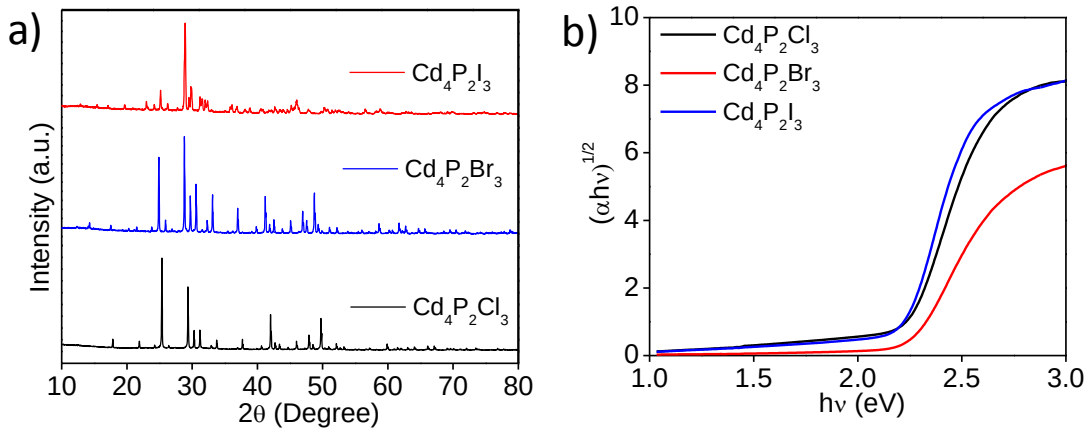


Figure 1. a) PXRD patterns, and b) Tauc plots of $Cd_4P_2X_3$ compounds.

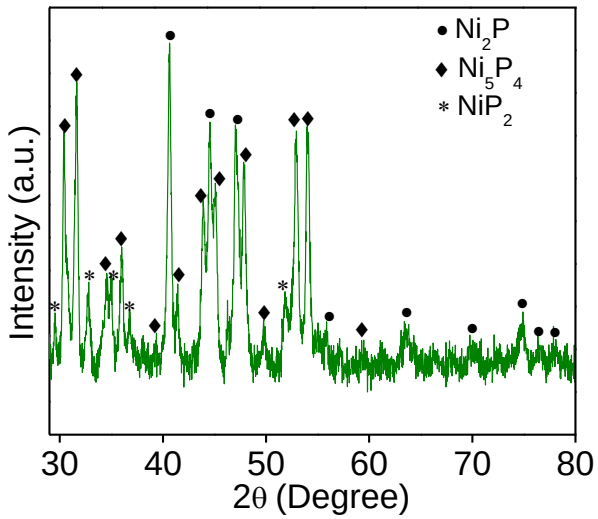


Figure 2. PXRD pattern of $Ni_xP_y$.

The PXRD pattern of $Ni_xP_y$, shows diffraction due to $Ni_5P_4$, $Ni_2P$ and $NiP_2$ phases with $Ni_5P_4$ as the dominant component which is in agreement with the literature (**Figure 2**).[8] TEM image of $Ni_xP_y$ shows the presence of nanoparticles (NPs) of the size in the range of 20-30 nm (**Figure 3a**). TEM image of $Cd_4P_2Br_3/Ni_xP_y$ (**Figure 3b)** shows the presence of $Ni_xP_y$ NPs of the size 20-30 nm on the surface of $Cd_4P_2Br_3$. The HRTEM image of $Ni_xP_y$ NPs in **Figure 3c**, shows the lattice fringes with a *d*-spacing of 0.283 nm corresponding to the (201) plane of major phase $Ni_5P_4$. We do not observe any diffraction peaks of $Ni_xP_y$ in the PXRD-pattern of $Cd_4P_2X_3/Ni_xP_y$ probably due to high crystalline nature of $Cd_4P_2X_3$. EDAX-elemental mapping of $Cd_4P_2Br_3/Ni_xP_y$ reveals that Cd, Ni, P and Br elements are homogenously distributed throughout the sample (**Figure 3d**) implying that the $Ni_xP_y$ NPs were present on the surface of $Cd_4P_2Br_3$.

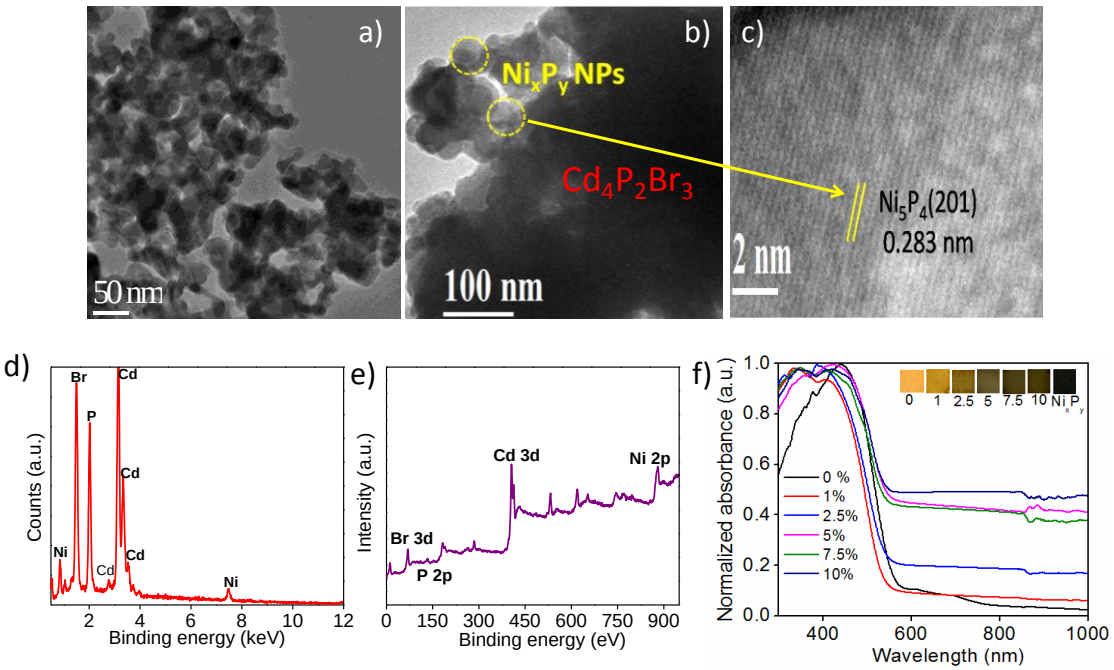


Figure 3. a) TEM image of $Ni_xP_y$ NPs, b) TEM image of $Cd_4P_2Br_3/Ni_xP_y$, c) HRTEM image of $Ni_xP_y$ NPs on the surface of $Cd_4P_2Br_3$, d) EDAX spectrum of $Cd_4P_2Br_3/Ni_xP_y$ (5 wt%), e) XPS Survey-can spectrum of $Cd_4P_2Br_3/Ni_xP_y$(5 wt %), and f) UV-Vis-NIR absorption spectrum of $Cd_4P_2Br_3/Ni_xP_y$.

Presence of $Ni_xP_y$ on the surface of $Cd_4P_2Br_3$ photocatalysts was further confirmed by X-ray photoelectron spectroscopy (XPS). Thus, the XPS survey scan of $Cd_4P_2Br_3/Ni_xP_y$ (5 wt % $Ni_xP_y$) (**Figure 3e**), shows signals due to Cd, Ni, P and Br. The exact composition of $Cd_4P_2X_3$ compounds by EDAX and XPS measurements showed some amount of halogen vacancy in these compounds. The Cd/X ratio was 1.42-1.46 and the Cd/P ratio was 1.97-1.98 which are both close to the ideal ratio of 1.33 (Cd/X) and 2.0 (Cd/P).

The UV-Vis-NIR diffuse reflectance spectrum of $Cd_4P_2X_3/Ni_xP_y$ **(Figures 3f)** shows that $Cd_4P_2Br_3$ compounds absorb in the visible-region with an absorption edge close to 565 nm corresponding to the band gap of 2.2 eV. A slight red-shift in the absorption band edge of $Cd_4P_2Br_3$ is observed after loading $Ni_xP_y$, indicating existence of electronic coupling between the two.[15] Increase in the tail absorption of the $Cd_4P_2X_3$ compounds across the UV-Vis-NIR region with loading amount of $Ni_xP_y$ is attributed to the narrow band gap and black color of $Ni_xP_y$. Core-level XPS spectra of $Cd_4P_2Br_3/Ni_xP_y$ show the characteristic peaks for Cd, Ni, P and Br in the compound (**Figure 4**). EDAX spectra of $Cd_4P_2X_3/Ni_xP_y$ (X= Cl and I) is shown in **Figure 5,**

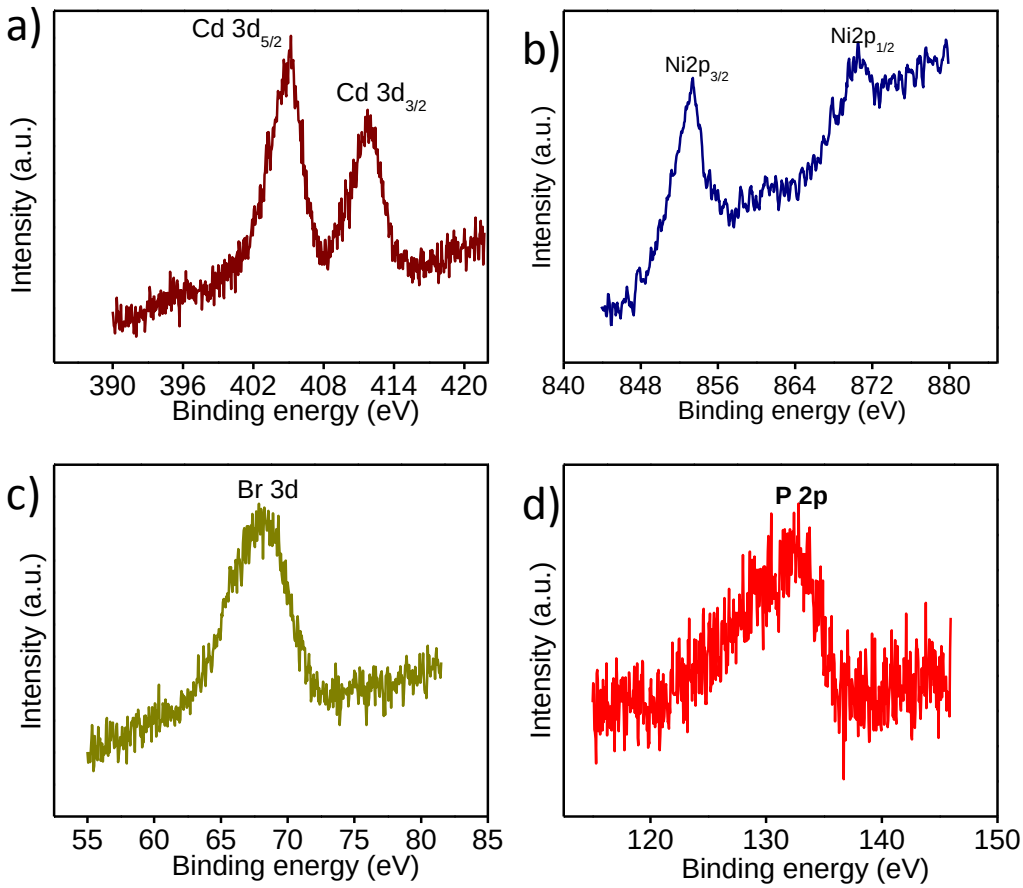


Figure 4. Core-level XPS spectrum of $Cd_4P_2Br_3/Ni_xP_y$ showing peaks for a) Cd, b) Ni, C) Br, and d) P.

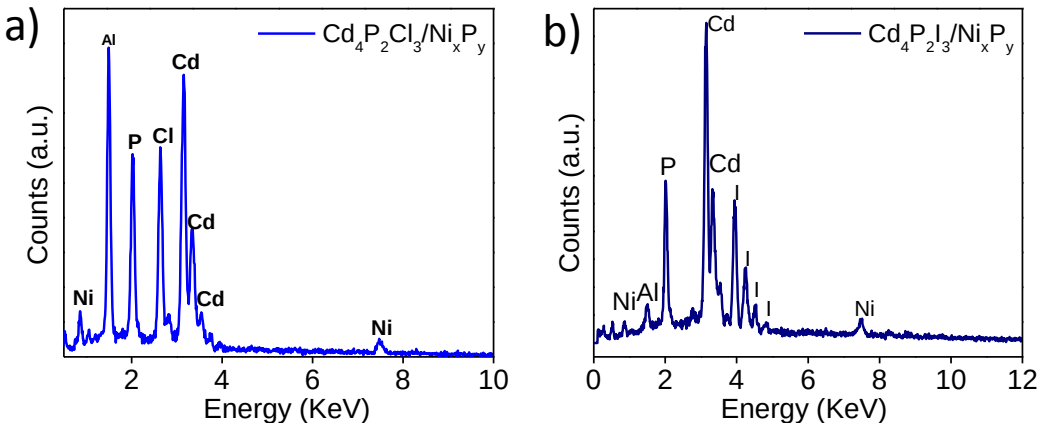


Figure 5. EDAX spectra of a) $Cd_4P_2Cl_3/Ni_xP_y$ (5 wt% $Ni_xP_y$), and b) $Cd_4P_2I_3/Ni_xP_y$ (5 wt% $Ni_xP_y$).

whereas XPS spectra of $Cd_4P_2X_3/Ni_xP_y$ (X= Cl, I) is shown in **Figure 6 and Figure 7**. The UV-Vis absorption spectra of $Cd_4P_2Cl_3/Ni_xP_y$ and $Cd_4P_2I_3/Ni_xP_y$ is shown in **Figure 8.**

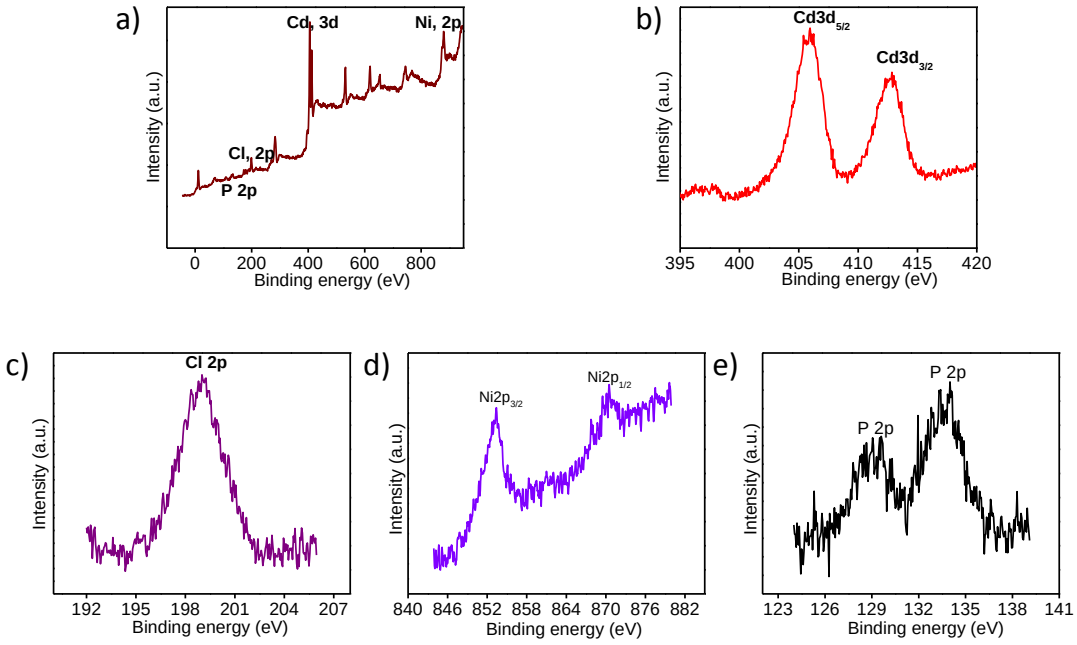


Figure 6. a) XPS survey scan spectrum of $Cd_4P_2Cl_3/Ni_xP_y$ (5 wt% $Ni_xP_y$), Core level spectra of b) Cd, c) Cl, d) Ni, and e) P.

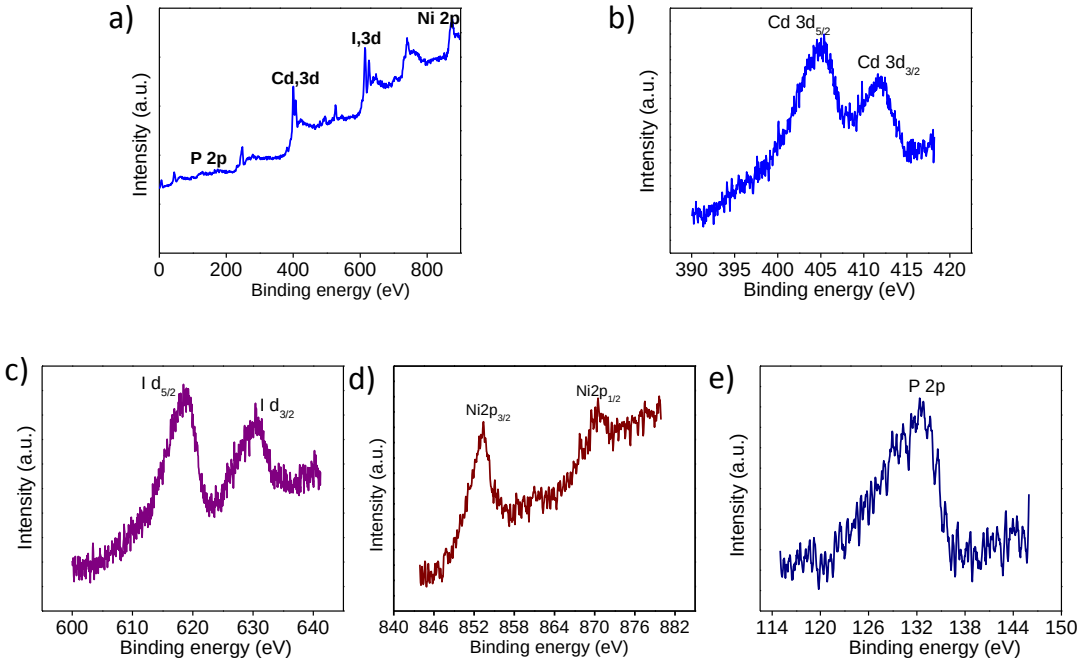


Figure 7. a) XPS survey scan spectrum of $Cd_4P_2I_3/Ni_xP_y$ (5 wt%); core level spectra for b) Cd, c) I, d) Ni, and e) P.

Similar features as observed in the case $Cd_4P_2Br_3/Ni_xP_y$ can be seen in these composites as well.

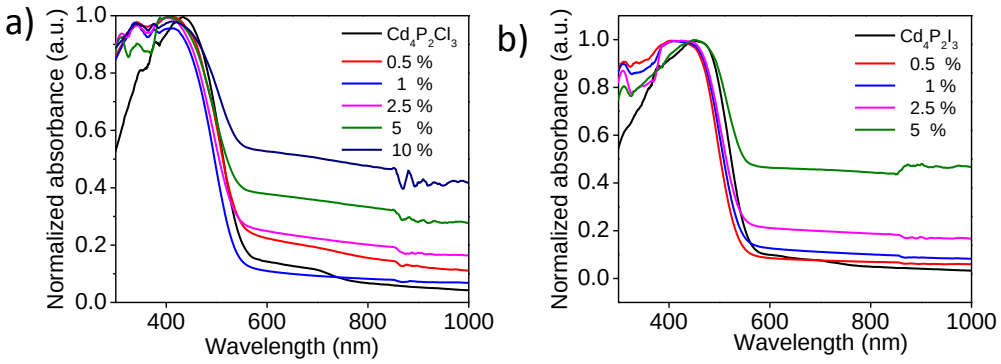


Figure 8. UV-Vis-NIR absorption spectra of a) $Cd_4P_2Cl_3$, and b) $Cd_4P_2I_3$ with different loading amount of $Ni_xP_y$ co-catalyst.

**Photocatalytic $H_2$ evolution studies**

We have studied the hydrogen evolution from $Cd_4P_2X_3$ compounds in visible-light irradiation in the presence of $Na_2S$ and $Na_2SO_3$ as a hole scavenger. **Figure 9a** shows photocatalytic $H_2$ evolution from pristine $Cd_4P_2X_3$ (X= Cl, Br, or I) compounds, under visible-light irradiation without $Ni_xP_y$ loading. All the three $Cd_4P_2X_3$ compounds show robust $H_2$ evolution, with $Cd_4P_2Br_3$ exhibiting the highest activity (2074 $\mu molh^{-1}g^{-1}$) followed by $Cd_4P_2Cl_3$ (1160 $\mu molh^{-1}g^{-1}$); least activity is found in the case of $Cd_4P_2I_3$ (910 $\mu molh^{-1}g^{-1}$). A small loading of $Ni_xP_y$ (0.5 wt %) results in enhancement in the $H_2$ evolution activity of $Cd_4P_2Cl_3$ from 1160 to 2483 $\mu molh^{-1}g^{-1}$ which increases further on increasing the loading of $Ni_xP_y$ reaching a maximum value of 2699 $\mu molh^{-1}g^{-1}$ for 1 wt % of loading. Further increase in the $Ni_xP_y$ content decreases the $H_2$ evolution activity (**Figure 9b**). $Cd_4P_2Br_3$ shows a $H_2$ evolution activity of 2074 $\mu molh^{-1}g^{-1}$, and with 1 wt % loading of $Ni_xP_y$, it showed a $H_2$ evolution activity of 3098 $\mu molh^{-1}g^{-1}$. The yield increases further with increase in $Ni_xP_y$ loading, to a maximum of 3870 $\mu molh^{-1}g^{-1}$ for 5 wt% of $Ni_xP_y$ (**Figure 9c**). Similarly, in the case of $Cd_4P_2I_3/Ni_xP_y$ (**Figure 9d**) pristine $Cd_4P_2I_3$ exhibited the $H_2$ evolution rate of 910 $\mu molh^{-1}g^{-1}$, which reaches a maximum of 2386 $\mu molh^{-1}g^{-1}$ for 1 wt% loading of $Ni_xP_y$. Retardation in the photocatalytic activities of $Cd_4P_2X_3/Ni_xP_y$ photocatalysts beyond an optimum loading of $Ni_xP_y$ is known to occur due to the following factors: "covering of the active sites on the photocatalyst surface, shielding of the light absorption, agglomeration of co-catalyst nanoparticles and reduction in the active surface area of co-catalyst".[16] The apparent quantum yield (AQY) obtained from $Cd_4P_2Cl_3/Ni_xP_y$,

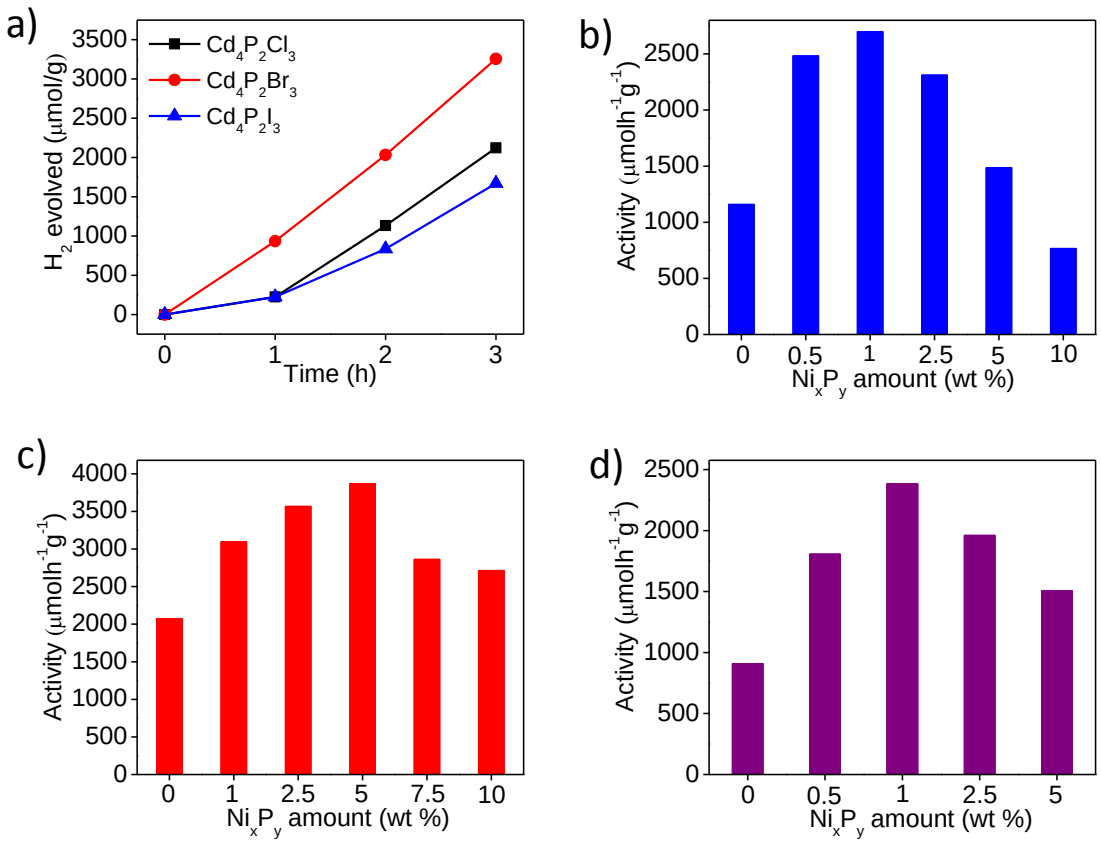


Figure 9. a) Time course of $H_2$ evolution from pristine $Cd_4P_2X_3$ compounds (X= Cl, Br, or I) without $Ni_xP_y$ loading. The rate of $H_2$ evolution from $Cd_4P_2X_3/Ni_xP_y$ photocatalysts under visible-light irradiation with different loading amount of $Ni_xP_y$ on, b) $Cd_4P_2Cl_3$, c) $Cd_4P_2Br_3$, and d) $Cd_4P_2I_3$. All the photocatalytic experiment were done under visible-light irradiation ($\lambda$>395 nm) in the presence of 0.18 M $Na_2S$ and 0.24 M $Na_2SO_4$ as a sacrificial agent in 75 mL Di-water, using a Xe-lamp (400 W).

$Cd_4P_2Br_3/Ni_xP_y$, and $Cd_4P_2I_3/Ni_xP_y$ at the optimum loading of $Ni_xP_y$ are 2.8, 4.1, and 2.5 % respectively.

We have further examined photocatalysis of $Cd_4P_2X_3$ with an optimum loading of $Ni_xP_y$ (5 wt % for $Cd_4P_2Br_3$ and 1 wt% for $Cd_4P_2Cl_3$ and $Cd_4P_2I_3$). In this context, we have carried out the recyclability and stability test of $Cd_4P_2X_3/Ni_xP_y$ under photochemical reaction condition. **Figure 10a** shows the time course of $H_2$ evolution from $Cd_4P_2Br_3/Ni_xP_y$ (5 wt% of $Ni_xP_y$). No substantial inactivation is observed, and the photocatalytic activity remained intact even after five cycles (15h). Similar recyclability study of $Cd_4P_2Cl_3/Ni_xP_y$ (1 wt% of $Ni_xP_y$) (**Figure 10b**) and $Cd_4P_2I_3/Ni_xP_y$ (1 wt% $Ni_xP_y$) (**Figure 10c**) photocatalysts showed robust activity in the case of $Cd_4P_2Cl_3$, but in the

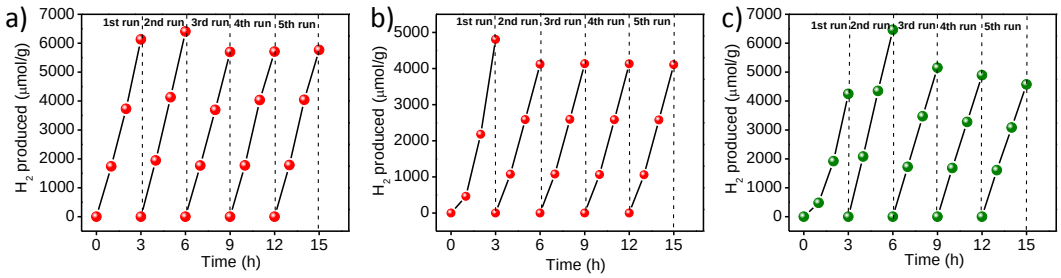


Figure 10. Cyclic $H_2$ evolution test of a) $Cd_4P_2Br_3/Ni_xP_y$ (5wt% $Ni_xP_y$), b) $Cd_4P_2Cl_3/Ni_xP_y$ (1 wt %), and c) $Cd_4P_2I_3/Ni_xP_y$ (1 wt %) under visible-light in the presence of 0.18 M $Na_2S$ and 0.24 M $Na_2SO_3$ hole scavenger.

case of $Cd_4P_2I_3$ slight decline in the activity was observed after second cycle. It is noteworthy that $Cd_4P_2X_3/Ni_xP_y$ (X= Cl, Br, I) catalysts show remarkable stability and robust rate of $H_2$ evolution for several hours under visible-light irradiation. We characterized the photocatalysts after their use of five cycles. **Figure 11** shows the PXRD patterns of $Cd_4P_2X_3/Ni_xP_y$ before and after catalysis, and we see no change in the diffraction patterns suggesting stability of the compounds. The XPS spectrum of $Cd_4P_2Cl_3/Ni_xP_y$ after irradiation (15 h) showed no change in peak positions of Cd, P, Cl, and Ni (**Figure 12**). There was no evidence of metallic Ni, suggesting the stability of the $Ni_xP_y$ co-catalyst. However, a P 2p peak in fresh sample at 134 eV due to surface phosphate species was not seen after photocatalytic reaction probably due to the dissolution of phosphate species in solution during the reaction. The composition of the photocatalysts determined by XPS and EDAX before and after catalysis also shows their stability under photocatalytic reaction condition. To obtain an estimate of the stability of the $Cd_4P_2X_3$ photocatalysts, possible leaching of $Cd^{2+}$ ions from the photocatalysts solution was probed by employing ICP measurements. The irradiated photocatalyst solution was collected at intervals of 3, 6 and 9 h, and centrifuged at 8000 rpm for 5 min followed by the filtration of the supernatant solution using syringe filter. ICP analysis of this solution did not reveal any trace of $Cd^{2+}$, suggesting the absence of leaching of $Cd^{2+}$-ions from the photocatalysts under irradiation.

We have also investigated $H_2$ evolution from these photocatalysts under direct sun-light irradiation instead of Xe-lamp irradiation. **Figure 13a** represents photocatalytic $H_2$ evolution from $Cd_4P_2Br_3/Ni_xP_y$ (5 wt % $Ni_xP_y$) under direct sun-light irradiation. An average $H_2$ evolution rate of 9258 $\mu molh^{-1}g^{-1}$ was obtained by this photocatalyst under sun-light irradiation.

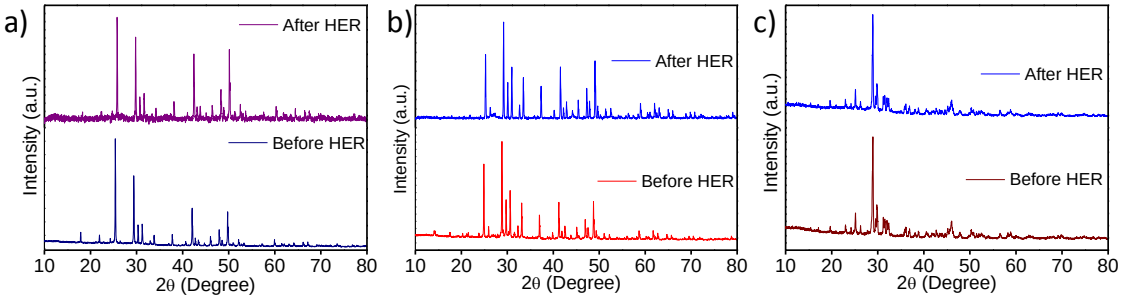


Figure11. PXRD patterns of photocatalysts after their use in 5 cycles (15 h) reaction for a) $Cd_4P_2Cl_3/Ni_xP_y$ (1 wt% $Ni_xP_y$), b) $Cd_4P_2Br_3/Ni_xP_y$ (5 wt% $Ni_xP_y$) and, c) $Cd_4P_2I_3/Ni_xP_y$ (1 wt% $Ni_xP_y$).

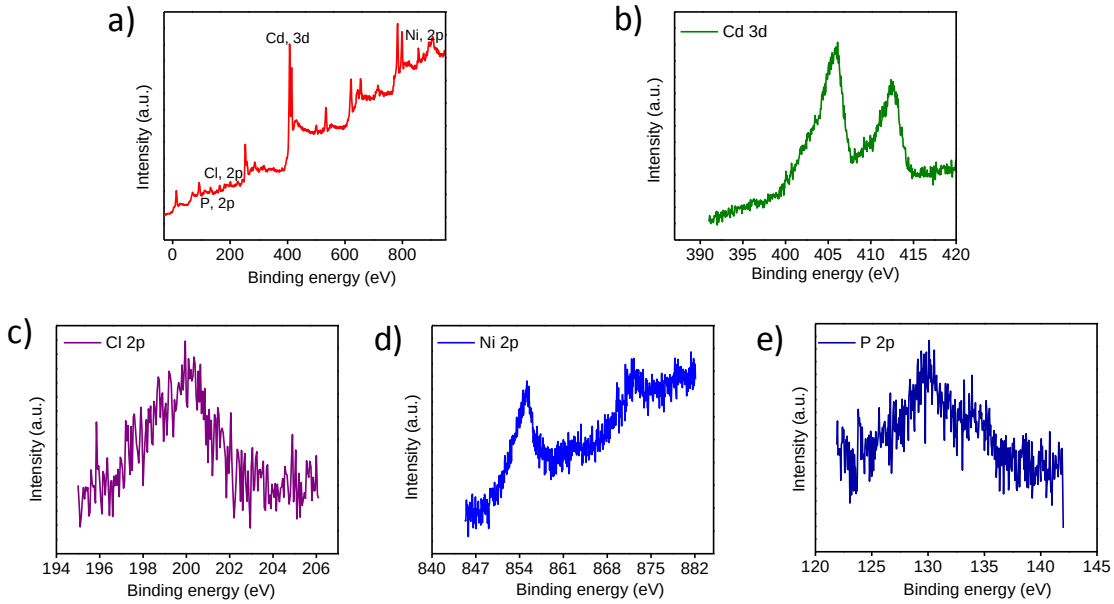


Figure 12. XPS of $Cd_4P_2Cl_3/Ni_xP_y$ sample after 5 cycles (15 h) of irradiation, a) survey-scan spectrum, core level spectra for b) Cd, c) Cl, d) Ni, and e) P

Due to cloudy weather slight decline in activity was observed on the second day (Inset **Figure 13a** shows the $H_2$ bubbles). Under sun-light irradiation, the $H_2$ yield from $Cd_4P_2Cl_3/Ni_xP_y$ (1wt % $Ni_xP_y$) and $Cd_4P_2I_3/Ni_xP_y$ (1 wt % $Ni_xP_y$) were 9089 and 4750 $\mu molh^{-1}g^{-1}$ respectively (**Figure 13b and 13c**). Thus, all the $Cd_4P_2X_3/Ni_xP_y$ photocatalysts showed better activity and stability under long runs in the direct sun-light irradiation. Higher HER activity of these photocatalyst under sun-light irradiation is probably linked with lower rate of recombination of electron-hole pairs under low intense light excitation and UV-light contribution (2-3 % solar irradiation).[17]

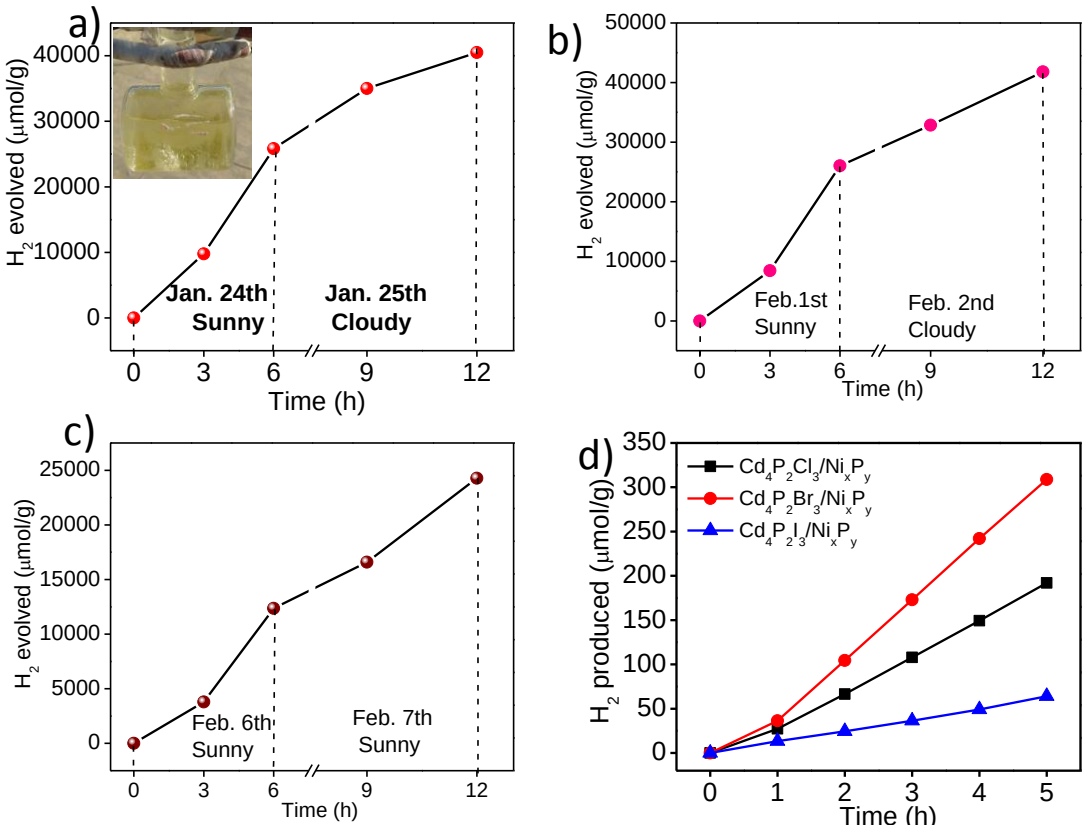


Figure 13. Time course of hydrogen evolution from a) $Cd_4P_2Br_3/Ni_xP_y$ (5wt% $Ni_xP_y$), b) $Cd_4P_2Cl_3/Ni_xP_y$ (1wt% $Ni_xP_y$), and c) $Cd_4P_2I_3/Ni_xP_y$ (1wt% $Ni_xP_y$) under direct sun-light irradiation in the presence of 0.18 M $Na_2S$ and 0.24 M $Na_2SO_3$ hole scavenger.

A photocatalyst which can produce $H_2$ from pure water without the use of a sacrificial agent and exhibits stability against photocorossion would be most desirable for overall water splitting.[4b, 18] We have investigated $H_2$ evolution from $Cd_4P_2X_3/Ni_xP_y$ photocatalysts in alkaline medium in the absence of sacrificial electron donors. Photocatalytic $H_2$ evolution activity of 108.6, 172.9 and 37.4 $\mu molh^{-1}g^{-1}$ was exhibited by $Cd_4P_2Cl_3/Ni_xP_y$ (1wt% $Ni_xP_y$), $Cd_4P_2Br_3/Ni_xP_y$ (5wt% $Ni_xPy$) and $Cd_4P_2I_3/Ni_xP_y$ (1wt% $Ni_xP_y$) respectively, and most importantly we did not observe any decline in the photocatalytic activity even in the absence of sacrificial donors, suggesting their unique stability against photocorrosion (**Figure 13d**). The advantage of the $Cd_4P_2X_3$ family of photocatalysts over CdS as far as hydrogen evolution reaction (HER) is concerned stems from the fact that while CdS fails to produce $H_2$ without the aid of a sacrificial agent, $Cd_4P_2X_3$ family of photocatalysts show stability

and can produce $H_2$ with the steady rate from pure water without any sacrificial agent.[18a]

To understand the origin and trend of the photocatalytic hydrogen evolution activity of the $Cd_4P_2X_3$ family of compounds, electrochemical and photoelectrochemical studies were carried out. Mott-Schottky (MS) plots of $Cd_4P_2X_3$ in KOH electrolyte obtained at the working pH (pH~12) is shown in **Figure 14a**. The flat band potentials calculated from the MS plots of $Cd_4P_2Cl_3$, $Cd_4P_2Br_3$ and $Cd_4P_2I_3$ are -1.05, -1.01 and -1.06 V vs. Ag/AgCl respectively. Since it is known that for n-type semiconductors, the Fermi energy lies near to the conduction band edge (CBM), the CBM and the flat band potential would be close. Thus, the flat band potentials give an approximate estimation of CBM levels.[19] Knowledge of CBM and band gap of compound helps us to predict the valence band minima (VBM) positions. **Figure 14b** shows CBM and VBM positions of $Cd_4P_2X_3$ compounds with respect to water redox potentials at working pH condition. It can be clearly seen that CBM positions of all three $Cd_4P_2X_3$ compounds are more negative than the $H^+/H_2$ potential hence $H^+/H_2$ would be feasible by these compounds.

After confirming the suitability of these compounds for the hydrogen evolution reaction from water, we next investigated the reason for the trend in the HER activity, $Cd_4P_2Br_3$>$Cd_4P_2Cl_3$>$Cd_4P_2I_3$. In order to

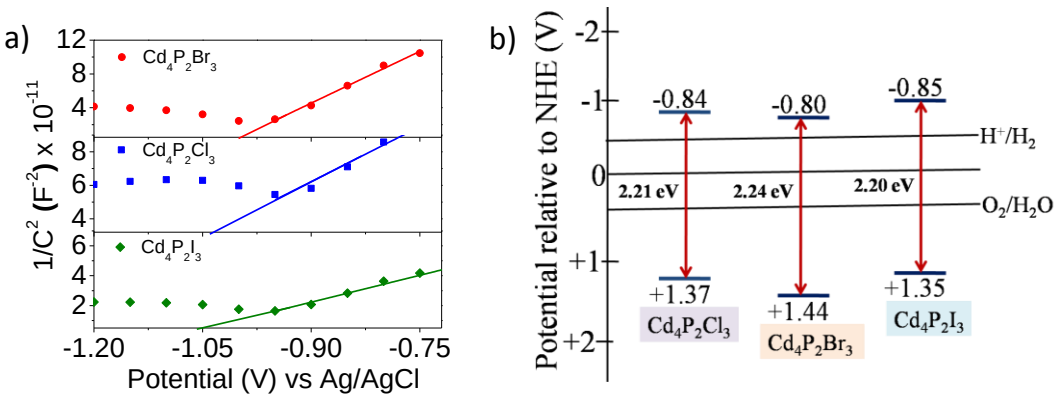


Figure 14. a) Mott-Schottky plots of $Cd_4P_2X_3$ compounds in KOH electrolyte at working pH condition (pH~12) at an applied frequency of 1000 Hz, b) Corresponding conduction band minimum (CBM) and Valence band maxima (VBM) of $Cd_4P_2X_3$ compounds with respect to water redox potential.

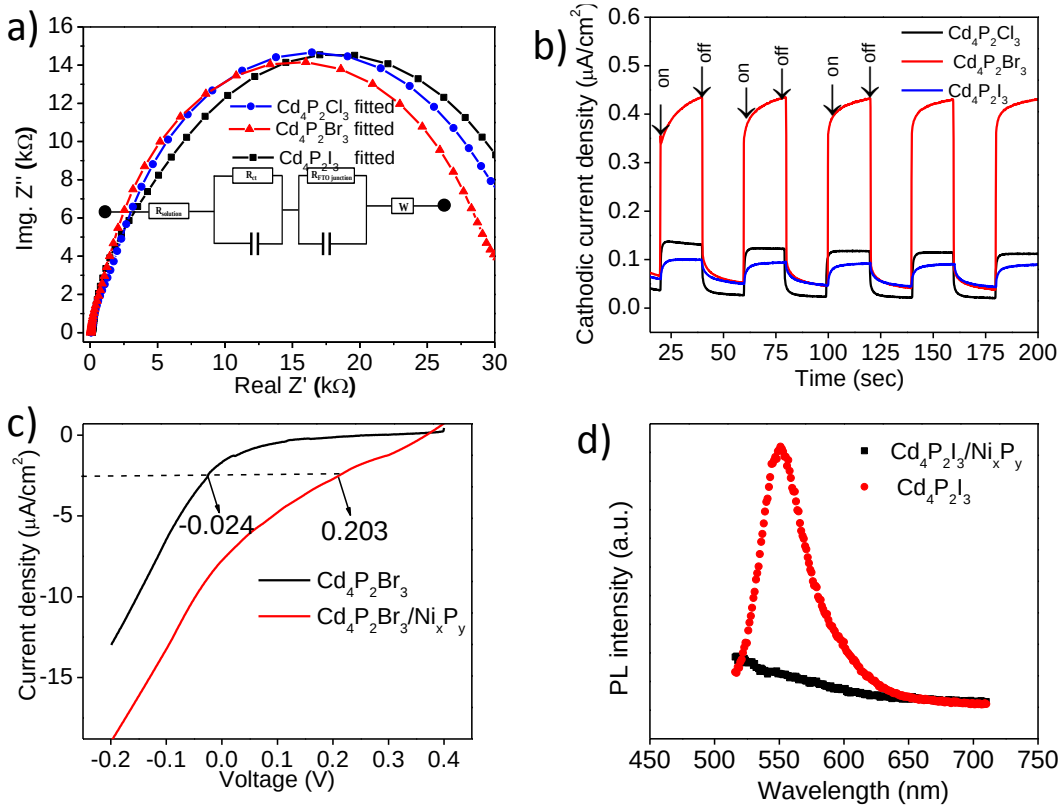


Figure 15. a) EIS Nyquist plot of $Cd_4P_2X_3$ film on FTO electrodes, b) Transient photocurrent density of $Cd_4P_2X_3$ compounds, c) LSV curve of $Cd_4P_2Br_3$ and $Cd_4P_2Br_3/Ni_xP_y$ in 0.5 M $Na_2SO_4$ electrolyte with a scan rate of 5 mV/s in the presence of 1 sun light, and d) Steady state photoluminescence spectra of $Cd_4P_2I_3$ and $Cd_4P_2I_3/Ni_xP_y$ (1wt% $Ni_xP_y$).

understand the HER trend of $Cd_4P_2X_3$ compounds electrochemical impedance spectroscopy (EIS) were carried out. Nyquist plot of $Cd_4P_2X_3$ compounds obtained from EIS is shown in **Figure 15a**. The diameter of the semicircular arc in the Nyquist plot gives the measure of the charge transfer resistance ($R_{ct}$) at the electrode/electrolyte interface, wherein larger diameter manifest higher resistance and hence greater possibility of electron-hole pairs recombination. Under the 1 sun (AM 1.5 G) light irradiation, charge transfer resistance was found to follow the $Cd_4P_2Br_3$<$Cd_4P_2Cl_3$<$Cd_4P_2I_3$ trend which is in the line with their photocatalytic hydrogen evolution activity trend. Therefore, $Cd_4P_2Br_3$ with minimum charge transfer resistance (better utilization of photogenerated charges at the electrode/electrolyte interface thereby leading to efficient separation of electron-hole pairs) shows highest activity whereas $Cd_4P_2I_3$ with maximum charge transfer resistance (least separation of

electron-holes pairs) shows lowest HER activity. To further understand the generation and separation of photogenerated electrons-hole pairs in $Cd_4P_2X_3$ compounds transient photocurrent measurements were carried out. The photocurrent obtained from these compounds follows the trend of $Cd_4P_2Br_3$>$Cd_4P_2Cl_3$>$Cd_4P_2I_3$, which is again in the line with their HER activities (**Figure 15b**). $Cd_4P_2Br_3$ with the highest photocurrent (better separation of photogenerated charge carriers) shows the highest HER activity whereas $Cd_4P_2I_3$ with the lowest photocurrent (higher recombination of photogenerated charge carriers) shows the least HER activity among the three $Cd_4P_2X_3$ photocatalysts. Interestingly the photocurrent of $Cd_4P_2Br_3$ gradually increases during the 25 s illumination periods. In order to find an answer to this, we studied the I-t behaviour of $Cd_4P_2Br_3$ under the same conditions without chopping the light and found that the photocurrent stabilizes after ca. 100 seconds showing a similar behaviour to that of the other two electrodes. This may be due to the differences in the charge transport properties and recombination rates on the surfaces of the different electrodes.

To examine the role of $Ni_xP_y$ as a co-catalyst when loaded on $Cd_4P_2X_3$, linear sweep voltammetry (LSV) characteristics were studied for $Cd_4P_2Br_3$ and $Cd_4P_2Br_3/Ni_xP_y$ (**Figure 15c)**. The value of the overpotential required for $H^+/H_2$ redox (with and without $Ni_xP_y$) at working electrode helps to estimate the role of $Ni_xP_y$. To drive $H_2$ production at a cathodic current density of 2.5 µA/cm$^2$, pristine $Cd_4P_2Br_3$ requires larger cathodic potential compared to $Cd_4P_2Br_3/Ni_xP_y$ (**Figure 15c**, depicted by dotted lines), suggesting that the presence of $Ni_xP_y$ reduces the overpotential for $H^+/H_2$ reduction and gives rise to the high photocatalytic $H_2$ evolution activity. Radiative recombination quenching in $Cd_4P_2X_3$ was examined by employing photoluminescence (PL) spectroscopy. It is known that intimate contact with a suitable co-catalyst on the surface of photocatalyst results in the transfer of photogenerated electrons from the photocatalyst to the co-catalyst surface resulting in the separation of photogenerated electron-hole pairs.[20] We have used $Cd_4P_2I_3$ for the PL quenching study because of its good fluorescence characteristics. **Figure 15d** exhibits PL emission from $Cd_4P_2I_3$ and $Cd_4P_2I_3/Ni_xP_y$ (1wt % $Ni_xP_y$) recorded at an excitation wavelength of 480 nm. Presence of $Ni_xP_y$ effectively quenches the band edge emission (552 nm) of $Cd_4P_2I_3$, attributed to the fast transfer of the photogenerated electron from the conduction band of $Cd_4P_2I_3$ to the $Ni_xP_y$.

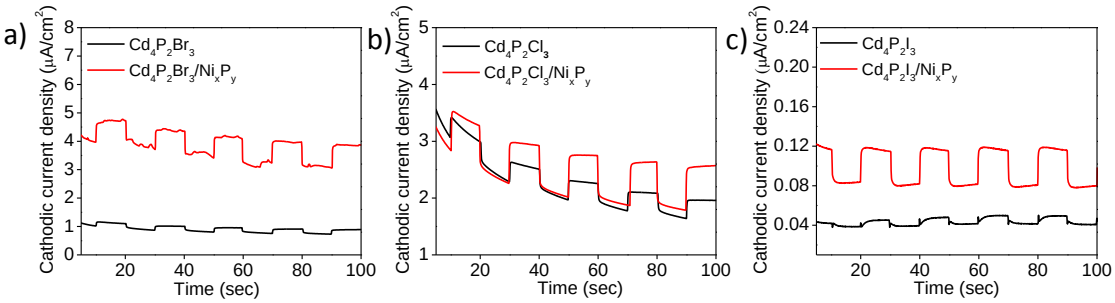


Figure 16. Transient photocurrent density of a) $Cd_4P_2Cl_3$ vs. $Cd_4P_2Cl_3/Ni_xP_y$ (1wt% $Ni_xP_y$), b) $Cd_4P_2Br_3$ vs. $Cd_4P_2Br_3/Ni_xP_y$(5wt% $Ni_xP_y$) and c) $Cd_4P_2I_3$ vs. $Cd_4P_2I_3/Ni_xP_y$ (1wt% $Ni_xP_y$). In all photoelectrochemical measurements, spin coated electrode was used as working electrode and the electrical connections were given with Cu wire using conducting Ag paste. The area of electrode except the exposed part of the deposited film was electrically insulated by transparent epoxy coating.

This transfer of electrons causes decrease in the recombination rate of electron-hole pairs and therefore enhances the photocatalytic $H_2$ evolution activity. Transient photocurrent measurements were also carried out to further verify the role of $Ni_xP_y$ as an acceptor of photogenarted electrons in $Cd_4P_2X_3$ (**Figures 16**).[21]$Cd_4P_2X_3/Ni_xP_y$ showed an enhancement in the photocurrent with respect to pristine $Cd_4P_2X_3$ suggesting the reduction in the rate of recombination of photogenerated charge carriers due to transfer of electron from $Cd_4P_2X_3$ to $Ni_xP_y$. Photocurrent values of $Cd_4P_2Cl_3/Ni_xP_y$ (1wt %$Ni_xP_y$), $Cd_4P_2Br_3/Ni_xP_y$ (5 wt % $Ni_xP_y$) and $Cd_4P_2I_3/Ni_xP_y$ (1 wt % $Ni_xP_y$) are consistent with their hydrogen yield. These studies clearly suggest intimate contact between the photosensitizer, $Cd_4P_2X_3$, and the co-catalyst $Ni_xP_y$.

**Theoretical Results**

First-principles calculations on $Cd_4P_2X_3$ compounds present analysis of their electronic structure and photocatalytic properties. Their experimental photocatalytic hydrogen evolution activity is in the trend $Cd_4P_2Br_3$> $Cd_4P_2Cl_3$> $Cd_4P_2I_3$. The electronic structure along high symmetry lines in the Brillouin Zone exhibit a direct band gap at Γ-point for each of $Cd_4P_2X_3$ (X= Cl, Br, or I) compounds (**Figure 17**). From the theoretical estimates and experimentally measured band gaps, it is clear that the band-gaps estimated with hybrid functional-based calculations are quite close to their experimental values. From the projected density of states (**Figure 18a**, **18b)** it is

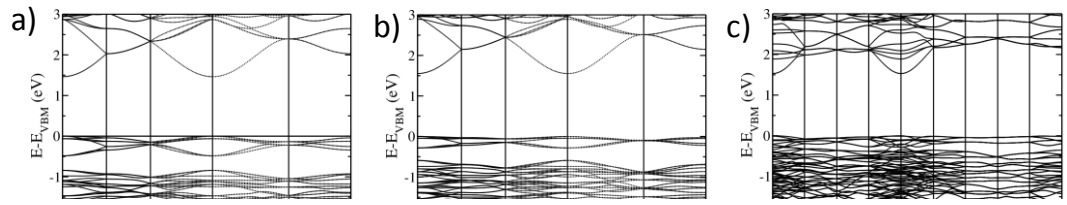


Figure 17. Electronic structures of a) $Cd_4P_2Cl_3$, b) $Cd_4P_2Br_3$, and c) $Cd_4P_2I_3$ along high symmetry lines in the Brillouin Zone.

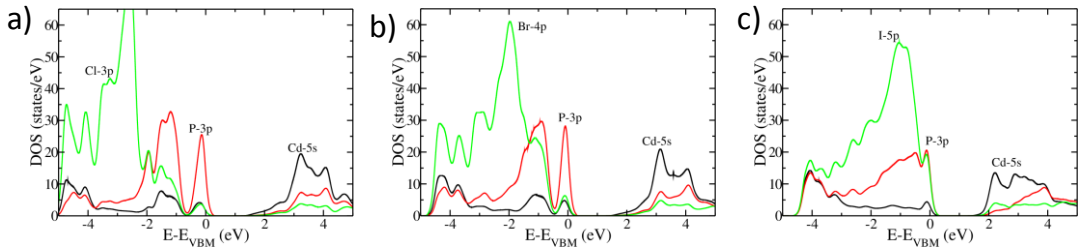


Figure 18. Density of electronic states of a) $Cd_4P_2Cl_3$, b) $Cd_4P_2Br_3$, and c) $Cd_4P_2I_3$ projected onto atomic orbitals.

clear that the electronic bands near the valence band maximum (VBM) have a dominant contribution from 3p-orbitals of P, with a slight mixing with 3p-orbitals of Cl (or 4p-orbitals of Br) and 5s-orbitals of Cd in $Cd_4P_2Cl_3$ ($Cd_4P_2Br_3$). The dominant contribution to the states near the conduction band minimum (CBM) comes from 5s orbitals of Cd and with a slight mixing with 3p-orbitals of P, and 3p-orbitals of Cl (or 4p-orbitals of Br) is also seen in $Cd_4P_2Cl_3$ ($Cd_4P_2Br_3$) (**Figure18a and 18b**). In contrast, the states near the VBM of $Cd_4P_2I_3$ have comparable contributions from 5p orbitals of I and 3p orbitals of P, with a slight mixing with 5s-orbitals of Cd. 5s orbitals of Cd are the dominant contributors to the CBM with a small component of 3p-orbitals of P and 5p-orbitals of I (**Figure 18c).** To assess the suitability of electronic structure of these compounds for photocatalytic water splitting, we align their CBMs relative to vacuum and compared with the redox potential of water splitting and $CO_2$ reduction.

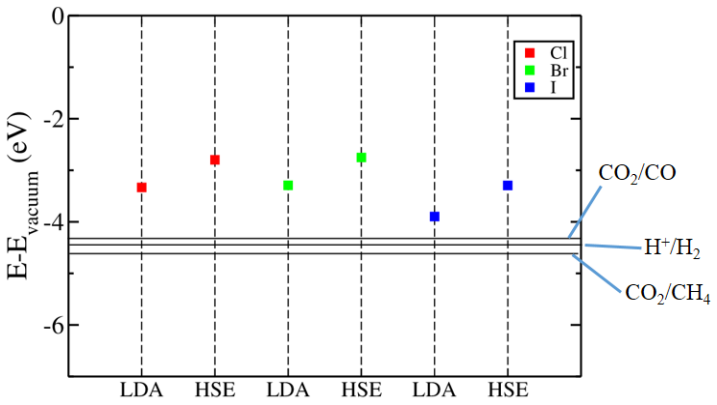


Figure 19. The energy of the conduction band minimum (CBM) of $Cd_4P_2X_3$ (X= Cl, Br, or I) aligned with respect to the vacuum potential, along with the redox potentials of $CO_2$ reduction reactions and hydrogen evolution reaction marked in solid lines.

For this, we determine ΔV, the difference between potentials in the vacuum and deep inside the bulk from simulations of slabs. We obtain the energies of VBM and CBM of the bulk relative to its macroscopic average potential. We then align the bulk bands with respect to vacuum using ΔV.

It is clear that the CBM edge of these compounds is above the HER potential, hence, $Cd_4P_2X_3$ (X= Cl, Br, I) compounds are suitable for HER (**Figure 19**). Since the CBM positions of $Cd_4P_2Cl_3$ and $Cd_4P_2Br_3$ are almost at the same level, we have examined the possible effect of vacancies on the catalytic activity by acting as an electron/hole traps.[22] We introduced 4.2% of X vacancies in $Cd_4P_2X_3$ (X= Cl, Br, I), and estimated the vacancy formation energy ($E_{vac.}$) using:

$$E_{vac.} = E_{Cd_4P_2X_{3-\delta}} - (E_{Cd_4P_2X_3} - \frac{1}{2}E_{X_2})$$

Here, $E_{Cd_4P_2X_{3-\delta}}$ is the energy of $Cd_4P_2X_3$ with X vacancies, $E_{Cd_4P_2X_3}$ is the energy of pristine crystal and $E_{X_2}$ is the energy of isolated gaseous $X_2$ molecule. From the vacancy formation energies (**Table 1**), it is relatively easier to introduce I vacancy as compare to Cl vacancy. As a result of the Cl vacancy, we identify a new (defect-related) peak in its VBM (**Figure 20a**). The peak has contribution mainly from P-3p and Cd-5s. We found a new peak in the CBM due to Br vacancy in $Cd_4P_2Br_3$ (**Figure 20b**).

| Systems | $E_{vac.}$ (eV) |
|---|---|
| $Cd_4P_2Cl_3$ | 3.04 |
| $Cd_4P_2Br_3$ | 2.83 |
| $Cd_4P_2I_3$ | 1.95 |

Table1. Energy of vacancy formation ($E_{vac.}$) in $Cd_4P_2X_3$ (X= Cl, Br, I).

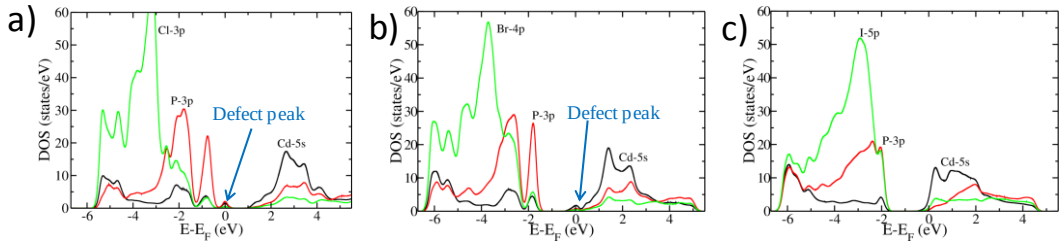


Figure 20. Electronic density of states of (a) $Cd_4P_2Cl_3$, (b) $Cd_4P_2Br_3$, and (c) $Cd_4P_2I_3$, with Cl, Br, and I vacancies respectively projected onto atomic orbitals.

The defect peak has a dominant contribution from 5s-orbitals of Cd compound. In $Cd_4P_2Cl_3$, we see that the two Cd atoms come closer and form a bond of length 3.2 Å near the Cl vacancy site. There are no such structural changes in $Cd_4P_2Br_3$ upon introduction of Br vacancy. We find defect peaks near the VBM and CBM of $Cd_4P_2Cl_3$ and $Cd_4P_2Br_3$ respectively. In contrast, $Cd_4P_2I_3$ does not show any new peak in the gap (**Figure 20c**). Consequently, the CBM moves up by 0.16 eV and down by 0.3 eV with respect to that of the pristine compound due to Cl and Br vacancies in $Cd_4P_2Cl_3$ and $Cd_4P_2Br_3$ respectively. The new defect states in $Cd_4P_2Cl_3$ and $Cd_4P_2Br_3$ possibly acting as a hole and electron traps respectively. This would reduce the electron-hole recombination leading to their good photocatalytic activity compared to $Cd_4P_2I_3$.[22b] Based on the redox potentials of reactions involved in $CO_2$ reduction (**Figure 19**), we expect $Cd_4P_2X_3$ compounds to be suitable for catalytic $CO_2$ reduction as well.

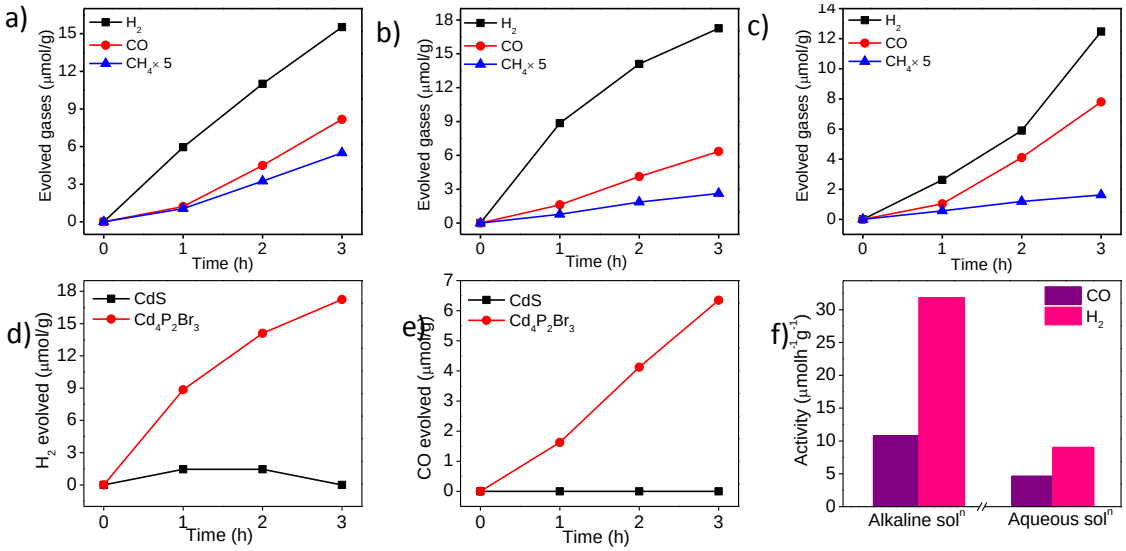


Figure 21. Photocatalytic $CO_2$ reduction in pure water (without pH adjustment) using a) $Cd_4P_2Cl_3$, b) $Cd_4P_2Br_3$, and C) $Cd_4P_2I_3$ photocatalyst. Figure d), and e) show comparison of the catalytic activity of CdS and $Cd_4P_2Br_3$ for $CO_2$ photoreduction in pure water (without pH adjustment) f) $CO_2$ reduction rate of $Cd_4P_2Cl_3$ catalyst under alkaline (0.5 M NaOH) and aqueous solution (water without pH adjustment). Reaction condition: 60 mL di-water, 40 mg photocatalyst, Xe-lamp (400 W).

In the light of the experimental and theoretical CBM positions of $Cd_4P_2X_3$ compounds, we have investigated the photocatalytic reduction of $CO_2$ by these compounds, in the absence of any sacrificial electron donor or a co-catalyst, with water as the source of electrons. All the three $Cd_4P_2X_3$ compounds showed steady rate of production of CO and $CH_4$ along with $H_2$. $Cd_4P_2Cl_3$ exhibits a $H_2$, CO and $CH_4$ production rate of 10.8, 4.6 and 0.36 $\mu molh^{-1}g^{-1}$ respectively (**Figure 21a**). $Cd_4P_2Br_3$ exhibits a $H_2$, CO and $CH_4$ production rate of 13.4, 4.0 and 0.35 $\mu molh^{-1}g^{-1}$ respectively (**Figure 21b**) whereas $Cd_4P_2I_3$ compound showed the $H_2$, CO and $CH_4$ production rate of 7.0, 4.3 and 0.21 $\mu molh^{-1}g^{-1}$ respectively (**Figure 21c)**. Control experiments showed no trace of any $CO_2$ reduction products under the following reaction conditions; a) $CO_2$ + $H_2O$ + catalyst, without light, b) $CO_2$ + $H_2O$ + light, without any catalyst, c) $H_2O$ + light + catalyst, without $CO_2$. These results confirm that the production of CO and $CH_4$ is due to the photoreduction of $CO_2$ in the presence of the $Cd_4P_2X_3$ catalysts. We have examined the catalytic activity of commercial CdS for the photocatalytic $CO_2$ reduction in an aqueous medium (pure water without pH adjustment) but did not observe any $CO_2$ reduction product,

$Cd_4P_2Br_3$, on the other hand, showed robust production of CO, $CH_4$ and $H_2$ gases (**Figures 21d and 21e**) suggesting the superiority of $Cd_4P_2X_3$ compounds as photocatalysts. We further examined $CO_2$ reduction in 0.5 M NaOH aqueous solution using $Cd_4P_2Cl_3$ catalyst, since there would be greater absorption of $CO_2$ in alkaline medium.[23] **Figure 21f** presents the histogram comparing photocatalytic activity of $Cd_4P_2Cl_3$ in pure water and 0.5 M aqueous NaOH solutions. An enhancement in the activity of $H_2$ production rate from 10.8 to 31.8 $\mu molh^{-1}g^{-1}$ and of CO production from 4.6 to 9.0 $\mu molh^{-1}g^{-1}$ is observed in alkaline medium. Since $Cd_4P_2X_3$ compounds reduce $H_2O$ and $CO_2$ in the absence of sacrificial agents, it would be expected that holes are getting consumed in the oxidation of the water. To verify the oxidation products parallel to $H_2O$ and $CO_2$ reduction, we have measured the $O_2$ evolution using ocean optics fluorescence-based sensor. Continuous evolution of $O_2$ was observed from these photocatalysts confirming $O_2$ as the oxidation product (**Figure 22**). Oxidation of water into $O_2$ by the holes generated in the valence band of $Cd_4P_2X_3$ compounds can be rationalized in terms of the VBM position of the $Cd_4P_2X_3$ compounds, which is below (more positive) than the oxidation potential of $H_2O/O_2$. It is noteworthy that $Cd_4P_2X_3$ compounds oxidizes $H_2O$ whereas CdS itself oxidizes under irradiation. Photocatalytic $CO_2$ reduction using $Cd_4P_2Cl_3/Ni_xP_y$ (1wt% $Ni_xP_y$) in an aqueous medium showed significant enhancement in $H_2$ evolution rate from 8.4 to 50.5 $\mu molh^{-1}g^{-1}$ whereas CO production decreased from 2.8 to 0.74 $\mu molh^{-1}g^{-1}$ (**Figure 23**) suggesting the suitability of $Ni_xP_y$ co-catalyst for proton reduction ($H^+/H_2$) over $CO_2$ reduction. Clearly $Ni_xP_y$ should not be used as a co-catalyst for $CO_2$ reduction in aqueous medium. We have also studied the photocatalytic $CO_2$ reduction from pristine $Cd_4P_2X_3$ compounds under direct sun-light irradiation in pure water.

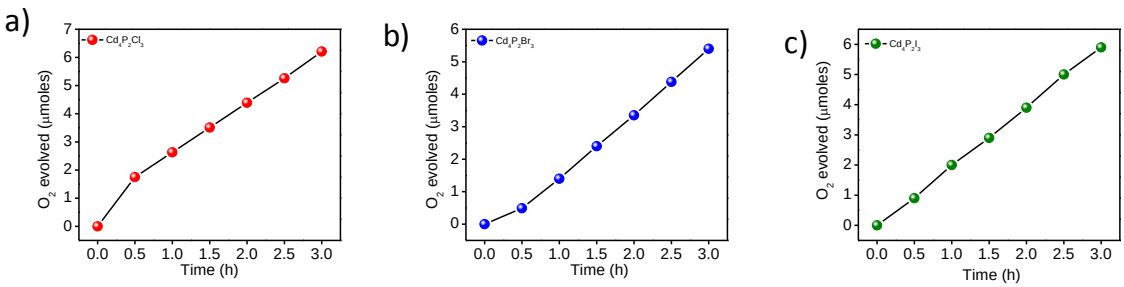


Figure 22. Photocatalytic $O_2$ evolution from a) $Cd_4P_2Cl_3$, b) $Cd_4P_2Br_3$, and c) $Cd_4P_2I_3$ photocatalysts.

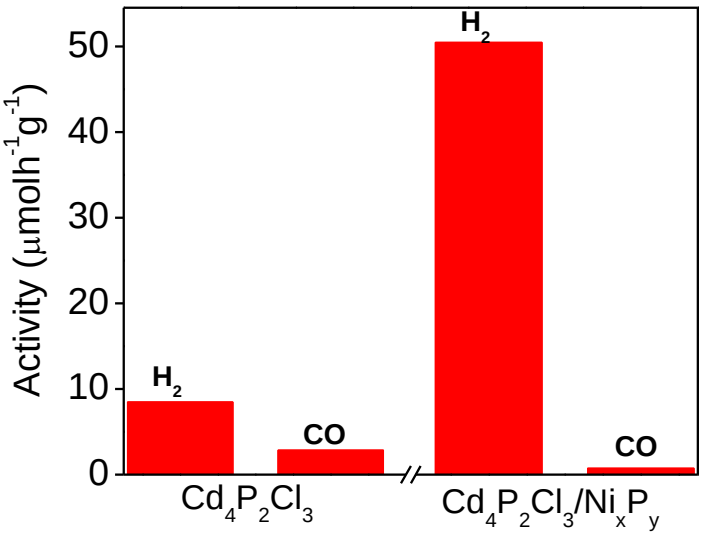


**Figure 23.** Photocatalytic $CO_2$ reduction from pristine $Cd_4P_2Cl_3$, and $Cd_4P_2Cl_3/Ni_xP_y$ (1 wt % $Ni_xP_y$) photocatalyst in Di-water (without pH adjustment).

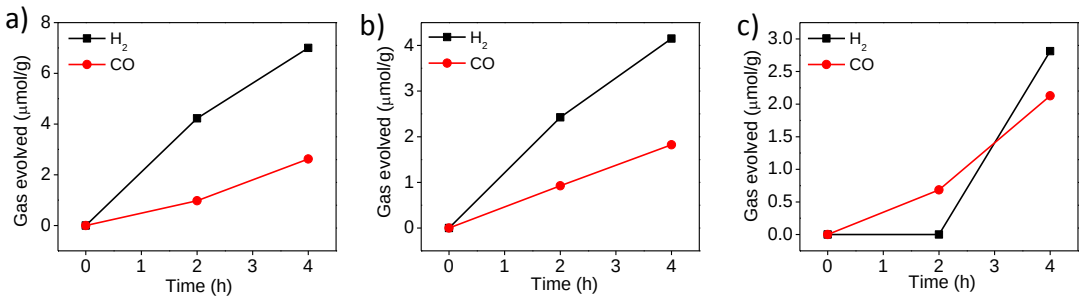


**Figure 24.** Photocatlytic $CO_2$ reduction in Di-water (without pH adjustment) under direct sun-light irradiation using a) $Cd_4P_2Cl_3$, b) $Cd_4P_2Br_3$, and c) $Cd_4P_2I_3$ photocatalysts.

All the three compounds showed robust photocatalytic activity with continuous CO and $H_2$ production even under sun-light irradiation (**Figure 24**).

To the best of our knowledge, there are very few semiconductor photocatalysts known to perform the photoreduction of $CO_2$ in aqueous medium without any sacrificial agents or co-catalyst.[24] It is noteworthy that pristine $Cd_4P_2X_3$ (X = Cl, Br, I) compounds shows the potential of photoreduction of $CO_2$ in pure water without any sacrificial agent or a co-catalyst.

# 5. Conclusions

In summary, we report a new family of photocatalysts of the composition, $Cd_4P_2X_3$ (X= Cl, Br, or I) with direct band gaps in the 2.21-2.23 eV range and are able to make use of a large fraction of the visible-light. Theoretical calculations show suitable alignment of the conduction band position of these compounds in relation to the $H_2O$ and $CO_2$ redox potentials to perform water splitting and $CO_2$ reduction. Experimentally, it is found that $Cd_4P_2X_3$ show excellent catalytic activity for hydrogen evolution and $CO_2$ reduction even in the absence of a sacrificial agent. By employing the strategy of aliovalent substitution in CdS, we have been able to suppress the inherent problem of $S^{2-}$ photocorrosion. In the $Cd_4P_2X_3$ family, $Cd_4P_2Br_3$ is the best catalyst for the hydrogen evolution reaction whereas $Cd_4P_2I_3$ shows the highest selectivity for $CO_2$ reduction. Comprehensive photoelectrochemical and theoretical studies have been employed to understand the catalytic behavior of this family of compounds. Electrochemical impedance and transient photocurrent measurements have shown least charge transfer resistance and highest photocurrent density in the case of $Cd_4P_2Br_3$ in accordance with its superior catalytic activity.

# 6. References


[1] a) G. Centi, S. Perathoner, *Catal. Today* **2009**, *148*, 191-205; b) A. Dhakshinamoorthy, S. Navalon, A. Corma, H. Garcia, *Energy Environ. Sci.* **2012**, *5*, 9217-9233; c) W. Wang, S. Wang, X. Ma, J. Gong, *Chem. Soc. Rev.* **2011**, *40*, 3703-3727; d) S. C. Roy, O. K. Varghese, M. Paulose, C. A. Grimes, *ACS Nano* **2010**, *4*, 1259-1278.

[2] E. V. Kondratenko, G. Mul, J. Baltrusaitis, G. O. Larrazábal, J. Pérez-Ramírez, *Energy Environ. Sci.* **2013**, *6*, 3112-3135.

[3] a) A. Fujishima, K. Honda, *Nature* **1972**, *238*, 37-38; b) L. A. Silva, S. Y. Ryu, J. Choi, W. Choi, M. R. Hoffmann, *J. Phys. Chem. C* **2008**, *112*, 12069-12073; c) S. Y. Tee, K. Y. Win, W. S. Teo, L.-D. Koh, S. Liu, C. P. Teng, M.-Y. Han, *Adv. Sci.* **2017**, *4*, 1600337; d) K. Li, M. Han, R. Chen, S.-L. Li, S.-L. Xie, C. Mao, X. Bu, X.-L. Cao, L.-Z. Dong, P. Feng, Y.-Q. Lan, *Adv. Mater.* **2016**, *28*, 8906-8911; e) X. Chen, C. Li, M. Grätzel, R. Kostecki, S. S. Mao, *Chem. Soc. Rev.* **2012**, *41*, 7909-7937.

[4] a) A. Kudo, Y. Miseki, *Chem. Soc. Rev.* **2009**, *38*, 253-278; b) D. J. Fermin, E. A. Ponomarev, L. M. Peter, *J. Electroanal. Chem.* **1999**, *473*, 192-203.

[5] a) M. Zhao, F. Huang, H. Lin, J. Zhou, J. Xu, Q. Wu, Y. Wang, *Nanoscale* **2016**, *8*, 16670-16676; b) H. Kaga, Y. Tsutsui, A. Nagane, A. Iwase, A. Kudo, *J. Mater. Chem. A* **2015**, *3*, 21815-21823; c) I. Tsuji, H. Kato, A. Kudo, *Chem. Mater.* **2006**, *18*, 1969-1975.

[6] A. Roy, U. S. Shenoy, K. Manjunath, P. Vishnoi, U. V. Waghmare, C. N. R. Rao, *J. Phys. Chem. C* **2016**, *120*, 15063-15069.

[7] a) A. V. Shevelkov, L. N. Reshetova, B. A. Popovkin, *J. Solid State Chem.* **1998**, *137*, 138-142; b) L. Suchow, N. R. Stemple, *J. Electrochem. Soc.* **1963**, *110*, 766-769.

[8] J. Li, J. Li, X. Zhou, Z. Xia, W. Gao, Y. Ma, Y. Qu, *ACS Appl. Mater. Interfaces* **2016**, *8*, 10826-10834.

[9] A. Iwase, S. Yoshino, T. Takayama, Y. H. Ng, R. Amal, A. Kudo, *J. Am. Chem. Soc.* **2016**, *138*, 10260-10264.

[10] J. Yang, D. Wang, H. Han, C. Li, *Acc. Chem. Res.* **2013**, *46*, 1900-1909.

[11] P. Giannozzi, S. Baroni, N. Bonini, M. Calandra, R. Car, C. Cavazzoni, D. Ceresoli, G. L. Chiarotti, M. Cococcioni, I. Dabo, A. Dal Corso, S. de Gironcoli, S. Fabris, G. Fratesi, R. Gebauer, U. Gerstmann, C. Gougoussis, A. Kokalj, M. Lazzeri, L. Martin-Samos, N. Marzari, F. Mauri, R. Mazzarello, S. Paolini, A. Pasquarello, L. Paulatto, C. Sbraccia, S. Scandolo, G. Sclauzero, A. P. Seitsonen, A. Smogunov, P. Umari, R. M. Wentzcovitch, *J. Phys.: Condens. Matter.* **2009**, *21*, 395502.

[12] J. P. Perdew, K. Burke, M. Ernzerhof, *Phys. Rev. Lett.* **1996**, *77*, 3865-3868.

[13] J. Heyd, G. E. Scuseria, M. Ernzerhof, *J. Chem. Phys.* **2003**, *118*, 8207-8215.

[14] A. Rebbah, J. Yazbeck, A. Deschanvres, *Acta Cryst. B* **1980**, *36*, 1747-1749.

[15] H. N. Kim, T. W. Kim, I. Y. Kim, S.-J. Hwang, *Adv. Funct. Mater.* **2011**, *21*, 3111-3118.

[16] J. Ran, J. Zhang, J. Yu, M. Jaroniec, S. Z. Qiao, *Chem. Soc. Rev.* **2014**, *43*, 7787-7812.

[17] a) Y. Tamaki, A. Furube, M. Murai, K. Hara, R. Katoh, M. Tachiya, *Phys. Chem. Chem. Phys.* **2007**, *9*, 1453-1460; b) L. Xiao-e, A. N. M. Green, S. A.

Haque, A. Mills, J. R. Durrant, *J. Photochem. Photobiol., A* **2004**, *162*, 253-259; c) J. Tang, J. R. Durrant, D. R. Klug, *J. Am. Chem. Soc.* **2008**, *130*, 13885-13891.

[18] a) Y. Tang, X. Hu, C. Liu, *Phys. Chem. Chem. Phys.* **2014**, *16*, 25321-25329; b) W. Lee, H. J. Son, D.-K. Lee, B. Kim, H. Kim, K. Kim, M. J. Ko, *Synth. Met.* **2013**, *165*, 60-63.

[19] a) A. Pareek, P. Paik, P. H. Borse, *Electroanalysis* **2014**, *26*, 2403-2407; b) E. Gao, W. Wang, M. Shang, J. Xu, *Phys. Chem. Chem. Phys.* **2011**, *13*, 2887-2893.

[20] L. Li, Z. Deng, L. Yu, Z. Lin, W. Wang, G. Yang, *Nano Energy* **2016**, *27*, 103-113.

[21] a) Y. Min, G. He, Q. Xu, Y. Chen, *J. Mater. Chem. A* **2014**, *2*, 2578-2584; b) Y. B. Xie, *Adv. Funct. Mater.* **2006**, *16*, 1823-1831.

[22] a) F. Dong, X. Xiao, G. Jiang, Y. Zhang, W. Cui, J. Ma, *Phys. Chem. Chem. Phys.* **2015**, *17*, 16058-16066; b) H. Tan, Z. Zhao, W.-b. Zhu, E. N. Coker, B. Li, M. Zheng, W. Yu, H. Fan, Z. Sun, *ACS Appl. Mater. Interfaces* **2014**, *6*, 19184-19190.

[23] a) J. Mao, T. Peng, X. Zhang, K. Li, L. Zan, *Catal. Commun.* **2012**, *28*, 38-41; b) Z.-Y. Wang, H.-C. Chou, J. C. S. Wu, D. P. Tsai, G. Mul, *Appl. Catal., A* **2010**, *380*, 172-177.

[24] K. Li, X. An, K. H. Park, M. Khraisheh, J. Tang, *Catal. Today* **2014**, *224*, 3-12.

# Chapter 6

# Effect of $Mn^{2+}$ Substitution in Cadmium Phosphochlorides


## Summary*

Cadmium phosphochlorides form a class of materials with the members, $Cd_2P_3Cl$, $Cd_3PCl_3$, $Cd_4P_2Cl_3$, and $Cd_7P_4Cl_6$, which possess different structural features and photophysical properties. Among the members of cadmium phosphochlorides $Cd_4P_2Cl_3$ and $Cd_7P_4Cl_6$ possess striking differences in structure and properties though both the compounds crystallize in cubic structure. $Cd_7P_4Cl_6$ exhibits superior photochemical hydrogen evolution activity than $Cd_4P_2Cl_3$, but $Cd_4P_2Cl_3$ exhibits superior photostability than $Cd_7P_4Cl_6$. The cadmium atoms in these compounds are of different nature. Substitution of paramagnetic $Mn^{2+}$ at place of $Cd^{2+}$ in these cadmium phosphochlorides results in the formation of thermodynamically less favored $Cd_7P_4Cl_6$ at high temperatures. Manganese incorporation is more preferred in $Cd_{7-y}Mn_yP_4Cl_6$ compare to $Cd_{4-x}Mn_xP_2Cl_3$. Substitution of Mn in $Cd_{7-y}Mn_yP_4Cl_6$ causes change in the nature of charge carriers from n-type (in the case of pristine $Cd_7P_4Cl_6$) to p-type. However, even a high proportion of Mn incorporation in $Cd_{4-x}Mn_xP_2Cl_3$ does not change the nature of carriers. Effect of Mn-substitution on the photochemical HER properties of compounds has been explored. First principles calculations illustrate the effect of Mn-substitution on the lattice parameters, electronic structure and properties of these compounds.

# 1. Introduction

Cadmium phosphochlorides of different compositions such as $Cd_4P_2Cl_3$, $Cd_7P_4Cl_6$, $Cd_3PCl_3$, $Cd_2P_3Cl$, and $Cd_2PCl_2$ are known.[1] Change of Cd/P and Cd/Cl ratio not only changes the structural features of these compounds but also has a notable impact on the electronic and optical properties.[1] For instance, $Cd_3PCl_3$ and $Cd_2P_3Cl$ with highest and lowest Cl/Cd ratio crystallize in the orthorhombic (Pnma) and monoclinic (C2/c) structures respectively, whereas $Cd_4P_2Cl_3$ and $Cd_7P_4Cl_6$ with the intermediate Cl/Cd ratio crystallize in the cubic structure (Pa-3).[2] Except for $Cd_2P_3Cl$, all the compounds have two different types of cadmium atoms coordinated by only Cl atoms or both P and Cl atoms. One of the unique properties of cadmium phophochlorides is the variation of band gap with Cl/Cd and P/Cd ratios.[3] Electronic structures reveal direct band gaps of these semiconducting compounds except for $Cd_2P_3Cl$ which is an indirect band gap semiconductor.[3] The Valence bands in $Cd_4P_2Cl_3$, $Cd_7P_4Cl_6$, and $Cd_2P_3Cl$ are primarily constituted of P p-orbitals whereas in the case of $Cd_3PCl_3$ there is a nearly equal contribution of p-orbitals P and Cl. Electronic structure of $Cd_2P_3Cl$ is unique because of its conduction band has significant contribution from P p-orbitals whereas all other compounds have Cd 5s-orbitals as a significant contributor to the conduction band.[3] Among different cadmium phosphochlorides cubic $Cd_4P_2Cl_3$ and $Cd_7P_4Cl_6$ are known to exhibit better photochemical HER activity and photostability.[3]

There have been studies to alter the structural, electronic and optical properties of semiconductors by means of cation substitution. Substitution of cations in a semiconductor material can alter its properties. Doping of bulk semiconductor material with paramagnetic ions gives rise to sp-d exchange interaction between paramagnetic dopant ions and semiconductor charge carriers resulting in the remarkable magnetic and magneto-optical properties.[4] Doping of $Mn^{2+}$ is known to modify the photophysical and electronic properties of semiconductor quantum dots.[5] $Mn^{2+}$ creates electronic states in the mid gap region of host semiconductor and influences the charge carrier separation and recombination dynamics.[6] Synthesis of Mn-doped CdS quantum dots and their use in the solar cell device is known to

improve the performance because of the trapping of photogenerated electrons by Mn-states.[7] Bhargava et al. have reported that $Mn^{2+}$ substitution in ZnS exhibits high luminescence due to $Mn^{2+}$ emission.[5a] Other than II-VI semiconductors, III-V semiconductors have also been doped with $Mn^{2+}$ ions.[4a] Inspired by these reports, we have investigated the effect of Mn-substitution in cadmium phosphochlorides. A striking difference between cadmium phophochlorides and other material relates to the structural features wherein there are two kinds of Cd1 and Cd2 atoms bounded with P and Cl differently in different compounds. It was of interest to study the substitution of manganese at the place of cadmium (1) and cadmium (2) in these compounds and their effect on the photophysical properties of cadmium phosphochlorides. First-principles calculations demonstrates the effect of Mn-substitution in cadmium phosphochlorides when substituted to two different Cd sites.

## 2. Scope of the Present Investigations

In the present work, we for the first time report the synthesis of manganese substituted cadmium phosphochlorides ($Cd_{4-x}Mn_xP_2Cl_3$ and $Cd_{7-y}Mn_yP_4Cl_6$). Mn-substitution in these compounds has been characterized using ICP-OES, EDAX, and XPS measurements. Effect of Mn-substitution on the structural, optical photoelectrochemical and photochemical properties have been described. Present work open a possibility to explore the doping of different transition metal ions in cadmium phophochlorides and their impact on the structural and photophysical properties.

## 3. Experimental Section

In a typical synthesis $Cd_3P_2$ (1.10 mmol), $CdCl_2$ (1.99 mmol), red-P (0.89 mmol), and different amounts of $MnCl_2$ were weighed inside glove-box and ground homogenously. This homogenous precursor was transferred in a quartz tube (I.D. = 10 mm, O.D.=12 mm) and sealed under vacuum. The sealed quartz tube was annealed at 500 °C for 24 h, followed by the cooling of the tube to the room temperature with the rate of 2.5 °/min. The reaction yielded a polycrystalline powder sample of two different colors (depending on the concentration of $MnCl_2$ taken) in the form of lump which was manually separated and ground in the form of fine powder.

**Photocatalytic hydrogen generation**

The photocatalytic reactions were carried out at ambient conditions using home-made quartz cells with head space for gas collection closed by high-quality rubber septa. In a typical procedure, semiconductor photocatalyst samples were dispersed in a 0.1 M NaOH aqueous solution (50 mL), and a calculated amount of $H_2PtCl_6$ solution was added (equivalent to 1wt% of Pt). The reaction solution was purged with Ar-gas for 15-20 minutes, and UV-light was switched on for 1h to photo-deposit the Pt nanoparticles on the semiconductor. After the photo-deposition reaction, cell was removed from the light irradiation and septa was taken out to add $Na_2S$ and $Na_2SO_3$ dissolved in 25 mL distilled water in order to make a total volume of 75 mL with a $Na_2S$ and $Na_2SO_3$ concentrations of 0.18 M and 0.24 M respectively. The solution was further purged with Ar-gas for 15-20 minutes and irradiated with visible light ($\lambda >$ 395 nm) using a Xe-Lamp (400 W). Sacrificial free hydrogen evolution was carried out in 3 M NaOH aqueous solution under same light irradiation.

**Characterization**

Powder X-ray diffraction (PXRD) patterns were recorded with a Bruker D8 Diffraction system using a Cu Kα source ($\lambda$ = 0.1541 nm). UV-vis absorption spectra were collected with Perkin Elmer Model Lambda 900 spectrometer. Energy dispersive spectroscopy (EDS) and elemental mapping analysis were carried out with an EDAX Genesis instrument attached to the SEM instrument. X-ray photoelectron spectra (XPS) were recorded with an Omicron Nanotechnology spectrometer using Al-Kα (1486.6 eV) X-ray source. Inductively coupled plasma-optical emission spectroscopy (ICP-OES) was carried out using Perkin Elmer Optima 7000 DV machine.

**Photoelectrochemical (PEC) Measurements**

Photoelectrochemical measurements were carried out on a CHI 1760E electrochemical work station (CH instrument Inc.) in a conventional three-electrode set-up. Spin-coated samples on FTO served as the working electrode, with a platinum wire as the counter electrode and an Ag/AgCl (saturated KCl) electrode as the reference electrode. The working electrode was prepared by spin coating. First, the catalyst slurry was prepared by ultrasonicating 20-25 mg photocatalyst in 50 µL Nafion (5.0 wt%, Sigma Aldrich) and 250 µL of ethanol for 20-30 minutes. Fluorine-

doped tin oxide (FTO) (2x1cm$^2$ pieces) which was used as the substrate was cleaned and dried at 100 ºC. An area of 1cm$^2$ of the substrate was masked by scotch tape and spin coating (750 rpm, 60seconds) was performed by collecting 15 µL of slurry each time. The electrode films were then dried under vacuum at 100ºC for 1 hour and Cu wire connections were made with the help of Ag paste. The portion of electrode, except the photocatalyst part, was electronically sealed by transparent epoxy coating and left overnight. A 0.5 M $Na_2SO_4$ aqueous solution was used as the electrolyte. A 300 W Xenon lamp, with a calibrated intensity of 100 mW/cm$^2$ was used as the light source.

**Computational Methods**

We have carried out first principles calculations based on density functional theory (DFT) employing the Quantum Espresso (QE) software package.[8] The exchange correlation energy is treated in the Generalized Gradient Approximation, parameterized by the Perdew Burke Erzwehof (PBE) ultra-soft pseudopotentials (US-PP). Periodic boundary conditions are used for the electronic structure calculations. We have used kinetic energy cut off of 40 Ry to truncate the plane wave basis. A uniform k-mesh of 4x4x4 is used to sample the integration of the Brillouin zone. The valence electron configurations used in the calculations are 4d9.55s2.05p0.5 (Cd), 3s2 3p5 3d-2 (Cl) and 3s2 3p3 3d-2 (P) respectively. We have relaxed the structure, to minimize the Hellmann-Feynman forces such that the forces acting on individual atoms are less than 0.02 eV/Å. For achieving self-consistency in the Kohn-Sham solution, a convergence criterion of 10-7 eV was imposed. The dielectric properties are calculated by employing the post processing tools available in QE.For the density of states calculations, the VASP package is used and a Monkhorst Pack K grid of 16x16x16 is employed.[9] We have used PAW-PBE pseudopotentials employing the GGA approximation.

# 4. Results and Discussion

Powder X-ray diffraction (PXRD) patterns of cadmium phosphochlorides with different amount of manganese substitution is shown in **Figure 1**. The absence of $MnCl_2$ in the precursor mixture results in the formation of the thermodynamically stable $Cd_4P_2Cl_3$ phase with cubic structure (Pa-3).[2b] The presence of $MnCl_2$ in the precursor mixture affects the formation of thermodynamically favourable $Cd_4P_2Cl_3$ phase.The diffraction pattern of the sample prepared in the presence of small amount of $MnCl_2$ ($\chi_{Mn}^{2+}$ = 0.04, with respect to $Cd^{2+}$) revealed the emergence of the $Cd_7P_4Cl_6$ phase (cubic, Pa-3) (~ 12% ) along with the dominant $Cd_4P_2Cl_3$ phase (~ 88 %) (**Figure 1a**). An increase in the proportion of $MnCl_2$ ($\chi_{Mn}^{2+}$ = 0.08) resulted in the enhancement in the proportion of $Cd_7P_4Cl_6$ in the mixture from 12 to 20%, indicating that incorporation of $Mn^{2+}$ favors the formation of $Cd_7P_4Cl_6$ (**Figure 1a**). Further increase in the proportion of $MnCl_2$, above $\chi_{Mn}^{2+}$ = 0.08, results in phase segregation wherein two different kinds of product, greenish yellow (major product) and orange-yellow (minor product) were obtained in the different lumps. The PXRD pattern of the orange-yellow product revealed the presence of $Cd_4P_2Cl_3$ as the major contributor along with the small proportion of orthorhombic $Cd_3PCl_3$ phase (**Figure 1a**). The PXRD pattern of the greenish yellow compound revealed it to be pure $Cd_7P_4Cl_6$ (**Figure 1b**). Further increase in $MnCl_2$ amount ($\chi_{Mn}^{2+}$ = 0.15) in the precursor, results in the exclusive formation of $Cd_7P_4Cl_6$ phase (**Figure 1b**). $MnCl_2$ content above $\chi_{Mn}^{2+}$ = 0.15 in the precursor again results in the formation of orange-yellow ($Cd_4P_2Cl_3$+$Cd_3PCl_3$) (**Figure 1a**) and greenish yellow ($Cd_7P_4Cl_6$) (**Figure 1b**) products. The distribution of products remained the same in repeated experiments suggesting reproducibility of the reactions.

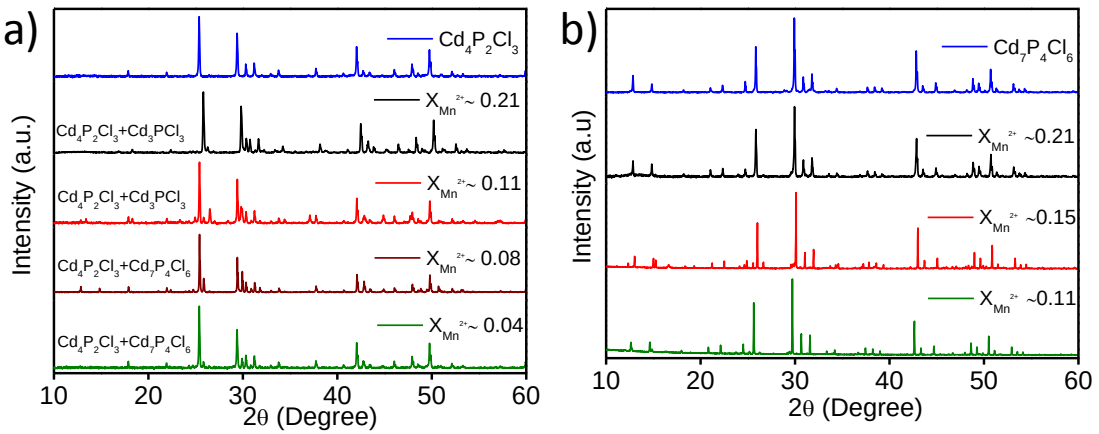


Figure 1. PXRD patterns of a) mixed phase compounds, and b) $Cd_{7-y}Mn_yP_4Cl_6$ compounds with different amount of Mn-substitution.

**Figure 2** presents the concentration of manganese in the mixed phase (**Figure 2a**) and $Cd_7P_4Cl_6$ (**Figure 2b**), estimated by ICP-OES. Percentage of Mn with respect to Cd in the mixed phase of $Cd_{4-x}Mn_xP_2Cl_3$+$Cd_{7-y}Mn_yP_4Cl_6$ was 3.8 and 6.3 % in the case of 12 and 20 % of $Cd_{7-y}Mn_yP_4Cl_6$ phase in the mixture, confirming increase in Mn-incorporation increases the proportion of $Cd_{7-y}Mn_yP_4Cl_6$ (**Figure 2a**). Substitution of ≥12.3 % of manganese in place of cadmium in $Cd_{7-y}Mn_yP_4Cl_6$ causes it to crystallize separately from mixed phase ($Cd_{4-x}Mn_xP_2Cl_3$+$Cd_{3-z}Mn_zPCl_3$). Interestingly, even at higher manganese concentration in the precursor, incorporation of manganese is favored in $Cd_{7-y}Mn_yP_4Cl_6$ compare to the $Cd_{4-x}Mn_xP_2Cl_3$+$Cd_{3-z}Mn_zPCl_3$ mixture. We have been able to prepare $Cd_{7-y}Mn_yP_4Cl_6$ with the compositions $Cd_{6.1}Mn_{0.9}P_4Cl_6$, $Cd_{5.8}Mn_{1.2}P_4Cl_6$, and $Cd_{5.5}Mn_{1.5}P_4Cl_6$ (**Figure 2b**). The maximum amount of Mn-substitution achieved in the case of mixed phase ($Cd_{4-x}Mn_xP_2Cl_3$+$Cd_{3-z}Mn_zPCl_3$) is 15.2%, however exact compositions (value of x and z) of mixed phase compounds cannot be calculated.

Incorporation of manganese in cadmium phosphochlorides was confirmed by energy dispersive X-ray absorption spectroscopy (EDAX) and X-ray photoelectron spectroscopy (XPS) measurments.

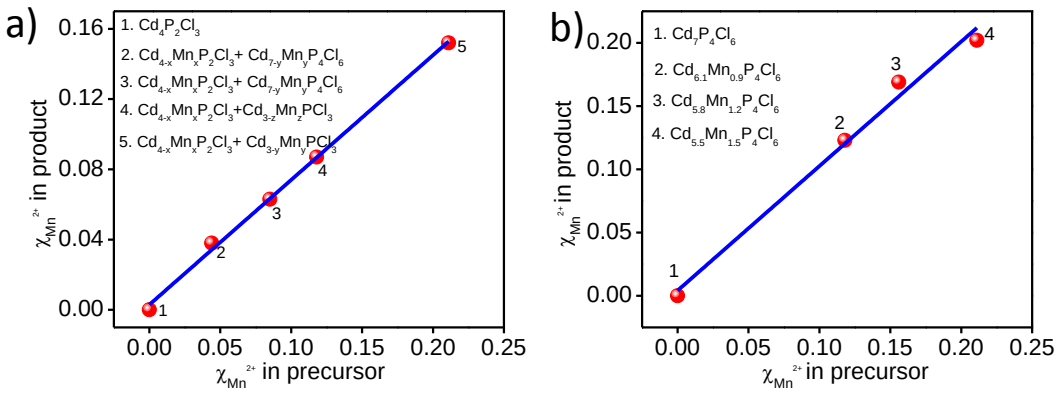


Figure 2. Mole fractions of manganese in product (obtained by ICP-OES) as a function of the mole fractions of manganese used in the precursor in a) mixed phase compounds, and b) $Cd_{7-y}Mn_yP_4Cl_6$ compounds.

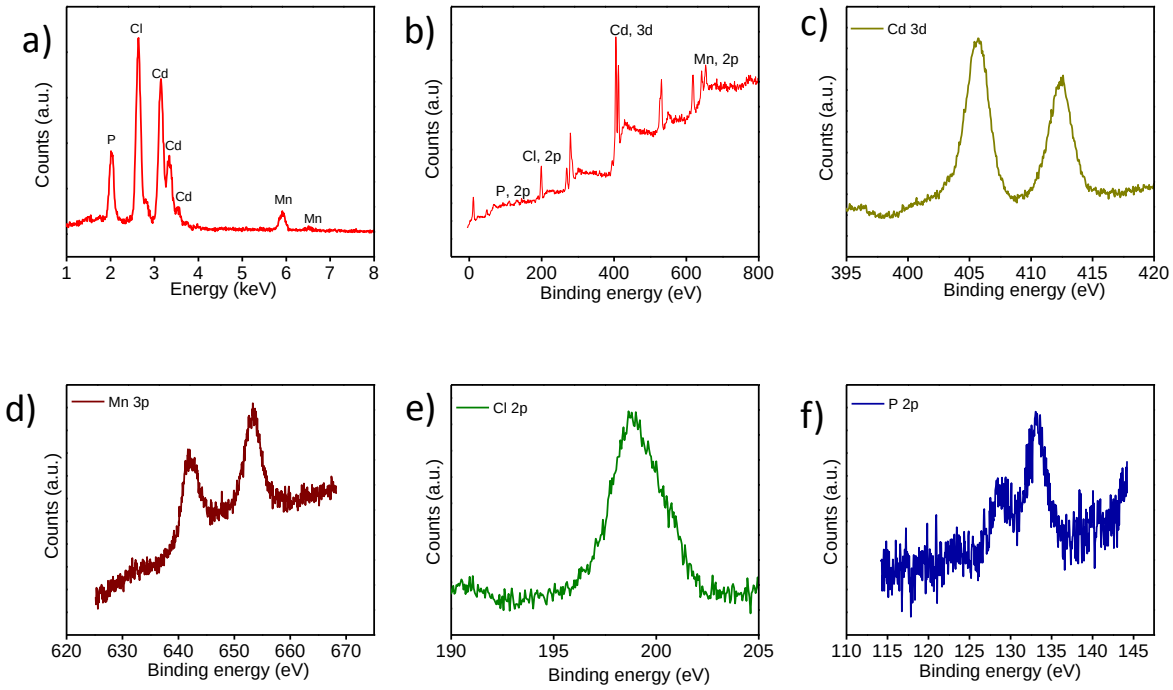


Figure 3. a) EDAX and b) XPS-survey scan spectrum of $Cd_{5.8}Mn_{1.2}P_4Cl_6$ compound, c) to f) core-level spectra of Cd, Mn, Cl, and P.

EDAX spectrum of $Cd_{5.8}Mn_{1.2}P_4Cl_6$ revealed the signals corresponding to Cd, Mn, P, and Cl (**Figure 3a**). XPS survey scan of $Cd_{5.8}Mn_{1.2}P_4Cl_6$ revealed the peaks corresponding to Cd, Mn, P, and Cl (**Figure 3b**). High-resolution XPS-core level spectra of Cd and Mn (**Figure 3c and 3d**) show a energy differences of 6.8 and 11.2 eV respectively between $3d_{5/2}$ and $3d_{3/2}$ (in the case of Cd)

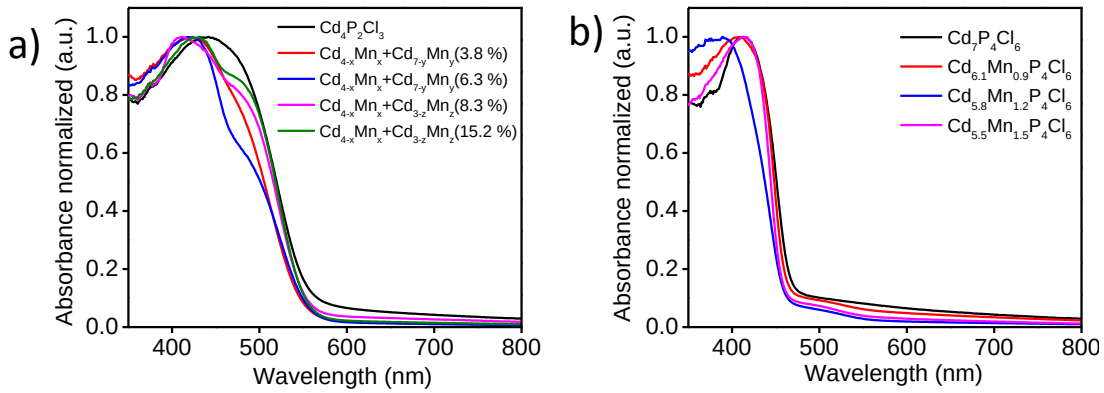


Figure 4. UV-vis absorption spectra of a) mixed phase, and b) $Cd_{7-y}Mn_yP_4Cl_6$ compounds, with different amount of Mn-substitution.

and $2p_{3/2}$ and $2p_{1/2}$ (in the case of Mn), characteristic of $Cd^{2+}$ and $Mn^{2+}$ states. High-resolution spectra of P and Cl are shown in **Figure 3e and 3f**.

UV-visible absorption spectra of pristine and manganese substituted compounds are shown in **Figure 4.** The mixed phase compounds exhibit absorption edge at ~560 nm, corresponding to the major contributor $Cd_{4-x}Mn_xP_2Cl_3$, along with the additional features towards lower wavelengths corresponding to $Cd_{7-y}Mn_yP_4Cl_6$ or $Cd_{3-z}Mn_zPCl_3$(**Figure 4a**). Pristine and manganese substituted $Cd_7P_4Cl_6$ show an absorption edge at ~469 nm (**Figure 4b**). Interestingly, both $Cd_{4-x}Mn_xP_2Cl_3$ and $Cd_{7-y}Mn_yP_4Cl_6$ phases exhibit a slight blue shift of the absorption edge with respect to the pristine compounds.

**First-principles calculations on Pristine and Mn-Substituted $Cd_4P_2Cl_3$**

We have carried out a detailed First-principles calculations to understand the effect of Mn-substitution on the structural and electronic properties of these compounds. The crystal structure of $Cd_4P_2Cl_3$ (**Figure 5**) can be described as based on a distorted face centered cubic packing of Cd atoms. There are two distinct Cd and P atoms as well as one Cl atom. The P(1) atoms paired with a distance of 2.19 Å and occupy 1/8 octahedral voids, while P(2) atoms fill 1/8 octahedral voids. The Cl atoms occupy the ¾ octahedral voids in a manner that they are shifted from the center of the octahedra towards one of the faces. Three Cd-Cl distances are nearer (2.62, 2.68 and 2.86A°) and hence can be considered as bonding while the other three are at farther distances (3.56, 3.65, and 3.75 A°). The P and Cl atoms arrange in such a way as to

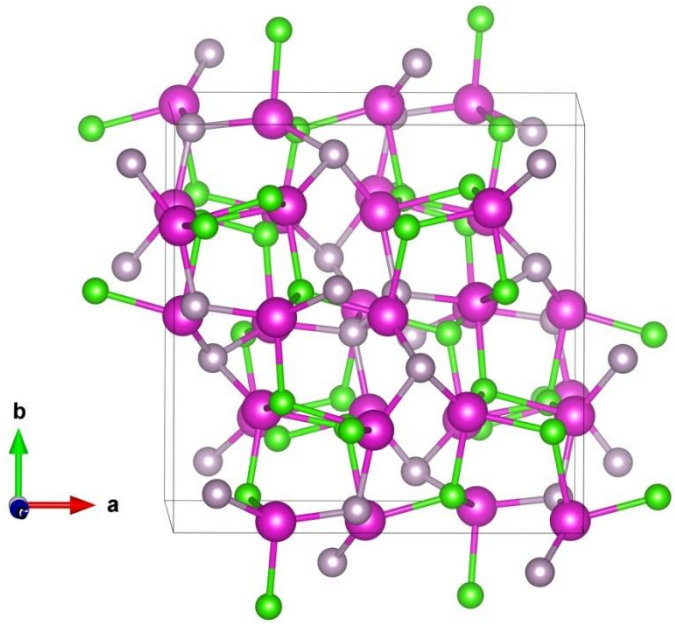


Figure 5. The structural unit of $Cd_4P_2Cl_3$ crystal. The Pink, grey and green atoms represent Cd, P and Cl respectively.

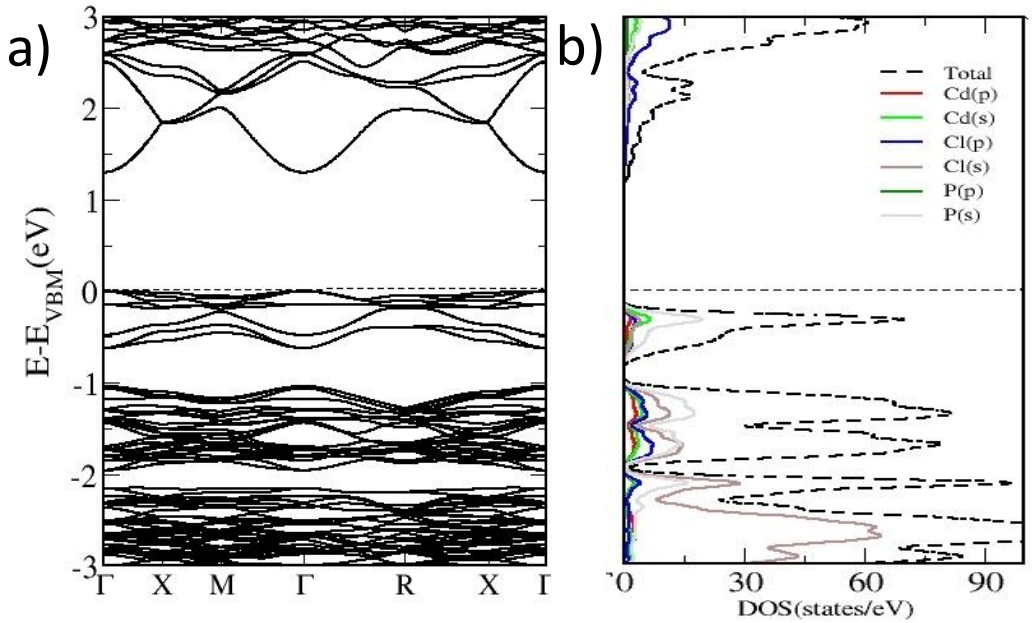


Figure 6. a) The electronic structure (left), and b) density of states (right) projected on to various atomic orbitals for $Cd_4P_2Cl_3$ plotted using GGA.

give a tetrahedral arrangement for the Cd atoms. The Cd(1) is surrounded by 3Cl+1P and Cd (2) by 2P+2Cl. We use Quantum Espresso (QE) Package to relax the structure with PAW-PBE pseudopotentials. A Monkhorst Pack k-grid of 4x4x4 is used for relaxations. The relaxed lattice parameters are 12.36 Å, while the experimental lattice

parameter is 12.14 Å. We use the software VASP to carry out the density of states and electronic structure with comparable parameters as that of QE. A k grid of 8x8x8 is used for the density of states calculations. In the density of states, major contribution in the valence band comes from p-orbitals of Cd and P, whereas the Cd s-orbitals also dominates the conduction band states (**Figures 6**).

**Mn-Substitution in $Cd_4P_2Cl_3$**

We substitute one Mn atom to two Cd sites, named as $Mn_{Cd1}$ and $Mn_{Cd2}$ to generate two different configurations. The energy difference between the pristine $Cd_4P_2Cl_3$ supercell and Mn substituted supercell is shown in the below **Table 1**. The two Cd sites are chosen in such a way that $Mn_{Cd1}$ is bonded to 1P and 3Cl atoms (**Figure 7a)** while, $Mn_{Cd2}$ is bonded to 2P and 2Cl atoms (**Figure 7b**). The relaxed lattice parameter for the $Mn_{Cd1}$ is 12.42Å, while that of the pristine $Cd_4P_2Cl_3$ was 12.36 Å, and which demonstrates that there is an expansion in lattice with the introduction of Mn. We define the energy difference between the spin polarized and non-spin polarized calculations with Mn substitution as $\Delta E/cell = E_{mag} - E_{non\text{-}mag}$ (eV). It can be

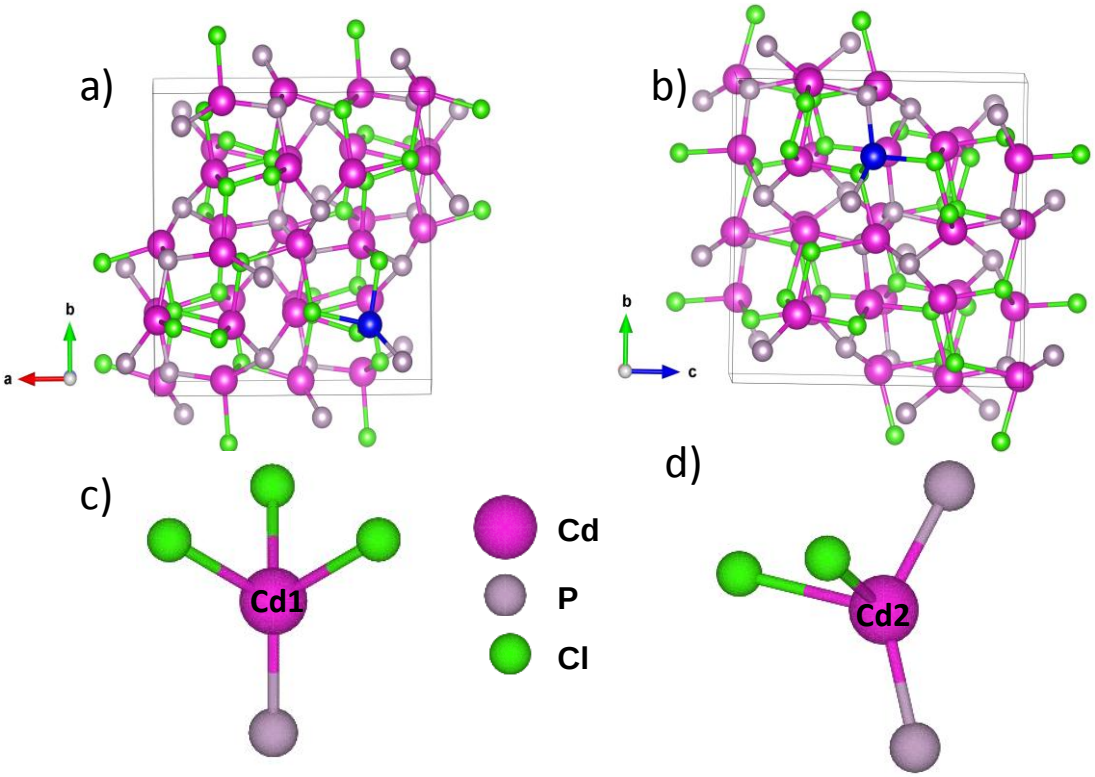


Figure 7. $Cd_{3.875}Mn_{0.125}P_2Cl_3$ with (a) Mn substituted at Cd-site that is bonded to 1-P and 3-Cl atoms, (b) Mn substituted at Cd site that is bonded to 2-P and 2-Cl atoms, c) Cd1 coordination geometry, and d) Cd2 coordination geometry.

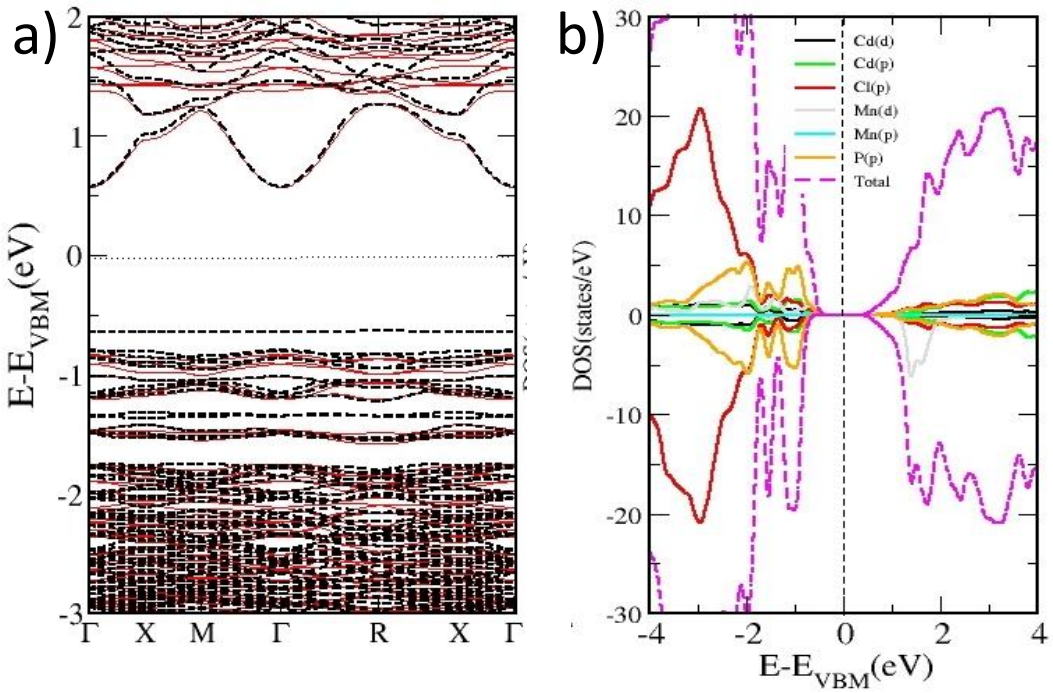


Figure 8. a) The spin polarized band structure (left), and b) density of states (right) of $Cd_{3.875}Mn_{0.125}$ $P_2Cl_3$ where $Cd_1$ is substituted with Mn. In the band structure, red and black lines represent spin-up and spin-down bands respectively.

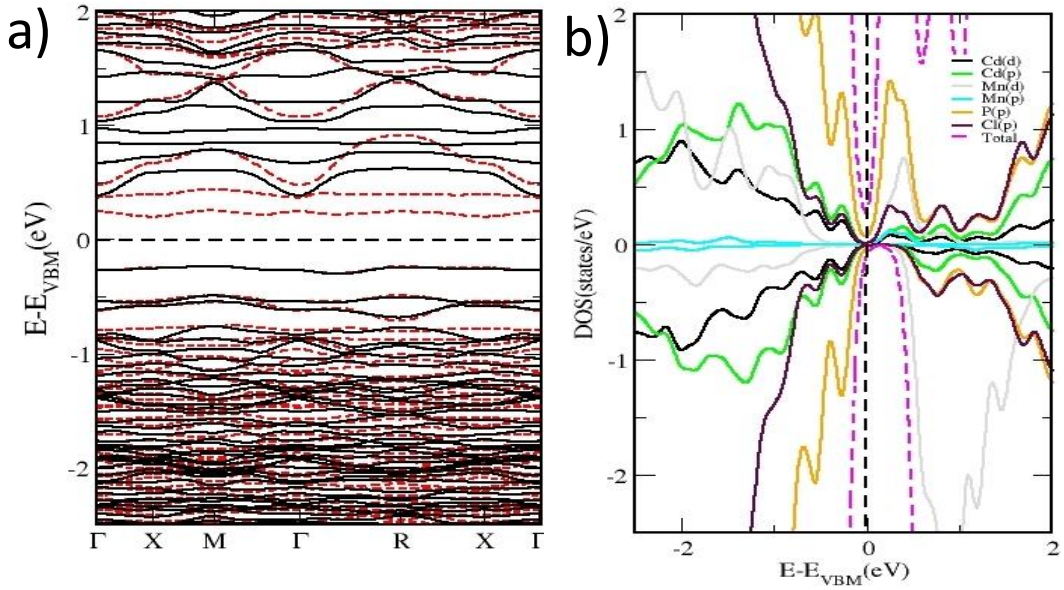


Figure 9. a) The spin polarized band structure (left), and b) density of states (right) of $Cd_{3.875}Mn_{0.125}$ $P_2Cl_3$, where $Cd_2$ is substituted with Mn. In the band structure, red and black lines represent spin-up and spin-down bands respectively.

| Structure | Relaxed lattice parameter (Å) | $\Delta E/cell = E_{mag} - E_{non\text{-}mag}$(eV) | Magnetic moment (Mn moment in parenthesis) ($\mu_B$) |
|---|---|---|---|
| $Cd_{3.875}Mn_{0.125}P_2Cl_3(Mn_{Cd1})$ | 12.42 | -2.02 | -4.454 (-4.256) |
| $Cd_{3.875}Mn_{0.125}P_2Cl_3(Mn_{Cd2})$ | a=12.62<br>b=12.12<br>c=13.05 | -2.24 | 3.073 (3.402) |

Table 1. The composition, theoretical estimates of lattice parameters, difference in free energy between magnetic and non-magnetic calculations, and magnetic moment of $Cd_4P_2Cl_3$with Mn substitution at $Cd_1$ and $Cd_2$ sites, calculated using VASP.

seen that the magnetic configuration is more stable when Mn is substituted into $Cd_4P_2Cl_3$. The relaxed lattice parameter for $Cd_4P_2Cl_3$ with Mn substituted at the $Cd_2$ position is a= 12.62Å, b= 12.12 Å and c= 13.05 Å (**Table 1**). It is noticed that Mn substituted at difference Cd sites (Cd1 and Cd2) changes the electronic structure of the pristine crystal in different ways. The band gap is reduced with Mn at Cd2 position (**Figures 8 and 9**).

**First-Principles Calculations on Pristine and Mn-Substituted $Cd_7P_4Cl_6$**

The bulk $Cd_7P_4Cl_6$ lattice is optimized without any constraints and the calculated lattice parameter, 12.08 Å is within the typical error of GGA estimations, while the experimental value being 11.936 Å (**Figure 10**). The crystal structure of $Cd_7P_4Cl_6$ consists of an octahedral anionic complex $[CdCl6]^{4-}$ and a three-dimensional cationic network, $[Cd_3P_2]^{2+}$, as shown in. The 3D network, $[Cd_3P_2]^{2+}$, consists of 3 Cd1, P-P bonds and the P-P bond length is 2.19 Å. The Cd-Cl bond length in the octahedral $[CdCl_6]^{4-}$ is 2.66 Å. These paired P atoms constitute the $P_2^{4-}$ anions. A slightly distorted tetrahedron is further formed by the bonding of each P atom to the three Cd (1) atoms. We also calculate the band structure (**Figure 11a**) and obtained a direct band gap of 1.8 eV at the Gamma point using the GGA approximation, while the experimentally reported band gap is 2.67 eV. The density of states analysis has been carried out using the VASP package, (**Figure 11b**).

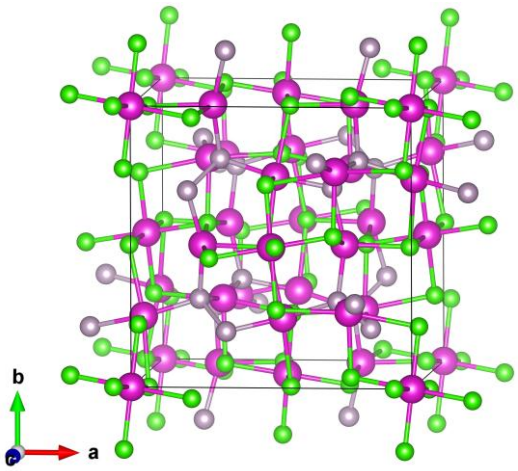


Figure 10. The structural unit of $Cd_7P_4Cl_6$ crystal. Pink, grey and green atoms indicate Cd, P and Cl respectively.

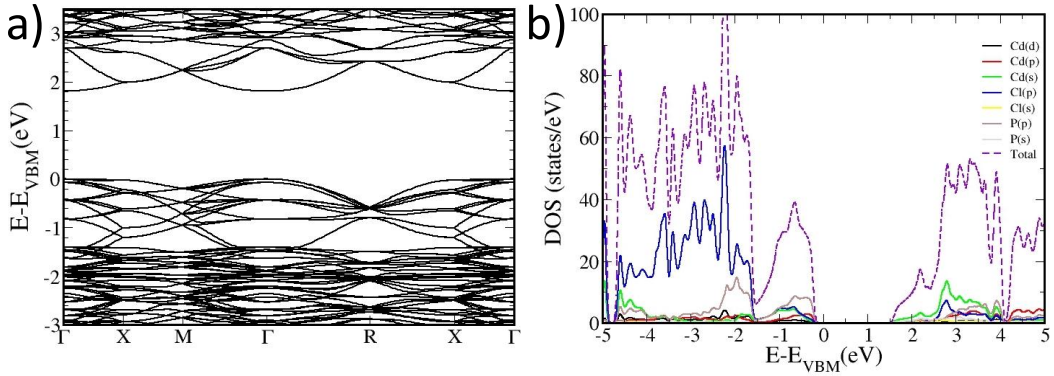


Figure 11. a) The electronic structure, and b) projected density of states of $Cd_7P_4Cl_6$.

The projected density of states (PDOS) show that the states at the valence band maximum (VBM) are mostly dominated by p-orbitals of Cl and P, while the contribution of P outweighs the others. While in the conduction band minimum (CBM) 5s-orbitals of the Cd and p-orbitals of Cl are mainly contributing.

**Mn-Substitution in $Cd_7P_4Cl_6$**

We have substituted an Mn atoms at two inequivalent Cd sites in $Cd_7P_4Cl_6$ to study the alloying effects, which amounts to $Cd_{6.75}Mn_{0.25}P_4Cl_6$. The two Cd sites are chosen in such a way that (a) Cd is bonded to two P atoms as well as to four Cl atoms such that the P-P distance is 2.19 Å, Cd-P distance is 2.48 Å, here one of the Cl atoms is at a closer distance of 2.76 Å while the other three Cl atoms are placed at 3.03 Å, 3.08 Å and 3.28Å, and (b) Cd is bonded to only Cl atoms placed at a distance of 2.662 Å. The **Figures 12a and 12b** show the positions of Mn substitution in $Cd_7P_4Cl_6$.

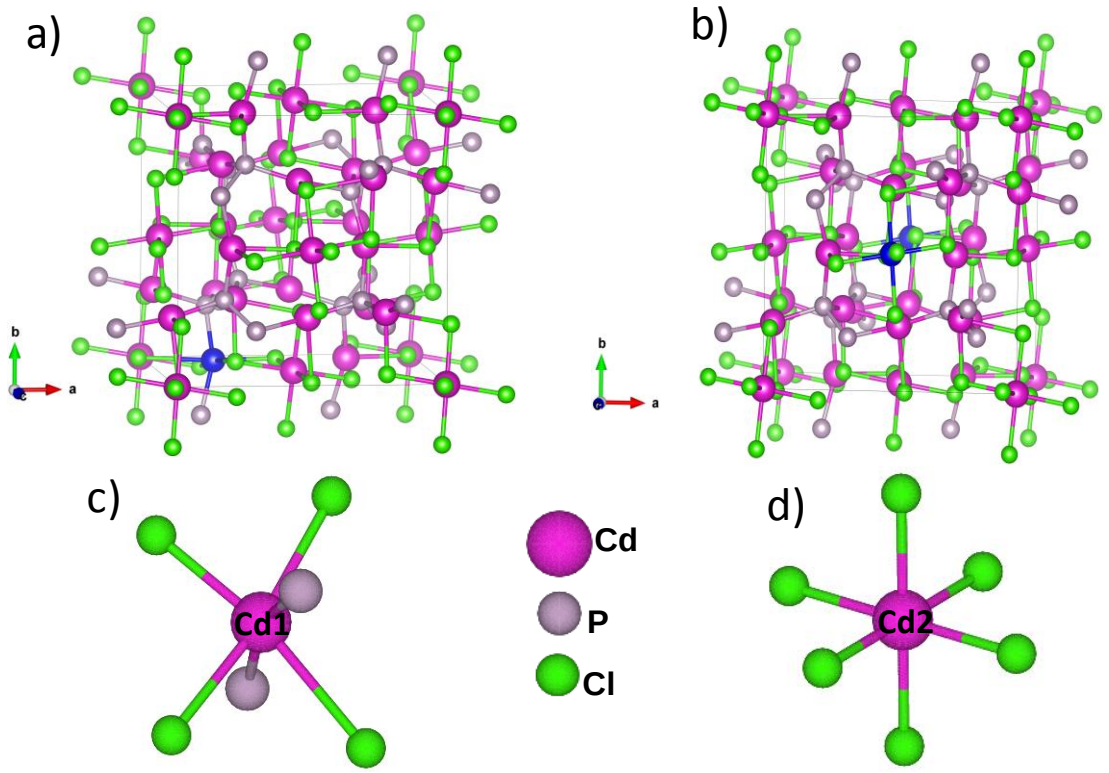


Figure 12. a) Mn substituted $Cd_7P_4Cl_6$, with MnCd1 is bonded to two P atoms and four Cl atoms, (b) MnCd2 bonded only to Cl atoms, c) coordination geometry of Cd1, and d) coordination geometry of Cd2 atoms.

We see that the lattice parameter is changed with Mn substitution to adjust the lattice strain as the relaxed lattice parameter without Mn substitution is 12.08 Å. The total energies for nonmagnetic and magnetic calculations show that the magnetic configuration is more stable than the non-magnetic one, which emphasize the importance of considering spin polarization, while calculating the ground state of the system (**Table 2**). Mn also induces a magnetic moment to the compound. We define the energy difference between the spin polarized and non-spin polarized calculations with Mn substitution as $\Delta E/cell = E_{mag} - E_{non\text{-}mag}$ (eV). It can be seen that the magnetic configuration is more stable than the non-magnetic one in this system also, in presence of Mn substitution in $Cd_7P_4Cl_6$ (**Table 2**). Since Mn is a magnetic atom, we have conducted spin polarized calculations and calculated band structure and density of states for $Cd_{6.75}Mn_{0.25}P_4Cl_6$. We have substituted Mn for both Cd1 and Cd2 positions and the respective band structure and density of states are shown in **Figures 13 and 14** respectively.

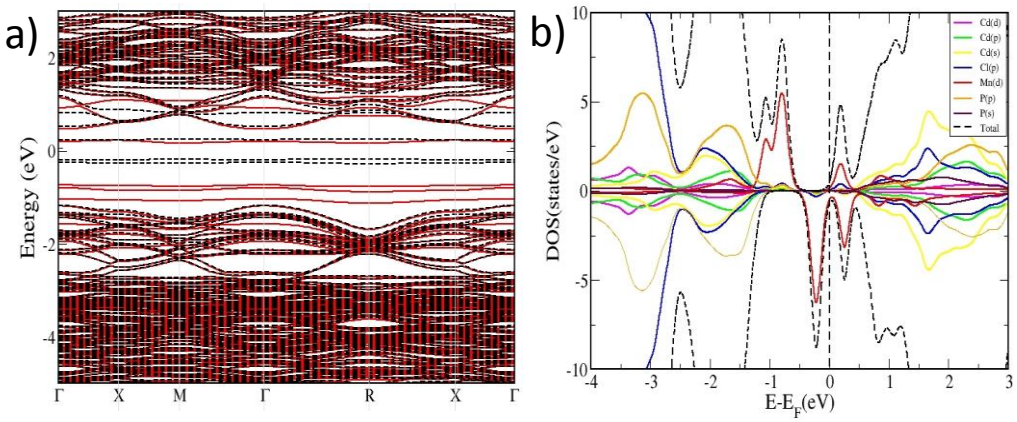


Figure 13. Electronic structure a) with red and black lines denoting energies of spin up and spin down states, and b) Spin polarized DOS with +ve and –ve DOS represent spin-up and spin-down states of $Cd_{6.75}Mn_{0.25}P_4Cl_6$; where Mn is substituted at the Cd1 position (MnCd1).

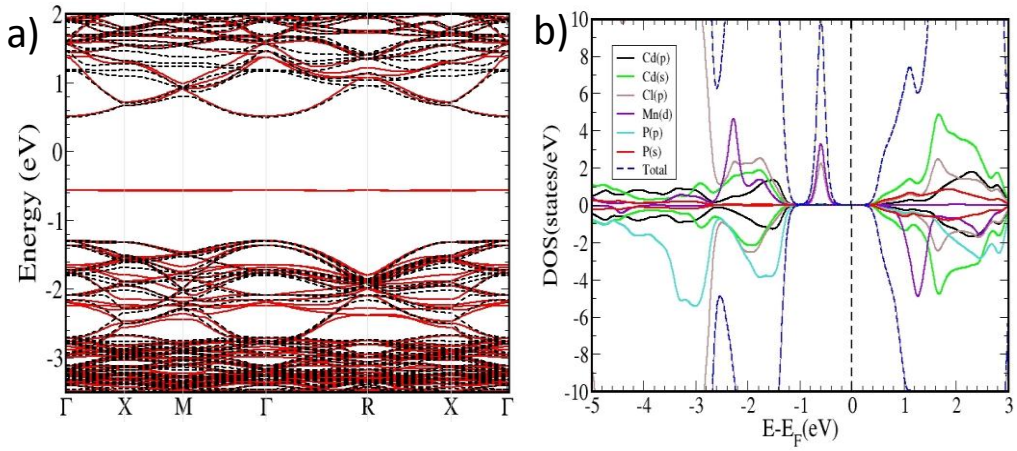


Figure 14. Electronic structure a) with red and black lines denoting energies of spin up and spin down states, and b) Spin polarized DOS with +ve and –ve DOS represent spin-up and spin-down states of $Cd_{6.75}Mn_{0.25}P_4Cl_6$; where Mn is substituted at the Cd2 position (MnCd2).

It is seen that the additional levels are introduced in the band gap compared to the pristine $Cd_7P_4Cl_6$. Spin polarized DOS shows that these are the spin-up states introduced by the Mn (d) and Cl(p) states. The band structure shows that the band gap is reduced with the introduction of Mn atoms.

| Structure | Relaxed-lattice parametrs (Å) | ΔE/cell = E*mag* – E*non-mag* (eV) | Magnetic moment (Mn moment in parenthesis) (μ**B**) |
|---|---|---|---|
| $Cd_{6.75}Mn_{0.25}P_4Cl_6$ (MnCd1) | a= 11.97, b= 12.11, c= 12.07 | -0.195 | 1.002 (1.058) |
| $Cd_{6.75}Mn_{0.25}P_4Cl_6$ (MnCd2) | a=b=c=12.07 | -0.117 | 4.519 (4.248) |

Table 2. The composition, theoretical estimates of lattice parameters, difference in free energy between magnetic and non-magnetic calculations, and magnetic moment of Cd7P4Cl6 with Mn substitution at Cd1 and Cd2 sites, calculated using VASP.

We optimize the compounds $Cd_7P_4Cl_6$ and $Cd_4P_2Cl_3$ using the software package VASP using GGA approximation and the free energy for the optimized structure with and without Mn substitution is shown in the **Table 3**. Now the main points that can be drawn from the datas are $Cd_4P_2Cl_3$ is more stable than $Cd_7P_4Cl_6$, from lowest energy point of view, which is in the line with the experimental findings wherein authors claims high temperature favours $Cd_4P_2Cl_3$ whereas $Cd_7P_4Cl_6$ forms at comparatively lower temperature. Now, taking the $Cd_7P_4Cl_6$ and substituting Mn atom in two different positions as shown in **Figure 12**, we see that the Mn substitution lowers the free energy significantly. This indicates that the compound is more stable with Mn substitution. From the energetics, it is seen that Cd2 position is easier to substitute with Mn, with lower energy. Probably this is due to the ease with which Mn can occupy the Cd position (**Figure 12b**), where all surrounding atoms are Cl, however for Cd1 position, both Cl and P atoms are there in the neighborhood. The difference in energy between the Mn substituted compound and the pristine compound is more negative for $Cd_7P_4Cl_6$, than $Cd_4P_2Cl_3$. Therefore, Mn incorporation is more prefered in $Cd_7P_4Cl_6$ phase compare to $Cd_4P_2Cl_3$ which is in the line with the experimental findings, wherein authors find higher Mn-concentration in $Cd_{7-y}Mn_yP_4Cl_6$ phases than $Cd_{4-x}Mn_xP_2Cl_3$.

| Compound | Free energy (eV) | ΔE (eV) |
|---|---|---|
| $Cd_7P_4Cl_6$ | -196.93 | |
| $Cd_{6.75}Mn_{0.25}P_4Cl_6(Mn_{Cd1})$ | -202.68 | -5.67 |
| $Cd_{6.75}Mn_{0.25}P_4Cl_6(Mn_{Cd2})$ | -204.17 | -7.24 |
| $Cd_4P_2Cl_3$ | -199.94 | |
| $Cd_{3.875}Mn_{0.125}$ $P_2Cl_3$ ($Mn_{Cd1}$) | -204.82 | -4.88 |
| $Cd_{3.875}Mn_{0.125}$ $P_2Cl_3$ ($Mn_{Cd2}$) | -198.54 | +1.4 |

Table 3. The free energy of $Cd_7P_4Cl_6$ and $Cd_4P_2Cl_3$ with and without Mn substitution. ΔE is the energy difference between the pristine $Cd_7P_4Cl_6$ or $Cd_4P_2Cl_3$ and the corresponding Mn substituted compound.

**Photocatalytic $H_2$ evolution**

The conduction and valence band positions of cadmium phosphochlorides have been reported theoretically as well as experimentally.[10] It possesses suitable alignment of conduction and valence band edges with respect to water redox potential and does indeed perform hydrogen evolution reaction (HER). We have investigated the effect of Mn-substitution on the visible-light-induced hydrogen evolution from cadmium phosphochlorides in this purpose, Pt (1wt%) was photo-deposited on the surface of pristine as well as manganese substituted compounds to study the photochemical HER in the presence of $Na_2S$ and $Na_2SO_3$ as a sacrificial electron donor. Pristine $Cd_4P_2Cl_3$ exhibited a HER activity of 1.69 mmol/h-g (**Figure 15a**). Since, $Cd_7P_4Cl_6$ exhibits superior HER activity than $Cd_4P_2Cl_3$, we anticipated a better HER performance of the mixed phase ($Cd_{4-x}Mn_xP_2Cl_3$+$Cd_{7-y}Mn_yP_4Cl_6$) with 3.8 % of manganese substitution. However, this mixture exhibited a HER activity of 0.88 mmol/h-g nearly two times lesser than pristine $Cd_4P_2Cl_3$ (**Figure 15a**).

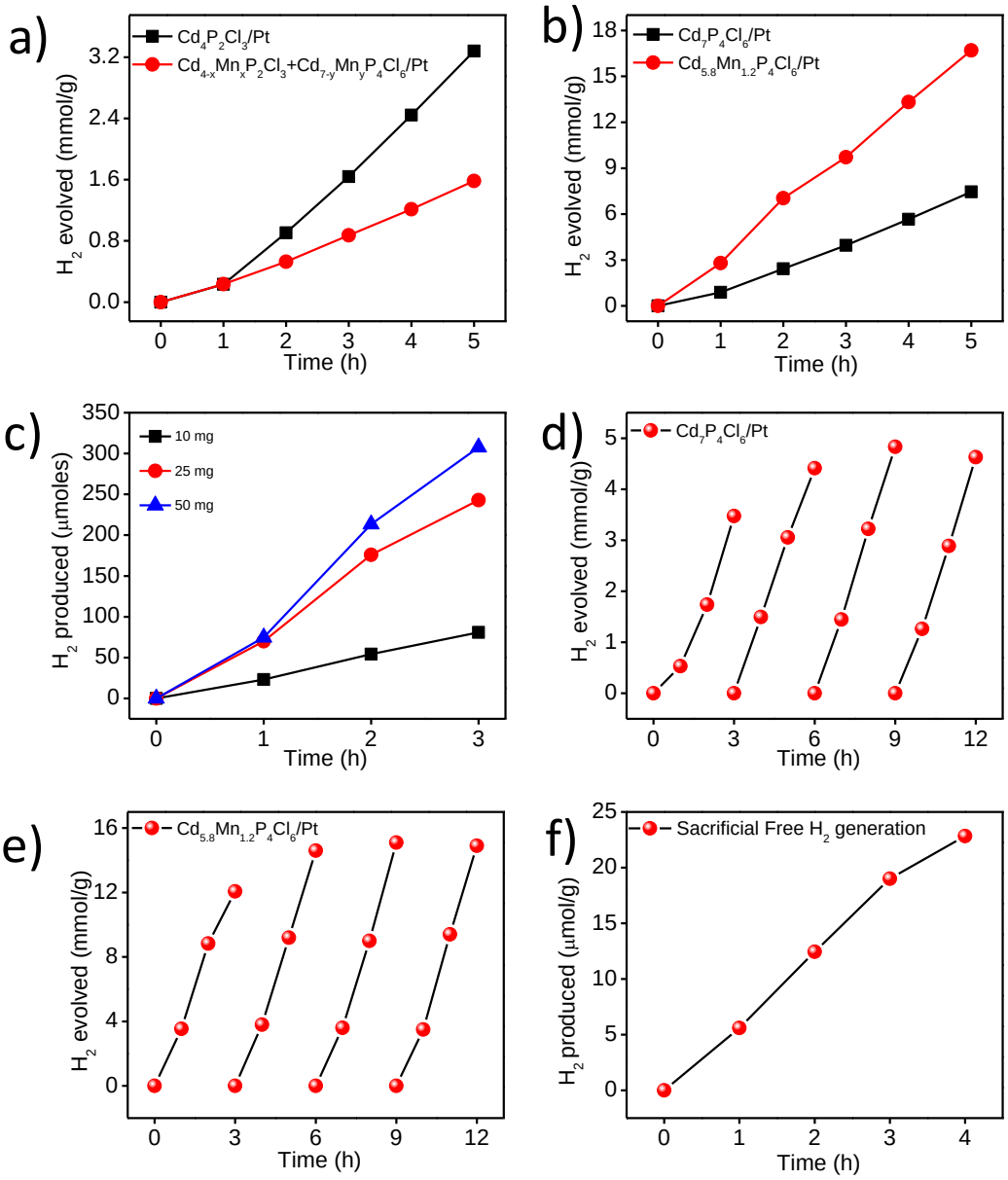


Figure 15. Time course of hydrogen evolution of a) $Cd_4P_2Cl_3$ versus mixed phase compound with 3.8 % Mn substitution, b) $Cd_7P_4Cl_6$ versus $Cd_{5.8}Mn_{1.2}P_4Cl_6$, c) Optimization of weight of semiconductor photocatalyst for HER. Cyclic Hydrogen evolution activity test for d) $Cd_7P_4Cl_6$ and e) $Cd_{5.8}Mn_{1.2}P_4Cl_6$ in the presence of 0.18 and 0.24 M $Na_2S$-$Na_2SO_3$ sacrificial electron donor. f) Time course of hydrogen evolution reaction obtained from $Cd_{5.8}Mn_{1.2}P_4Cl_6$ under sacrificial free reaction condition.

This decrease in the HER activity is probably due to the trapping of photogenerated electrons by the Mn-states below the conduction band minimum of cadmium

phosphochlorides. $Cd_7P_4Cl_6$ exhibits a HER activity of 4.07 mmol/h-g superior to the manganese substituted mixed phase compounds and pristine $Cd_4P_2Cl_3$ (**Figure 15b**). Interestingly, $Cd_{7-y}Mn_yP_4Cl_6$ exhibited superior activity than pristine $Cd_7P_4Cl_6$ unlike the mixed phases (with $Cd_{4-x}Mn_xP_2Cl_3$ as the major phase) which exhibits a lower HER activity than pristine $Cd_4P_2Cl_3$. A HER activity of 9.9 mmol/h-g has been obtained from $Cd_{5.8}Mn_{1.2}P_4Cl_6$ which is 2.5 times the HER activity of unsubstituted $Cd_7P_4Cl_6$ (**Figure 15b**). We optimized the weight of semiconductor photocatalyst for hydrogen evolution and found 25 mg as the optimum (**Figure 15c**). In order to examine the recyclability and stability of the semiconductors photocatalyst, we have carried out four HER cycles for a total duration of 12h. $Cd_7P_4Cl_6$ as well as $Cd_{5.8}Mn_{1.2}P_4Cl_6$ both exhibited an enhancement in the activity after the first cycle, and the activity remained consistent for all the cycles (**Figures 15d and 15e**). PXRD patterns of Pt loaded $Cd_7P_4Cl_6$ obtained after the cyclic HER study showed a broadening of peaks, suggesting a loss in crystallinity due to the leaching of $Cd^{2+}$ ions (**Figure 16a**). However, the PXRD pattern of Pt loaded $Cd_{5.8}Mn_{1.2}P_4Cl_6$ did not lose crystallinity and remained the same even after several HER cycles indicating its superior photostability (**Figure 16b**). It is remarkable that Mn-substituted $Cd_{5.8}Mn_{1.2}P_4Cl_6$ not only exhibits superior HER activity but also better photostability than pristine compound. In addition, Mn-substituted $Cd_{7-y}Mn_yP_4Cl_6$ performs robust hydrogen evolution reaction even in the absence of sacrificial electron donors unlike unsubstituted $Cd_7P_4Cl_6$ which undergoes severe damage and the HER activity reduces with time (**Figure 15f**).

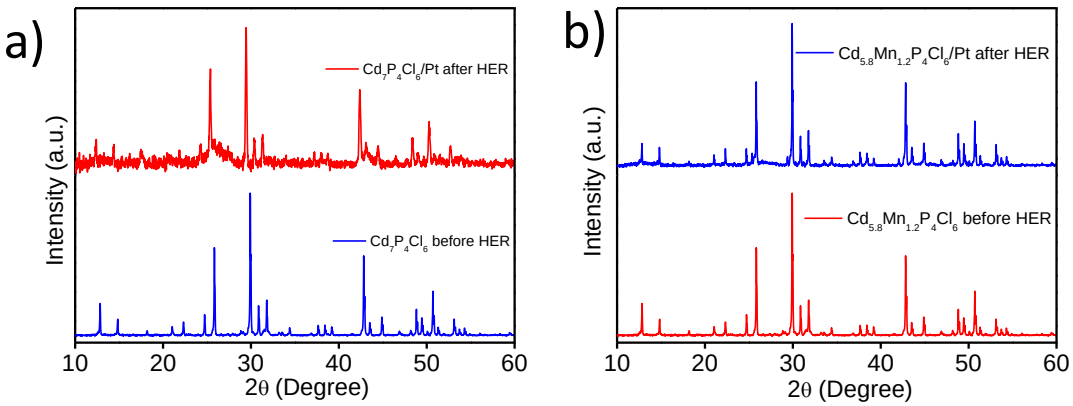


Figure 16. PXRD patterns of a) Pristine $Cd_7P_4Cl_6$, and b) $Cd_{5.8}Mn_{1.2}P_4Cl_6$, after their use in multiple cycles of hydrogen evolution reaction.

Considering the origin of the reduction in the HER activity of Mn-substituted $Cd_4P_2Cl_3$ to be the presence Mn-atomic states (behaving as electron traps) below the conduction band minima, we expected the same effect of manganese substitution on the HER activity of $Cd_7P_4Cl_6$ since their conduction band positions are close. Nevertheless, contrasting features of manganese substituted $Cd_{7-y}MnyP_4Cl_6$ with respect to the manganese substituted $Cd_{4-x}Mn_xP_2Cl_3$ suggest the role of the other factors on the catalytic activity. We have carried out photoelectrochemical measurements and studied the charge-carriers dynamics. Open circuit potential measurement of photoelectrodes demonstrate the process of charge carrier generation and recombination in semiconductors.[11] Pristine $Cd_4P_2Cl_3$ and $Cd_7P_4Cl_6$ exhibit a cathodic shift in the potential upon light irradiation, indicating n-type conductivity, similar to the earlier report (**Figures 17a and 17c**).[3] Mn-substituted $Cd_{4-x}Mn_xP_2Cl_3$+$Cd_{7-y}Mn_yP_4Cl_6$ exhibits same behavior upon light-irradiation (**Figure 17b**) suggesting no change in the conductivity after Mn-substitution, although there is a slow $V_{oc}$ build-up with respect to pristine $Cd_4P_2Cl_3$ suggests the formation of mid-gap or trap states, known to adversely affect the HER rate. In contrast to the cathodic shift of the potential in pristine $Cd_7P_4Cl_6$, manganese substituted analogues ($Cd_{5.8}Mn_{1.2}P_4Cl_6$ or $Cd_{6.1}Mn_{0.9}P_4Cl_6$) exhibited an anodic shift upon light irradiation, indicating p-type conductivity (**Figure 17d**). Even a high manganese concentration (15.6 % Mn substitution at the place of Cd) in the mixed phase compound, $Cd_{4-x}Mn_xP_2Cl_3$+$Cd_{3-z}Mn_zPCl_3$ did not change the nature of conductivity.

In order to further verify the nature of conductivity in the compounds with and without Mn-substitution, Hall measurements were carried out at room temperature on the rectangular pallet of samples. Hall measurements on pristine and Mn-substituted mixed phase compounds showed negative Hall coefficient (negative slope) of the mixed phase compound ($Cd_{4-x}Mn_xP_2Cl_3$+$Cd_{7-y}Mn_yP_4Cl_6$) confirming its n-type conductivity (**Figure 18**). Unlike the negative Hall coefficient of pristine $Cd_7P_4Cl_6$ compound (**Figure 19a**), $Cd_{5.8}Mn_{1.2}P_4Cl_6$, on the other hands exhibited positive Hall coefficient confirming p-type conductivity (**Figure 19b**).

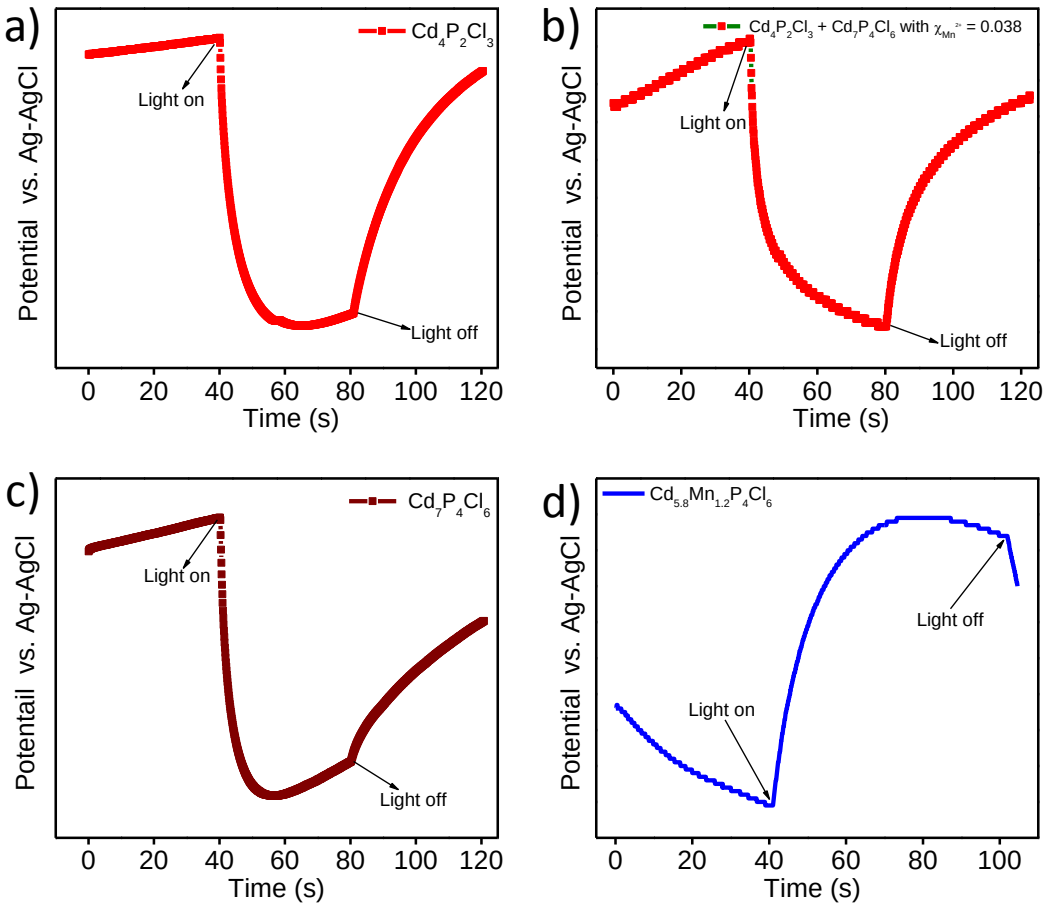


Figure 17. Open circuit potential (OCP) of a) pristine $Cd_4P_2Cl_3$, b) ($Cd_{4-x}Mn_xP_2Cl_3$+$Cd_{7-y}Mn_yP_4Cl_6$) with 3.8 % Mn substitution c) pristine $Cd_7P_4Cl_6$, and d) $Cd_{5.8}Mn_{1.2}P_4Cl_6$.

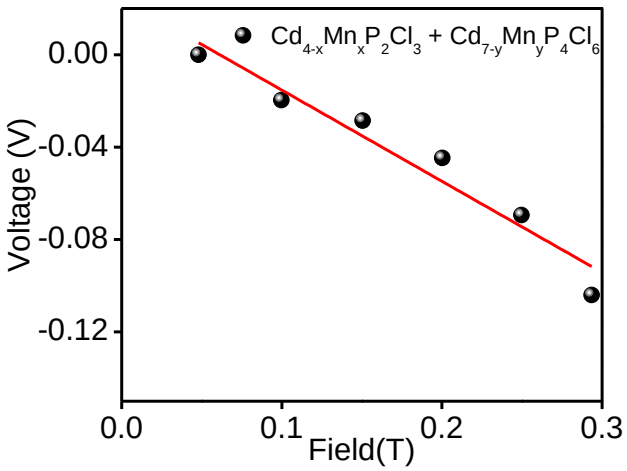


Figure 18. Variation of the Hall voltage with applied magnetic field in mixed phase compound with 3.8 % Mn-substitution.

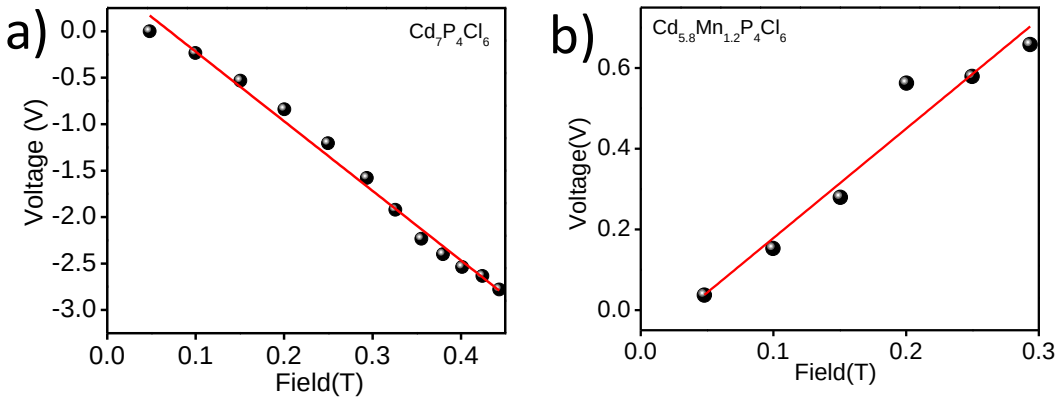


Figure 19. Variation of the Hall voltage with applied magnetic field in a) $Cd_7P_4Cl_6$, and b) $Cd_{5.8}Mn_{1.2}P_4Cl_6$.

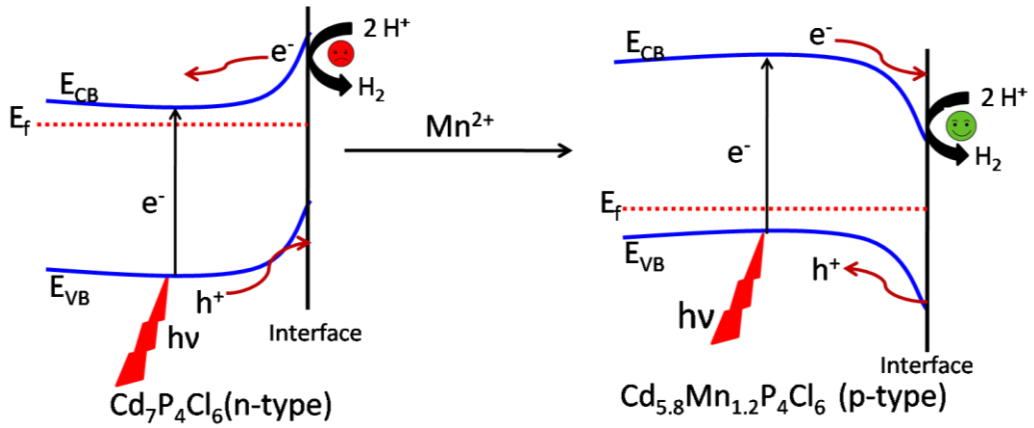


Figure 20. Mechanism of hydrogen evolution from n-$Cd_7P_4Cl_6$, and p-$Cd_{5.8}Mn_{1.2}P_4Cl_6$ compounds.

Since the photocatalytic activity of semiconductor materials is markedly influenced by the majority charge carriers, it was exciting to understand the effect of the change in the nature of majority carriers on the photocatalytic properties of these compounds. It is known that when an extrinsic semiconductor comes in the contact of an electrolyte bending of bands occur at the surface of the semiconductor in order to equilibrate the Fermi level.[12] A p-type semiconductor undergoes downward band bending in the contact of electrolyte, resulting in the concentration of photogenerated electrons at the semiconductor-$H_2O$ interface and holes are pushed towards the bulk of the semiconductor (**Figure 20**).[12] This decreases the surface charge recombination and increases the hot electron concentration at the interface (space charge regeion) which catalyzes the reduction of $H_2O$ into $H_2$.[13] In contrast, an n-type semiconductor

undergoes upward band bending in the contact of electrolyte, resulting in the electron migration towards the bulk of semiconductor and hole migration towards the interface, causing the decrease in the hot electron concentration at the interface and hence reduction in the $H_2O$ reduction process (**Figure 20**). This phenomenon clearly explains superior HER activity of p-type $Cd_{1-y}Mn_yP_4Cl_6$ over n-type $Cd_7P_4Cl_6$.

## 5. Conclusions

In summary, we have been able to dope high concentration of manganese in cadmium phophochlorides. Substitution of $Mn^{2+}$ ions in place of $Cd^{2+}$ results in the preferential formation of the low-temperature $Cd_7P_4Cl_6$ phase at high temperatures. $Mn^{2+}$ substitution is favored in $Cd_{7-y}Mn_yP_4Cl_6$ over $Cd_{4-x}Mn_xP_2Cl_3$. $Cd_{4-x}P_2Cl_3$ always crystallizes with impurity phases such as $Cd_{7-y}Mn_yP_4Cl_6$ (in the case of less $\chi_{Mn}^{2+}$ in precursor) or $Cd_{3-Z}Mn_zPCl_3$ (in the case of high $\chi_{Mn}^{2+}$ in precursor) whereas $Cd_{7-y}Mn_yP_4Cl_6$ crystallizes in pure form. UV-vis absorption spectra of the Mn-substituted compounds exhibit slight blue shift with respect to the pristine compounds. First-principles calculations suggest substitution of Mn reduces the free energy of system significantly in the case of $Cd_7P_4Cl_6$ resulting in the formation of Mn-substituted phase as the major product, consistent with the experimental findings. In addition, it is found that Mn-substitution is more favoured at the $Cd_2$ position (octahedrally coordinated by Cl atoms) than the $Cd_1$ position in this compound. Mn-substitution changes the electronic structure and the density of states. Mn-substitution in $Cd_{7-y}Mn_yP_4Cl_6$ causes change in the conductivity from n-type to p-type, whereas Mn substitution in $Cd_{4-x}Mn_xP_2Cl_3$ does not show such behaviour. $Cd_{7-y}Mn_yP_4Cl_6$ exhibits superior HER activity than pristine $Cd_7P_4Cl_6$. Superior HER activity of $Cd_{7-y}Mn_yP_4Cl_6$ is linked with the p-type conductivity.

# 6. References


[1] H. Rebbah, A. Rebbah, *J. Solid State Chem.* **1994**, *113*, 1-8.

[2] a) P. C. Donohue, *J. Solid State Chem.* **1972**, *5*, 71-74; b) A. V. Shevelkov, L. N. Reshetova, B. A. Popovkin, *J. Solid State Chem.* **1998**, *137*, 138-142.

[3] A. Roy, A. Singh, S. A. Aravindh, S. Servottam, U. V. Waghmare, C. N. R. Rao, *Angew. Chem. Int. Ed.*, *0*. doi:10.1002/anie.201900936

[4] a) H. Ohno, *Science* **1998**, *281*, 951; b) S. D. Sarma, *American Scientist* **2001**, *89*, 516-523.

[5] a) R. N. Bhargava, D. Gallagher, X. Hong, A. Nurmikko, *Phys. Rev. Lett.* **1994**, *72*, 416-419; b) S. Jana, B. B. Srivastava, N. Pradhan, *J. Phys. Chem. Lett.* **2011**, *2*, 1747-1752; c) R. Beaulac, P. I. Archer, S. T. Ochsenbein, D. R. Gamelin, *Adv. Funct. Mater.* **2008**, *18*, 3873-3891.

[6] R. Zeng, M. Rutherford, R. Xie, B. Zou, X. Peng, *Chem. Mater.* **2010**, *22*, 2107-2113.

[7] P. K. Santra, P. V. Kamat, *J. Am. Chem. Soc.* **2012**, *134*, 2508-2511.

[8] P. Giannozzi, S. Baroni, N. Bonini, M. Calandra, R. Car, C. Cavazzoni, D. Ceresoli, G. L. Chiarotti, M. Cococcioni, I. Dabo, A. Dal Corso, S. de Gironcoli, S. Fabris, G. Fratesi, R. Gebauer, U. Gerstmann, C. Gougoussis, A. Kokalj, M. Lazzeri, L. Martin-Samos, N. Marzari, F. Mauri, R. Mazzarello, S. Paolini, A. Pasquarello, L. Paulatto, C. Sbraccia, S. Scandolo, G. Sclauzero, A. P. Seitsonen, A. Smogunov, P. Umari, R. M. Wentzcovitch, *J. Phys: Condens. Mater.* **2009**, *21*, 395502.

[9] G. Kresse, J. Hafner, *Phys. Rev. B* **1994**, *49*, 14251-14269.

[10] A. Roy, M. Chhetri, S. Prasad, U. V. Waghmare, C. N. R. Rao, *ACS Appl. Mater. Interfaces* **2018**, *10*, 2526-2536.

[11] Y. Zhang, D. Wang, X. Zhang, Y. Chen, L. Kong, P. Chen, Y. Wang, C. Wang, L. Wang, Y. Liu, *Electrochimica Acta* **2016**, *195*, 51-58.

[12] Z. Zhang, J. T. Yates, *Chem. Rev.* **2012**, *112*, 5520-5551.

[13] M. G. Kibria, F. A. Chowdhury, S. Zhao, B. AlOtaibi, M. L. Trudeau, H. Guo, Z. Mi, *Nat. Commun.* **2015**, *6*, 6797.

# Summary of the Thesis

**Part 1** of the thesis describes the importance of semiconductor-based heterostructures for photochemical hydrogen production in the presence of sacrificial electron donors. The first chapter **(Chapter 1)** presents the introduction about photocatalytic water splitting and various factors which influences photocatalytic efficiency of materials to obtain solar energy to chemical energy transformation. The **Chapter 2** investigate the role of oxide nanostructures in the ZnO/Pt/CdS or $TiO_2$/Pt/$Cd_{0.8}Zn_{0.2}S$ heterostructures which are used for the very efficient hydrogen evolution reaction (HER) under visible-light irradiation. In these heterostructures CdS or $Cd_{0.8}Zn_{0.2}S$ act as photosensitizer which absorb visible-lights and generates electron-hole pairs. Vectorial transfer of photogenerated electrons from the conduction band of CdS or $Cd_{0.8}Zn_{0.2}S$ to the oxide conduction bands and finally at the Pt surface results in the very efficient separation of charge carriers and hence produces good HER activity. Investigation showed that in the case of $TiO_2$ or ZnO nanostructures with higher active surface area exhibit superior HER rate and vice-versa. In the case of $TiO_2$/Pt/$Cd_{0.8}Zn_{0.2}S$, $H_2Ti_3O_7$ with highest surface area exhibited highest HER rate whereas, in the case of ZnO/Pt/CdS, ZnO nanorod with highest surface area exhibited highest HER activity. Photocatalytic activities of all these heterostructures generally follow the trend in the BET surface areas of the oxide nanostructures wherein high surface area favoring higher hydrogen evolution activity.

**Chapter 3** describes the synthesis and use of $(TiO_2)_{1-x}(NiO)_x$/$Cd_{0.8}Zn_{0.2}S$ and ZnO/NiO/$Cd_{1-x}Zn_xS$ (x=0.0, 0.2) heterostructures for visible-light induced hydrogen generation wherein expensive and scarce Pt has been replaced by the earth abundant low coast co-catalyst NiO. Combination of NiO with $TiO_2$ or ZnO markedly changes the photocatalytic efficiency of the heterostructures in the presence of CdS or $Cd_{0.8}Zn_{0.2}S$ as a photosensitizer. While the $H_2$ evolution activity of $(TiO_2)_{1-x}(NiO)_x$/$Cd_{0.8}Zn_{0.2}S$ increases smoothly with NiO mole fraction up to x ~ 0.50, it increases further reaching a maximum at x ~ 0.83, yielding 1.6 mmol $h^{-1}g^{-1}$ (AQY ~ 2.9%) with $Na_2S$-$Na_2SO_3$ as sacrificial agents under visible-light irradiation we obtain 6.84 mmol $h^{-1}g^{-1}$ (AQY ~ 11.7%) and 13.5 mmol $h^{-1}$ $g^{-1}$ (AQY ~ 10%) with benzyl alcohol-acetic acid as sacrificial agents under visible and UV-visible light irradiation respectively. Thus, high hydrogen evolution activity to the tune of three times that due to Pt-containing heterostructures has been

attained, with a NiO mole fraction of 0.83 in the heterostructures. It seems likely that the p-n junction between n-$TiO_2$ and p-NiO plays a role in determining the photocatalytic activity. In the case of ZnO/NiO/CdS photocatalytic hydrogen evolution activity was good where NiO was used as heterostructures with ZnO, (ZnO/NiO) than that of where NiO was present as a solid solution ($Zn_{1-y}Ni_yO$). The hydrogen evolution activities of ZnO/NiO/CdS and ZnO/NiO/$Cd_{1-x}Zn_xS$ are 2.2 and 8.2 mmol $h^{-1}g^{-1}$ respectively with an apparent quantum yield of 2.3 and 14 % under visible-light irradiation. These values of activities are comparable or superior to those obtained with ZnO/Pt/$Cd_{1-x}Zn_xS$ and ZnO/Au/$Cd_{1-x}Zn_xS$ heterostructures.

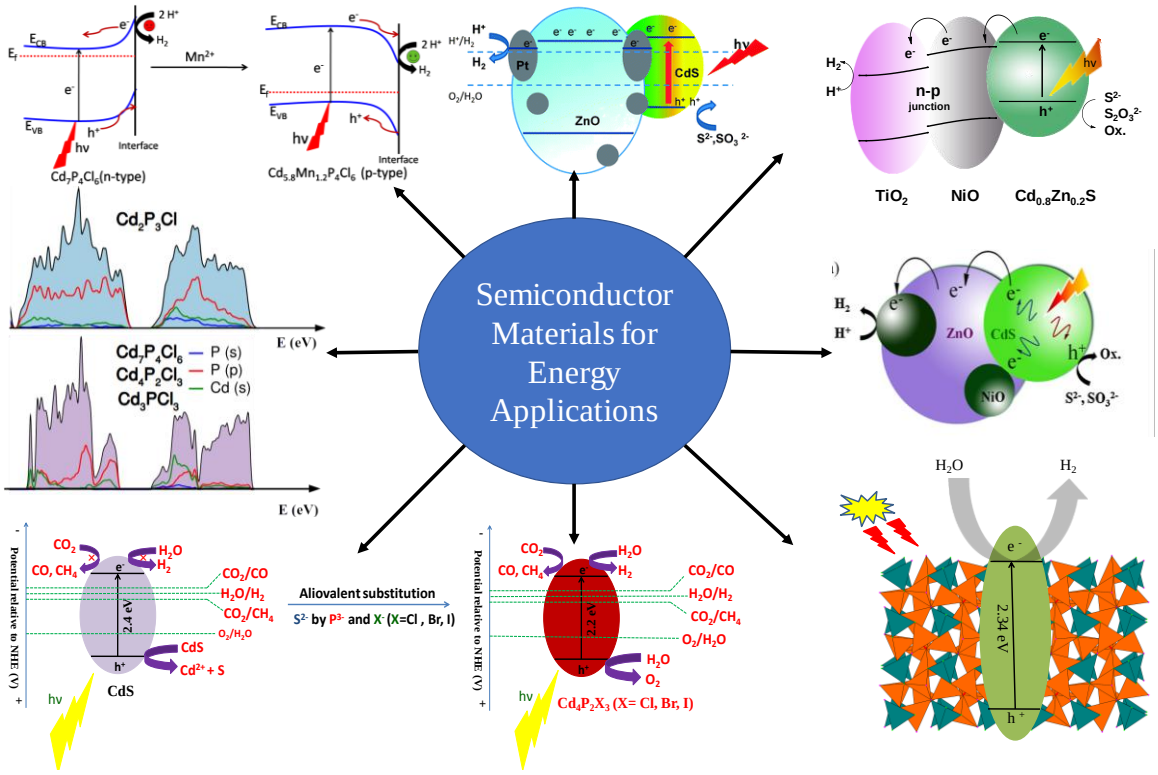


**Part 2** of the thesis describes the synthesis, properties and application of semiconductor materials obtained by partial or complete aliovalent substitution of ions. The **Chapter 1** presents a brief overview of aliovalent anionic substitution in transition metal oxides such as ZnO and $TiO_2$ and transition metal sulfides such as ZnS. **Chapter 2** gives the results of the investigation wherein CdS is co-substituted by P and Cl in the place of S. It was

found theoretically and experimentally that co-substitution of $P^{3-}$ and $Cl^{-}$ is more favored than the unisubstitution of either $P^{3-}$ or $Cl^{-}$ ions alone in CdS. First-principles DFT calculations showed that CdS and ZnS in hexagonal and cubic structures possesses a sub-band of the trivalent phosphorus with strong bonding with the cation appears in the gap just above the valence band, causing a reduction in the gap and enhancement of dielectric properties. It was found experimentally that P, Cl substitution in CdS results of the reduction in the band gap. Interestingly, substitution of Cl-alone in CdS does not change the absorption edge of the host but affects the photoluminescence properties.

**Chapter 3** describe the synthesis and properties of compounds of the compositions $Cd_4P_2Cl_3$, $Cd_4As_2Br_3$, and $Cd_4Sb_2I_3$ which are analogues of CdS, CdSe and CdTe respectively wherein the anions S, Se, and Te have been substituted by the aliovalent anions. The synthesis of $Cd_4P_2Cl_3$ has been achieved by three different routes. All the three compounds crystallize in the cubic structure, with two different kinds of cadmium atoms bound differently to the anions. Interestingly, these compounds are direct-gap semiconductors with the band gaps of 2.3, 1.9 and 1.8 eV in the case of $Cd_4P_2Cl_3$, $Cd_4As_2Br_3$ and $Cd_4Sb_2I_3$ respectively. These band gaps are comparable to the gaps of their analogues, CdS, CdSe, and CdTe respectively. All the compounds exhibit a photoluminescence band in the visible-region. First-principles calculations show the nature of alignment of conduction band positions of all the three compounds with respect to the water redox potential. $Cd_4P_2Cl_3$ exhibits much superior HER activity than the other two compounds. $Cd_4As_2Br_3$ exhibits superior activity than $Cd_4Sb_2I_3$ as predicted by the first-principle calculations. Hydrogen evolution in the absence of any sacrificial agent and the absence of photo corrosion seems to be unique features of $Cd_4P_2Cl_3$.

**Chapter 4** deals with the synthesis, properties and theoretical understandings of a family of cadmium phosphochlorides with members $Cd_2P_3Cl$, $Cd_3PCl_3$, $Cd_4P_2Cl_3$, and $Cd_7P_4Cl_6$. Motivated from the properties of $Cd_4P_2Cl_3$ we have investigated the other cadmium phosphochlorides and examined their properties. These compounds possess unique structural features and electronic properties. The phosphochlorides possess optical band gaps in the range of 1.87 to 2.70 eV which is sensitive to Cl/Cd and P/Cd ratios, the band

gap showing an increase with increasing Cl/Cd ratio and the P/Cd ratio having the opposite effect. Hence, $Cd_2P_3Cl$ with minimum Cl/Cd ratio possesses the smallest band gap (1.87 eV) whereas $Cd_3PCl_3$ with the highest Cl/Cd ratio possesses the largest band gap (2.70 eV). First-principles calculations have been employed to understand the bonding and electronic structures. Except for $Cd_2P_3Cl$, the other phosphochlorides possess direct band gaps. Dielectric constants and Born effective charges from first-principles calculations throw light on the bonding, hybridization and ionic character in these compounds. The band positions of these compounds are appropriate with respect to $H_2O$ redox potential for performing the water splitting reaction. All cadmium phosphochlorides exhibit hydrogen evolution reaction (HER) activities with $Cd_7P_4Cl_6$ showing best activity whereas $Cd_3PCl_3$ with least activity. The apparent quantum yield (20.1%) is highest in $Cd_7P_4Cl_6$ even without the assistance of a co-catalyst. Photoelectrochemical measurements were carried out to understand the HER activity of the compounds. The photostability under reaction conditions follow the trend $Cd_4P_2Cl_3$>$Cd_7P_4Cl_6$>$Cd_3PCl_3$~$Cd_2P_3Cl$.

**Chapter 5** in this part describe the combined experimental and theoretical studies on a family of a compounds of formula $Cd_4P_2X_3$ (X= Cl, Br, and I) wherein the effect of substitution of halides in $Cd_4P_2X_3$ has been studied. $Cd_4P_2Cl_3$ and $Cd_4P_2Br_3$ crystallize in the cubic structure whereas $Cd_4P_2I_3$ crystallizes in the orthorhombic structure. Interesting to note that the band gap of compounds varies in the range of 2.20 to 2.24 eV, indicating the change in halides do not affect the band gap in these compounds markedly. Unlike CdS, the $Cd_4P_2X_3$ compounds exhibit hydrogen evolution and $CO_2$ reduction from water even in the absence of a sacrificial agent or a co-catalyst. Use of $Ni_xP_y$ as the co-catalyst, enhances hydrogen evolution, reaching 3870 (AQY= 4.11) and 9258 $\mu molh^{-1}g^{-1}$ respectively under artificial and natural (sunlight) irradiation, in the case of $Cd_4P_2Br_3/Ni_xP_y$. Unlike most of the semiconductor-based photocatalysts, $Cd_4P_2X_3$ catalysts reduce $CO_2$ to CO and $CH_4$ in the absence of a sacrificial-agent or a co-catalyst using water as the electron source. CO, $CH_4$, and $H_2$ are obtained under artificial as well as sunlight irradiation. $Cd_4P_2Br_3$ is the best catalyst for the hydrogen evolution reaction

whereas $Cd_4P_2I_3$ shows the highest selectivity for $CO_2$ reduction. Comprehensive photoelectrochemical and theoretical studies have been employed to understand the catalytic behavior of this family of compounds. Electrochemical impedance and transient photocurrent measurements have shown least charge transfer resistance and highest photocurrent density in the case of $Cd_4P_2Br_3$ in accordance with its superior catalytic activity.

**Chapter 6** deals with the effect of Mn-substitution on the structural and photophysical properties of cadmium phosphochlorides. Among various cadmium phosphochlorides $Cd_4P_2Cl_3$ and $Cd_7P_4Cl_6$ with intermediate Cl/Cd ratios crystallize in the cubic structure with two different types of cadmium atoms and show striking difference in the optical band gaps. Substitution of paramagnetic $Mn^{2+}$ at the place of $Cd^{2+}$ in these cadmium phosphochlorides results in the formation of thermodynamically less favored $Cd_7P_4Cl_6$ compound at high temperature. Substitution of manganese is more preferred in $Cd_{7-y}Mn_yP_4Cl_6$ than $Cd_{4-x}Mn_xP_2Cl_3$. UV-vis absorption spectra of all the Mn-substituted compounds exhibit a slight blue shift concerning the pristine compounds. First-principles calculations illustrate the effect of Mn-substitution on the lattice parameters, electronic structure, and properties of these compounds. First-principles calculations suggest the substitution of Mn reduces the free energy of system significantly in the case of $Cd_7P_4Cl_6$ hence resulting in the formation of Mn-substituted phase as major product which is in line with experimental findings. In addition, it is found that Mn-substitution is more favored at $Cd_2$ position than $Cd_1$ position in this compound. Mn-substitution changes the electronic structure and related density of states in compounds. Substitution of Mn in $Cd_{7-y}Mn_yP_4Cl_6$ causes changes in the conductivity type from n-type (in the case of pristine $Cd_7P_4Cl_6$) to p-type. However, even a high amount of Mn incorporation in $Cd_{4-x}Mn_xP_2Cl_3$ could not change the conductivity type. Effect of Mn-substitution on the photochemical HER properties has been explored wherein the role of p-type conductivity on photochemical HER performance of samples has been illustrated.